Award Number: W81XWH-20-1-0576

TITLE: Low-Cost, High-Throughput 3D Pulmonary Imaging Using Hyperpolarized Propane Gas

PRINCIPAL INVESTIGATOR: Eduard Y. Chekmenev, Ph.D.

CONTRACTING ORGANIZATION: Wayne State University, Detroit, MI

REPORT DATE: August 2022

TYPE OF REPORT: Annual

PREPARED FOR: U.S. Army Medical Research and Development Command
Fort Detrick, Maryland, 21702-5012

DISTRIBUTION STATEMENT: Approved for Public Release;
Distribution Unlimited

The views, opinions and/or findings contained in this report are those of the author(s) and should not be construed as an official Department of the Army position, policy or decision unless so designated by other documentation

REPORT DOCUMENTATION PAGE

Form Approved
OMB No. 0704-0188

Public reporting burden for this collection of information is estimated to average 1 hour per response, including the time for reviewing instructions, searching existing data sources, gathering and maintaining the data needed, and completing and reviewing this collection of information. Send comments regarding this burden estimate or any other aspect of this collection of information, including suggestions for reducing this burden to Department of Defense, Washington Headquarters Services, Directorate for Information Operations and Reports (0704-0188), 1215 Jefferson Davis Highway, Suite 1204, Arlington, VA 22202-4302. Respondents should be aware that notwithstanding any other provision of law, no person shall be subject to any penalty for failing to comply with a collection of information if it does not display a currently valid OMB control number. **PLEASE DO NOT RETURN YOUR FORM TO THE ABOVE ADDRESS.**

1. REPORT DATE	2. REPORT TYPE	3. DATES COVERED
August 2022	Annual	15Jul2021-14Jul2022

4. TITLE AND SUBTITLE
Low-Cost, High-Throughput 3D Pulmonary Imaging Using Hyperpolarized Propane Gas

5a. CONTRACT NUMBER
W81XWH-20-1-0576

5b. GRANT NUMBER

5c. PROGRAM ELEMENT NUMBER

6. AUTHOR(S)
Eduard Y. Chekmenev, Ph.D.

E-Mail: chekmenev@wayne.edu

5d. PROJECT NUMBER

5e. TASK NUMBER

5f. WORK UNIT NUMBER

7. PERFORMING ORGANIZATION NAME(S) AND ADDRESS(ES)
Wayne State University
5101 Cass Ave
DETROIT, MI, 48202

8. PERFORMING ORGANIZATION REPORT NUMBER

9. SPONSORING / MONITORING AGENCY NAME(S) AND ADDRESS(ES)
U.S. Army Medical Research and Development Command
Fort Detrick, Maryland 21702-5012

10. SPONSOR/MONITOR'S ACRONYM(S)

11. SPONSOR/MONITOR'S REPORT NUMBER(S)

12. DISTRIBUTION / AVAILABILITY STATEMENT
Approved for Public Release; Distribution Unlimited

13. SUPPLEMENTARY NOTES

14. ABSTRACT
This report covers the second year of this three-year project. During the indicated period of performance, we have focused our activities on all three specific aims. With regards to Aim #1 (to develop a clinical low-cost and high-throughput device for production and administration of HP propane contrast agent for ultimate research use in volunteers), we have continued working on testing the robustness of the portable propane hyperpolarizer device. With respect to Aim #2 (To develop a safe method for HP propane gas administration and utilization, and test the purity and safety of the HP contrast agent produced by our device) we have employed previously developed approaches (during Y1) to continue work on testing the quality of the produced gas in the context of reaction completeness and the levels of polarization. While the progress of working on all aims of this project has been substantially impacted by the COVID-19 pandemic, this year we made some progress towards Aim #3 (To assess the feasibility of MRI using HP propane gas for *in vivo* functional imaging of normal lungs and in a bleomycin-induced COPD model in sheep)—specifically, we have completed the installation of 0.35 T clinical MRI scanner, performed personnel training, and installed ^{129}Xe torso imaging coil and performed MRI scanner upgrade with ^{129}Xe capability at WSU. Moreover, the partnering site (SIUC) has completed installation of a portable MRI scanner and has demonstrated its utility for hyperpolarized proton MRI.

15. SUBJECT TERMS
low-field MRI; pulmonary imaging, high-throughput; low cost

16. SECURITY CLASSIFICATION OF:			17. LIMITATION OF ABSTRACT	18. NUMBER OF PAGES	19a. NAME OF RESPONSIBLE PERSON
a. REPORT	b. ABSTRACT	c. THIS PAGE			USAMRDC
Unclassified	Unclassified	Unclassified	Unclassified	114	19b. TELEPHONE NUMBER *(include area code)*

Table of Contents

Page

1. INTRODUCTION 4

2. KEYWORDS 4

3. ACCOMPLISHMENTS 5

SUBTASK #1-3: OPTIMIZE PROPANE HYPERPOLARIZER PERFORMANCE 5

SUBTASK #2-2: ASSESS PURITY OF PRODUCED HP PROPANE GAS BY DETECTING THE EXCIPIENTS 6

WHAT OPPORTUNITIES FOR TRAINING AND PROFESSIONAL DEVELOPMENT HAS THE PROJECT PROVIDED? 9

HOW WERE THE RESULTS DISSEMINATED TO COMMUNITIES OF INTEREST? 9

4. IMPACT 9

WHAT WAS THE IMPACT ON THE DEVELOPMENT OF THE PRINCIPAL DISCIPLINE(S) OF THE PROJECT? 9

WHAT WAS THE IMPACT ON OTHER DISCIPLINES? 9

WHAT WAS THE IMPACT ON TECHNOLOGY TRANSFER? 9

WHAT WAS THE IMPACT ON SOCIETY BEYOND SCIENCE AND TECHNOLOGY? 9

5. CHANGES / PROBLEMS 9

6. PRODUCTS 10

ORAL PRESENTATIONS. 10

CONFERENCE ABSTRACTS 10

PEER-REVIEWED MANUSCRIPTS, DISSERTATION & BOOK CHAPTERS 10

INVENTIONS, PATENT APPLICATIONS AND LICENSES: 11

FUNDING APPLIED FOR BASED ON WORK SUPPORTED BY THIS AWARD 11

7. PARTICIPANTS & OTHER COLLABORATING ORGANIZATIONS 12

INDIVIDUALS WHO WORKED ON THE PROJECT 12

HAS THERE BEEN A CHANGE IN THE ACTIVE OTHER SUPPORT OF THE PD/PI(S) OR SENIOR/KEY PERSONNEL SINCE THE LAST REPORTING PERIOD? 16

8. SPECIAL REPORTING REQUIREMENTS 17

COLLABORATIVE AWARD 17

9. APPENDICES 18

APPENDIX 1: ORIGINAL STATEMENT OF WORK, YEARS 1-3 18

APPENDIX 2: ABSTRACTS PRESENTED AND MANUSCRIPTS PUBLISHED AND ACCEPTED 20

1. Introduction

We are developing a low-cost and high-throughput propane hyperpolarization and 3D sub-second imaging technology that can be potentially employed for functional MRI imaging of lungs, and that can be deployed to remote areas without specialized infrastructure (e.g. cryogens). The other essential component, the FDA-approved 0.35 T MRI scanner, is already commercially available. Thus, the integrated imaging platform (0.35 T MRI scanner and propane hyperpolarizer) will enable high-throughput population screening and monitoring response to treatment for a wide range of lung diseases. The end result of the project will be the development of a clinical propane hyperpolarizer, *in vivo* validation of the hyperpolarizer and contrast agent administration system, and commercialization. The next step will be an FDA-approved clinical trial. We focus our research effort on the high-risk critical challenges that must be solved to enable clinical implementation of hyperpolarized gases for pulmonary imaging.

Here, we propose taking the next significant step to develop and test a hyperpolarized propane production technology device under the Specific Aims described below:

Specifically, the research efforts during Year 2 have focused on all three Specific Aims as described in the Statement of Work (Appendix 1). The work under Aim #3 (substantially delayed due to covid-19 pandemic) has resumed as discussed below.

Aim 1. Develop a clinical low-cost and high-throughput biomedical device for production of hyperpolarized propane contrast agent: the future propane hyperpolarizer will be developed to enable its Good Manufacturing Practices (GMP), mass-production, and robust use.

Our efforts have focused on studying the robustness of polarizer operation with respect to its preparation (including catalyst packaging with inert copper media), chemical conversion, level of polarization, and percentage of active ingredient (Rh) deposition on the surfaces of titania catalyst supports.

We have also investigated the feasibility of butane gas hyperpolarization using butane and butadiene hydrogenation precursors.

Aim 2. Develop a safe method for HP propane gas administration and utilization, and test the purity and safety of the HP contrast agent produced by our device.

The activities during Year 2 of the project primarily focused on using a new approach for safe gas administration. We have also performed extensive quantitative testing of propylene impurities in produced HP propane gas batches.

Aim 3. Assess the feasibility of MRI using HP propane gas for *in vivo* functional imaging of normal lungs and in a bleomycin-induced COPD model in sheep. We will compare the effectiveness of hyperpolarized propane MRI to that using a more established contrast agent (hyperpolarized ^{129}Xe gas—created using a polarizer we developed in our previous DOD-funded work), and also to the standards of care: computed tomography and spirometry. Furthermore, we will also investigate the effectiveness of hyperpolarized propane gas MRI to monitor the progression of bleomycin-induced lung injury in the sheep animal model.

No progress was made towards this Aim during Y1 of the project due to compounding effects of the pandemic, because the 0.35 T MRI scanner (proposed for this work) could not be installed during Year 1. In Year 2, we have worked with the Health safety committee at Wayne State University to facilitate the installation visit of two vendors engineers to perform installation or MRI scanner and its upgrade to enable ^{129}Xe scanning. We have also performed personnel training, which was largely performed remotely. The installation process took approximately 2 months. This is a critical milestone that will allows us to make progress in the future. The partnering PI SIUC site has successfully completed the acquisition and installation of portable low-field MRI scanner, and started its utilization in hyperpolarized MRI research.

2. Keywords

Low-field MRI, lung imaging, molecular imaging, functional imaging; propane; xenon-129; NMR; MRI; hyperpolarization.

3. ACCOMPLISHMENTS

Please refer to Appendix 1 for the statement of work (SOW) of the entire project. The following sections describe the specific areas/tasks of the project performed during Year 2 of this project. As detailed in the corresponding section below, our research progress has been delayed substantially due to compounding challenges of covid-19 pandemic.

Aim 1. To develop a clinical low-cost and high-throughput device for production and administration of HP propane contrast agent for ultimate research use in volunteers.

Subtask #1-3: Optimize propane hyperpolarizer performance

Systematic studies of the new reactor. A new portable and handheld propane polarizer design was reported last year. Moreover, we have developed approaches for quantitative characterization of a given propane hyperpolarizer with respect to: 1) level of residual (unreacted) propylene and 2) level of proton polarization. Specifically, we have developed an automated protocol for data analysis to measure propane polarization and residual propylene fraction using a 1.4 T bench-top NMR spectrometer (see last year report). We have determined that the presence of a small excess of parahydrogen in the propylene:parahydrogen mixture (by ~5%) does not lead to any substantial loss of polarization or changes in relaxation properties – we have performed over 200 hyperpolarization runs with propane alone in a systematic manner using over 10 reactor modules filled with ~200 mg of 1% Rh/TiO_2 and ~6 g of inert copper metal. Based on the results of our studies, we have concluded that 1) 100% chemical conversion of propylene is achieved even under conditions of high flow rates (over 10 standard liters per minute); 2) we achieve 1% propane polarization robustly and reproducibly with our standard preparation procedure; 3) the reactors maintain their performance (without any noticeable decrease of performance) for preparing tens of liters of HP propane gas (corresponding to over 20 doses of HP propane gas – based on the results so far, we anticipate that a reactor could be reused for at least 100 cycles). The limited longevity studies revealed that reactor performance may deteriorate (detected as decrease of propane polarization level and reduction of chemical conversion), but we were not able yet to make any quantitative measurements yet. These results were presented at two conferences and one workshop and are being prepared for publication.

Catalyst concentration. So far, we have performed the bulk of our studies with 1% Rh/TiO_2 catalyst. Because Rh is a relatively expensive metal, we have investigated the feasibility of performing propane hyperpolarization with lower Rh nanoparticle loading. Specifically, we have studied the performance of 1%, 0.1% and 0.01% Rh loading. Propane polarization was similar in all three cases, but the chemical conversion efficiency was markedly decreased for 0.01% loading—clearly indicating that we have reached the limit of catalytic conversion activity for this material. Therefore, we conclude that 0.1-1% catalyst load would be a good choice for biomedical applications.

Catalyst concentration. Previously, we have performed studies to investigate the limits of T_1 and T_S (singlet) relaxation of hyperpolarized propane, efforts that clearly indicated that per-deuteration of propylene substrate does not improve the relaxation properties of HP propane gas (for reference, T_S is ~3 seconds at clinically relevant conditions of 1 atm). Therefore, we have looked into feasibility of butane hyperpolarization as a potential alternative to propane hyperpolarization. We have found that butadiene substrate is “toxic” to our catalyst and resulted in quick reactor poisoning (observed as loss of hydrogenation activity and levels of polarization). Butene-1 and butene-2 substrates have also been investigated. Remarkably, both precursors lead to production of HP butane, seen as HP resonances of methyl and methylene protons. We hypothesized that butane-2 undergoes the process of isomerization on our catalyst, leading to the same intermediate—we have confirmed this hypothesis by preparing a 3-D-propylene (i.e., mono-deuterated in position 3) precursor and its hydrogenation studies that revealed that pairwise parahydrogen addition follows 1,2- and 2,3- routes (studies are in progress to investigate the feasibility of 1,3-addition). Systematic relaxation studies of HP butane indeed revealed longer (by ~20%) T_1 and T_S for this larger (compared to propane) molecule. This gain in relaxation constants is welcomed in the context of biomedical applications because the HP state can be retained longer. Polarization levels of HP butanes were similar to that of propane. However, one translational disadvantage of HP butane was quickly realized – the maximum partial butene gas pressure was approximately 3 times lower than that of propene, resulting in undesirable gas condensation in our apparatus. While this may not necessarily be a show-stopper for clinical translation of HP butane, low precursor pressure limits the propelling capacity of the content for the hyperpolarization process. These results are being prepared for publication in three separate manuscripts.

The efforts in Y3 (for Aim 1) will focus on development of good manufacturing practices and the preparation of a bill of materials for our propane hyperpolarizer.

Specific Aim 2 - To develop a safe method for HP propane gas administration and utilization, and test the purity and safety of the HP contrast agent produced by our device.

Subtask #2-2: Assess purity of produced HP propane gas by detecting the excipients

As described above (our progress under Aim 1), we have developed an automated spectroscopic protocol to detect residual propylene in produced gas mixtures. Using this approach and ~5% parahydrogen excess in the gas mixture, we have been able to consistently achieve complete precursor conversion: no residual propylene was detected in the produced propane gas.

In Y3, elemental analysis for excipients (Rh, Ti, Si, Al, Cu) using our polarizer design will be performed. We will also work on confirming the capturing of used propane gas by the carbon filters to mitigate any residual flammability of the HP propane gas contrast agent.

Specific Aim 3 - To assess the feasibility of MRI using HP propane gas for *in vivo* functional imaging of normal lungs and in a bleomycin-induced COPD model in sheep.

0.35 T clinical MRI scanner installation at WSU site. As reported previously, in Year 1 of the project, we could not make any progress towards Aim 3 due to covid-19 pandemic restrictions because the MRI scanner installation was incomplete due to travel restrictions in the US and other countries. With the third scheduling attempt and in coordination with WSU health and safety committee, we were able to schedule the installation of the MRI scanner. Two engineers based in India and Indonesia traveled to WSU to complete the scanner installation, with total duration of their stay exceeding three months.

The 0.35 MRI scanner was installed without any substantial challenges (besides covid-related limitations on the WSU campus). Following scanner installation, the WSU team (consisting of the PI, a PD fellow and two PhD students, see Figure 1(left)) was trained to use this MRI scanner for proton imaging. One week of rigorous training covering the MRI fundamentals was supplied by the vendor in person and also remotely (to mitigate covid-related issues). This 0.35 T MRI scanner fully met the vendor's specification and the accreditation requirements in the US for clinical utilization. Following scanner installation, the trainees took turns for their hands-on experience with this MRI scanner. **Figure 2** shows an example of a practice session to record high-resolution images of squash by the trainees.

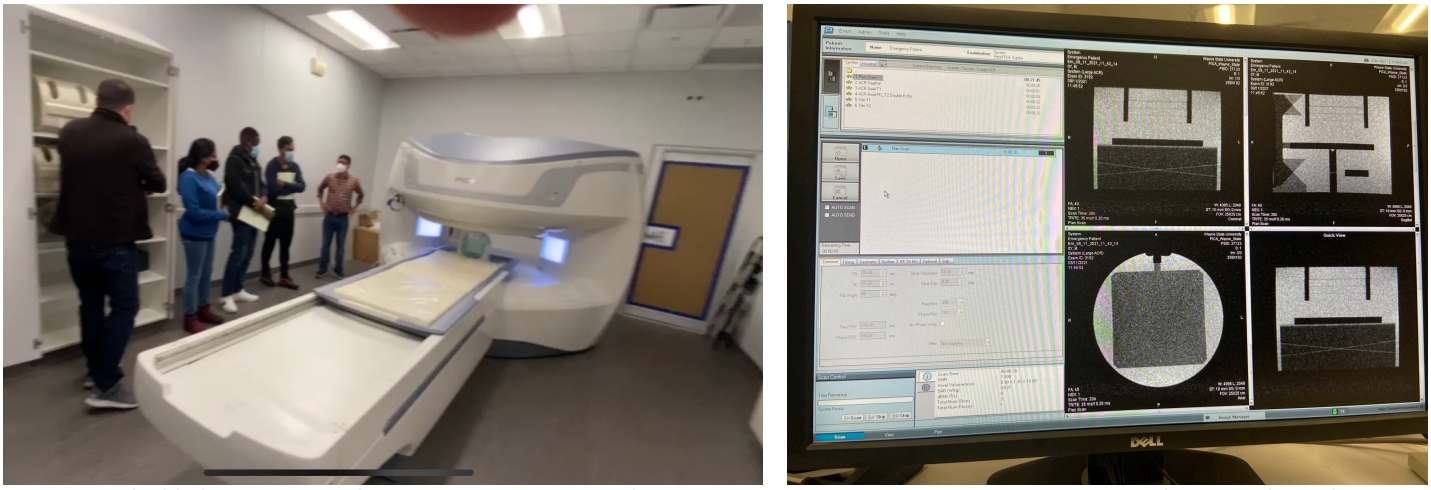

Figure 1. (**left**) Screenshot of the video recording of the MRI scanner training session at the WSU site. (**right**) Regular clinical quality assurance of the MRI phantom for the installed 0.35 T MRI scanner.

0.35 T clinical MRI scanner upgrade for ^{129}Xe capability. The standard configuration of this MRI scanner (as with any clinical MRI scanner) allows for scanning protons. The scanner purchase also included a scanner upgrade to be able to perform ^{129}Xe scanning natively using the scanner environment. The vendor has delivered a ^{129}Xe detection torso RF coil, and also installed a ^{129}Xe transmit coil inside the MRI scanner. In this sense, the ^{129}Xe capability is designed and built for our typical clinical workflow (instead of using a custom-made single transmit and receive coil). While the upgrade has been successful overall, we were not able to properly calibrate the ^{129}Xe transmit RF coil (in a straightforward manner), which we will continue working on with the vendor on developing the advanced approaches for RF coil calibration. This is not a trivial task since ^{129}Xe does not ordinarily have sufficient sensitivity in the non-hyperpolarized state. Nevertheless, we remain optimistic that we will be able to develop a good approach for pulse calibration.

Having this scanner installed at WSU clears a substantial roadblock for the overall progress of this project. We anticipate the activities in Year 3 will focus heavily on phantom imaging, and we will likely be requesting the no-cost extension to allow for sufficient amount of time for in vivo studies.

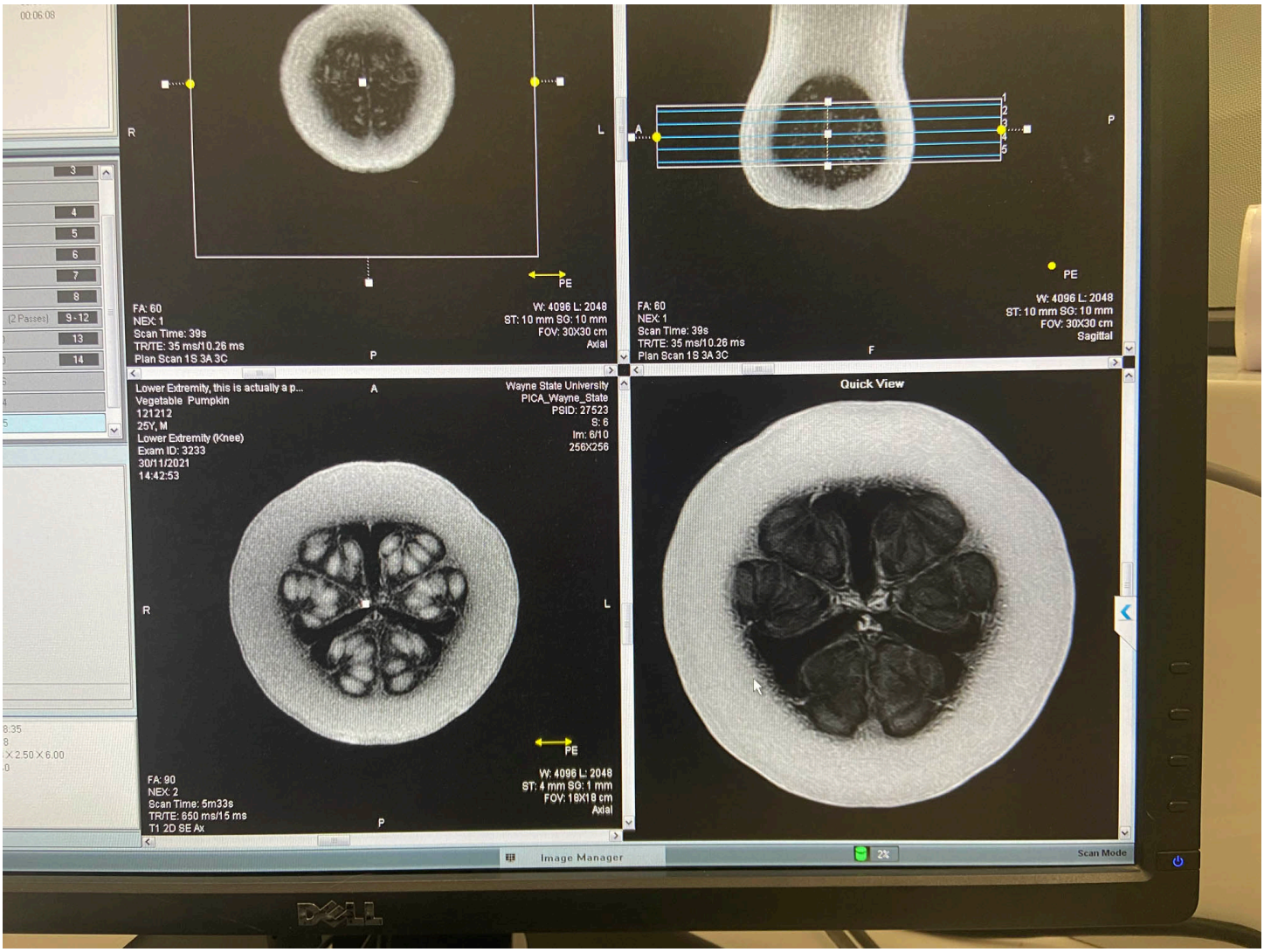

Figure 2. Photograph from an imaging session involving high-resolution multi-slice imaging of a squash.

Portable MRI scanner installation at SIUC. MRI can provide exquisite high-resolution images of anatomical features, function, and pathology of soft tissues in the body, without ionizing radiation. However, the increasingly stronger magnets used in most clinical scanners (~1–7 T) are expensive, bulky, and immobile, and the scans can be time-consuming and confining for many patients. Moreover, these stronger magnetic fields (along with concomitantly higher RF resonance frequencies) can present safety concerns in some circumstances, as well as contraindications for a number of patients and health conditions. Low-field (LF) MRI has gained renewed interest because it can potentially obviate all of these limitations. However, signal strength, detection sensitivity, and contrast limitations present ongoing challenges to many LF MRI technologies and their applications.

One approach to mitigate the sensitivity and contrast limitations of conventional NMR/MRI is hyperpolarization, which can increase NMR/MRI detection sensitivity by orders of magnitude. Moreover, because the magnetization is endowed by a given hyperpolarization method (and not the magnet), hyperpolarized (HP) LF MRI can even be more sensitive than high-field MRI. Thus, hyperpolarization can be highly synergistic with LF MRI, particularly if the hyperpolarization technique is itself low-cost, rapid, and portable. One such approach is signal amplification by reversible exchange (SABRE). In SABRE, para-hydrogen (p-H_2) and molecular substrates are transiently bound to organometallic complexes (“catalysts”), allowing spin order to transfer spontaneously from p-H_2 to substrates when placed within an appropriate magnetic field.

With current DoD support, we have sited a new type of portable, point-of-care, low-field (64 mT) clinical MRI scanner (Hyperfine) in the partnering PI’s Lab at SIUC, **Figure 3**. This type of scanner has already been demonstrated elsewhere in clinical settings for bed-side imaging, including of brain injury and cerebral

hemorrhage. Here we are investigating the potential for adapting this type of MRI scanner for use with HP substances. While we will report more of this effort next cycle, we are pleased to report here a brief summary of some of our initial efforts (which we have presented at this past ENC conference and are currently writing up for publication).

Figure 3. The portable, point-of-care 64 mT clinical MRI scanner (Hyperfine "Lucy") in the Goodson Lab at SIUC. Scanner runs with a wireless (iPad), and DICOM images are stored on a cloud server.

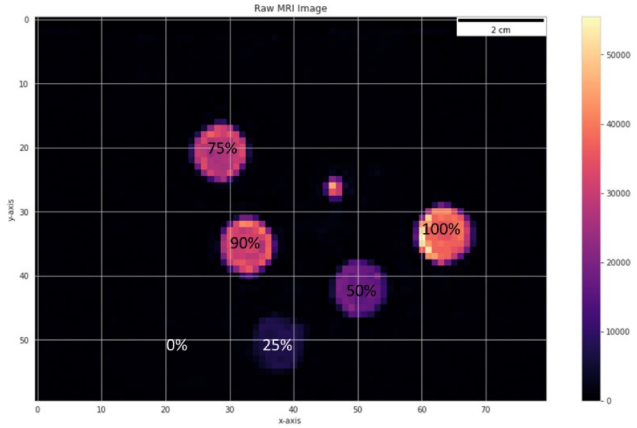

Figure 4. Demonstration of SABRE-enhanced ^{1}H low-field MRI. The image shows MRI signals from a central tube (smallest circular cross-section) containing a SABRE catalyst and 100 mM of pyrazine in deuterated methanol; outer circles are from thermally polarized water in falcon tubes with different concentrations of protonated water (100%, 90%, 75%, 50%, 10%, 0%) in deuterated water. Image was obtained with a fast spin echo (FSE) sequence under conditions of slow but continuous p-H_2 bubbling (<20 sccm).

In one study, pyrazine was successfully hyperpolarized via SABRE under continuous p-H_2 bubbling conditions and the HP agents were imaged using the 64 mT clinical MRI scanner (**Figure 4**). A 5 mm NMR tube was filled with a deuterated methanol solution containing the iridium-based SABRE catalyst and 100 mM of pyrazine. The sample was connected to a p-H_2 "bubbler" (~65 psi). Following confirmation of ^{1}H SABRE on a benchtop spectrometer, SABRE MRI was demonstrated with pyrazine following sample transfer to the 64 mT MRI and in situ imaging under continuous but reduced p-H_2 flow (20 sccm); low-field scanners suffer much less from susceptibility distortions, enabling imaging with gentle bubbling. The absence of signal in a control image using deuterated pyrazine (not shown) supports the conclusion that the p-H_2-enhanced MRI signal is coming from SABRE-hyperpolarized pyrazine (and not, say, from hyperpolarized o-H_2 or hydrides). The use of phantoms containing known and varying quantities of H versus D spins enabled the development of a simple approach to quantify the product of concentration and polarization from a given region of an image with good reliability. This approach allowed the ^{1}H SABRE enhancement in the central tube of the image to be estimated (~240-fold).

The current results demonstrate the ability to easily image and quantify SABRE hyperpolarization under in situ conditions of continuous p-H_2 delivery within the 64 mT MRI scanner. However, these conditions are non-ideal for two reasons: 1) 64 mT is non-optimal for ^{1}H SABRE (the field is too strong for efficient transfer of spin order); and 2) the current approach using standard sequences and parameters does not allow for "ultrafast" imaging of a bolus of an administered HP agent (thus missing out on one of the inherent advantages offered by hyperpolarization). Thus, ongoing / future efforts include optimization of the MRI sequences for faster SABRE imaging, as well as integration of the SABRE HP apparatus with a continuous recirculation setup to enable SABRE at optimal fields (e.g. ~6 mT) and rapid movement of HP liquids to the scanner, for extended periods of time. We also will investigate scaling up of the HP agent production to allow stopped-flow or continuous SABRE imaging of larger objects. Finally, we will also be working to adapt our approach to more biologically relevant target molecules / agents.

What opportunities for training and professional development has the project provided?

Students and other trainees attended conferences (virtually and in person) and presented results. For example, along with the PI and partnering PI, a number of students (including grad students Md Shahabuddin Alam, Ishani Senanayake, Tobi Gafar, Nadiya Iqbal, Shiraz Nantogma, Raduan Chowdhury, Clementinah Oladun, and Firoz Ahmed, undergrads Drew Brittin, Tony Petrilla, Maggie Pugh, and postdoc Nuwandi Ariyasingha, attended in person the 63rd ENC conference this past April (grad student Zahid Siraj attended virtually); all helped to present the posters listed in the products section (for most of them, it was their first in-person conference). The WSU team members attended selected sections of the ISMRM conference virtually. We can also mention that both our groups attended a recent all-day SABRE-simulations training seminar that was presented by Dr. Jacob Lindale, of the Warren Lab at Duke. Students at both sites are currently being trained in synthesis, catalysis, characterization, and NMR. Lastly, students at both sites received MRI training for the above-mentioned MRI scanners installed at each site.

In other news: In the last cycle, Nuwandi Ariyasingha (former PhD student at WSU), became a postdoc and successfully submitted an F32 application to NHLBI (this application was reported in our last-year progress report), which was funded. The partnering PI (Goodson) successfully matched ~10 CHEM 205/205H students with research opportunities on campus. Finally, we can add to this section a brief report on some awards that our team members have recently received this cycle:

* Travel Award to Md Shahabuddin Alam (PhD student, SIUC team), to present a poster: Characterization and Investigation of aMOF-Based(IrIMes@NU-1000) Catalyst for Hyperpolarization via Heterogeneous SABRE-SHEATH. 63rd ENC Conference, Orlando, Florida, April 24-29, 2022.
* Thomas C. Rumble University Graduate Fellowship Award to Shiraz Nantogma (PhD Student, WSU team) by the Department of Chemistry at Wayne State University, Detroit, MI. The fellowship provides a stipend of $20,000 for the academic year in addition to a tuition scholarship that provides payment of 7.5 – 10 credits for each of the fall and winter semesters at the effective tuition rate. The fellowship provides subsidized medical, vision and dental insurance.

How were the results disseminated to communities of interest?

Via oral and poster presentations (see below), as well as publications (see below).

4. IMPACT

What was the impact on the development of the principal discipline(s) of the project?

Nothing to Report.

What was the impact on other disciplines?

Nothing to Report.

What was the impact on technology transfer?

Nothing to Report.

What was the impact on society beyond science and technology?

Nothing to Report.

5. CHANGES / PROBLEMS

As with much of the world, we have been impacted by Covid-19 in a number of ways. First, the pandemic has limited (or in some cases outright eliminated) opportunities for outreach, career development for trainees, and personnel exchange; it has also caused us to postpone certain technologies: most importantly the 0.35 T MRI scanner (key instrument required for Aim #3) installation has been delayed. To mitigate some of these issues, we have continued our regular teleconferences (e.g., with Dr. Barlow from the UK). The main negative impact of the covid-19 pandemic during this reported period of performance was the lab re-opening phase of the initiating and partnering PI laboratories. As a result, a substantial amount of effort was focused on personnel training, and restarting our laboratories. Nevertheless, we look forward to catching up with research progress under this award.

6. PRODUCTS

Oral Presentations

1) BM Goodson. “Hyperpolarizing nuclear spins of atoms and molecules with light and parahydrogen.” Invited Chemistry Department Seminar, Missouri University of Science & Technology, 9/24/2021.
2) BM Goodson. “Putting a new ‘Spin’ on MRI” Invited evening lecture presented at the Illinois State Science and Humanities Symposium, Carbondale, IL, March 24, 2022.
3) BM Goodson. “‘Cutting-Edge’ Tools to Hyperpolarize NMR and MRI: From Lasers to SABRE” Invited Chemistry Department Seminar, North Carolina State University, Raleigh, NC, 4/5/2022.
4) Chekmenev, E. Y. Order-Unity ^{13}C Nuclear Polarization of [1-^{13}C]Pyruvate in Seconds. *2022 International Society for Magnetic Resonance in Medicine (ISMRM) & SMRT Virtual Conference & Exhibition*, May 9; 2022, London, UK.
5) Chekmenev, E. Y. SABRE-SHEATH hyperpolarization of pyruvate and other structurally similar biomolecules. *International Workshop on Hyperpolarization Methods in Magnetic Resonance*, May 27; 2022, Organized by a network of European NMR societies.

Conference Abstracts

1. Ariyasingha, N. M.; Samoilenko, A.; Birchall, J. R.; Kovtunov, K. V.; Kovtunova, L. M.; Bukhtiyarov, V. I.; Koptyug, I. V.; Qian, C.; Chekmenev, E. Y. In *Disposable and Handheld Clinical-scale HP Propane Hyperpolarizer*, 63rd Experimental NMR Conference, Orlando, FL, USA, April 24-29; Orlando, FL, USA, 2022.
2. Chekmenev, E. Y. In *Next-generation Equipment for Clinical-scale Parahydrogen Induced Polarization*, 63rd Experimental NMR Conference, Orlando, FL, USA, April 24-29; Orlando, FL, USA, 2022.
3. Chekmenev, E. Y.; Samoilenko, A.; Birchall, J. R.; Kovtunov, K. V.; Kovtunova, L. M.; Bukhtiyarov, V. I.; Koptyug, I. V.; Qian, C.; Goodson, B. M.; Ariyasingha, N. M. In *Disposable and Handheld Clinical-scale HP Propane Hyperpolarizer for Pulmonary MRI*, Joint Annual Meeting ISMRM-ESMRMB & ISMRT 31st Annual Meeting, London, UK (presented and attended virtually), May 07-12; London, UK (presented and attended virtually), 2022.
4. Chowdhury, R. H. C.; Birchall, J. R.; Nikolaou, P.; Barlow, M. J.; Shcherbakov, A.; Goodson, B. M.; Chekmenev, E. Y. In *Temperature-Ramped Batch-Mode Spin Exchange Optical Pumping of Xenon-129 using 3rd-generation Automated XeUS Hyperpolarizer*, 63rd Experimental NMR Conference, Orlando, FL, USA, April 24-29; Orlando, FL, USA, 2022.
5. Gafar, A. T.; Lu, H.; Basler, D.; Cocking, D.; Prince, M.; Molway, M. J.; Bales-Shaffer, L.; Alam, M. S.; Siraj, Z.; Petrilla, A. F., et al. In *Two-Orders-of-Magnitude Improvement in SEOP Production (P*N) of Hyperpolarized 131Xe and Measurement of 131Xe and 129Xe Spin-Dependent Neutron Scattering Lengths via Pseudomagnetic Precession*, 63rd Experimental NMR Conference, Orlando, FL, USA, April 24-29; Orlando, FL, USA, 2022.
6. Shahabuddin, A.; Brittin, D.; Iqbal, N.; Gafar, T.; Siraj, Z.; Petrilla, A.; Senanayake, I.; Pugh, M.; Poorman, M.; Sacolick, L., et al. In *Exploring SABRE-Enhanced Imaging with a Portable Clinical Low-field MRI Scanner*, 63rd Experimental NMR Conference, Orlando, FL, USA, April 24-29; Orlando, FL, USA, 2022.
7. Nantogma, S.; Adelabu, I.; Ariyasingha, N.; Samoilenko, A.; Chowdhury, R.; Kabir, M. S. H.; Goodson, B. M.; Chekmenev, E. Y. In *Next-generation Clinical-scale Instrumentation for Parahydrogen-Induced Polarization*, The Future of Molecular MR Workshop, Pasadena, CA, USA, July 23-26; Pasadena, CA, USA, 2022.

Peer-Reviewed Manuscripts, Dissertation & Book Chapters

1. Birchall, J. R.; Chowdhury, M. R. H.; Nikolaou, P.; Chekmenev, Y. A.; Shcherbakov, A.; Barlow, M. J.; Goodson, B. M.; Chekmenev, E. Y. Pilot Quality-Assurance Study of a Third-Generation Batch-Mode Clinical-Scale Automated Xenon-129 Hyperpolarizer. *Molecules* **2022,** *27* (4), 1327.
2. Burueva, D. B.; Kozinenko, V. P.; Sviyazov, S. V.; Kovtunova, L. M.; Bukhtiyarov, V. I.; Chekmenev, E. Y.; Salnikov, O. G.; Kovtunov, K. V.; Koptyug, I. V. Gas-Phase NMR of Hyperpolarized Propane with 1H-to-13C Polarization Transfer by PH-INEPT. *Applied Magnetic Resonance* **2022,** *53*, 653–669.

3. Chekmenev, E. Y.; Goodson, B. M.; Bukhtiyarov, V. I.; Koptyug, I. V. Bridging the Gap: From Homogeneous to Heterogeneous Parahydrogen-induced Hyperpolarization and Beyond. *ChemPhysChem* **2021,** *22* (8), 710-715.
4. Joalland, B.; Theis, T.; Appelt, S.; Chekmenev, E. Y. Background-Free Proton NMR Spectroscopy with Radiofrequency Amplification by Stimulated Emission Radiation. *Angewandte Chemie International Edition* **2021,** *60* (50), 26298-26302.
5. Lehmkuhl, S.; Fleischer, S.; Lohmann, L.; Rosen, M. S.; Chekmenev, E. Y.; Adams, A.; Theis, T.; Appelt, S. RASER MRI: Magnetic resonance images formed spontaneously exploiting cooperative nonlinear interaction. *Science Advances* **2022,** *8* (28), eabp8483.
6. Schmidt, A. B.; Bowers, C. R.; Buckenmaier, K.; Chekmenev, E. Y.; de Maissin, H.; Eills, J.; Ellermann, F.; Glöggler, S.; Gordon, J. W.; Knecht, S., et al. Instrumentation for Hydrogenative Parahydrogen-Based Hyperpolarization Techniques. *Analytical Chemistry* **2022,** *94* (1), 479–502.

Inventions, patent applications and licenses:

Nothing to Report.

Funding applied for based on work supported by this award

1. Ultrafast Functional Imaging of Lung Injury Using Clinical MRI Scanners
   PI: Chekmenev, Co-investigator (PI of a subcontract): Goodson
   Supporting agency: DOD CDMRP application, Army
   Performance period: 07/2023 to 06/2027
   Level of funding:
   Time Commitment: Principal Investigator: 12 calendar months; Mentor: 0 calendar months
   Project purpose: The goal of this project is to develop new instrumentation and approaches to enable detection of hyperpolarized 129Xe contrast agent on clinical MRI scanners.
   Overlap: None

2. Next-generation Lasers for Enabling Ultrafast Functional Pulmonary MRI
   PI: Chekmenev, Co-investigator (PI of a subcontract): Goodson
   Supporting agency: NIH NHLBI
   Performance period: 04/2023 to 03/2025
   Level of funding:
   Project purpose: The goal of this project is to test next-generation high-power laser technologies with the overarching aim of improving access to hyperpolarized 129Xe contrast agent in the clinical setting.
   Overlap: None

7. PARTICIPANTS & OTHER COLLABORATING ORGANIZATIONS

Individuals who worked on the project

The following personnel worked on the project

Name:	Eduard Chekmenev
Project Role:	Initiating PI (Wayne State University)
Researcher Identifier (ORCID ID):	orcid.org/0000-0002-8745-8801
Nearest person month worked:	3
Contribution to Project:	Dr. Chekmenev was responsible for the overall progress of the project, performing some experiments with hyperpolarized propane and hyperpolarized xenon-129, developing RF coils, analyzing some of the data for the above-mentioned experiments, preparing the manuscripts.
Funding Support:	W81XWH-20-10576; NIH 1R21CA220137; NSF CHE-1904780, NIBIB 1R01EB029829, NHLBI 1R21HL154032

Name:	Nuwandi M. Ariyasingha
Project Role:	PhD / PD Fellow
Researcher Identifier (ORCID ID):	
Nearest person month worked:	5
Contribution to Project:	Nuwandi M. Ariyasingha worked on many of the experiments concerning hyperpolarized clinical-scale propane hyperpolarization. She also analyzed the data, prepared figures, and manuscripts. She was also trained to operate 0.35 T MRI scanner.
Funding Support:	W81XWH-20-10576, NHLBI 1R21HL154032, 1F32HL160108

Name:	Md Raduan Chowdhury
Project Role:	PhD student
Researcher Identifier (ORCID ID):	
Nearest person month worked:	3
Contribution to Project:	Raduan worked on the Xenon-129 hyperpolarizer to ensure that HP 129Xe would be available for the in vivo part of this proposal. He also worked on the parahydrogen component of this award by providing upgrade to our parahydrogen production facility. He was also trained to operate 0.35 T MRI scanner.
Funding Support:	Wayne State University teaching fellowship and NSF CHE-1904780

Name:	Shiraz Nantogma
Project Role:	PhD student
Researcher Identifier (ORCID ID):	
Nearest person month worked:	2
Contribution to Project:	Shiraz has been developing instrumentation for parahydrogen-based hyperpolarization. He has also produced

	parahydrogen for this project. He was also trained to operate 0.35 T MRI scanner.
Funding Support:	Wayne State University teaching fellowship and NSF CHE-1904780.

Name:	Clementinah Oladun
Project Role:	PhD student
Researcher Identifier (ORCID ID):	
Nearest person month worked:	1
Contribution to Project:	Clementinah worked on Xenon-129 hyperpolarizer to ensure that HP 129Xe would be available for the in vivo part of this proposal.
Funding Support:	Wayne State University teaching fellowship.

Name:	Firoz Ahmed
Project Role:	PhD student
Researcher Identifier (ORCID ID):	
Nearest person month worked:	1
Contribution to Project:	Firoz worked on Xenon-129 hyperpolarizer.
Funding Support:	Wayne State University teaching fellowship

Name:	Anna Samoilenko
Project Role:	Pharm D
Researcher Identifier (ORCID ID):	
Nearest person month worked:	3
Contribution to Project:	Anna contributed to this project by working on the development of the clinical-scale propane hyperpolarizer and its testing. She prepared reactors, collected and processed data, and prepared reports.
Funding Support:	NSF CHE-1904780, W81XWH-20-10576, NHLBI 1R21HL154032

Name:	Igor V. Koptyug
Project Role:	consultant
Researcher Identifier (ORCID ID):	https://orcid.org/0000-0003-3480-7649
Nearest person month worked:	1
Contribution to Project:	Wrote contents for presentations and manuscripts. Consulted in aspects of parahydrogen addition mechanisms.
Funding Support:	DOD W81XWH2010576

Name:	Larisa Kovtunova
Project Role:	consultant
Researcher Identifier (ORCID ID):	https://orcid.org/0000-0003-0922-6594
Nearest person month worked:	1
Contribution to Project:	Wrote contents for manuscripts. Consulted in aspects of heterogeneous catalyst preparation for propane hyperpolarization.
Funding Support:	DOD W81XWH2010576

Name:	Juri G. Gelovani
Project Role:	consultant
Researcher Identifier (ORCID ID):	https://orcid.org/0000-0002-8413-6161
Nearest person month worked:	1
Contribution to Project:	Wrote contents for manuscripts. Consulted in aspects of clinical translation of hyperpolarized inhalable gases.
Funding Support:	DOD W81XWH2010576

Name:	Anton Scherbakov
Project Role:	consultant
Researcher Identifier (ORCID ID):	
Nearest person month worked:	2
Contribution to Project:	Provided support for Xenon-129 hyperpolarizer.
Funding Support:	DOD W81XWH2010576

Name:	Boyd M. Goodson
Project Role:	Partnering PI (SIUC)
Researcher Identifier (ORCID ID):	orcid.org/0000-0001-6079-5077
Nearest person month worked:	1
Contribution to Project:	Prof. Goodson was responsible for the overall progress of the project at the partnering site, performing some experiments with hyperpolarized xenon-129, xenon-131, as well as imaging experiments on the new 64 mT scanner, analyzing some of the data for the above-mentioned experiments, contributed to efforts with hyperpolarizer development at the SIUC site, and preparing manuscripts and presentations.
Funding Support:	SIUC DOD W81XWH2010578 NSF-CHE-1905341 NSF DMR-2150489
Name:	Abdulbasit Tobi (“Tobi”) Gafar
Project Role:	PhD chemistry graduate student
Researcher Identifier (ORCID ID):	
Nearest person month worked:	2
Contribution to Project:	Participated in xenon-129 and xenon-131 spin-exchange optical pumping experiments, as well as imaging experiments on the new 64 mT scanner; contributed to efforts with hyperpolarizer development at the SIUC site. Processed and analyzed data, wrote up contents for presentations and manuscripts.
Funding Support:	SIUC / NMR Facility

Name:	Panayiotis “Peter” Nikolaou
Project Role:	consultant
Researcher Identifier (ORCID ID):	Contributed significantly to various aspects of hyperpolarizer design and assembly.

	Wrote contents for presentations and manuscripts.
Nearest person month worked:	1
Contribution to Project:	
Funding Support:	DOD W81XWH2010578

Name:	Zahid Siraj
Project Role:	PhD graduate student researcher
Researcher Identifier (ORCID ID):	
Nearest person month worked:	2
Contribution to Project:	Assisted with experiments involving hyperpolarizer assembly and testing, as well as imaging experiments on the new 64 mT MRI scanner.
Funding Support:	Teaching assistantship

Name:	Nadiya Iqbal
Project Role:	PhD graduate student researcher
Researcher Identifier (ORCID ID):	
Nearest person month worked:	2
Contribution to Project:	Assisted with, then led imaging experiments on the 64 mT MRI scanner.
Funding Support:	Teaching assistantship

Name:	Md Shahabuddin (“Alam”) Alam
Project Role:	PhD chemistry graduate student
Researcher Identifier (ORCID ID):	
Nearest person month worked:	2
Contribution to Project:	Participated in xenon-129 and xenon-131 spin-exchange optical pumping experiments, as well as imaging experiments on the new 64 mT MRI scanner; contributed to efforts with hyperpolarizer development at the SIUC site. Processed and analyzed data. Contributed to manuscripts and conference presentations.
Funding Support:	SIUC / NMR Facility

Name:	Anthony Petrilla
Project Role:	undergraduate student researcher
Researcher Identifier (ORCID ID):	
Nearest person month worked:	1
Contribution to Project:	undergraduate student researcher (since graduated, and is now a new PhD graduate researcher at SIUC
Funding Support:	DOD W81XWH2010578, NSF DMR-2150489, SIUC

Has there been a change in the active other support of the PD/PI(s) or senior/key personnel since the last reporting period?

Yes

Title "*Next-generation ultrafast functional 3D pulmonary imaging*"

1F32HL160108-01 (PI=Ariyasingha, mentor=Chekmenev)

Performance period: 09/01/2021-08/31/2024

Supporting agency: NIH/NHLBI

Level of funding: ~ total direct costs to support salary and training of Dr. Ariyasingha.

Time Commitment: Principal Investigator: 12 calendar months; Mentor: 0 calendar months

We propose developing next-generation ultrafast MRI to assess lung function using hyperpolarized propane gas as an inhalable contrast agent. The proposed low-cost and high-throughput technology for clinical-scale production of hyperpolarized propane can be employed for sub-second gas MRI, which we envision as a novel contrast agent for functional regional mapping of lung functions in a wide range of lung diseases. Here, we will study three contrast mechanisms in excised sheep lung model to demonstrate the robustness of this new quantitative 3D imaging method.

Aim 1: 3D MRI of lungs with deuterated HP propane. We will employ previously developed deuterated HP propane to acquire 3D MRI of excised sheep lungs. Deuterated HP propane has a directly detectable HP state and can be imaged directly on clinical MRI scanners. This aim will enable us to investigate the feasibility of this approach and to investigate the effect of background signal interference from the protons of tissue.

Aim 2: 3D MRI of lungs using HP propane. The advantage of HP propane versus deuterated HP propane is the possibility to employ specialized pulse sequences to filter the background signal of tissue protons. We will study the effectiveness of this filtering approach to obtain background-free images.

Aim 3: Creation of ultra-long-lived spin states (ULLS) in partially deuterated HP propane. We will investigate on the use of highly symmetric molecules to enable ultra-long lived spin states that can potentially lengthen the in vivo utility window to 1-2 minutes.

Overlap: Although this project is focused around propane, there is no overlap with the specific aims of the project. Moreover, this is a training award designed to develop the next-generation of researchers in the area of pulmonary imaging. The project additionally differs from this award in two ways. First, it emphasizes the contrast mechanism (rather than applications). Second, it focuses on mechanistic studies in excised lungs versus the animal model used under this award.

Overlap: none

Personnel exchanges with collaborators:

While covid had greatly slowed the planned student exchange process, this cycle we were able to ramp that back up and enjoyed several visits. For example, SIUC team members (the PI, Md Shahabuddin Alam, Tobi Gafar, Drew Brittin, and Ishani Senanayake) visited the WSU team for training and experiments for nearly 1 week in the fall, and other trips are planned for the future (the SIUC team also took home a new SABRE hyperpolarizer built by the WSU team). Other hosting events by the WSU team in the past cycle included:

* SIUC Student Tobi Gafar: 2 additional long-term visits for over two months total;
* Henri de Maissin, PhD student, University of Freiburg, Germany: 2.5 months, 1 visit;
* Chris Nelson, PhD student, North Carolina State University: 2 weeks, 1 visit;
* Iuliia Mandzhieva, PhD student, North Carolina State University: 2 weeks, 2 visits;
* Dr. Andreas Schmidt, PhD: 1 visit 2 weeks — after that he was employed by WSU for 4 months;
* Prof. Alexei Ouriadov (with a trainee): The University of Western Ontario, Canada, 1 day, 1 visit;
* Prof. Dan Xiao: University of Windsor, Canada, 1 day, 1 visit;
* Dr. Jessica Ettegui: NHLBI, NIH, Bethesda, MD, 1 visit, 4 days.

We have also been interacting with collaborating scientists remotely.

Organization Name: University of Nottingham

Location of Organization: Nottingham, UK

Partner's contribution to the project:

In-kind support: Our collaborators provided their insights in the imaging aspects of hyperpolarized gases.

Collaboration: We have enjoyed regular (weekly to bi-weekly) teleconferences with the Nottingham team (lead PI: Dr. Michael J. Barlow).

8. SPECIAL REPORTING REQUIREMENTS

Collaborative Award

This is a collaborative award with two partnering PIs. Each PI submits a copy of the identical report with face page adjusted for each report.

9. APPENDICES

Appendix 1: Original Statement of work, Years 1-3

STATEMENT OF WORK – 07/03/2019
PROPOSED START DATE Apr. 01, 2020

Site 1: Wayne State University
Department of Chemistry
5101 Cass Ave
Detroit, MI 48202
PI: Dr. Chekmenev

Site 2: Southern Illinois University Carbondale
Neckers Building,
1245 Lincoln Dr
Carbondale, IL 62901
PI: Dr. Goodson

Specific Aim 1 – To develop a clinical low-cost and high-throughput device for production and administration of HP propane contrast agent for ultimate research use in	**Timeline**	**Site 1**	**Site 2**
Major Task 1	Months		
Subtask 1: Design of the clinical propane hyperpolarizer	1-6	X	X
Milestone # 1 clinical propane polarizer is designed	6	X	X
Subtask 2: Propane hyperpolarizer construction	7-12	X	
Milestone # 2 clinical propane hyperpolarizer is constructed	12	X	
Subtask 3: Optimize propane hyperpolarizer performance	13-18	X	X
Subtask 4: Development of Good Manufacturing Practices (GMP) of hyperpolarized propane production	19-24	X	X
Milestone # 3 HP propane production GMP is developed	24	X	X
Subtask 5: Create bill of materials for propane hyperpolarizer	25-30	X	
Specific Aim 2 - To develop a safe method for HP propane gas administration and utilization, and test the purity and safety of the HP contrast agent produced by our device			
Major Task 2			
Subtask 1: Address flammability of HP propane gas in the clinical hyperpolarizer by developing inhalation procedures, using carbon filter to capture exiting propane gas	4-18	X	X
Milestone # 4 Reduction of propane content in the exhaled gas mixture to ≤ 1% (i.e. significantly below LEL) in 3 air inhalation/exhalation cycles after the inhalation and MRI imaging of HP propane gas; propane content in the room less than 1000 ppm (i.e. below the mandated safety level).	16-18	X	X
Subtask 2: Assess purity of produced HP propane gas by detecting the excipients	1-15	X	X
Milestone # 5 No detectable compounds except propane (>98%), H_2 (<2%), and propylene (<0.1%) in the produced contrast agent	15	X	X

Specific Aim 3 - To assess the feasibility of MRI using HP propane gas for *in vivo* functional imaging of normal lungs and in a bleomycin-induced COPD model in sheep

Major Task 3			
Subtask 1: Establish ventilation 3D ^{129}Xe MRI on a single sheep breath hold on 0.35 T using phantoms of hyperpolarized ^{129}Xe gas placed in Tedlar Bags	1-12	X	X
Milestone # 6 3D ^{129}Xe MRI imaging sequence / protocol is developed for 0.35 T MRI scanner	12	X	X
Subtask 2: Establish sub-second ventilation 3D HP propane MRI on 0.35 T using phantoms of hyperpolarized propane gas	1-12	X	
Milestone # 7 Sub-second 3D MRI imaging sequence / protocol is developed for 0.35 T MRI scanner to record MRI of propane gas ventilation	12	X	
Subtask 3: Submit documents for ACURO approval	13-16	X	X
Milestone # 8 ACURO approval obtained	18	X	X
Subtask 4: Test-retest study of HP ^{129}Xe and HP propane gas in healthy sheep [6 sheep X 4 test/re-test exams = 24 sheep scan sessions total]	19-33	X	X
Milestone # 9 Reproducibility and effectiveness of HP propane MRI to report on regional lung ventilation is demonstrated in sheep animal model	34	X	X
Subtask 3D: Bleomycin-induced lung injury detection using HP ^{129}Xe and HP propane gas in sheep [6 sheep X 2 time point exams = 12 sheep scan sessions total]	19-33	X	X
Milestone #10 Effectiveness OF HP propane MRI to detect lung injury is demonstrated in sheep animal model	34	X	X

Appendix 2: Abstracts Presented and Manuscripts Published and Accepted

7 conference abstracts and 6 published peer-reviewed publications are reported. All PDF files of 7 abstracts and 6 publications are provided below in the Appendix 2.

Check for updates

A Journal of the German Chemical Society

Angewandte International Edition Chemie

GDCh

www.angewandte.org

2021–60/50

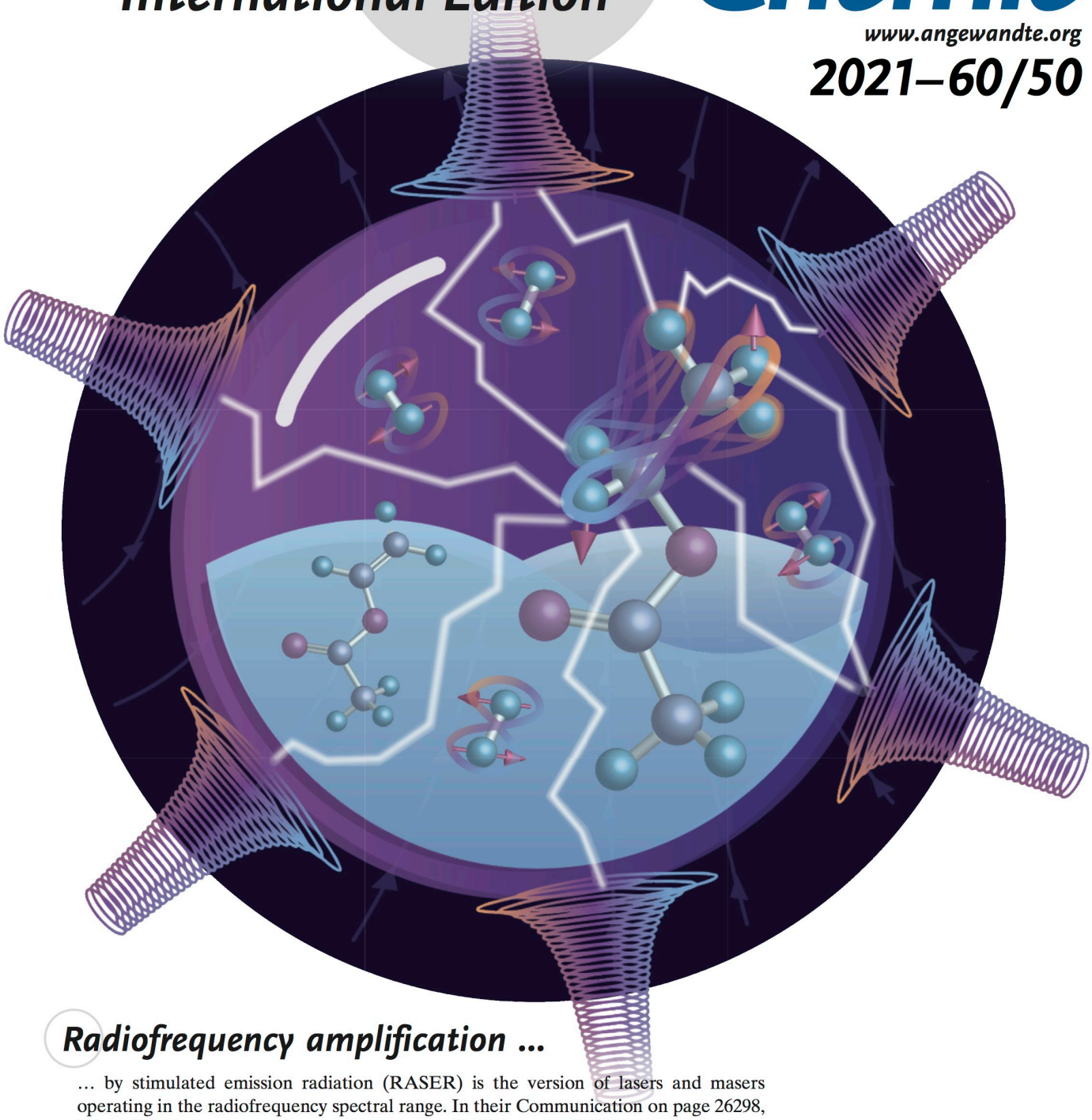

Radiofrequency amplification ...

... by stimulated emission radiation (RASER) is the version of lasers and masers operating in the radiofrequency spectral range. In their Communication on page 26298, Eduard Y. Chekmenev and co-workers employ 61 MHz proton RASER to demonstrate robust background-free detection of biomolecular NMR resonances even in the extreme cases of fully protonated solvents and biological fluids. This approach paves the way to a wide range of high-resolution NMR and in vivo MRI applications of background-free proton detection of hyperpolarized molecules.

WILEY-VCH

Check for updates

How to cite: *Angew. Chem. Int. Ed.* **2021**, *60*, 26298–26302
International Edition: doi.org/10.1002/anie.202108939
German Edition: doi.org/10.1002/ange.202108939

NMR Spectroscopy | Hot Paper

Background-Free Proton NMR Spectroscopy with Radiofrequency Amplification by Stimulated Emission Radiation

*Baptiste Joalland, Thomas Theis, Stephan Appelt, and Eduard Y. Chekmenev**

Abstract: *We report on the utility of Radiofrequency Amplification by Stimulated Emission Radiation (RASER) for background-free proton detection of hyperpolarized biomolecules. We performed hyperpolarization of ≈0.3 M ethyl acetate via pairwise parahydrogen addition to vinyl acetate. A proton NMR signal with signal-to-noise ratio exceeding 100 000 was detected without radio-frequency excitation at the clinically relevant magnetic field of 1.4 T using a standard (non-cryogenic) inductive detector with quality factor of Q = 68. No proton background signal was observed from protonated solvent (methanol) or other added co-solvents such as ethanol, water or bovine serum. Moreover, we demonstrate RASER detection without radio-frequency excitation of a bolus of hyperpolarized contrast agent in biological fluid. Completely background-free proton detection of hyperpolarized contrast agents in biological media paves the way to new applications in the areas of high-resolution NMR spectroscopy and in vivo spectroscopy and imaging.*

NMR hyperpolarization techniques allow for transient increase of nuclear spin polarization (P) by several orders of magnitude.[1–3] The sensitivity boost enabled by NMR hyperpolarization is geared towards boosting high-resolution NMR spectroscopy as well as in vivo MR spectroscopic imaging (MRSI) to probe in vivo metabolism in real time.[4,5] ^{13}C[6,7] and ^{15}N nuclei[8] have been the primary focus as the temporary carriers of hyperpolarization, because they have long T_1 and T_2, and a wide dynamic range of chemical shifts, which are sensitive to local environment and chemical structure.[9,10] Indeed, numerous clinical trials are pending with hyperpolarized (HP) [1-^{13}C]pyruvate.[11–13] Moreover, the greatly improved sensitivity enabled by hyperpolarization can be used for even larger relative gains at low magnetic fields.[14]

Despite these substantial HP sensitivity gains, some MR sensitivity limitations remain, especially with regard to the large thermal background from molecules at much higher concentrations than those of the hyperpolarized agents.[2,11,12,15] Also, by definition, P cannot be greater than 1 or 100%, and many hyperpolarization techniques have already exhausted their potential by producing HP compounds with P near unity.[16–19]

A number of additional strategies have been developed to boost the signal-to-noise ratio (SNR) of HP detection. For example, polarization transfer from HP ^{13}C or ^{15}N to spin-spin coupled protons is employed, and protons are utilized for HP readout.[20,21] This approach has merit because protons have substantially greater gyromagnetic ratio, γ, (by 4- and 10-fold compared to ^{13}C and ^{15}N respectively)—as a result, substantially increased SNR can be obtained—up to the square of the ratio of the gyromagnetic ratios, $(\gamma_{1H}/\gamma_{het})^2$, in the best case.[22] Moreover, the vast majority of MR instrumentation is optimized for proton detection. Despite this nominal benefit of proton detection, the practical utility is hampered by a substantial background signal of thermally polarized protons, e.g., water or fat protons of tissue, which are present at substantially higher concentration than that of hyperpolarized contrast agents.[15,23]

Here we suggest a new approach to address the large thermal background problem, which is to create conditions, where HP nuclear spins spontaneously develop transverse magnetization without radio-frequency (RF) pulses. Such radio amplification by stimulated emission of radiation (RASER) can be obtained,[24–26] when a) the hyperpolarization is negative, that is, corresponds to a population inversion, and b) when the radiation damping rate $1/\tau_{RD}$ satisfies the condition of $1/\tau_{RD} > 1/T_2^*$, where T_2^* is the effective transverse relaxation time, and the radiation damping rate is given by Equation (1):

$$1/\tau_{RD} = -(\mu_0/4)\eta Q\gamma^2 \hbar\, n_S\, P \qquad (1)$$

where μ_0 is the vacuum permeability, η is the filling factor, Q is the quality factor of the resonator, $\hbar$ is Planck's constant, γ is the nucleus gyromagnetic ratio and n_S is the spin number density.[26]

The RASER phenomenon was first demonstrated in low magnetic fields through the use of high-Q resonators.[24–27] Besides the SNR boost achieved by high-Q RF coils, the NMR signal can in principle persist indefinitely (as long as P

[*] Dr. B. Joalland, Prof. E. Y. Chekmenev
Department of Chemistry, Integrative Biosciences (Ibio), Wayne State University, Karmanos Cancer Institute (KCI)
5101 Cass Ave, Detroit, MI 48202 (USA)
E-mail: chekmenevlab@gmail.com
Prof. T. Theis
Department of Chemistry, North Carolina State University
Raleigh, North Carolina, 27695-8204 (USA)
Prof. Dr. S. Appelt
Institut für Technische und Makromolekulare Chemie (ITMC), RWTH Aachen University
52056 Aachen (Germany),
and
Central Institute for Engineering, Electronics and Analytics—Electronic Systems (ZEA 2), Forschungszentrum Jülich GmbH
52425 Jülich (Germany)
Prof. E. Y. Chekmenev
Russian Academy of Sciences
Leninskiy Prospect, 14, 119991 Moscow (Russia)
The ORCID identification number(s) for the author(s) of this article can be found under:
https://doi.org/10.1002/anie.202108939.

 © 2021 Wiley-VCH GmbH

is maintained) resulting in line narrowing well below of the linewidth given by T_2*.[26,28] The latter effect leads to two key practical RASER benefits: improved spectral resolution and improved SNR (through indirect proton detection of ^{13}C HP contrast agents). Therefore, RASER is a potential game-changing technology that can substantially boost the detection sensitivity of HP NMR and avoid all background signals because excitation pulses are not required.

Recently, RASER has been demonstrated using standard commercial NMR hardware at high magnetic fields of up to 14 T.[29–31] Moreover, RASER has been demonstrated at the clinically relevant field of 1.4 T using a bolus of HP compounds, that is, under conditions of non-replenishable hyperpolarization.[28,32–34] It follows from Equation (1) that high-γ spins are more RASER potent, and therefore, can induce RASER at lower spin densities. Nevertheless, RASER has been already successfully demonstrated for low-γ ^{17}O at 9.4 T via Dynamic Nuclear Polarization (DNP).[35] As a result of these demonstrations, the RASER effect is poised to expand the reach of high-resolution HP NMR and in vivo MRSI by providing three clear benefits: I: substantially improved spectral resolution, II: higher NMR sensitivity and III: background free signals. These gains can be amplified further using high-Q resonators.[24]

Here, we focus on the demonstration of background-free proton RASERs in the highly unfavourable case of fully protonated solvents. Moreover, we extend this concept to biological media, demonstrating biocompatible, background-free RASER.

We employ parahydrogen-induced polarization (PHIP)[36,37] to induce NMR hyperpolarization in ethyl acetate (EA). Our rationale for choosing EA is threefold. First, acetate can be hyperpolarized using both PHIP[38] and DNP.[39] Second, HP acetate has demonstrated in vivo utility.[39] Finally, HP acetate was already imaged in vivo using proton detection.[40]

Pairwise parahydrogen (p-H_2) addition to vinyl acetate (Figure 1 a) leads to production of *proton*-hyperpolarized EA (note that proton polarization must be transferred to [1-^{13}C] nucleus and HP EA must be de-esterified for biological applications). The 300 mM vinyl acetate sample ($\approx$0.5 mL) was hydrogenated for 10 s using 4 mM catalyst in either methanol or [D_4]MeOH at Earth's magnetic field by p-H_2 (> 98.5 % *para*- fraction[41]) bubbling via Teflon catheter inside standard 5-mm NMR tube as described previously.[34] After cessation of p-H_2 bubbling, the catheter was removed, and the HP sample was inserted into the NMR spectrometer. As detailed in Figure 2, some samples were spiked with comparable volumes of neat ethanol, water or bovine serum. The acquisition of NMR signal was initiated approximately 2–3 seconds before sample insertion into the NMR spectrometer. The total acquisition time always was 16 s as indicated in Figure 1 b and reflected in the time axis in Figure 2. RASER activity was observed in all studied samples, see Figures 2 and 3. As can be seen in panels (a) and (b) of both Figure 2 (FID's) and Figure 3 (FT spectra), samples employing [D_4]MeOH or protonated methanol exhibit similar signatures during the first burst and the remainder of the RASER activity. Despite the high proton concentration of methyl protons in methanol (ca. 74 M), their magnetization is too low to induce RASER activity. Furthermore, the thermal polar-

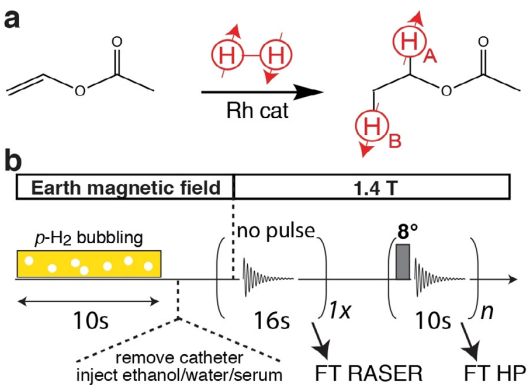

Figure 1. a) Reaction Scheme for pairwise p-H_2 addition onto vinyl acetate (VA) leading to HP ethyl acetate (EA). b) Event sequence for the performed experiments. In the Earth's magnetic field, p-H_2 was bubbled in either methanol or [D_4]MeOH while ethanol, water, or serum was injected immediately after the reaction. In all experiments, the catheter employed for p-H_2 bubble through the solution was removed. Note that the samples were placed in the bore of the 1.4 T spectrometer $\approx$5 s after the spectrometer's receiver was open and left open for $\approx$16 s (no RF pulse). Afterwards, a series of low flip angle (8°) pulse-acquisition (2 s pulse-acquisition + 8 s relaxation) was performed to monitor the decay of the HP states.

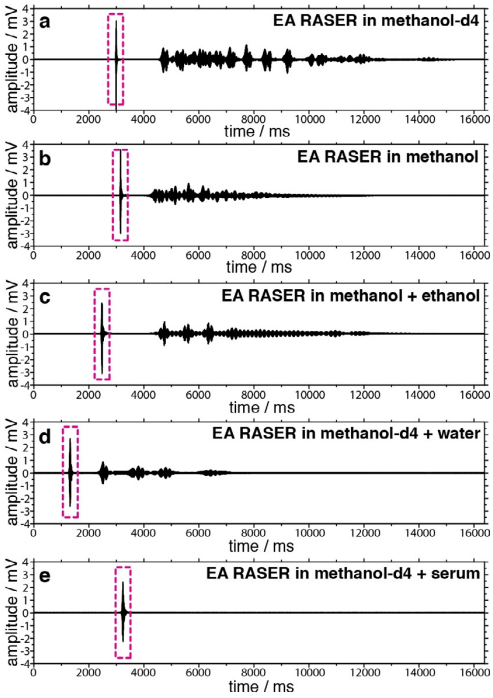

Figure 2. ^{1}H ALTADENA[42] RASER signals of HP EA in [D_4]MeOH (a), non-deuterated methanol (b), methanol with post-reaction injection of ethanol (c), [D_4]MeOH with post-reaction injection of water (d) or serum (e). All signals were recorded without RF pulse. Magenta boxes highlight the RASER bursts occurring at the time the samples were placed in the NMR spectrometer.

© 2021 Wiley-VCH GmbH

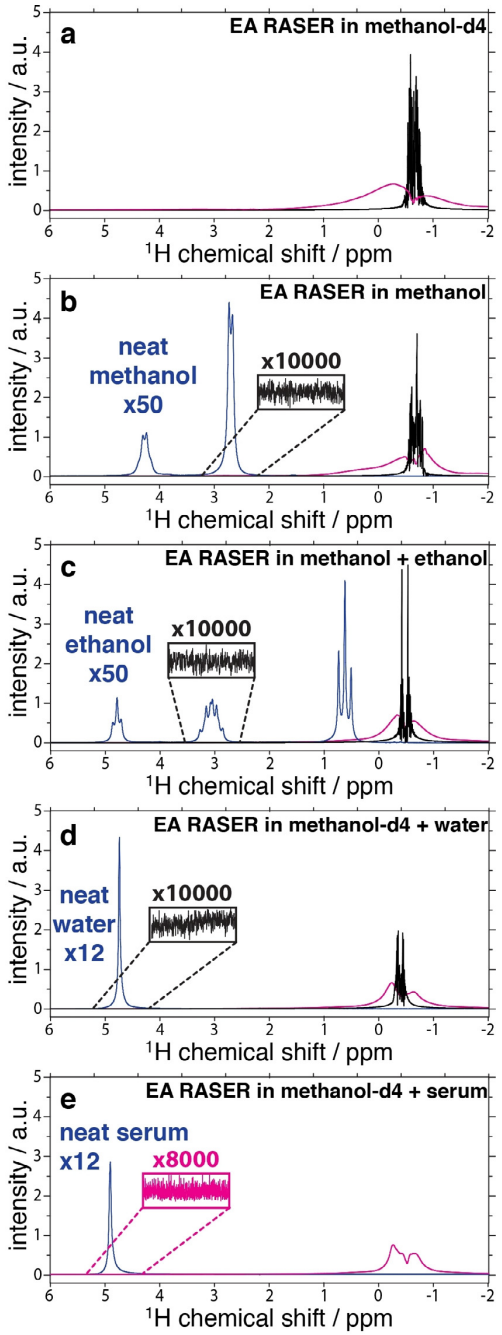

Figure 3. ¹H (Fourier transformed) spectra of the ALTADENA RASER signals emitted by HP EA in various solvents (same as Figure 2): [D_4]MeOH (a), non-deuterated methanol (b), methanol with post-reaction injection of ethanol (c), [D_4]MeOH with post-reaction injection of water (d) or serum (e). In each subpanel, the magenta spectrum corresponds to the RASER burst observed at the time of sample insertion in the spectrometer while the black spectrum corresponds to the subsequent RASER activity. The respective spectra of thermally polarized samples yielding the signals from non-deuterated solvent (methanol, ethanol, water) or serum are superimposed in blue.

ization is aligned with the magnetic field (not against the field, no population inversion) and thus, spontaneous emission of radiation is not possible, therefore no background signal from solvent protons is seen (see the corresponding insets). Only in exceptional cases, detailed below, the solvent may also attain negative polarization.

When the RASER acquisition was completed (Figure 1b), a series of 1D spectra was recorded using small tip angle (8°) pulses to monitor the decay of HP state as shown in Figure 4. The measured decay constants of the HP protons A and B allowed extrapolated calculation of original polarization $P_H \approx -0.25$.[34] We also note that the first few pulse-acquire transients clearly exhibit line narrowing of H_B due to residual RASER activity. Note that methanol solvent polarization during RASER experiments also deviated from thermal equilibrium due to cross-relaxation from less concentrated HP H_B. This is evidenced by the negative amplitude (corresponding to a population inversion) of both solvent peaks during the first few frames in Figure 4. Despite this altered polarization of solvent, no solvent RASER activity was seen from the protonated solvent, Figure 3b.

Additional control experiments were performed to simulate injection of HP solution. The spectra shown in Figures 2c,d and Figures 3c,d were recorded after mixing the solution of HP EA in methanol with ethanol, and in [D_4]MeOH with water, respectively (both without deoxygenation). Despite the HP EA dilution and likely decrease in

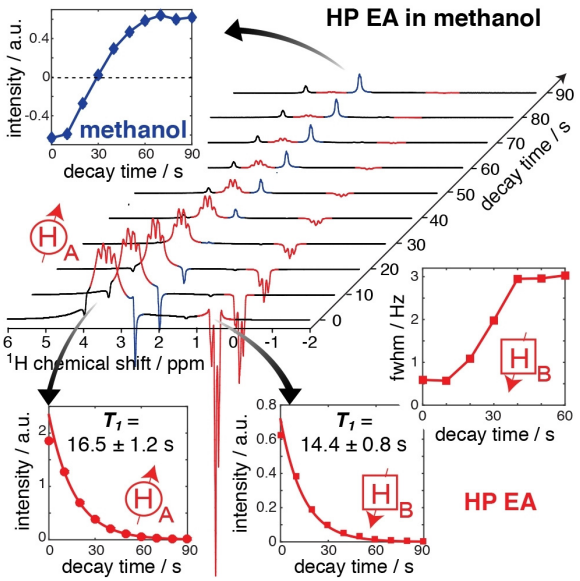

Figure 4. Fourier spectra of HP EA in non-deuterated methanol recorded every 10 s after ALTADENA RASER. The FWHM of the H_B signal is ≈0.5 Hz for the first two timeframes (RASER still active) and then increases toward reaching a constant value of ≈3 Hz (RASER non-active) after 40 s decay (bottom insert), that is, more than 1 min after the hydrogenation reaction was terminated. The solvent (blue, top insert) is also hyperpolarized (note the negative amplitude of both solvent resonances) by PHIP. The negative amplitude of solvent resonances changes to the positive because the sample gains Boltzmann polarization with time in 1.4 T magnet.

© 2021 Wiley-VCH GmbH

T_2*, RASER effects are clearly observable from HP protons, but not from the solvent. Specifically, the HP RASER SNR in Figure 3c exceeds 10^5, yet no background proton signal is detected above the noise.

Finally, the HP EA in [D_4]MeOH was injected with serum (blood derived biofluid free from white and red blood cells) resulting in more significant decrease of T_2* as evident from the thermal spectrum (Figure 3e) and a likely decrease of T_1. Nevertheless, the initial RASER signal "burst" was detected after injection of the biological fluid without any background signal, as seen on the magenta trace in Figures 2e and 3e. This observation is important, because it shows RASER detection in biological fluids at the clinically relevant magnetic field of 1.4 T without the use of any specialized RF hardware.

In summary, we demonstrated that RASER phenomenon can be employed for background-free detection of HP resonances even in the extreme cases of protonated solvents and biological fluids. This approach can potentially be employed for a wide range of high-resolution and in vivo applications of proton detection of HP molecules. In particular, we envision that in vivo use could benefit tremendously as water background suppression techniques are typically difficult and cause undesirable polarization losses and artefacts. Development of NMR imaging exploiting the RASER effect is the next logical step and subject of ongoing work in our laboratories.

Acknowledgements

This work was supported by NSF under Grant CHE-1904780, National Cancer Institute under 1R21CA220137, and by DOD CDMRP under W81XWH-15-1-0271 and W81XWH-20-10576. Research reported in this publication was also supported by NIBIB R21EB025313 and R01EB029829, and NHLBI R21 HL154032. The content is solely the responsibility of the authors and does not necessarily represent the official views of the National Institutes of Health. T.T. acknowledges funding from the North Carolina Biotechnology Center and the Mallinckrodt Foundation.

Conflict of Interest

E.Y.C. has a stake of ownership in XEUS Technologies LTD. T.T. has a stake of ownership in Vizma LLC.

Keywords: hyperpolarization · NMR spectroscopy · parahydrogen · RASER

[1] B. M. Goodson, N. Whiting, A. M. Coffey, P. Nikolaou, F. Shi, B. M. Gust, M. E. Gemeinhardt, R. V. Shchepin, J. G. Skinner, J. R. Birchall, M. J. Barlow, E. Y. Chekmenev, *eMagRes* **2015**, *4*, 797 – 810.

[2] P. Nikolaou, B. M. Goodson, E. Y. Chekmenev, *Chem. Eur. J.* **2015**, *21*, 3156 – 3166.

[3] J. H. Ardenkjaer-Larsen, B. Fridlund, A. Gram, G. Hansson, L. Hansson, M. H. Lerche, R. Servin, M. Thaning, K. Golman, *Proc. Natl. Acad. Sci. USA* **2003**, *100*, 10158 – 10163.

[4] K. Golman, R. in't Zandt, M. Thaning, *Proc. Natl. Acad. Sci. USA* **2006**, *103*, 11270 – 11275.

[5] K. Golman, O. Axelsson, H. Johannesson, S. Mansson, C. Olofsson, J. S. Petersson, *Magn. Reson. Med.* **2001**, *46*, 1 – 5.

[6] S. E. Day, M. I. Kettunen, F. A. Gallagher, D. E. Hu, M. Lerche, J. Wolber, K. Golman, J. H. Ardenkjaer-Larsen, K. M. Brindle, *Nat. Med.* **2007**, *13*, 1382 – 1387.

[7] K. M. Brindle, *J. Am. Chem. Soc.* **2015**, *137*, 6418 – 6427.

[8] C. Cudalbu, A. Comment, F. Kurdzesau, R. B. van Heeswijk, K. Uffmann, S. Jannin, V. Denisov, D. Kirik, R. Gruetter, *Phys. Chem. Chem. Phys.* **2010**, *12*, 5818 – 5823.

[9] O. G. Salnikov, N. V. Chukanov, A. Svyatova, I. A. Trofimov, M. S. H. Kabir, J. G. Gelovani, K. V. Kovtunov, I. V. Koptyug, E. Y. Chekmenev, *Angew. Chem. Int. Ed.* **2021**, *60*, 2406 – 2413; *Angew. Chem.* **2021**, *133*, 2436 – 2443.

[10] R. Hata, H. Nonaka, Y. Takakusagi, K. Ichikawa, S. Sando, *Chem. Commun.* **2015**, *51*, 12290 – 12292.

[11] J. Kurhanewicz, D. B. Vigneron, J. H. Ardenkjaer-Larsen, J. A. Bankson, K. Brindle, C. H. Cunningham, F. A. Gallagher, K. R. Keshari, A. Kjaer, C. Laustsen, D. A. Mankoff, M. E. Merritt, S. J. Nelson, J. M. Pauly, P. Lee, S. Ronen, D. J. Tyler, S. S. Rajan, D. M. Spielman, L. Wald, X. Zhang, C. R. Malloy, R. Rizi, *Neoplasia* **2019**, *21*, 1 – 16.

[12] S. J. Nelson, J. Kurhanewicz, D. B. Vigneron, P. E. Z. Larson, A. L. Harzstark, M. Ferrone, M. van Criekinge, J. W. Chang, R. Bok, I. Park, G. Reed, L. Carvajal, E. J. Small, P. Munster, V. K. Weinberg, J. H. Ardenkjaer-Larsen, A. P. Chen, R. E. Hurd, L. I. Odegardstuen, F. J. Robb, J. Tropp, J. A. Murray, *Sci. Transl. Med.* **2013**, *5*, 198ra108.

[13] R. V. Shchepin, J. R. Birchall, N. V. Chukanov, K. V. Kovtunov, I. V. Koptyug, T. Theis, W. S. Warren, J. G. Gelovani, B. M. Goodson, S. Shokouhi, M. S. Rosen, Y.-F. Yen, W. Pham, E. Y. Chekmenev, *Chem. Eur. J.* **2019**, *25*, 8829 – 8836.

[14] A. M. Coffey, M. L. Truong, E. Y. Chekmenev, *J. Magn. Reson.* **2013**, *237*, 169 – 174.

[15] J. Wang, F. Kreis, A. J. Wright, R. L. Hesketh, M. H. Levitt, K. M. Brindle, *Magn. Reson. Med.* **2018**, *79*, 741 – 747.

[16] J. H. Ardenkjaer-Larsen, *J. Magn. Reson.* **2016**, *264*, 3 – 12.

[17] J. R. Birchall, R. K. Irwin, P. Nikolaou, A. M. Coffey, B. E. Kidd, M. Murphy, M. Molway, L. B. Bales, K. Ranta, M. J. Barlow, B. M. Goodson, M. S. Rosen, E. Y. Chekmenev, *J. Magn. Reson.* **2020**, *319*, 106813.

[18] P. J. Rayner, M. J. Burns, A. M. Olaru, P. Norcott, M. Fekete, G. G. R. Green, L. A. R. Highton, R. E. Mewis, S. B. Duckett, *Proc. Natl. Acad. Sci. USA* **2017**, *114*, E3188 – E3194.

[19] M. Fekete, F. Ahwal, S. B. Duckett, *J. Phys. Chem. B* **2020**, *124*, 4573 – 4580.

[20] E. Y. Chekmenev, V. A. Norton, D. P. Weitekamp, P. Bhattacharya, *J. Am. Chem. Soc.* **2009**, *131*, 3164 – 3165.

[21] R. Sarkar, A. Comment, P. R. Vasos, S. Jannin, R. Gruetter, G. Bodenhausen, H. Hall, D. Kirik, V. P. Denisov, *J. Am. Chem. Soc.* **2009**, *131*, 16014 – 16015.

[22] D. I. Hoult, R. E. Richards, *J. Magn. Reson.* **1976**, *24*, 71 – 85.

[23] M. L. Truong, A. M. Coffey, R. V. Shchepin, K. W. Waddell, E. Y. Chekmenev, *Contrast Media Mol. Imaging* **2014**, *9*, 333 – 341.

[24] M. Suefke, A. Liebisch, B. Blumich, S. Appelt, *Nat. Phys.* **2015**, *11*, 767 – 771.

[25] M. Suefke, S. Lehmkuhl, A. Liebisch, B. Blumich, S. Appelt, *Nat. Phys.* **2017**, *13*, 568 – 572.

[26] S. Appelt, A. Kentner, S. Lehmkuhl, B. Blümich, *Prog. Nucl. Magn. Reson. Spectrosc.* **2019**, *114 – 115*, 1 – 32.

[27] H.-Y. Chen, Y. Lee, S. Bowen, C. Hilty, *J. Magn. Reson.* **2011**, *208*, 204 – 209.

[28] S. Appelt, S. Lehmkuhl, S. Fleischer, B. Joalland, N. M. Ariyasingha, E. Y. Chekmenev, T. Theis, *J. Magn. Reson.* **2021**, *322*, 106815.

 © 2021 Wiley-VCH GmbH

[29] A. N. Pravdivtsev, F. D. Sönnichsen, J.-B. Hövener, *ChemPhysChem* **2020**, *21*, 667 – 672.
[30] E. M. M. Weber, D. Kurzbach, D. Abergel, *Phys. Chem. Chem. Phys.* **2019**, *21*, 21278 – 21286.
[31] S. Korchak, L. Kaltschnee, R. Dervisoglu, L. Andreas, C. Griesinger, S. Glöggler, *Angew. Chem. Int. Ed.* **2021**, *60*, 20984 – 20990.
[32] N. M. Ariyasingha, B. Joalland, H. R. Younes, O. G. Salnikov, N. V. Chukanov, K. V. Kovtunov, L. M. Kovtunova, V. I. Bukhtiyarov, I. V. Koptyug, J. G. Gelovani, E. Y. Chekmenev, *Chem. Eur. J.* **2020**, *26*, 13621 – 13626.
[33] B. Joalland, N. M. Ariyasingha, H. R. Younes, S. Nantogma, O. G. Salnikov, N. V. Chukanov, K. V. Kovtunov, I. V. Koptyug, J. G. Gelovani, E. Y. Chekmenev, *Chem. Eur. J.* **2021**, *27*, 2774 – 2781.
[34] B. Joalland, N. M. Ariyasingha, S. Lehmkuhl, T. Theis, S. Appelt, E. Y. Chekmenev, *Angew. Chem. Int. Ed.* **2020**, *59*, 8654 – 8660; *Angew. Chem.* **2020**, *132*, 8732 – 8738.
[35] M. A. Hope, S. Björgvinsdóttir, C. P. Grey, L. Emsley, *J. Phys. Chem. Lett.* **2021**, *12*, 345 – 349.
[36] C. R. Bowers, D. P. Weitekamp, *Phys. Rev. Lett.* **1986**, *57*, 2645 – 2648.
[37] T. C. Eisenschmid, R. U. Kirss, P. P. Deutsch, S. I. Hommeltoft, R. Eisenberg, J. Bargon, R. G. Lawler, A. L. Balch, *J. Am. Chem. Soc.* **1987**, *109*, 8089 – 8091.
[38] F. Reineri, T. Boi, S. Aime, *Nat. Commun.* **2015**, *6*, 5858.
[39] M. Mishkovsky, A. Comment, R. Gruetter, *J. Cereb. Blood Flow Metab.* **2012**, *32*, 2108 – 2113.
[40] M. Mishkovsky, T. Cheng, A. Comment, R. Gruetter, *Magn. Reson. Med.* **2012**, *68*, 349 – 352.
[41] S. Nantogma, B. Joalland, K. Wilkens, E. Y. Chekmenev, *Anal. Chem.* **2021**, *93*, 3594 – 3601.
[42] M. G. Pravica, D. P. Weitekamp, *Chem. Phys. Lett.* **1988**, *145*, 255 – 258.

Manuscript received: July 5, 2021
Version of record online: September 30, 2021

 © 2021 Wiley-VCH GmbH

analytical chemistry

Made available for a limited time for personal research and study only License.

pubs.acs.org/ac Review

Instrumentation for Hydrogenative Parahydrogen-Based Hyperpolarization Techniques

Andreas B. Schmidt,* C. Russell Bowers, Kai Buckenmaier, Eduard Y. Chekmenev, Henri de Maissin, James Eills, Frowin Ellermann, Stefan Glöggler, Jeremy W. Gordon, Stephan Knecht, Igor V. Koptyug, Jule Kuhn, Andrey N. Pravdivtsev, Francesca Reineri, Thomas Theis, Kolja Them, and Jan-Bernd Hövener*

Cite This: *Anal. Chem.* 2022, 94, 479−502

Read Online

ACCESS | Metrics & More | Article Recommendations

CONTENTS

Analysis of pH_2 Polarizers 480
- Parahydrogen Addition 480
- Spin-Order Transfer 481
- Purification and Quality Assurance 481
- Components and Capabilities of a Polarizer 481

Review of Published Instruments 482
- Parahydrogen Generators 482
- Spin Order Transfer (SOT) 483
  - SOT Conditions 483
- SOT at Millitesla Fields 485
  - SOT Conditions 485
  - Published Setups 485
  - Challenges 486
- SOT at Ultralow Fields (ULF) 487
  - SOT Conditions 487
  - Published Setups 487
  - Challenges 487
- Magnetic Field Cycling (MFC) 487
  - SOT Conditions 487
  - Published Setups 488
  - Challenges 490

PHIP of Gases 490
- Published Setups 490
- Challenges 491

Purification 491
- Catalyst Scavenging 491
- Liquid−Liquid Phase Separation 493
- Heterogeneous Catalysts 493
- Precipitation 494

Other Promising Developments 494
- PHIP-on-a-Chip 494
- Radio Amplification by Stimulated Emission of Radiation (RASER) 494
- PHIP-X 494

Toward Clinical Application 494

Conclusions 495

Author Information 495
- Corresponding Authors 495
- Authors 495
- Author Contributions 496
- Notes 496
- Biographies 496

Acknowledgments 497

References 498

The unique properties of the entangled, antisymmetric nuclear spin state of dihydrogen, parahydrogen (pH_2), has intrigued physicists, chemists, and other scientists for almost a century. pH_2 was used as a model system in the early days of quantum mechanics[1] and is used for fueling rockets as well as combustion-free cars today. In the 1980s, pH_2 was discovered as a convenient and potent source of spin order, allowing the enhancement of the signals of magnetic resonance (MR) by several orders of magnitude.[2−4] In the advent of hyperpolarized (HP) contrast agents (CA) for biomedical MR imaging (MRI) that followed, pH_2-based hyperpolarization methods played an important role in the acquisition of the first HP ^{13}C *in vivo* images (Figure 1).[5,6] Ever since, pH_2 has proven to be highly valuable for analytical investigations and fundamental research, *e.g.*, in analytical and catalytic chemistry or in the physics of singlet spin states.[7−10]

pH_2 can be produced rapidly and stored easily. As one of four (nuclear) spin states of dihydrogen, 25% of H_2 at room temperature is pH_2, while the other 75% is orthohydrogen (oH_2), following the Boltzmann distribution). At lower temperatures, however, the *para*-fraction increases until at approximately 25 K, where 100% pH_2 is obtained. While the *para*-enrichment is fast using an appropriate catalyst, pH_2 can be stored for hours to days at room temperature without significant loss if the catalyst is absent. These unique properties make pH_2 an ideal host of pure spin order that can be produced easily, stored conveniently (in a pressurized bottle),

Special Issue: Fundamental and Applied Reviews in Analytical Chemistry 2022

Published: January 1, 2022

Downloaded via WAYNE STATE UNIV on January 12, 2022 at 19:13:35 (UTC).
See https://pubs.acs.org/sharingguidelines for options on how to legitimately share published articles.

ACS Publications © 2022 American Chemical Society

https://doi.org/10.1021/acs.analchem.1c04863
Anal. Chem. 2022, 94, 479−502

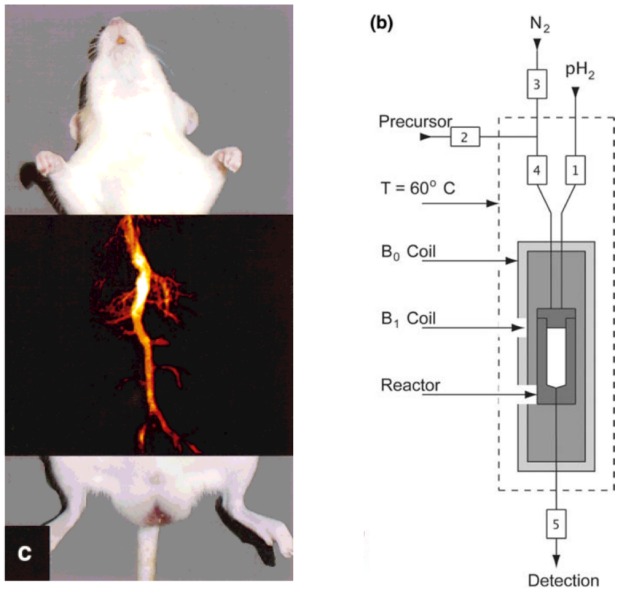

Figure 1. First hyperpolarized ^{13}C *in vivo* MRI ever published (a). The contrast agent, hydroxyethyl [1-^{13}C]propionate-d_3 (HEP), was produced using a prototype commercial PHIP polarizer (Amersham Biosciences, healthcare company), similar to the one shown schematically in (b). Broadly speaking, the polarizers consisted of a unit handling the fluids, the actual hyperpolarization (spin-order transfer), and the coordination of the entire process (numbers 1−5 represent valves). Images reproduced from Parahydrogen-Induced Polarization in Imaging: Subsecond ^{13}C Angiography, Golman, K.; Axelsson, O.; Johannesson, H.; Mansson, S.; Olofsson, C.; Petersson, J. S. *Magn. Reson. Med.*, Vol. *46*, Issue 1, 1−5 (ref 5). Copyright 2001 Wiley (a) and reprinted by permission from Springer: *Magn. Reson. Mater. Phys.*, PASADENA Hyperpolarization of ^{13}C Biomolecules: Equipment Design and Installation, Hövener, J.-B.; Chekmenev, E. Y.; Harris, K. C.; Perman, W. H.; Robertson, L. W.; Ross, B. D.; Bhattacharya, P. *Magn. Reson. Mater. Phys.* Vol. 22, 111−121 (ref 90). Copyright Springer 2009 (b).

and used on demand, *e.g.*, for producing hyperpolarized CAs or observing chemical reactions with enhanced sensitivity.

When it comes to clinical applications, however, dissolution dynamic nuclear polarization (dDNP) evolved faster than pH_2-based HP methods.[11,12] The reasons for this may be that (a) at first, only a few biologically relevant CAs were available (because of limited chemistry at that time), (b) that mastering the complex process of parahydrogen induced polarization (PHIP) was not straightforward (involving quantum mechanics, chemical reactions, and magnetic resonance methods tailored to each individual CA), and that (c) no pH_2-polarizers were commercially available, while there were at least three different dDNP polarizer generations.

While pH_2 is easily produced in large quantities, at low cost and with a shelf life of days (depending on the storing conditions), there are some hurdles to overcome before a CA is ready for administration. For one, the pH_2 spin order *per se* is MR invisible (total spin of 0!) and well hidden inside the dihydrogen molecule. To obtain a hyperpolarized CA from pH_2, typically, the following steps have to be taken: (a) to bring pH_2 and the target into contact (by catalytic addition or reversible exchange), (b) to transfer or transform the pH_2-derived spin order into a desired form, and (c) the purification and quality assurance (QA) prior to an *in vivo* application.

These steps usually involve a chemical reaction at elevated temperatures, pressures, sometimes in aggressive media or extreme pH, synchronized with quantum mechanical spin order transfer (SOT) mediated by evolution at constant or varying magnetic fields and radiofrequency (RF) pulses. To realize this process, various devices have been devised; however, a single, unified design has not yet emerged. The lack of such a device may be attributed to the fact that the power and versatility of pH_2 has resulted in quite a few different methods; the magnetic fields alone vary by a factor of 10^9 (from nanotesla to tesla). Even today, pH_2 hyperpolarization methods keep evolving at a fast pace; among the ground-breaking advances, SABRE,[13] gases,[14,15] continuous HP,[16−18] PHIP-SAH,[19] RASER,[20−23] purification methods,[24] and relay methods[25,26] are only a few examples from the past decade. These methods require specific experimental conditions and ultimately dedicated instrumentation, which differs from method to method.

For a standardized, clinical application of a specific contrast agent, however, a consolidated setup is required that can be certified and approved and provides reliable polarization and quality assurance. In this respect, much can be learned from SEOP[27] and DNP[11,12] with respect to polarizers and regulatory approval.

Here, we review the different instrumentations for pH_2 hyperpolarization, with an emphasis on biomedical applications. To keep this review concise, we focus on setups for hydrogenative pH_2-based hyperpolarization alone and the most recent literature (∼last 5 years); still, we refer to pioneering and game-changing developments whenever appropriate and when other methods (SABRE, DNP, SEOP, etc.) show similar instrumentational aspects. Dedicated reviews on SABRE-related instrumentation, spin-order transfer, and pH_2 production are expected to be published elsewhere.

■ ANALYSIS OF pH_2 POLARIZERS

The requirements for a biomedical polarizer may be defined as to (i) provide a clean, (ii) aqueous solution of (iii) highly polarized, (iv) appropriately concentrated agents at (v) physiological conditions that is preferably produced in a (iv) good-manufacturing process (GMP). To make such a contrast agent, the role of hardware may be categorized as follows:

1. Making the pH_2 spin order available to the target molecule (hydrogenation);
2. Transferring the pH_2-derived spin order into the desired spin hyperpolarization (typically longitudinal X-nuclear magnetization);
3. Purification of the solution and assuring quality.

We will elaborate on these steps in the following.

Parahydrogen Addition. Before the addition, the lifetime of gaseous[28−30] or dissolved[31−33] pH_2 is typically long (days or many minutes, respectively). However, once bound to the catalyst[34] or the precursor,[9,35−39] the lifetime of the spin order is drastically reduced because the added protons, referred to as I_1 and I_2, interact with the environment and the rest of the (now larger) spin system. Thus, the hydrogenation should be conducted as fast as possible to reduce relaxation losses. The hydrogenation kinetics are typically affected by a multitude of coupled reaction parameters, like temperature, pH_2-availability, solvent, catalyst, precursor molecule, and pH. While the catalyst is needed for the addition, it may cause relaxation at

https://doi.org/10.1021/acs.analchem.1c04863
Anal. Chem. 2022, 94, 479−502

the same time and needs to be removed before an injection if it is harmful.

The starting point for the SOT, *i.e.*, the density matrix after the hydrogenation, is strongly dependent on the coupling between I_1 and I_2. It is determined by the molecular structure and the external static magnetic field B_0. If the spins are "strongly coupled" (that is, if their mutual *J*-coupling J_{12} is much larger than the difference of their Larmor precession frequencies $\delta\nu$ ($\delta\nu \ll J_{12}$)), the eigenstates of the two-spin system are essentially the singlet-triplet (S-T) basis states. In this case, the "singlet spin order" $\mathbf{I_1 \bullet I_2} = I_{1x}I_{2x} + I_{1y}I_{2y} + I_{1z}I_{2z}$ (also known as the J-order) is usually the starting point for the SOT. In the opposite case ($\delta\nu \gg J_{12}$), the spins are referred to as weakly coupled. Then, the $I_{1z}I_{2z}$ spin order is typically the starting point for SOT after the off-diagonal elements of the density matrix were averaged away during the hydrogenation.[40] However, the $\mathbf{I_1 \bullet I_2}$ order can be preserved in weakly coupled systems by applying sufficiently strong ^{1}H decoupling[41,42] or can be encountered in effectively instantaneous reactions as in photo-PHIP experiments,[43,44] where reactions with pH_2 happen within a few microseconds.

The exact form of the spin order in the intermediate coupling regime, including the effect from singlet-triplet (S-T) mixing at the hydrogenation catalysts, was described by Bowers, Natterer, and others.[39,45−48] Such S-T mixing takes place in high and low fields and is one of the main reasons for reduced hyperpolarization yield.

In so-called PASADENA experiments (pH_2 and synthesis allows dramatically enhanced nuclear alignment), hydrogenation and SOT (or direct proton detection) take place at the same magnetic field.[3] Another experimental scheme often applied is referred to as adiabatic longitudinal transport after dissociation engenders net alignment (ALTADENA).[49] The latter typically features hydrogenation at lower fields (with S-T eigenbasis) followed by an adiabatic (slow) increase of B_0 into the weakly coupled regime.[50] This results in population of either the $|\alpha\beta\rangle$ or the $|\beta\alpha\rangle$ state of the high-field Zeeman eigenbasis, where α is the spin up, and β is the spin down state in the combined spin angular momentum state of both nuclei.

Spin-Order Transfer. As the literature on SOT may fill an entire review article alone,[51] we are focusing on the parts relevant for the instrumentation only. The available spin order after hydrogenation, the spin system, its eigenstates, and its interactions determine the most-effective SOT strategy. While the molecular spin system as such is usually fixed (with workarounds, *e.g.*, PHIP-SAH,[19] PHIP-X[26]), the interactions can be tailored to some extent by varying the (static) external magnetic field (B_{SOT}) or by applying B_1 fields over a period of time.[52] Likewise, the spin system can be affected, to some degree, by isotope labeling and reaction parameters such as temperature and pH. Deuteration is a convenient way to reduce relaxation and simplify the spin system, *e.g.*, to an effective 3-spin-1/2 system in RF-pulsed SOT.[42,53,54]

Roughly speaking, a SOT can be achieved by

- Evolution at one static field (sometimes referred to as "spontaneous" transfer);
- Evolution at different fields, magnetic field cycling (MFC-SOT);[19,24,55,56]
- Evolution plus specific manipulations by RF pulses (RF-SOT).[9,40,42,51,57−64]

Understanding the SOT requires profound knowledge of the underlying quantum mechanics. While analytical equations can be derived for simple systems, numerical simulations are usually required to determine the optimal parameters of more complex or realistic systems. These simulations can be implemented in any programming environment capable of matrix algebra. Using or building on existing (open source) packages may be convenient.[65−68]

Realizing the different variants of SOT usually requires a magnet (superconducting, resistive, permanent; sometimes shims), sometimes a multilayer mu-metal shield (to reach fields B_{SOT} in the nanotesla or microtesla range), and an NMR unit to excite and receive MR signals.

Purification and Quality Assurance. While the addition of pH_2 is performed by catalysis at sometimes harsh conditions, a physiological solution devoid of the catalyst is needed for *in vivo* administration. Various approaches have been described to achieve this goal, including:

- Filtering homogeneous catalysts,[69]
- Using immobilized catalysts that remain in the polarizer,[70−72]
- Heterogeneous catalysts that facilitate filtration;[17,71,73−78]
- Phase separation and precipitation.[24,79−82]

Different agents will generally require individual approaches as their chemical properties vary significantly. A QA module similar to that used for DNP will have to encompass (at least) purity, pH, a low bioburden, and temperature; no such device has emerged yet. For all approaches, time is of the essence, as precious signal enhancement is rapidly lost once the agent is hyperpolarized.

Components and Capabilities of a Polarizer. Orchestrating these steps requires a dedicated unit, often referred to as a "polarizer". Some have been described, with varying goals, properties, and capabilities, *e.g.*, SOT schemes, pressures, temperatures, *in situ* detection, automation, dosing, etc.[24,36,38,42,55,83−91] For convenience, such a polarizer may be separated in different units, some of which were described in literature:

- A fluid unit, handling the gases and liquids. It is typically composed of electromagnetic, manual, or pneumatic valves and tubes, borrowed, *e.g.*, from high-performance liquid chromatography (HPLC) as well as a custom-made reaction chamber or a (high-pressure) NMR tube. Inert materials and pressure and temperature resistance are important factors, as is the option to clean or sterilize.[92]
- An NMR unit, taking care of the SOT either by applying a constant magnetic field, a defined field cycle, or RF pulses. Low-field detection facilitates flip angle calibration and quality assurance.[92−94]
- A control unit: a software controlling a digital-to-analog converter (DAC) and an analog-to-digital converter (ADC), *e.g.*, for switching valves, B_0 control, temperature readings, and NMR. These needs have been addressed by using the hardware of the NMR/MRI,[87,88,95] by PC-controlled digital-acquisition boards (DAQ) with[85,86] and without[42,55,83,89,90,96] an additional NMR spectrometer. As a minimum, the control software will have to accommodate easy access to the (sometimes overlapping) timings of each step in the polarization procedure and may extend to acquiring NMR signal *in situ* to facilitate calibrations and improve polarization

https://doi.org/10.1021/acs.analchem.1c04863
Anal. Chem. 2022, 94, 479−502

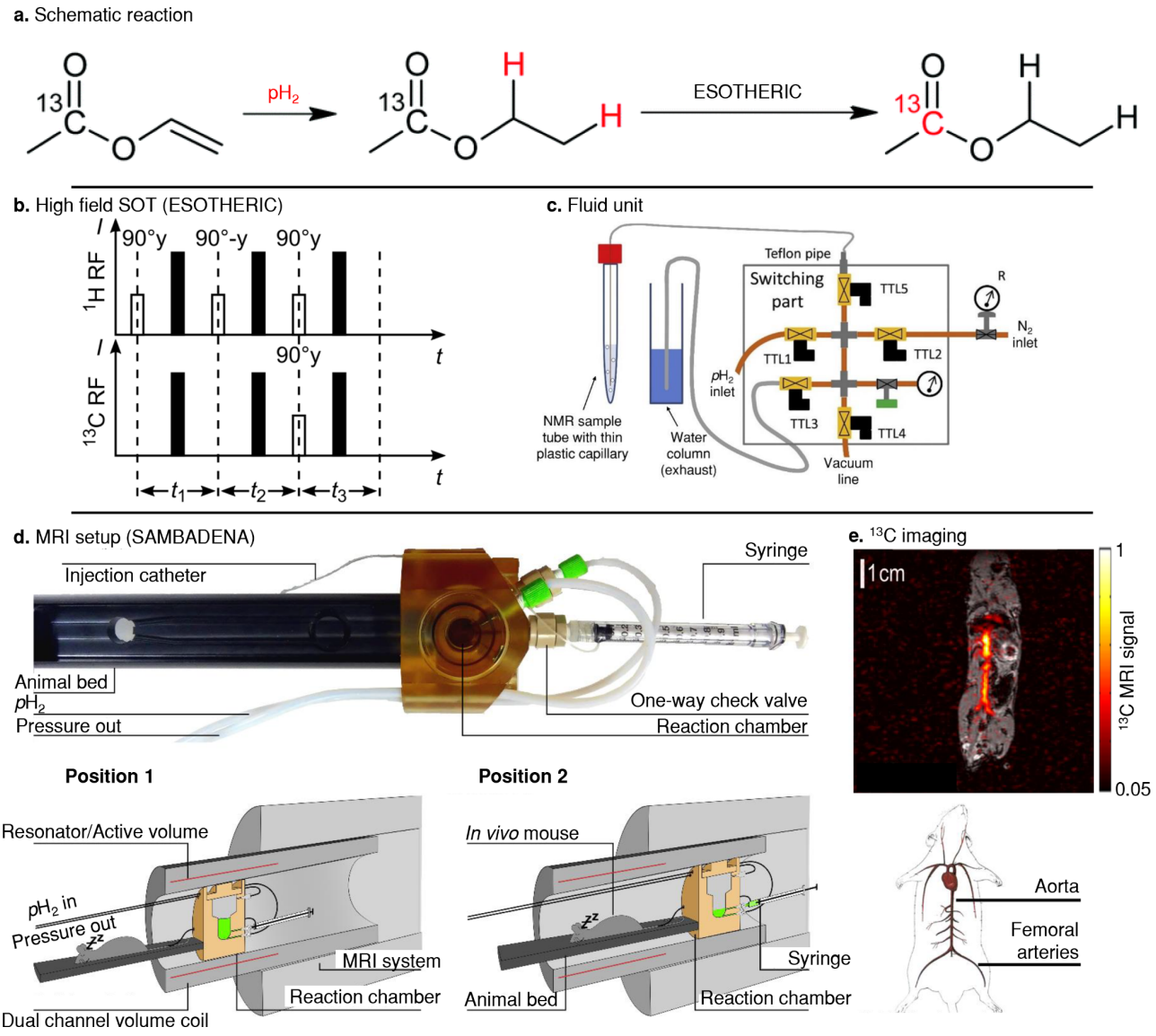

Figure 2. PHIP setups for SOT at constant magnetic fields >1 T, where spin systems are typically in the weak-coupling regime. Schematic view of the hyperpolarization process at high field, where ethyl acetate is polarized by adding pH_2 (a) and spin order transfer with ESOTHERIC (b) or spin-lock induced crossing (SLIC).[214,215] The fluidics are usually handled by a unit consisting of switchable magnetic valves and flow regulation for guiding gases or to apply vacuum to a tube or reactor (c). For MRI systems, dedicated reaction chambers were combined with animal beds allowing animal monitoring, anesthesia, life support, and fast administration of the HP contrast agent (d). As an example, subsecond *in vivo* ^{13}C angiography of a mouse was demonstrated only seconds after the polarization (e), while compatible temperature, pressure, and sterility were assured. Part (a) is reproduced from Pulsed Magnetic Resonance to Signal-Enhance Metabolites within Seconds by Utilizing Para-Hydrogen, Korchak, S.; Yang, S.; Mamone, S.; Glöggler, S., *ChemistryOpen*, Vol. 7, Issue 5, 344−348 (ref 62). Copyright 2018 Wiley. Part (c) is reprinted from *J. Magn. Reson.*, Vol. 285 (Supplement C), Kiryutin, A. S.; Sauer, G.; Hadjiali, S.; Yurkovskaya, A. V.; Breitzke, H.; Buntkowsky, G. A Highly Versatile Automatized Setup for Quantitative Measurements of PHIP Enhancements, pp. 26−36 (ref 95). Copyright 2017, with permission from Elsevier. Parts (d) and (e) are reproduced from In Vivo 13C-MRI Using SAMBADENA, Schmidt, A. B.; Berner, S.; Braig, M.; Zimmermann, M.; Hennig, J.; Elverfeldt, D. von; Hövener, J.-B. *PLoS One*, Vol. *13*, Issue 7, e0200141 (ref 91). Copyright 2018 Public Library of Science.

(*e.g.*, Paravision, LabVIEW,[85−87,93,97] and MATLAB[38,96]).

REVIEW OF PUBLISHED INSTRUMENTS

This section comprises a brief description of instrumentation to produce pH_2, setups for producing HP solutions, HP gases, purification methods, and translation. The section on setups to produce HP liquids is structured by the magnetic field B_{SOT}, where the SOT takes place.

Parahydrogen Generators. As a manifestation of the generalized Pauli exclusion principle, hydrogen molecules exist as two different nuclear spin isomers: the triplet spin states, called oH_2, and the singlet spin state, called pH_2. The energy separation between the ground states of pH_2 and oH_2 is 170.6 K.[83] Hence, in thermal equilibrium at low temperatures (below 25 K), almost all hydrogen molecules are in the singlet state, *i.e.*, nearly pure pH_2. Note that the temperature determines the achievable pH_2-fraction f_{pH2}.

https://doi.org/10.1021/acs.analchem.1c04863
Anal. Chem. 2022, 94, 479−502

The production of pH_2 is straightforward: letting hydrogen gas flow over an ortho-para conversion catalyst at low temperatures results in enriched pH_2. Common conversion catalysts are granular materials with high surface area, such as FeO(OH),[28,29,98] nickel sulfate,[99] or chromic oxide (CrO_3) supported on silica gel.[100] Activated charcoal has been used as an ortho-para conversion catalyst in early works, but the efficiency appears to be lower than for the ferromagnetic oxide materials, especially at high flow rates. The catalytic effect originates from (ferro- or para-) magnetic properties, which induce highly inhomogeneous local magnetic fields that accelerate ortho-para conversion.[36]

The published pH_2 generator designs offer different properties with respect to cost, pH_2-fraction, pressure, flow rate, and ease of use. Aside from commercial products (Bruker BPHG 90, XeUS Technologies LTD, HyperSpin Scientific UG, Advanced Research Systems, IDB Budzylek), many designs for home-built generators have arisen over the last decades. In particular, three primary coolant technologies dominate: single-stage or dual-stage closed-cycle helium cryostats operating at 13.5 to 40 K,[29,36,101−105] liquid helium dewars at 14 to 30 K,[99,100,106,107] and liquid nitrogen dewars at 77 K.[17,98,108−112] Consequently, a dual stage or liquid-helium-based pH_2 generator can practically reach enrichments approaching 100% and a liquid-nitrogen-based pH_2 generator enrichments of up to 52%, respectively. In a liquid N_2 generator pumped below ambient pressure, the enrichment can be increased by lowering the temperature further, *e.g.*, to 63 K at 21 mbar allowing a pH_2 fraction of ≈65%.[113]

The quantification of the pH_2 enrichment can be done optically (*e.g.*, Raman) or by NMR spectroscopy. Raman spectroscopy is about 500 times faster than NMR and does not require a reference sample since it detects both oH_2 and pH_2 directly.[111] However, NMR spectroscopy is generally the quantification method of choice since it is already available in the MR laboratories where PHIP experiments are carried out. The details of quantification have been reviewed thoroughly previously.[114]

Spin Order Transfer (SOT). *SOT Conditions.* In PASADENA experiments, the hydrogenation reaction, observation, and SOT take place at the high magnetic field of an NMR or MRI system (≈ Tesla). If pH_2 is added at chemically nonequivalent sites, I_1 and I_2 typically become weakly coupled (Figure 2a). The strongly coupled case is typically only present if $\delta\nu \approx 0$.[39,115]

For the former case, PHIP ^{1}H signal can be observed as antiphase peaks by a simple 45° excitation. Alternatively, spin order can be converted into in-phase magnetization using RF pulse sequences[116−118] which also enables detection in inhomogeneous B_0 fields.[119,120] However, the first in-phase PHIP ^{1}H spectra were obtained by Pravica et al. by field cycling (ALTADENA),[49] an approach that has also enabled polarization transfer to ^{19}F.[50]

Several techniques have been published to convert $I_{1z}I_{2z}$ into observable magnetization of X-nuclei (often ^{13}C). Here, most RF-SOT sequences are adaptations of the insensitive nuclei enhanced by polarization transfer (INEPT) sequence that considers initial $I_{1z}I_{2z}$ spin order, Figure 2b.[59,121] After the early work from Haake, Natterer, and Bargon, who introduced the pH_2 INEPT+ (phINEPT+) sequence,[60] l-PHINEPT+,[51] selective excitation of polarization using PASADENA (SEPP) INEPT,[122] selective-90 (s90) phINEPT,[54,123,124] and efficient SOT to heteronuclei via relayed INEPT chains (ESOTHERIC, Figure 2b)[62,82] sequences were suggested. Note that depending on the spin system, and neglecting relaxation, all RF-SOT schemes can yield ∼100% ^{13}C-polarization, in principle, except phINEPT+, which has a theoretical maximum of ∼50% because of the initial 45° ^{1}H pulse.[38,125] If the initial spin order is $\mathbf{I_1 \bullet I_2}$, different SOT schemes are required, *e.g.*, Goldman's sequence[42] for succinate obtained by reacting a fumarate precursor molecule.[39,48] Additional RF-SOT techniques for strongly coupled protons will be introduced in the next section (SOT at millitesla fields). Adiabatic passages through level anti crossings (also referred to as avoided crossings) were shown to be efficient for the transfer of singlet pH_2 spin order to ^{13}C polarization.[126−128]

Published Setups. Various setups for performing PHIP in NMR[95,123] and MRI systems have been described.[38,91] Such implementations offer the advantage that parts of the sophisticated MR machines, including NMR excitation and acquisition and highly homogeneous field over a large volume, can be employed in the hyperpolarization process. Typically, the NMR or MRI system offers TTL outputs that allow control of the fluid path directly from within the pulse program.

To perform the hyperpolarization in an NMR system, Kiryutin et al. introduced a setup consisting of several valves for supplying gases or liquids, *e.g.*, a cleaving agent to convert a precursor into the desired metabolite.[95] Using standard 5 mm or 10 mm NMR tubes for hydrogenation, SOT, detection, and purification, the system can be implemented in all standard and benchtop NMR spectrometers and has been done so by many laboratories (Figure 2c).[62,120,123,129,130] For *in vivo* imaging, the HP contrast agent has to be transferred to an imaging system.

Performing hyperpolarization within the bore of an MRI system allows *in vivo* imaging only seconds after the hydrogenation (SAMBADENA). Here, the hydrogenation takes place in a reactor enclosed in a dual tune, transmit-receive ^{1}H/^{13}C volume coil, equipped with a local receive coil, for RF-SOT and *in vivo* MRI.[38] The reactor was mounted on the animal bed (with animal warming, vital sign monitoring, anesthesia) such that the contrast agent was delivered directly into a syringe for injection at high field, Figure 2e.[91] *In vivo* imaging of a sterile solution of hydroxyethyl [1-^{13}C]-propionate-d_3 within 15 s after hyperpolarization was demonstrated (Figure 2f), although no purification (*i.e.*, catalyst filtering) was performed.[91]

Published Agents. High ^{13}C polarizations for highly concentrated molecules have been demonstrated with phINEPT+ and ESOTHERIC sequences and SAMBADENA.[38,120,129] Promising PHIP agents that were produced at high field with polarization above 10% are tetrafluoropropyl [1-^{13}C]propionate-d_3 (TFPP),[131] [1-^{13}C]succinate-d_2,[39,48] and [2-^{13}C]pyruvate.[132] The latter was achieved using PHIP-SAH, ESOTHERIC, and subsequent cleavage of the side arm of cinnamyl [2-^{13}C]pyruvate. Remarkable polarizations were also achieved for other promising PHIP-SAH molecules, namely, ethyl [1-^{13}C]acetate[120,129] and cinnamyl [1-^{13}C]pyruvate.[62,82]

Challenges. The main challenges of *in situ* polarizer setups such as SAMBADENA are due to the limited space within the bore of the MRI or NMR magnet: accommodating production, purification, QA, and the administration within a small volume is not an easy task. RF-SOT sequences, theoretically, achieve ≈100% ^{13}C-polarization but only in fully ^{2}H-labeled molecules, as additional *J*-couplings will interfere (neglecting relaxation).[38,54,123,129,130] In NMR spectrometers, radiation damping can disturb the SOT, while the limited RF power is a serious

https://doi.org/10.1021/acs.analchem.1c04863
Anal. Chem. 2022, 94, 479−502

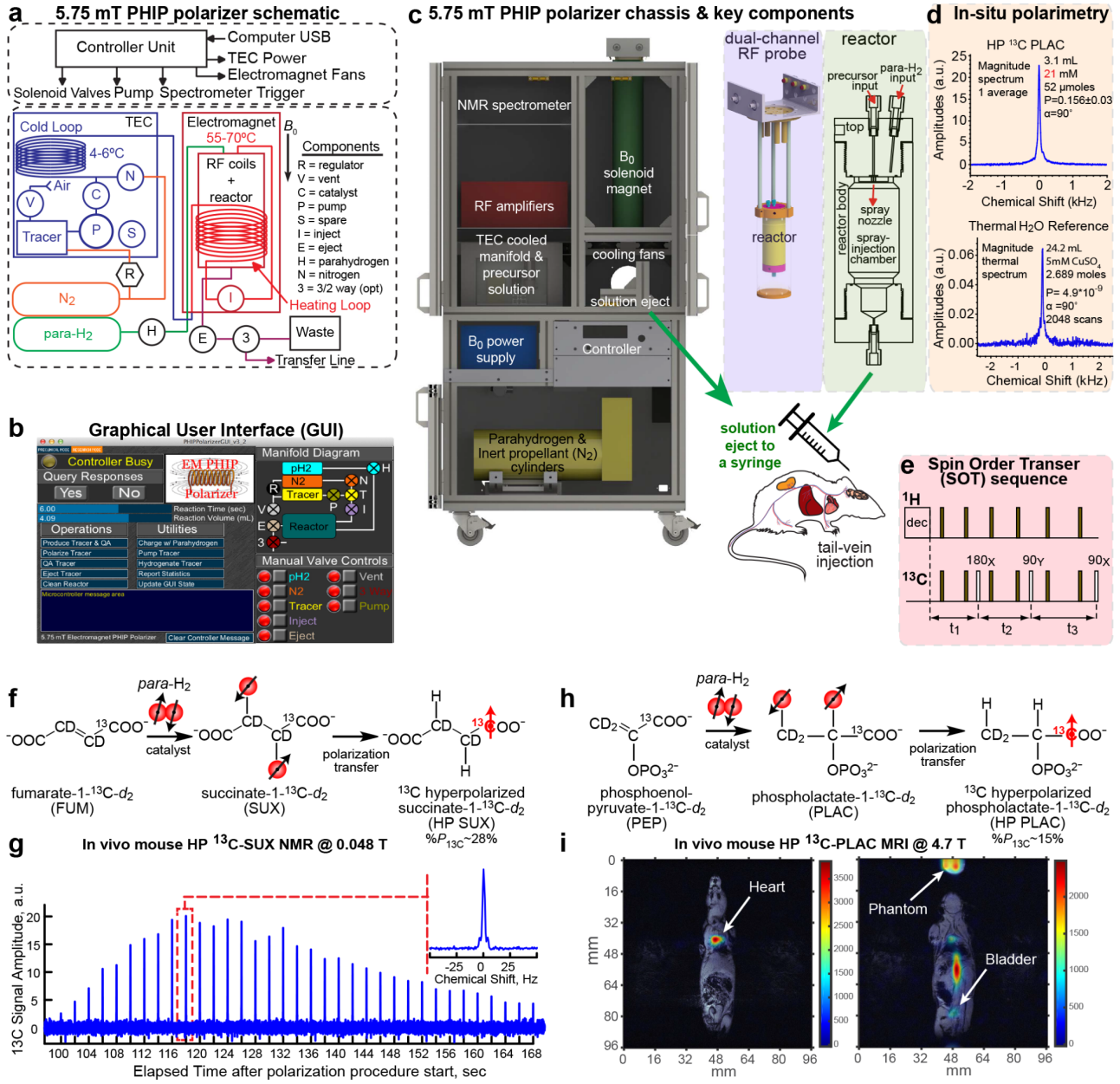

Figure 3. Setups and examples for PHIP at millitesla fields: Overall schematic (a), graphical user interface (b), and rendering (c) of a 5.75 mT automated, preclinical, open-source PHIP polarizer. A dual-channel, $^{1}H/^{13}C$ RF coil was placed inside a B_0 solenoid electromagnet (c, left), and a spray-injection reactor was nested inside the coil. *In situ* NMR detection at ~62 kHz enabled RF calibration and quantification of ^{13}C polarization with respect to thermally polarized water (d). During the hydrogenation reaction of a few seconds, ^{1}H-decoupling was applied to preserve **I·S** spin order and before the polarization was transferred to ^{13}C using the sequence proposed by Goldman et al. (e) Note that there are only three "effective" pulses (white) used while the others (gray) are for refocusing of the Zeeman evolution only. Reaction scheme (f) and *in vivo* ^{13}C NMR (g) of contrast agent SUX detected at low magnetic fields (~0.048 T). Reaction scheme (h) and *in vivo* ^{13}C MRI imaging (i) of contrast agent PLAC at 4.7 T: ^{13}C-MRI (color) was acquired approximately 5−10 s after the injection of ~0.2 mL, ~30 mM hyperpolarized PLAC into the tail vein of a healthy nude mouse (prior to tumor implantation) and overlaid on representative ^{1}H images (gray scale, ^{13}C: GRE, 3 × 3 mm^2 in-plane resolution, 6 mm slice thickness, FOV = 96 × 96 mm^2). Parts (a−d), (h), and (i) are reproduced from Coffey, A. M.; Shchepin, R. V.; Truong, M. L.; Wilkens, K.; Pham, W.; Chekmenev, E. Y. Open-Source Automated Parahydrogen Hyperpolarizer for Molecular Imaging Using 13C Metabolic Contrast Agents. *Anal. Chem.* **2016**, *88*, 8279−8288 (ref 86). Copyright 2016 American Chemical Society. Further permissions related to the material excerpted should be directed to the ACS. Parts (f) and (g) reprinted from *J. Magn. Reson.*, Vol. *281* (Supplement C), Coffey, A. M.; Feldman, M. A.; Shchepin, R. V.; Barskiy, D. A.; Truong, M. L.; Pham, W.; Chekmenev, E. Y. High-Resolution Hyperpolarized in Vivo Metabolic ^{13}C Spectroscopy at Low Magnetic Field (48.7 mT) Following Murine Tail-Vein Injection, pp. 246−252 (ref 149). Copyright 2017, with permission from Elsevier.

concern in MRI setups[120,133−135] because of the large excitation bandwidth needed.[136] Moreover, translational

https://doi.org/10.1021/acs.analchem.1c04863
Anal. Chem. 2022, 94, 479−502

motion of the molecules in the inhomogeneous field of the relatively large reaction chamber in an MRI during SOT can reduce the polarization.[137]

SOT at Millitesla Fields. *SOT Conditions.* The characteristic feature of SOT in the millitesla range is the strongly coupled regime ($\delta\nu \ll J_{I1I2}$). Typically, the pairwise pH_2 addition takes place under proton decoupling at B_{SOT}, in part to reduce relaxation, but also to preserve the $\mathbf{I_1 \bullet I_2}$ spin order (Figure 3f,h). After the decoupling, RF-SOT sequences are used to transfer the spin order to a ^{13}C nucleus. A wide range of efficient pulse sequences have been reported[51,57,58] to accomplish polarization transfer in millitesla field range including the pioneering sequence developed by Goldman and co-workers (Figure 3e).[42,83]

Published Setups. As the ^{13}C hyperpolarization can persist for several minutes, the contrast agent can be transferred from the polarizer to the detector without overwhelming loss, *e.g.*, for polarimetry (*i.e.*, measuring the degree of induced polarization) or ultimate application (*i.e.*, *in vivo* imaging). As a result, several millitesla setups with the main static magnetic field ranging from 1.7 mT[89,90] to 50 mT were developed and reported.[85]

The use of the low magnetic field offers certain advantages: (1) the field can be generated by inexpensive electromagnets, resulting in an overall cost-efficient, portable setup;[93] (2) susceptibility effects are low, and B_0 inhomogeneities can be compensated for by magnet design,[93] shims, and sufficiently strong RF pulses. Utilizing an electromagnet has allowed SOT over large reaction volumes, up to 100 mL were reported,[90] enabling the production of clinical-scale doses of ^{13}C-hyperpolarized contrast agents.[83]

These translational advantages were likely decisive for Amersham Biosciences, a healthcare company, to choose this approach for the first commercial prototype. *In vivo* feasibility studies using the Amersham polarizer have been reported extensively.[42,69,83,138] The overall design of the Amersham polarizer was not reported in detail,[42,83,84,139] but several closely related PHIP millitesla polarizer designs were subsequently reported.[36,85−87,89,90,92−94,97]

As described above, the lifetime of the pH_2-derived ^1H spin order is on the order of seconds, and hence, for effective ^{13}C HP, the hydrogenation needs to be completed quickly.[36,140] In practice, fast hydrogenation is achieved through the use of a reactor pressurized to ∼10 bar with pH_2 followed by a spray injection of a hot stream of precursor solution into the chamber.[89,90] For biomedical applications, the reaction is performed in aqueous media employing water-soluble PHIP catalyst at elevated temperature (70−95 °C).[36,86,89,90,139] As a result, the entire bolus of the precursor molecule can be reacted quickly (in a few seconds), i.e., on a time scale that is faster or similar to the decay of the $\mathbf{I_1 \bullet I_2}$ spin order.

The experimental hardware for the hyperpolarization process is relatively similar among reported millitesla PHIP polarizers (Figure 1). By definition, such a system employs a B_0 magnet operating in the millitesla range with typical field strength of 2−9 mT,[36,86,89,90] although the use of higher field (48 mT) permanent magnets have been reported.[85] A large-volume (∼300 mL) dual-channel RF probe is placed inside the magnet to deliver ^1H and ^{13}C RF pulses for the SOT sequence. The high-pressure reactor is nested inside the dual-channel RF coil; Figure 3c shows an example of such an electromagnet-based polarizer. A millitesla-PHIP polarizer is typically connected to (or contains) cylinders of compressed ultra-high-purity (>99.999% or 5.0) pH_2 and inert propellant gas (N_2 or Ar). A series of high-pressure valves and tubes form a manifold (Figure 3a) to fill the reaction chamber with pH_2.[141] This step is followed by the injection of hot precursor solution into the chamber through a nozzle using an inert propellant gas. Various setups were designed to inject a prescribed amount of the precursor solution into the reaction chamber and to eject the HP contrast agent into a receiver ready for transfer and *in vivo* MRI. Although specialized heaters can be employed to control the reaction temperature, the design shown in Figure 3c employs heating generated by a >100 W electromagnet.

Several approaches were developed to orchestrate the interplay of actuating multiple valves and playing out the RF-SOT, usually including software and a hardware interface (LabVIEW-,[36,90,96,97] Arduino-,[86] MATLAB,[96] and NMR spectrometer based[87]). A typical graphical user interface (GUI) allows setting various parameters (reaction time, precursor dose), choosing the SOT sequence, actuating individual valves, and executing various polarization or maintenance routines and sometimes performing NMR (Figure 3b, open-source Arduino-based controller software).[86] All published controller designs have their own merits.

To achieve high and reliable polarization through robust device operation, the accurate and precise application of the RF-SOT is critical.[51] Optimal RF-SOT performance requires calibrated B_1 power and transmission resonance frequencies for both RF channels in particular. Performing these calibrations *in situ* by detecting NMR signal in the reaction chamber using a transmit-receive polarizer design drastically facilitates these procedures. *In situ* calibrations, however, are not necessarily needed to produce the HP agents, because an external (*i.e.*, *ex situ*) NMR spectrometer, MRI scanner, or a low-field polarimetry station may be employed for the calibrations[89] and for probing the achieved ^{13}C polarization level.[69] This so-called transmit-only design is less complex and typically result in a lower device cost as no extra NMR receiver hardware is needed. The transmit RF pulses can be generated using simple waveform generators (*e.g.*, NI, Austin, TX), consumer-grade RF amplifiers (WRAT, Onkyo, Osaka, Japan), and untuned RF coils with a low Q factor, mitigating radiation damping issues noted in the above section.

The hyperpolarizers employing transmit-receive design were realized by using a commercial, low-frequency, dual-channel NMR spectrometer and dual tune transmit-receive coil (*e.g.*, Kea2, Magritek).[86,87] In another approach, a geometrically decoupled, single or dual tuned receive coil was added to the untuned transmit coil, using the same low-cost waveform generators, amplifiers, and ADC/DAC hardware as for the transmit-only design described above.[93,96]

These transmit-receive designs allow using the signal of thermally polarized water to calibrate B_0 and B_1.[86,87,93,96,142] As the polarization of HP samples is independent of the detection field, a high signal-to-noise ratio (SNR) spectrum was readily obtained in *in situ* low-field polarimetry as shown for the HP contrast agent [1-^{13}C]phospholactate-d_2 (PLAC) at ∼62 kHz (Figure 3d).

While transmit-receive designs are more complex and can be more expensive (by ∼$30 000 for the Kea2), calibration is relatively straightforward, and good reliability and reproducibility of the hyperpolarization yield is achieved. The efficiency of SOT can be improved further by reducing the complexity of the spin system. For example, deuteration was used to simplify

https://doi.org/10.1021/acs.analchem.1c04863
Anal. Chem. 2022, 94, 479−502

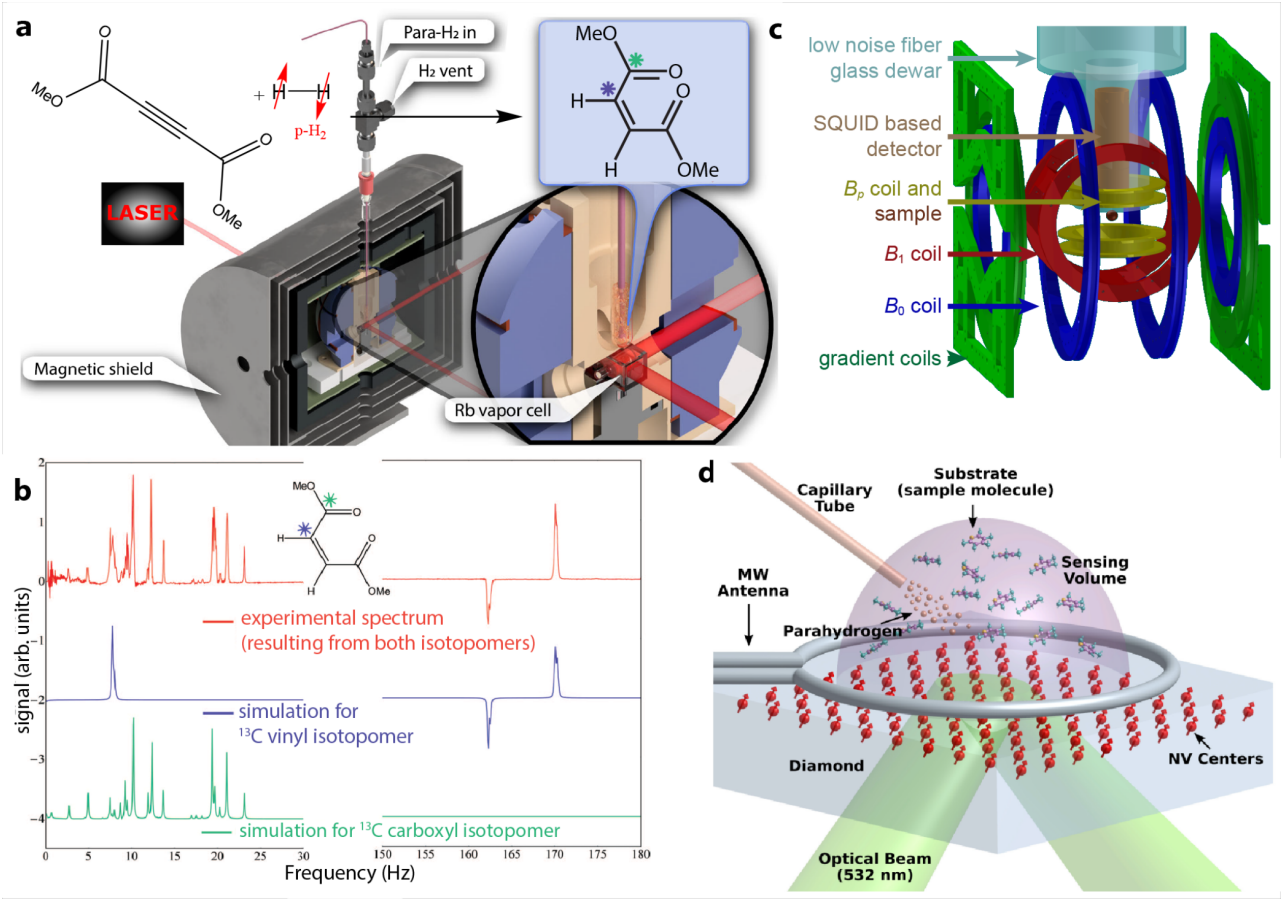

Figure 4. Setups and examples suitable for PHIP at ULF: (a) atomic magnetometer system based on a Rb vapor cell, (b) PHIP enhanced zero field NMR spectrum of dimethyl maleate acquired with a Rb vapor magnetometer, (c) SQUID based system, and (d) optically probed nitrogen-vacancy (NV)-NMR spectrometer. Part (a) is reproduced from Toward Large-Scale Steady-State Enhanced Nuclear Magnetization with in Situ Detection, Blanchard, J. W.; Ripka, B.; Suslick, B. A.; Gelevski, D.; Wu, T.; Münnemann, K.; Barskiy, D. A.; Budker, D. *Magn. Reson. Chem.*, **2021**, *59*, 1208 (ref 171). Copyright 2021 Wiley. Part (b) is reprinted from Parahydrogen-Induced Polarization at Zero Magnetic Field, Butler, M. C.; Kervern, G.; Theis, T.; Ledbetter, M. P.; Ganssle, P. J.; Blanchard, J. W.; Budker, D.; Pines, A., *J. Chem. Phys.*, **2013**, Vol. *138*, Issue 23, 234201 (ref 154), with permission of AIP Publishing. Part (c) is reprinted from Mutual Benefit Achieved by Combining Ultralow-Field Magnetic Resonance and Hyperpolarizing Techniques, Buckenmaier, K.; Rudolph, M.; Fehling, P.; Steffen, T.; Back, C.; Bernard, R.; Pohmann, R.; Bernarding, J.; Kleiner, R.; Koelle, D.; Plaumann, M.; Scheffler, K., *Rev. Sci. Instrum.*, **2018**, Vol. *89*, Issue 12, 125103 (ref 170), with permission of AIP Publishing. Part (d) is reproduced from Micron-Scale NV-NMR Spectroscopy with Signal Amplification by Reversible Exchange, Arunkumar, N.; Bucher, D. B.; Turner, M. J.; TomHon, P.; Glenn, D.; Lehmkuhl, S.; Lukin, M. D.; Park, H.; Rosen, M. S.; Theis, T.; Walsworth, R. L., *PRX Quantum*, Vol. 2, Issue 1, 010305 (ref 172). Copyright 2021 American Physical Society.

HEP, SUC, and PLAC to an effective 3-spin-1/2 system (two nascent protons and one ^{13}C nucleus), which increased the final ^{13}C polarization for PLAC to 15% versus 1% for the fully protonated variant, Figure 3h.[53,143] While deuterium (and phosphorus-31) nuclei possess a spin, they are not excited by the RF and hence not effectively involved in the SOT.[42] In favorable cases, P_{13C} of more than 20% was achieved with millitesla polarizers,[36,42,139] *e.g.*, P_{13C} = 28% for [1-^{13}C]-succinate-d_2 (SUX, Figure 3f). Despite the enormous signal enhancement provided by hyperpolarization, metabolic imaging with HP contrast agents usually results in limited-SNR images. Thus, it is not surprising that only deuterated precursors with high P_{13C} were translated to *in vivo* studies using millitesla PHIP polarizers so far.[69,83,86,89,90,144−150]

To date, millitesla-polarizers were employed for *in vivo* ^{13}C MRI or MRS with SUX,[149,151] SUX esters,[147] HEP,[5,69,152] TFPP,[145] and PLAC,[86] Figure 3g,i. Thorough reviews covering the *in vivo* applications can be found elsewhere.[114,153]

Two interesting developments, which broaden the scope of polarizable molecules drastically, are PHIP-SAH[19] and PHIP-X.[26] The experimental realizations of these techniques will be described in more detail below, but the millitesla polarizers described here appear to be well positioned for these emerging protocols.

Challenges. The millitesla PHIP polarizers have been shown to be successful devices for the efficient production of HP ^{13}C contrast agents in aqueous media with high P_{13C} exceeding 25% for *in vivo* applications. Using PHIP-SAH molecules may dramatically enlarge the pool of agents, *e.g.*, to ^{13}C-labeled pyruvate. Despite this success, however, all *in vivo* translated precursors so far require deuterated substrates in addition to ^{13}C labeling. While deuteration offers the benefit of a prolonged polarization lifetime, it also increases the cost and the complexity of synthesis of the precursors, which is a clear drawback compared to MFC-SOT. No millitesla polarizer incorporating a purification unit has been presented so far.

https://doi.org/10.1021/acs.analchem.1c04863
Anal. Chem. 2022, 94, 479−502

SOT at Ultralow Fields (ULF). *SOT Conditions.* At ultralow fields (micro- or nanotesla), the frequency differences between heteronuclei and protons (γ_{1H}-γ_X) are reduced to be on the order of the *J*-couplings or below. At such low fields, a spin bath between all spin−spin coupled nuclei is effectively established through which polarization can easily propagate spontaneously. In other words, if a part of a nuclear spin network is initialized in the singlet state via pH_2 and the Zeeman interactions are negligible compared to the *J*-couplings, then the polarization spreads through the network.[154,155] The beauty of this "spontaneous" polarization transfer approach is that it is general and does not require specialized pulse sequences that are highly dependent on the specific spin system under study. Note that this concept was realized early on, when the so-called ALTADENA approach was established,[49] where pH_2 was introduced into the spin system through hydrogenation and polarization "flows" to other ^{1}H spins at millitesla fields or below,[156] as mentioned in the section above and is as theoretically analyzed in the following section. However, to polarize a spin-1/2 heteronucleus, such as ^{13}C, ^{15}N, ^{31}P, *etc.*, ultralow microtesla fields are required to strongly couple the protons of the spin system with the target X-nucleus to allow spontaneous polarization transfer. Over the past decade, a wide variety of experiments have been demonstrated taking advantage of this heteronuclear spin bath at microtesla fields, including hydrogenative[19,126,157−162] and non-hydrogenative PHIP.[163−166] The newest approaches have used pulse sequences at microtesla fields,[127,167−169] which can focus polarization transfer in a more targeted way to specific nuclei but become highly dependent on the specific spin system under study.

Published Setups. While dedicated setups to produce diagnostically relevant contrast agent have not yet emerged, some interesting setups were described that allow exploiting the unique properties at these fields. Among these are (a) the distribution of the polarization across an entire molecule and different coherences,[107] (b) the unique sensors to detect signals in the Hz−kHz range,[170−172] and (c) the identification of molecules by their *J*-couplings rather than their chemical shift.[173−175]

To establish magnetic fields below the Earth's field, entering nanotesla to microtesla field regimes, typically mu-metal shields are used.[170,176] Inside such shielding, well-defined magnetic fields are commonly generated with conventional resistive coils in Helmholtz, solenoid, or other configurations driven by low noise current sources.

To acquire HP spectra (typically from small molecules in solution), a variety of ULF MR setups have been designed, Figure 4. The detection sensitivity for conventional RF coils, as used for high field MR experiments, decreases with frequency.[177] Therefore, at ultralow fields, different magnetic field detectors such as atomic magnetometers (Figure 4a)[154,155,171,176,178,179] or superconducting quantum interference devices (SQUIDs) (Figure 4b)[170,180] may be more sensitive than inductive detection. Such sensors are even sensitive enough to perform magnetoencephalography[181] but can also be used to detect nuclear spins. They can operate as broadband detectors (SQUIDs: DC, ≈1 GHz; atomic magnetometers: DC, ≈1 kHz), where no matching and tuning is required and the MR signal of different nuclei such as ^{13}C, ^{15}N, ^{19}F, and ^{1}H can be detected simultaneously.[107]

More recently, fluorescent nitrogen vacancy (NV) centers in diamonds (Figure 4c) have also been used to detect PHIP signal. While the NV centers typically have less absolute magnetic field sensitivity, the advantage is that they can be brought in direct contact with the solution (unlike SQUIDS or atomic magnetometers).[172,182] These can also be used for magnetometry at zero field.[183]

The linewidth of the detected MR signals for ULF setups can be less than 1 Hz down to tens of mHz,[173] so that *J*-couplings can be easily resolved. Narrow line widths are obtained since field inhomogeneities decrease with the field strength, which enables chemically specific, high resolution *J*-coupling spectroscopy.

Challenges. Generating and detecting HP signals at ULF offers unique insights into the investigated spin systems and provides NMR and MRI without requiring superconducting magnets. However, a disadvantage of all ULF detection methods remains, which is the frequency-dependent noise of the sensors (SQUIDs ≈ 1 $fT/Hz^{1/2}$, atomic magnetometers ≈10 $fT/Hz^{-1/2}$). Accordingly, there is an ongoing quest to decrease the noise level below the sample noise. Moreover, medically viable polarizers or sensors that take advantage of PHIP at ULF have not emerged yet. The aspiration remains that the described discoveries and techniques will soon be translated into broad applications.

Magnetic Field Cycling (MFC). *SOT Conditions.* MFC is another method that is widely used for the polarization transfer from the $\mathbf{I_1 \bullet I_2}$ spin order to heteronuclei. In contrast to the previous sections, which dealt with SOT at a constant magnetic field B_0, MFC exploits varying the magnetic field from values close to the geomagnetic field (30−50 μT) to nearly zero field and a few tesla. MFC-SOT was the first method to produce net ^{1}H magnetization[49] and used to produce the first ^{13}C HP contrast agents for *in vivo* MRI in 2001.[5] The method is not to be confused with the fast field cycling relaxometry where the magnetic field is varied to investigate relaxation or spin-state evolution at a low magnetic field in order to gain information about physical or chemical properties of the system under study.[184] For PHIP, a MFC process does not explicitly require *in situ* signal detection, although some setups do this.[88]

To give an idea of the effect of MFC on the spin state populations in PHIP-polarized molecules, we consider a three-spin system formed by two pH_2 protons (H and H′) and a heteronucleus (X). The spin states can be conveniently described using the singlet-triplet-Zeeman basis. The eight basis states are

$$|T_+\alpha\rangle = |\alpha\alpha\alpha\rangle,\ |T_+\beta\rangle = |\alpha\alpha\beta\rangle,$$

$$|T_0\alpha\rangle = \frac{1}{\sqrt{2}}|(\alpha\beta + \beta\alpha)\alpha\rangle,\ |T_0\beta\rangle = \frac{1}{\sqrt{2}}|(\alpha\beta + \beta\alpha)\beta\rangle,$$

$$|S_0\alpha\rangle = \frac{1}{\sqrt{2}}|(\alpha\beta - \beta\alpha)\alpha\rangle,\ |S_0\beta\rangle = \frac{1}{\sqrt{2}}|(\alpha\beta - \beta\alpha)\beta\rangle,$$

$$|T_-\alpha\rangle = |\beta\beta\alpha\rangle,\ |T_-\beta\rangle = |\beta\beta\beta\rangle$$

where the first letter refers to the proton spin state, and the second refers to the heteronuclear spin state.

Upon pH_2 addition to a precursor at geomagnetic fields, the states $|S_0\ \alpha\rangle$ and $|S_0\ \beta\rangle$ are populated almost equally. At these "higher" fields, the ^{1}H and heteronuclei are weakly coupled and no heteronuclear magnetization is obtained, because to a good approximation only the $|T_0\ \alpha\rangle - |S_0\ \alpha\rangle$ states and the $|T_0\ \beta\rangle - |S_0\ \beta\rangle$ states are mixed. However, when the magnetic field is low enough such that the difference in proton and heteronuclear

https://doi.org/10.1021/acs.analchem.1c04863
Anal. Chem. 2022, 94, 479−502

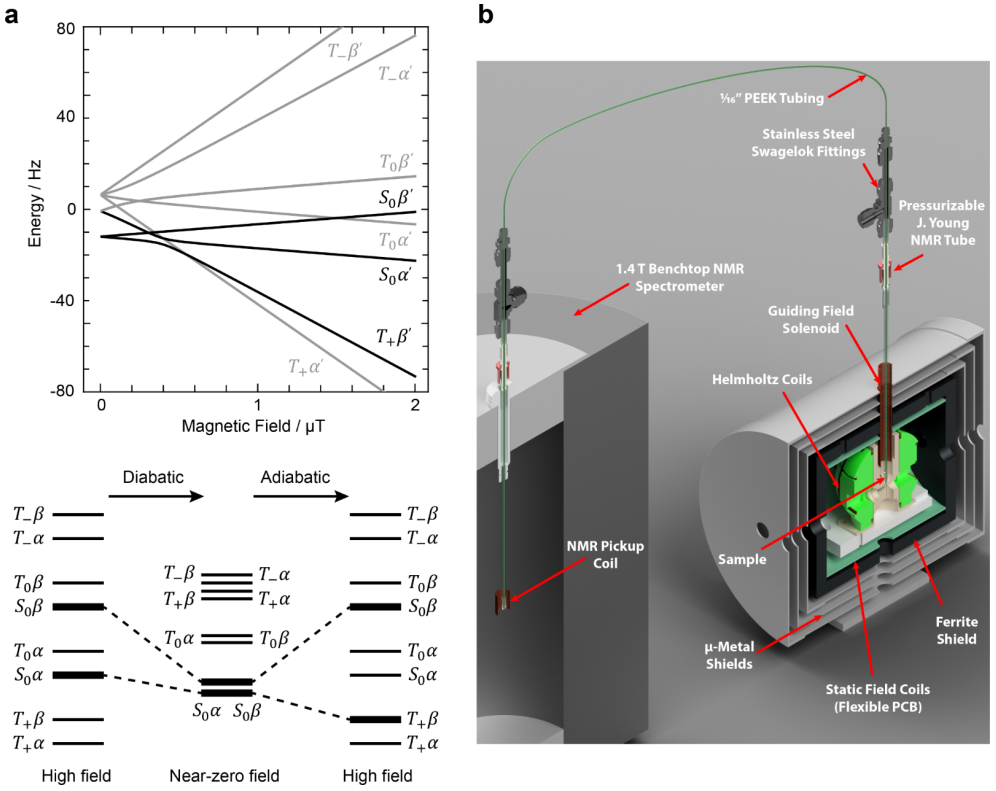

Figure 5. Diagrams and setups for PHIP by magnetic field cycling (MFC). (a) Energies of the eigenstates of [1-^{13}C]fumarate, plotted as a function of magnetic field strength, with states relevant to MFC-SOT highlighted in black (top). In an ideal MFC, the pH_2-derived singlet order $\mathbf{I}_1{\cdot}\mathbf{I}_2$ is converted into heteronuclear magnetization by the first diabatic passage to the near-zero-field, followed by adiabatic passage back to the microtesla field (bottom). The diabatic passage preserves the state of the system with the protons in a singlet state (*i.e.*, $|S_0\alpha\rangle$ and $|S_0\ \beta\rangle$), but during the subsequent adiabatic return to the high field, the state $|S_0\alpha\rangle$ evolves into $|T_+\beta\rangle$, meaning some degree of proton singlet order is lost, but heteronuclear polarization in the β state is gained. (b) Illustration of a polarizer where a sample is polarized by MFC or field sweeping and transferred to an NMR system for detection. Figure reprinted from Polarization Transfer via Field Sweeping in Parahydrogen-Enhanced Nuclear Magnetic Resonance, Eills, J.; Blanchard, J. W.; Wu, T.; Bengs, C.; Hollenbach, J.; Budker, D.; Levitt, M. H., *J. Chem. Phys.*, **2019**, Vol. *150*, Issue 17, 174202 (ref 158), with permission of AIP Publishing.

Larmor frequencies approximately matches the *J*-coupling frequencies, the states with equal angular momentum projection along the field axis (z): $|T_+\ \beta\rangle$, $|T_0\alpha\rangle$, $|S_0\alpha\rangle$, and $|T_-\alpha\rangle$, $|T_0\beta\rangle$, $|S_0\beta\rangle$ are mixed. This leads to level anticrossings (LACs) between the relevant states, and by varying the magnetic field either rapidly (diabatic passage) or slowly (adiabatic passage), it is possible to transfer spin state populations between the eigenstates.[185] The spin state energies and populations are shown in Figure 5a, and the relevant Hamiltonians are reported in ref 158.

In the most common example of MFC, the hydrogenation reaction using pH_2 is carried out in the laboratory field (usually tens of microtesla), which is high enough to prevent leakage of proton spin order onto heteronuclear spins but low enough that proton chemical shift differences, which would lead to loss of spin order, are suppressed, *i.e.*, the protons remain strongly coupled. The field is then diabatically (rapidly) reduced to near-zero field and then adiabatically (slowly) increased to the laboratory field such that the spin state populations follow the eigenstates as the field passes through the LACs. Overall, this process leads to the $\mathbf{I}_1{\bullet}\mathbf{I}_2$ order being transformed into both proton and heteronuclear magnetization. For biomedical applications, it is the heteronuclear Zeeman order that is of interest, Figure 5a.

Published Setups. The most basic MFC experiment is a hydrogenation in a few millitesla followed by transfer to a few tesla for detection.[49] To transfer polarization to X-nuclei, a mu-metal chamber can be used to reach near-zero field conditions (nanotesla). The two passages can be achieved manually, by dropping the sample after hydrogenation into the shield (diabatic passage) and lifting it out slowly (adiabatic passage).[5] In more sophisticated setups, the speed of passages is controlled by means of an electromagnet inside the mu-metal shield.[159,186] The use of coils allows more-precise control over the magnetic fields and has become a routine approach for MFC. A schematic of an experimental apparatus used for MFC is shown in Figure 5b.

The approach was first introduced experimentally by K. Golman et al. in 2001.[5,55] After pairwise addition of pH_2, the sample was (rapidly) dropped into a three-layer mu-metal shield at <100 nT and then slowly lifted at approximately 10 cm/s rate. Using this method, the authors generated 4% ^{13}C polarization on [1-^{13}C]maleic acid dimethyl ester. A more thorough theoretical explanation of the technique and description of the setup followed,[55,139] now including coils inside the magnetic shield to provide time-dependent variable fields. The magnetic field was initially held at 100 μT as the hydrogenated sample was inserted into the shield, then diabatically reduced to 30 nT in about 1 ms, and then

https://doi.org/10.1021/acs.analchem.1c04863
Anal. Chem. 2022, 94, 479−502

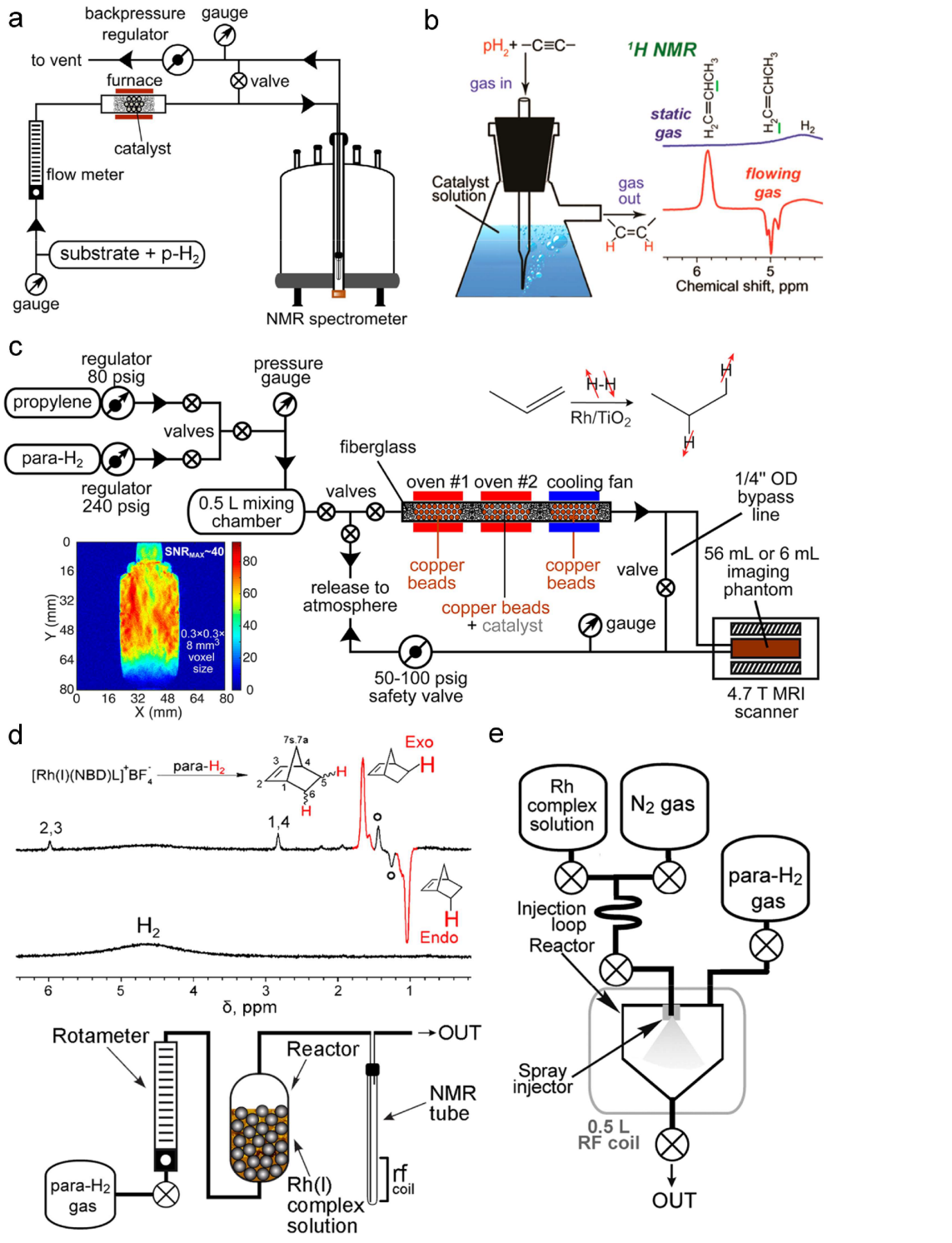

Figure 6. Setups for PHIP of gases. (a) Experimental setup employed for producing hyperpolarized gases or vapors via heterogeneous hydrogenation of unsaturated precursors premixed with pH_2. (b) Schematics of an experimental setup (left) for biphasic hydrogenation of gases upon bubbling their mixture with pH_2 through a homogeneous solution of metal complex catalyst, with the hyperpolarized product continuously escaping into the gas phase. The spectra shown as an example (right) are for biphasic hydrogenation of propyne to propylene. (c) Schematics of a more advanced experimental setup used for a rapid batch-mode production and MRI detection of hyperpolarized propane gas. The insets show the reaction scheme (top-right) and a gradient echo 2D MR image of ~200 mL of hyperpolarized propane gas in a ~56 mL container acquired at 4.7 T (bottom-left). (d) The diagram of the experimental setup used to produce hyperpolarized vapor of norbornene by bubbling pH_2 through an aqueous solution of a Rh(I) complex possessing a norbornadiene ligand (bottom), the reaction scheme (top), and the resulting gas-phase ^{1}H NMR spectra (middle). Open circles label the signals of norbornane. Plastic spheres in the reactor were used to reduce its volume. (e) The diagram of the experimental setup used for injecting Rh(I) complex solution into a 56 mL volume containing pH_2 at ≈7 bar pressure for subsequent *in situ* ^{1}H

https://doi.org/10.1021/acs.analchem.1c04863
Anal. Chem. 2022, 94, 479−502

Figure 6. continued

NMR spectroscopy of hyperpolarized norbornene at 47.5 mT. Part (a) is reproduced from Heterogeneous Parahydrogen-Induced Polarization of Diethyl Ether for Magnetic Resonance Imaging Applications, Salnikov, O. G.; Svyatova, A.; Kovtunova, L. M.; Chukanov, N. V.; Bukhtiyarov, V. I.; Kovtunov, K. V.; Chekmenev, E. Y.; Koptyug, I. V. *Angew. Chem. Int. Ed. Engl.*, Vol. *27*, Issue 4 1316−1320 (ref 198). Copyright 2021 Wiley. Part (b) is reproduced from Kovtunov, K. V.; Zhivonitko, V. V.; Skovpin, I. V.; Barskiy, D. A.; Salnikov, O. G.; Koptyug, I. V. Toward Continuous Production of Catalyst-Free Hyperpolarized Fluids Based on Biphasic and Heterogeneous Hydrogenations with Parahydrogen. *J. Phys. Chem. C* **2013**, *117* (44), 22887−22893 (ref 196). Copyright 2013 American Chemical Society. Part (c) is reproduced from Salnikov, O. G.; Nikolaou, P.; Ariyasingha, N. M.; Kovtunov, K. V.; Koptyug, I. V.; Chekmenev, E. Y. Clinical-Scale Batch-Mode Production of Hyperpolarized Propane Gas for MRI. *Anal. Chem.* **2019**, *91* (7), 4741−4746 (ref 202). Copyright 2019 American Chemical Society. Parts (d) and (e) are reproduced from Kovtunov, K. V.; Barskiy, D. A.; Shchepin, R. V.; Coffey, A. M.; Waddell, K. W.; Koptyug, I. V.; Chekmenev, E. Y. Demonstration of Heterogeneous Parahydrogen Induced Polarization Using Hyperpolarized Agent Migration from Dissolved Rh(I) Complex to Gas Phase. *Anal. Chem.* **2014**, *86* (13), 6192−6196 (ref 195). Copyright 2014 American Chemical Society. Further permissions related to the material excerpted should be directed to the ACS.

exponentially ramped back to 100 μT on the order of seconds. This approach, in combination with a spray-injection chamber for the hydrogenation with pH_2, led to ^{13}C polarization on hydroxyethyl-propionate of ≈21%. In later work, this experimental apparatus was used to produce HP ^{13}C contrast agents for coronary angiography imaging in pigs.[152]

There is merit to the approach of shuttling samples in and out of a magnetic shield by hand in the simplicity and low experimental requirements, and this approach was employed to hyperpolarize various heteronuclei such as ^{13}C,[187] ^{15}N,[188] and ^{129}Si.[189] A few years later, this approach was employed to hyperpolarize the ^{13}C spins in a number of molecules, including pyruvate and acetate, by means of PHIP-SAH.[19,56] A detailed description of a coil-based magnetic field cycling setup was provided by Shchepin et al. where they studied the dependence of ^{13}C polarization in [1-^{13}C]ethyl acetate on the minimum field used during the MFC.[186] They demonstrated that the MFC should reach fields below 1 μT for efficient ^{13}C polarization. Using this optimized coil-based approach, the ^{13}C polarization of [1-^{13}C]pyruvate generated via side arm hydrogenation was improved from 2.3%[19,56] to 8.3%,[159] and the method was also applied for hyperpolarizing [1-^{13}C]-fumarate (FUM).[24,190]

In FUM, derived from hydrogenation of ADC (acetylene dicarboxylate), an AA′X spin system is formed.[191] Because of its simplicity, the system is useful for studying and optimizing MFC methods. It was on this molecular system that an MFC variant known as magnetic field sweeping was tested.[158] In this method, rather than a diabatic field reduction followed by an adiabatic increase, the magnetic field is inverted adiabatically, *i.e.*, passing through a zero field. The field sweeping method was then applied to hyperpolarize vinyl acetate, and the effect of the magnetic field sweep step size and rate was investigated.[88] The authors found that for MFCs using a field range of a few microtesla, a sweep rate of 50 steps/μT/s was sufficient, with higher values leading to no improvement. Magnetic field sweeping does not need rapid field changes and hence seems more amenable for application to liquids under continuous flow. Its lower efficiency with respect to field cycling[158] is likely due to the deleterious effects of transverse magnetic fields when passing through the zero-field point, and hence in future work, an MFC approach was used for generating HP FUM.[24,190]

This molecular system was also used to study the benefits of constant-adiabaticity methods for MFC and field sweeping.[192] Under the constant-adiabaticity constraint, the magnetic field variations are slow at the LAC field, but the field can be varied more rapidly away from this key feature. This is particularly useful for spin systems that relax rapidly during the MFC process.

Challenges. More complicated molecular systems can present some pitfalls to the application of MFC, in particular when quadrupolar nuclei such as ^{2}H[193] or ^{14}N[188] are *J*-coupled to the pH_2-derived protons. The strong-coupling condition that is reached at nearly zero field brings these heteronuclei in contact with the spin order of pH_2 and quadrupolar relaxation can work as a hyperpolarization sink.

Another caveat to be considered is that exposure to magnetic fields magnetizes the mu-metal, and so the magnetic shielding should be periodically degaussed to ensure the near-zero field condition is met inside it. In cases where the magnetic shield is near a high-field magnet, it is common to use active shimming with coils inside the shield to achieve the near-zero field conditions.

PHIP OF GASES

While the low sensitivity of NMR often is an issue, it is particularly severe for gases as their densities at ambient pressure are ∼1000-fold lower compared to liquids. PHIP has been applied to produce HP molecules in the gas phase,[14,15,194] mostly gases but also vapors of volatile liquids and even solids. One approach is to use a solution of a metal complex in a homogeneous hydrogenation with subsequent transfer of the target species to the gas phase. For instance, aqueous stoichiometric hydrogenation of norbornadiene resulted in the release of water-insoluble hyperpolarized norbornene to the gas phase.[195] Bubbling of a mixture of pH_2 with propylene (propyne, *etc.*) through a solution of a rhodium or iridium complex was used to produce polarized gases.[196] Another approach relies on the use of solid catalysts to produce PHIP in heterogeneous hydrogenations (HET-PHIP). By bubbling pH_2 through a suitable volatile liquid, pH_2 is saturated with its vapor, and this gaseous mixture is then supplied to a cell with a solid catalyst for hydrogenation. Often, unsaturated gases premixed with pH_2 are used in HET-PHIP experiments.

Published Setups. Published examples include hydrogenation of vinyl acetate vapors over a Rh/TiO_2 catalyst with subsequent dissolution and hydrolysis of ethyl acetate to hyperpolarized ethanol and acetate,[197] and hydrogenation of vinylethyl ether to hyperpolarized diethyl ether, a known inhalable anesthetic.[198] Unsaturated gases are simply premixed with pH_2 and supplied to a catalytic reactor to yield a continuous stream of hyperpolarized gas.[14,15,194,199]

The experiments with gases can be performed under PASADENA or ALTADENA conditions. For propane ($H_3C-CH_2-CH_3$) produced upon hydrogenation of propy-

https://doi.org/10.1021/acs.analchem.1c04863
Anal. Chem. 2022, 94, 479−502

lene ($H_2C{=}CH{-}CH_3$), in PASADENA experiments, a pair of enhanced antiphase multiplets is observed with an admixture of in-phase contributions of opposite sign for the two signals. In ALTADENA experiments with hydrogenation at the Earth's field, where all ^1H spins in a product molecule are strongly coupled, transfer of the gas to the NMR probe results in the observation of polarization for all coupled ^1H nuclei. For propyne hydrogenation to propylene, it is possible to estimate the stereoselectivity of the hydrogenation by fitting the experimental spectra to ALTADENA numerical simulations, which would be otherwise impossible for this reaction.[200] The adiabatic condition of low-to-high field transfer is seldom met fully with gases as T_1 times are short, and slow transfer leads to major polarization losses. Short relaxation times in the gas phase are due to spin-rotation interaction, which also makes the T_1 of heteronuclei shorter than for protons. As a result, polarization transfer from ^1H to heteronuclei is impractical even though its feasibility has been demonstrated.[201]

PASADENA experiments with gases are particularly easy to implement; the substrate gas and pH_2 (and, if required, a diluent gas, *e.g.*, N_2) can be premixed in a gas cylinder or supplied by combining the outputs of mass flow controllers and the hydrogenation reaction performed in an NMR tube containing a solid catalyst, its suspension in a liquid, or a solution of a suitable transition metal complex. Continuous-flow ALTADENA experiments, performed using a setup such as the one illustrated in Figure 6a, provide a much broader flexibility in experimental conditions. A reactor can be as simple as a temperature-controlled section of stainless steel or copper tubing or a quartz U-tube containing solid catalyst powder, which is held in place by glass wool plugs. It is important to monitor the reactor bed temperature as hydrogenation is exothermic and run-away heating effects are possible. The gas is supplied via gas lines from a gas cylinder to the reactor and then from the reactor to the NMR tube and eventually toward the exhaust; all connections should be gastight to avoid gas leaks, and all components should withstand the required gas pressures. Commercially available flow NMR probes, popularized with the advent of liquid chromatography (LC) NMR, are well suited for acquiring the spectra on aliquots of the flowing hyperpolarized gases. However, gas flow rates through the smaller coil volumes of these probes need to be reduced accordingly to avoid residence-time line-broadening. Such effects can also be averted with an interrupted-flow system where the gas flow is allowed to bypass the probe during NMR acquisition while not perturbing the steady-state of the reactor bed. This is also a useful way to isolate a gas sample in the probe to acquire thermally equilibrated spectra. A provision for heating the reactor and catalyst pretreatment in a stream of H_2 or gas mixtures is useful. A somewhat more sophisticated setup was designed[202] for a controlled clinical-scale (>300 mL in 2 s) batch production of HP propane (Figure 6c). This systems has provisions for efficient preheating of reactants and subsequent dissipation of heat produced in the highly exothermic hydrogenation reaction as well as for operation at elevated pressures (~8 bar).

HP norbornene vapor was produced from an aqueous solution of Rh(I) complex incorporating a norbornadiene ligand by either bubbling pH_2 through it (for high-field NMR, Figure 6d) or by spraying it into a chamber pressurized with pH_2 (for NMR at 47.5 mT, Figure 6e).[195] Gas-liquid biphasic hydrogenations employed a dissolved catalyst, and gaseous reactants were bubbled through the solution, Figure 6b. The reaction product returned to the gas phase and retained a significant level of hyperpolarization, providing a complete separation of the hyperpolarized substance from the catalyst.[196]

Prepolarized propane was used in many studies to image voids in various objects[203−205] including microfluidic devices.[206,207] Imaging of HP reaction products formed in an operating model catalytic reactor facilitates mapping of their spatial distribution within the catalyst bed.[208−211]

Challenges. The main challenge with gases is the short T_1 time; for propane, it is below 1 s at 9.4 T and 1 bar but depends strongly on pressure and the gas mixture composition.[212] T_1 times tend to be longer for shorter molecular rotational correlation times, *i.e.*, for larger and/or heavier molecules, higher gas pressures, or gases in small pores. The T_1 values of small gas molecules generally increase upon dissolution in liquids. For example, $T_1 \approx 1$ ms for H_2 gas at 1 bar but it increases by ~1000-fold upon dissolution in methanol-d_4. Condensation of hyperpolarized diethyl ether vapor was also shown to prolong its hyperpolarization lifetime.[198] Furthermore, because of the strong coupling for protons at low fields, they can exhibit properties of long-lived spin states (LLSS).[213] For instance, measurements at 0.05 T for propane gas gave $T_{LLSS}/T_1 \approx 3.1$ at 3−7.6 bar, with $T_1 \approx 4$ s and $T_{LLSS} \approx 13$ s at 7.6 bar.[214] Similar trends were reported for diethyl ether vapor.[215] The spin-lock induced crossing (SLIC) pulse sequence can be conveniently used to convert LLSS to an observable signal.[214,215] Another challenge with heterogeneous hydrogenation is that it is outperformed by its homogeneous counterpart in the polarization levels achieved due to low selectivity to pairwise H_2 addition, often $P_{1H} = 1-3\%$ or even lower. Values of $P_{1H} = 7-10\%$[205,216−218] or even 60%[219] have been reported using heterogeneous catalysis but in most cases accompanied by low levels of catalytic conversion.

PURIFICATION

As soon as the development of PHIP as a hyperpolarization method for metabolic MRI began,[5,139] it became apparent that purification of the reaction solution would be necessary for preclinical and clinical *in vivo* applications. In this regard, PHIP presents some challenges. As outlined above, the hyperpolarization often requires rather nonphysiological conditions (organic solvents, pH value, temperature) and high concentrations of organometallic catalysts.[5,13,19,24,89,90,129,130,139,151] Moreover, the hydrogenation reaction may be incomplete or lead to side products.[24] Hence, purifying the polarized solution is important and, keeping in mind the short lifetime of liquid-state hyperpolarization, needs to be performed as quickly as possible, ideally within a few tens of seconds. Many purification strategies exist in chemistry already and some were adapted to PHIP as described below.

Catalyst Scavenging. One way to remove the catalyst is metal scavenging. In this approach, the scavenger is either used in a filtration column or mixed with the reaction solution and subsequently filtered out.[81,115,139,220] A commercially available metal scavenger (QuadraPure TU) was employed to clean a solution of HP fumarate prior to *in vivo* MRI.[115] Near complete removal of ruthenium was achieved by slowly passing the solution through the scavenger in about a minute, but a reduction of concentration from ~7 g/L to 100 mg/L was reached within seconds.[115] Similar scavenging approaches have

https://doi.org/10.1021/acs.analchem.1c04863
Anal. Chem. 2022, 94, 479−502

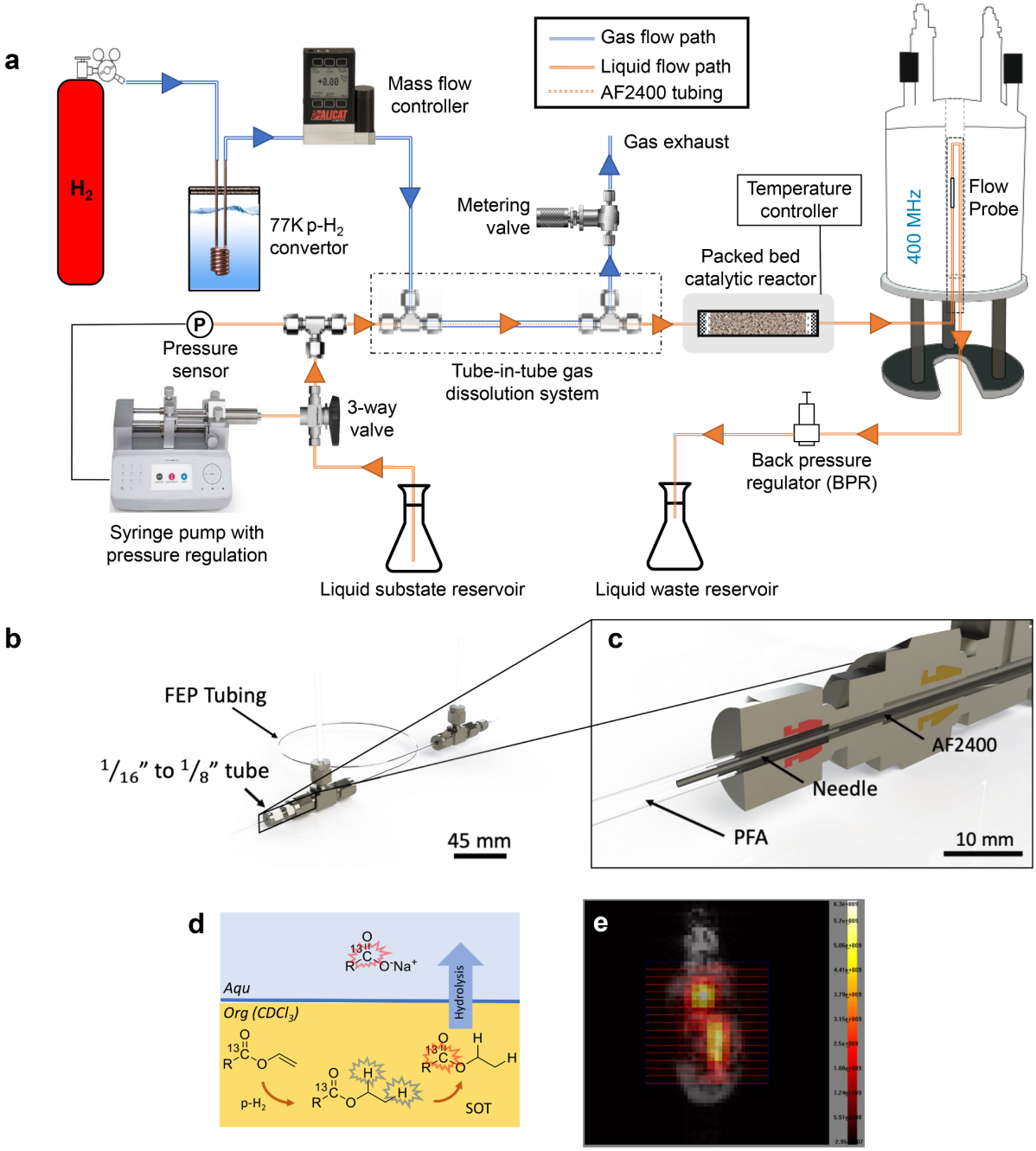

Figure 7. Upper panel: Continuous-flow liquid-state ALTADENA HET-PHIP polarizer. (a) The system incorporated a packed-bed heterogeneous reactor containing a solid Rh/TiO_2 nanorod catalyst and a tube-in-tube membrane system for bubble-free pH_2 dissolution. The liquid is drawn into the syringe from the left liquid reservoir and the 3-way valve is then changed to allow the liquid to flow through the tube-in-tube and then on to the heated catalyst cartridge. (b) Rendering of the tube-in-tube device. (c) Close up of the liquid inlet port showing the PFA (clear) tubing, 316 stainless steel needle (gray), and AF2400 membrane "inner tube" (black). Figure reproduced from Toward Continuous-Flow Hyperpolarisation of Metabolites via Heterogenous Catalysis, Side-Arm-Hydrogenation, and Membrane Dissolution of Parahydrogen, Hale, W. G.; Zhao, T. Y.; Choi, D.; Ferrer, M.-J.; Song, B.; Zhao, H.; Hagelin-Weaver, H. E.; Bowers, C. R. *ChemPhysChem*, Vol. 22, Issue 9, 822−827 (ref 17). Copyright 2021 Wiley. Lower panel: PHIP-SAH LL-separation (left) and HP *in vivo* ^{13}C-MRI (right). The scheme on the left shows the LL separation of a carboxylate sodium salt in the water phase from its ester in the organic phase. HP [1-^{13}C]pyruvate obtained using this method has been applied *in vivo* for metabolic studies (right): ^{13}C-CSI image of [1-^{13}C]pyruvate overlaid with an anatomical image (^{1}H-RARE) of a healthy mouse (image acquired at 3 T).

been introduced by Kidd et al.[220] and Barskiy et al.[81] to remove an iridium-based SABRE catalyst.

A shortcoming of metal scavenging is that although the catalyst is removed, unreacted starting materials and side products may remain. Nevertheless, it was found to be a useful step for reducing the remaining metal contamination further in already purified solutions.[81]

https://doi.org/10.1021/acs.analchem.1c04863
Anal. Chem. 2022, 94, 479−502

Liquid–Liquid Phase Separation. Liquid–liquid (LL) phase extraction was found to provide near catalyst-free aqueous solutions of PHIP contrast agents. This method relies on the following steps: (a) hydrogenation of a labile, lipophilic precursor of the target substrate in a hydrophobic organic solvent (*e.g.*, chloroform); (b) SOT; (c) hydrolysis of the hyperpolarized product by means of fast reaction with an aqueous base, for instance, carboxylate sodium salts (hydrophilic) can be obtained by hydrolysis of the corresponding esters (lipophilic); and (d) extraction of the aqueous phase that contains the hydrophilic product, Figure 7.[79] To obtain a biocompatible pH, an acidic buffer was added.[56,80,82,221] The technique was shown to work well with PHIP-SAH[19] and has provided aqueous solution of hyperpolarized sodium [1-^{13}C]-pyruvate and acetate, *e.g.*, by hydrogenating their propargylic or vinyl esters.

The LL phase extraction can be performed in any solvent-resistant container, *e.g.*, in NMR tubes or a dedicated reactor. Its efficiency depends on the level of dispersion of small droplets of the organic solution into the aqueous phase, as hydrolysis likely occurs at the LL interface. As the dispersion should happen as fast as possible, injecting heated and pressurized base solution into the organic phase was suggested (a video showing the procedure can be found in ref 222). Instead of using pure hydrophobic chloroform,[223] mixtures containing some (a few %) hydrophilic solvents (*i.e.*, ethanol, methanol) or toluene have been suggested[82,222] to further improve the LL mixing and hydrolysis as well as bubbling N_2 gas through the solution.[82] Ultimately, thanks to the instability of the LL mixture, the two phases separate within a few seconds.

Notably, this approach was used for the first *in cellulo* and *in vivo* metabolic studies with PHIP-polarized pyruvate,[80,221,223] after a first demonstration of hyperpolarized [1-^{13}C]succinate (from maleic anhydride).[79] Losses of polarization during hydrolysis and phase transfer of the ester derivatives have been observed and could not be explained by T_1 relaxation alone.[159] Instead, the effect has been attributed to the presence of paramagnetic impurities derived from catalyst degradation in the organic phase, and a beneficial effect on hyperpolarization has been obtained through the addition of a radical scavenger (sodium ascorbate) to the aqueous base. The concentration of the metal (rhodium) in the aqueous phase has been determined to be 30 μM.[224]

Solvents such as methanol, ethanol, and acetone mix well with water and are transferred to the aqueous phase during phase extraction. Therefore, their application in the hyperpolarization of substrates for biological use (in cells and *in vivo*) must be considered carefully, due to their toxicity, especially for methanol. Nevertheless, it must be mentioned that, even when pure hydrophobic solvents (chloroform and toluene) were used, their dissolution and ultimately the concentration in the aqueous phase is non-negligible and a cytotoxicity effect has been observed.[221] In order to solve this issue, filtration of the aqueous solution through a lipophilic resin (Tenax TA, Porous Polymer Adsorbent, 60–80 mesh, Supelco) was recently shown to lead to a reduction of the concentration of these solvents well below the concentration recommended by the Environmental Protection Agency (EPA).[69,222]

Heterogeneous Catalysts. In contrast to homogeneous catalysis, heterogeneous catalysis affords straightforward separation of the solution-state hyperpolarized hydrogenation products from the solid catalyst due to the insolubility of the latter. Moreover, heterogeneous catalysis is inherently compatible with continuous-flow production of HP gases and liquids. These advantages were already recognized in the initial demonstration of HET-PHIP[73] and continue to drive the development of HET-PHIP catalysts and reactor systems.

In ref 73, silica and a polymer were functionalized with phosphine groups to tether the Rh complex (*e.g.*, Wilkinson's catalyst). The linkage proved to be resilient, but the catalysts still suffered from low stability, with possible leaching into solution upon oxidation of the phosphine moieties, reduction during the reaction, and metal complex dimerization.[194] A recent article described an alternative linkage scheme, where a silica-supported polymer incorporating pyridyl groups was used to tether Wilkinson's catalyst.[225] This catalyst showed better stability and resistance to leaching. Modest signal enhancements of up to 200 were reported for the hydrogenation of styrene in acetone-d_6.

In the quest to realize efficient, stable, and robust HET-PHIP catalysts, metal-oxide-supported nanoparticle catalysts consisting of Pt, Pd, Rh, Ru, Ir as well as bimetallic compositions (*e.g.*, Pd–In)[226] and intermetallic nanoparticles (*e.g.*, PtSn, Pt_3Sn)[216] with varying shapes, sizes, and support materials have been explored.[194] Most of the published solution-state HET-PHIP studies were performed using a batch reactor configuration,[216,226–229] where hydrogen is bubbled through a heated NMR tube containing the insoluble solid catalyst and the unsaturated substrate in solution. For larger catalyst particles (millimeter size), settling out of the catalyst after cessation of bubbling can occur within seconds. Under the relatively mild conditions of solution-state hydrogenation, supported metal nanoparticles were found to resist leaching. For example, after hydrogenation of 2-hydroxyethyl acrylate over 25 mg of Pt_3Sn intermetallic nanoparticles in 2 mL of D_2O at 120 °C and 5.7 bar, Pt and Sn levels in the decanted solution were found to be well below 100 ppb (by mass).[216] Transfer of hyperpolarization to heteronuclei in aqueous media for biologically relevant compounds has been addressed as well.[230]

As noted above, MRI of HP ^{13}C pyruvate provides a means for detection of abnormal metabolism in malignant tumors and other pathologies. There is evidence, however, that administration of a continuous stream of the HP pyruvate over longer periods is preferable to a single large bolus for some applications.[231] Production of purified continuous-flow streams of HP pyruvate by either dissolution DNP or PHIP is challenging and has not yet been demonstrated.

Hale et al. recently presented a novel apparatus that allowed continuous production of hyperpolarized allyl acetate by hydrogenation of propargyl acetate with pH_2, Figure 7. The apparatus incorporated a packed-bed catalytic reactor, side arm hydrogenation, and pH_2 membrane dissolution.[17] The polarizer continuously achieved a conversion of 30% and ^{1}H signal enhancements up to 300 (relative to thermal equilibrium at 9.4 T) were shown to be feasible. However, the polarization transfer to ^{13}C, side arm cleavage, and transfer to the aqueous phase have yet to be demonstrated.

Challenges for heterogeneous catalysis include lower product concentrations and lower polarizations compared to homogeneous approaches. To solve these shortcomings, emphasis is made on improved flow reactor design as well as the rational design of catalysts to obtain higher pairwise selectivity without sacrificing yield.

https://doi.org/10.1021/acs.analchem.1c04863
Anal. Chem. 2022, 94, 479–502

Precipitation. Very recently, a scheme to purify HP molecules based on precipitation was introduced.[24,232] HP fumarate was generated in an aqueous solution using a trans-selective hydrogenation catalyst. After hydrogenation and polarization transfer, the reaction solution contained the ruthenium-based catalyst, unreacted starting material, and side products in addition to the desired HP fumarate salt. To purify the solution, acid and nonpolarized fumarate were added to the solution so that fumaric acid precipitated out of the solution almost immediately.

Because fumarate precipitated very efficiently and the catalyst, starting material, and side products remained mostly dissolved, separation was easily achieved by decanting the solution. Subsequently, the solid, HP fumaric acid was redissolved in aqueous solution. It was important to keep the solid fumarate (from precipitation to redissolution) at a sufficiently high magnetic field to avoid fast relaxation in the solid state. The remaining metal concentration was found to be 16 μM after a washing procedure.[24] While this method worked well for fumarate, the generality of this approach remains an open question, and further research toward this promising approach is certainly warranted.

OTHER PROMISING DEVELOPMENTS

PHIP-on-a-Chip. An emerging research area that is mainly pursued at high magnetic fields is the integration of PHIP into lab-on-a-chip devices.[17,233−236] The advantage offered by working at a microfluidic scale (*i.e.*, with sample volumes on the order of microliters) is in the much higher degree of experimental control that can be leveraged, in terms of sample contact time with pH_2, molecular diffusion, temperature, and pressure. The other important benefit of microfluidic implementation of PHIP experiments is the short transport paths (and hence time) between the point of the PHIP process occurring and signal detection. This is particularly important when nuclear spin relaxation times are short.

Radio Amplification by Stimulated Emission of Radiation (RASER). RASER using PHIP was recently discovered[20,237] in PASADENA and ALTADENA conditions.[21,238] RASER emission was detected at low (millitesla)[237] and high fields (tesla) and reproduced by simulations.[21,23] Although the RASER effect was first observed using other HP techniques,[239−241] PHIP has the advantage that the polarization can be continuously refreshed by a constant supply of pH_2 as long as substrate is not depleted. While a biomedical application of RASER was not described, newly emerged applications included observation of NMR spectra with very narrow signals,[21,237] background-free proton NMR spectroscopy,[238] and polarization transfer to other molecules via intermolecular dipole−dipole interaction.[22]

PHIP-X. PHIP relayed via proton exchange (PHIP-X)[26] enables polarization of molecules that participate in proton exchange like glucose.[25,242−244] First, pH_2 is added to an intermediary molecule by homogeneous catalysis, where the polarization is then transferred to an exchanging proton. Second, the polarization is incorporated by the target molecule by exchange of a polarized proton from the reacted intermediary molecule. Experimentally, this process was implemented by placing a high-pressure reaction chamber in millitesla fields. Upon hydrogenation, the sample was transferred to high-field NMR for detection. If necessary, the target molecule can be added after the hydrogenation to avoid interference with the hydrogenation step. Both millitesla and MFC setups appear to be well suited to host this process, which involves SOT in the intermediary and target molecule, for which the spin physics has yet to be fully elucidated.

TOWARD CLINICAL APPLICATION

The results described above impressively demonstrate the power, versatility, and maturity of pH_2-based hyperpolarization approaches and instrumentation. Indeed, HP [1-^{13}C]pyruvate produced by hydrogenative PHIP has been recently employed to detect the response of the heart to altered metabolism in real time (Figure 8).[80]

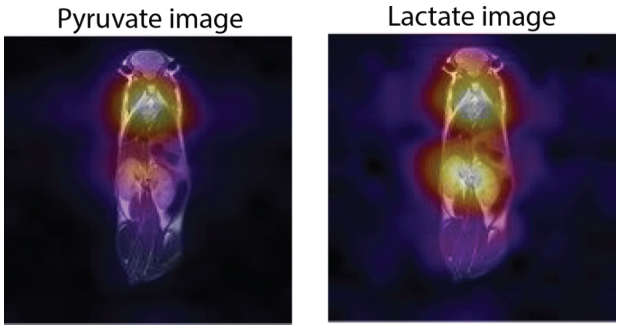

Figure 8. ^{13}C-chemical shift imaging reporting of pyruvate and lactate distribution acquired on living mice, obtained upon the injection of a dose of [1-^{13}C] pyruvate hyperpolarized using pH_2. The spatial localization of each metabolite is shown upon overlapping the ^{13}C-CSI results to the anatomical proton image (T_2 weighted fast spin echo image). Each metabolite map is scaled individually and is displayed on a fire color scale so that the region of highest metabolite signal appears white and the lowest appears black. Reprinted by permission from Nature: Sci. Rep., The 13C hyperpolarized pyruvate generated by ParaHydrogen detects the response of the heart to altered metabolism in real time, Cavallari, E.; Carrera, C.; Sorge, M.; Bonne, G.; Muchir, A.; Aime, S.; Reineri, F., *Sci. Rep.*, Vol. 8, Issue 1, 8366 (ref 80). Copyright Nature 2018.

While preclinical imaging with PHIP agents was demonstrated in more than 15 papers since 2001, this method has not been translated to human imaging yet.[5,36,69,80,86,87,90,91,115,144−148,152]

Still, we may have reached a tipping point, as all ingredients for producing clean, aqueous solutions of interesting (not only biocompatible) agents were described in the literature. As we speak, work continues at multiple locations to make studies with PHIP-polarized agents a reality.

Let us assume that all relevant technical hurdles were addressed and that there was a device that produces a clean and pure solution or solid of highly polarized contrast agent with a fast and relevant function *in vivo*. Still, there will be regulatory aspects to meet before human studies may commence. Here, much can be learned from the path taken so impressively by the DNP community.

Contrast agents are considered drugs by most regulatory bodies. As no injectable HP contrast agents are approved as drugs (yet), the guidelines for the application and evaluation of nonapproved drugs apply. On the other hand, propane (also known as E944) is approved for unlimited use in foods and is already regulated by FDA. The above regulatory requirements may vary between countries but are likely to include:

1. GMP manufacturing of ingredients by vendor or in-house: pH_2, catalyst, solvents, precursors;

https://doi.org/10.1021/acs.analchem.1c04863
Anal. Chem. 2022, 94, 479−502

2. ISO 5 clean bench (or higher depending on regulations) preparation of ingredients on site: mixing precursor solution, pH_2;
3. Polarization and rapid QC: measure sample concentration, temperature, pH, and polarization; residual catalyst concentration; perform sterile filter integrity test.

These steps would be followed by transfer, administration by an MD or qualified person, and imaging. However, prior to injection, the hyperpolarized CA should be passed through a 0.2 μm pore size filter (the integrity of the filter would need to be tested in accordance with manufacturer regulations to ensure sterility). Given the limited lifetime of hyperpolarization, the QC needs to be rapid (<30 s) and is recommended to be performed in parallel with the sample transfer and filter integrity test to minimize the time to injection. The transfer distance will be determined by the lifetime, and long-lived samples may be transported between sites. Attempts for individual treatment of patients on a small scale may require less stringent regulations. Safety and dose escalation trials would be followed by efficacy tests.

CONCLUSIONS

pH_2-based hyperpolarization has come a long way since its inception in the 1980s, and the first demonstration of hyperpolarized *in vivo* ^{13}C-MRI in 2001. For hyperpolarizing small molecules in solution for *in vivo* MRI application, dDNP is currently the state-of-the-art methodology, but PHIP is beginning to emerge as a viable alternative. Arguably, there is no hyperpolarization technique that is more flexible and that offers more variants than PHIP. Consequently, many applications have emerged, ranging from basic physics to chemistry and biomedicine. The latter, however, has not advanced as fast as, *e.g.*, with dDNP.

The main advantages of PHIP lie in the inherent low cost, ease of implementation, rate of hyperpolarized sample turnover, and scalability. These advantages stem mainly from the chemical nature of the technique; hyperpolarization is delivered via chemical reactions rather than requiring cryogenic cooling of the to-be-polarized substance and/or irradiation with high power microwaves, as is the case for dDNP. The chemical basis of the process unfortunately carries some drawbacks: (1) the method is limited to polarizing molecules that can be generated through hydrogenation reactions; (2) the HP solutions are contaminated with other chemicals from the reaction; and (3) polarization levels are often only modest since the nuclear spins relax during the hyperpolarization process.

All three drawbacks are being overcome through state-of-the-art research, much of which is covered in this review: Many biologically and diagnostically promising agents are available by direct hydrogenation (SUX, FUM, TFPP, PLAC) and variants such as PHIP-SAH and PHIP-X (pyruvate, acetate, glucose, lactate). Physicochemical methods for purifying the HP solutions through phase separation have been shown for a few PHIP-polarized metabolites, and scavenging can be used to remove the catalyst from solutions. Advances in instrumentation for hydrogenation, polarization transfer, and sample transport, have helped to improve the resulting polarization levels in PHIP-polarized molecules. PHIP seems to be a promising hyperpolarization method for preclinical MRI and *in vitro* studies where experiment turnover is high but requirements for high polarization and solution sterility/nontoxicity are lower.

Nonetheless, it remains to be seen whether PHIP has a future role to play in clinical imaging. To date, no device is commercially available, not even for *in vitro* and preclinical *in vivo* studies. Over the years, some initiatives were and still are active (Amersham, Stelar, Spindynamics, Bruker, XEUS Technologies LTD, NVision), and numerous patents were filed. The technical challenges toward clinical applications are accompanied by regulatory aspects, which must be met for use in humans. Here, the contrast agents do not only need to be pure and highly polarized but also produced effectively and compliant to GMP. The reactive nature of PHIP may pose a challenge, too. Ideally, agents must have a long-enough lifetime for testing and transport after polarization.

Although the focus of this review has largely been on producing PHIP-polarized biomolecules for *in vivo* applications, there are many more uses of PHIP. Examples include studying chemical reaction mechanisms and as a source of signal enhancement for high-resolution NMR. Advances in instrumentation have underpinned much of the method development made in recent years and will continue to pave the way into the future. Even if PHIP (or hyperpolarization in general) would eventually turn out to be ineligible for clinics, many more applications are lurking behind the corner; the marriage of pH_2 and MR are far from over yet, and the best is yet to come.

AUTHOR INFORMATION

Corresponding Authors

Andreas B. Schmidt − *Department of Radiology−Medical Physics, Medical Center, Faculty of Medicine, University of Freiburg, Freiburg 79106, Germany; German Cancer Consortium (DKTK), partner site Freiburg and German Cancer Research Center (DKFZ), Heidelberg 69120, Germany;* orcid.org/0000-0001-8944-7463; Email: andreas.schmidt@uniklinik-freiburg.de

Jan-Bernd Hövener − *Section Biomedical Imaging, Molecular Imaging North Competence Center (MOIN CC), Department of Radiology and Neuroradiology, University Medical Center Kiel, Kiel University, 24118 Kiel, Germany;* orcid.org/0000-0001-7255-7252; Email: jan.hoevener@rad.uni-kiel.de

Authors

C. Russell Bowers − *Department of Chemistry, University of Florida, Gainesville, Florida 32611, United States; National High Magnetic Field Laboratory, Tallahassee, Florida 32310, United States*

Kai Buckenmaier − *High-Field Magnetic Resonance Center, Max Planck Institute for Biological Cybernetics, 72076 Tübingen, Germany*

Eduard Y. Chekmenev − *Intergrative Biosciences (Ibio), Department of Chemistry, Karmanos Cancer Institute (KCI), Wayne State University, Detroit, Michigan 48202, United States; Russian Academy of Sciences (RAS), 119991 Moscow, Russia;* orcid.org/0000-0002-8745-8801

Henri de Maissin − *Department of Radiology−Medical Physics, Medical Center, Faculty of Medicine, University of Freiburg, Freiburg 79106, Germany; German Cancer Consortium (DKTK), partner site Freiburg and German Cancer Research Center (DKFZ), Heidelberg 69120, Germany*

James Eills − *Institute for Physics, Johannes Gutenberg University, D-55090 Mainz, Germany; GSI*

https://doi.org/10.1021/acs.analchem.1c04863
Anal. Chem. 2022, 94, 479−502

Helmholtzzentrum für Schwerionenforschung GmbH, Helmholtz-Institut Mainz, 55128 Mainz, Germany; orcid.org/0000-0001-8468-6860

Frowin Ellermann − *Section Biomedical Imaging, Molecular Imaging North Competence Center (MOIN CC), Department of Radiology and Neuroradiology, University Medical Center Kiel, Kiel University, 24118 Kiel, Germany;* orcid.org/0000-0001-6446-6641

Stefan Glöggler − *NMR Signal Enhancement Group Max Planck Institutefor Biophysical Chemistry Am Fassberg 11, 37077 Göttingen, Germany; Center for Biostructural Imaging of Neurodegeneration of UMG, 37075 Göttingen, Germany*

Jeremy W. Gordon − *Department of Radiology & Biomedical Imaging, University of California San Francisco, San Francisco, California 94158, United States*

Stephan Knecht − *NVision Imaging Technologies GmbH, 89081 Ulm, Germany*

Igor V. Koptyug − *International Tomography Center, Siberian Branch of the Russian Academy of Sciences (SB RAS), Novosibirsk 630090, Russia;* orcid.org/0000-0003-3480-7649

Jule Kuhn − *Section Biomedical Imaging, Molecular Imaging North Competence Center (MOIN CC), Department of Radiology and Neuroradiology, University Medical Center Kiel, Kiel University, 24118 Kiel, Germany*

Andrey N. Pravdivtsev − *Section Biomedical Imaging, Molecular Imaging North Competence Center (MOIN CC), Department of Radiology and Neuroradiology, University Medical Center Kiel, Kiel University, 24118 Kiel, Germany*

Francesca Reineri − *Department of Molecular Biotechnology and Health Sciences, University of Torino, 10124 Torino, Italy*

Thomas Theis − *Departments of Chemistry, Physics, and Biomedical Engineering, North Carolina State University, Raleigh, North Carolina 27695, United States;* orcid.org/0000-0001-6779-9978

Kolja Them − *Section Biomedical Imaging, Molecular Imaging North Competence Center (MOIN CC), Department of Radiology and Neuroradiology, University Medical Center Kiel, Kiel University, 24118 Kiel, Germany;* orcid.org/0000-0002-5512-0910

Complete contact information is available at: https://pubs.acs.org/10.1021/acs.analchem.1c04863

Author Contributions

The manuscript was written through contributions of all authors. All authors have given approval to the final version of the manuscript.

Notes

The authors declare the following competing financial interest(s): E.Y.C. has a stake of ownership in XeUS Technologies LTD. S.K. is employed at NVision Imaging GMBH Ulm, Germany. T.T. holds stock in Vizma Life Sciences LLC (VLS) and is President of VLS. The terms of this arrangement have been reviewed and approved by NC State University in accordance with its policy on objectivity in research. XeUS Technologies LTD, NVision Imaging GMBH, and VLS are developing products related to the research being reported. All other authors declare no competing interests.

Biographies

Andreas B. Schmidt studied physics at the University of Freiburg (Germany) and Complutense Madrid (Spain) and received his Diploma and Ph.D. from University of Freiburg in 2015 and 2020, respectively. He became a Postdoctoral Researcher at the University Medical Center Freiburg (Germany) where he took over the lead of the hyperpolarization group shortly after. Since 2021, Andreas is also affiliated with the German Cancer Consortium (DKTK) and German Cancer Research Center (DKFZ, Heidelberg, Germany) as principal investigator. His research activities focus on PHIP and nuclear spin singlet states for biomedical applications.

C. Russell Bowers received his B.A. degree in 1985 from Bowdoin College, Brunswick, ME, and a Ph.D. in Chemical Physics in 1990 with Daniel P. Weitekamp at the California Institute of Technology, Pasadena, CA. As a NATO-NSF Postdoctoral Fellow, Bowers spent a year in the lab of Michael Mehring at the 2nd Physics Institute, University of Stuttgart (Germany). From 1992 to 1993, he was a Postdoc with Alexander Pines at the University of California, Berkeley, and Lawrence Berkeley Laboratory. Bowers joined the faculty at the University of Florida, Gainesville, FL, in January 1994 where he is currently a Full Professor of Chemistry and an affiliate of the National High Magnetic Field Laboratory. Bowers has contributed to the development of multiple NMR hyperpolarization techniques with a recent focus on parahydrogen enhanced NMR by heterogeneous catalysis.

Kai Buckenmaier studied physics at the University of Tübingen (Germany), where he received his diploma and Ph.D. degrees in 2006 and 2010, respectively. He worked for 1 year as a Postdoctoral Researcher in the Department of Experimental Physics at the University of Tübingen (Germany) and for 2 years in the Physics Department at the University of California in Berkeley, CA. Since 2013, he has been a Researcher at the Magnetic Resonance Center of the Max Planck Institute for Biological Cybernetics, Germany. His current research activities include the development and implementation of different hyperpolarization methods for ultralow-field magnetic resonance imaging.

Eduard Y. Chekmenev earned his Ph.D. in Physical Chemistry in 2003 (supervisor Prof. Richard J. Wittebort), University of Louisville, KY. He studied as a Postdoctoral Fellow at the NHMFL in Tallahassee, FL (supervisor Prof. Timothy Cross), at Caltech (supervisor Prof. Daniel P. Weitekamp), and at HMRI (supervisor Dr. Brian D. Ross). In 2009, Dr. Chekmenev started his hyperpolarization program at Vanderbilt University Medical Center, where he was tenured in 2015. In 2018, Eduard moved to the Department of Chemistry and Karmanos Cancer Institute (KCI) at Wayne State University in Detroit, MI, to continue his research on MR hyperpolarization. His research interests include development of methods of hyperpolarization using parahydrogen induced polarization and spin exchange optical pumping and biomedical imaging and industrial use of NMR hyperpolarization techniques.

Henri de Maissin graduated from the Institut d'Optique Graduate School in Paris (France) in 2016, then studied biomedical technologies at the University of Tübingen (Germany) where he obtained his Master's Degree in 2021. For his Master's thesis, he worked at the University Medical Center Freiburg (Germany) on the topic "Effective spin order transfer at high field in an MRI system". He is now pursuing his Ph.D. in the same group in Freiburg. His research projects include *in situ* PHIP in MRI systems (SAMBADENA) and sequence development for ^{13}C imaging of hyperpolarized agents.

James Eills studied Chemistry at the University of Southampton (U.K.) from 2011 to 2015, doing his Master's research in that time at UC Berkeley, CA. During his Ph.D., he worked on hyperpolarization techniques for NMR and microfluidic engineering, earning his Ph.D. from the University of Southampton in 2019. He then moved to

https://doi.org/10.1021/acs.analchem.1c04863
Anal. Chem. 2022, 94, 479−502

Johannes Gutenberg University Mainz to work at the Helmholtz Institute as a Postdoctoral Research Fellow to develop zero- to ultralow-field NMR techniques, a unique type of NMR experiment performed in the absence of a magnetic field.

Frowin Ellermann studied Materials Science and Engineering at the University of Kiel (Germany), where he received his Bachelor's Degree in 2015 and his Master's Degree in 2018, respectively. After graduation, he worked as a Fellow in the Collaborative Research Center 1261 "Magnetoelectric Sensors" (German Research Foundation). Since 2019, he has been a Doctoral Candidate in hyperpolarization at the Section Biomedical Imaging at the University Medical Center Schleswig-Holstein, Kiel (Germany). As a part of the Research Training Group 2154 "Materials for Brain" (German Research Foundation), his current research activities include the development of contrast agents for metabolic MRI with a focus on instrumentation for parahydrogen-based hyperpolarization.

Stefan Glöggler obtained his Ph.D. from RWTH Aachen University (Germany) in 2013. He pursed Postdoctoral studies at UCLA in Los Angeles, CA, Université Bordeaux (France), and the University of Southampton (U.K.). In 2017, he started as an independent group leader at the Max-Planck Institute for Biophysical Chemistry in Göttingen (Germany) and is currently head of the Magnetic Resonance Signal Enhancement Lab. His research interests include the advancement of methods based on spin phenomena to answer biochemical and biological questions.

Jeremy W. Gordon earned his B.S. from the University of Georgia in Physics & Astronomy and received his Ph.D. from the University of Wisconsin-Madison in Medical Physics. He is currently an Assistant Professor in the Department of Radiology & Biomedical Imaging at UC San Francisco. His research focuses on the development of novel acquisition and reconstruction methods for quantitative imaging of cellular metabolism and the clinical translation of hyperpolarized ^{13}C MRI to provide unique metabolic characterization of organ function, disease staging, and response to therapy.

Stephan Knecht started his studies of Physics at the University of Tuebingen in 2006 and continued them at the University of Freiburg in 2008 (both Germany), where he received his Diploma and Ph.D. in Physics in 2014 and 2019, respectively. From 2018 to 2020, he joined the Physical Chemistry Department of the Technical University Darmstadt (Germany) as a Research Fellow. Since 2020, he has been the Associate Director of MR development at NVision Imaging Technologies GmbH Ulm, Germany.

Igor V. Koptyug studied Physics at the Novosibirsk State University, where he received his Diploma in Chemical Physics in 1985. He then became a Junior Researcher at the Institute of Chemical Kinetics and Combustion and received his Ph.D. Degree in 1991 there. In 1992–1995, he worked as a Postdoctoral Researcher in the Photochemistry Group of Prof. N. J. Turro (Columbia University, New York). Since 1995, he's been working at the International Tomography Center, Siberian Branch of the Russian Academy of Sciences in various capacities, where he currently holds positions of Head of Research, Chief Research Scientist, and a Research Group Leader, along with a part-time position at the Boreskov Institute of Catalysis, SB RAS. He earned his Dr. Sci. (Habilitation) Degree in Catalysis in 2003 and the title of Professor in 2006. His research interests include signal enhancement in NMR and applications of NMR and MRI in catalysis research.

Jule Kuhn received her Bachelor's Degree in Physics from the Institute of Physics at Kiel University (Germany) in 2019. She is currently a Master's student in the Section Biomedical Imaging at the University Medical Center Schleswig-Holstein, Germany. Her research is focused on PHIP of biological molecules as well as the development of experimental setups specialized for PHIP and PHIP-X.

Andrey N. Pravdivtsev received his Ph.D. in Chemical Physics at Novosibirsk State University and the International Tomography Center SB RAS (in the groups of Prof. K. L. Ivanov and Prof. A. V. Yurkovskaya) in 2017. From 2017 to 2019, he was a DAAD Fellow and later a Postdoctoral Researcher in the MRI and Hyperpolarization Group of Prof. J.-B. Hövener (Kiel University). Currently, he is a BMBF Juniorverbünde Fellow at Kiel University, where his research focuses on the development of PHIP and SABRE applications for *in vivo* MRI.

Francesca Reineri received her Master's and Ph.D. in Chemistry from University of Torino (Italy) in 1999 and 2002, respectively. Since 2008, she has been an Assistant Professor at the University of Torino, Department Molecular Biotechnology and Health Sciences, where she leads the Hyperpolarization Group at the Molecular Imaging Center. Her research focuses on the development of new hyperpolarized probes for imaging studies of cancer disease, development of cost-effective parahydrogen-based polarization methods, and diagnostic applications thereof.

Thomas Theis completed his undergraduate and Master's at the Georg-August University of Goettingen (Germany). He received his Ph.D. in 2012 from UC Berkeley, CA, working with Prof. Alexander Pines on "zero-field NMR" and "parahydrogen hyperpolarization schemes" for portable NMR. He conducted postdoctoral research at Duke University with Prof. Warren Warren that focused on "singlet states for hyperpolarization storage" and worked on "low-field NMR" as a Visiting Professor at RWTH Aachen University with Prof. Stephan Appelt (Germany). In 2015, he was promoted to Research Assistant Professor at Duke University developing "cost-efficient hyperpolarization techniques for molecular imaging". Since 2018, he leads the North Carolina State Hyperpolarization Laboratory. His research is focused on hyperpolarization technology and unconventional NMR and MRI detection schemes.

Kolja Them has studied Physics at the University of Hamburg, where he earned his diploma on Quantum Field Theory in Curved Space-Time. His Ph.D. was on the "C*-algebraic reformulation of Quantum Statistical Mechanics for the description of experimentally investigated spin systems". He was a Postdoc at the University-Medical Center Hamburg Eppendorf and worked on magnetic particle imaging. Now he is a Postdoc at the UKSH working on hyperpolarized MRI. He has more than 10 years of research experience in the field of spin systems.

Jan-Bernd Hövener studied Physics in Münster, Heidelberg, and Nice (France). After working in New York and in Pasadena, CA, he graduated in Physics at the University of Heidelberg in the group of Prof. P. Bachert. In 2009, he joined Prof. J. K. Hennig in Freiburg and was accepted to the Academy of Excellence in 2010 and the Emmy Noether Program of the DFG in 2014. In 2016, he received the Venia Legendi and Habilitation. In 2017, he became Professor for Translational MRI at Kiel University, where he heads the Section for Biomedical Imaging and the Molecular Imaging Competence Center North (MOIN CC). His research interests include novel imaging methods, focusing on conventional and hyperpolarized magnetic resonance imaging and spectroscopy.

■ ACKNOWLEDGMENTS

We acknowledge funding from German Federal Ministry of Education and Research (BMBF) within the framework of the e:Med Research and Funding Concept (Grant 01ZX1915C),

https://doi.org/10.1021/acs.analchem.1c04863
Anal. Chem. 2022, 94, 479−502

German Cancer Consortium (DKTK), DFG (Grants SCHM 3694/1-1, HO-4602/2-2, HO-4602/3, GRK2154-2019, EXC2167, FOR5042, SFB1479, and TRR287), Kiel University and the Faculty of Medicine, and Research Commission of the University Medical Center Freiburg (Grant SCHM2146-20), and support from the Core Facility Advanced Molecular Imaging Center (AMIR), Department of Radiology − Medical Physics of the University Hospital Freiburg. MOIN CC was founded by a grant from the European Regional Development Fund (ERDF) and the Zukunftsprogramm Wirtschaft of Schleswig-Holstein (Project No. 122-09-053), National Science Foundation (NSF) Grants CHE-2108306 and CBET-1933723, and the National High Magnetic Field Laboratory, which is supported by the NSF Cooperative Agreement No. DMR-1644779* and the State of Florida. This project has received funding from the European Union's Horizon 2020 Research and Innovation Programme under the Marie Skłodowska-Curie Grant Agreement No. 766402. T.T. acknowledges support from the National Institute of Biomedical Imaging and Bioengineering of the National Institutes of Health under Award Number NIH R01EB029829. E.Y.C thanks NSF CHE-1904780, DOD CDMRP W81XWH-20-10576, NIH NHLBI R21 HL154032. The content is solely the responsibility of the authors and does not necessarily represent the official views of the National Institutes of Health. I.V.K. acknowledges the Russian Ministry of Science and Higher Education (grant no. 075-15-2020-779) for financial support. The University of Torino was funded by the EU H2020 FETOPEN under the Grant Agreement No. 858149 (Alternatives to Gd). J.W.G. acknowledges support from the National Institutes of Health (Grant P41EB013598). We thank Dr. Mariya Pravdivtseva (UKSH, Kiel, Germany) for creating the TOC figure.

REFERENCES

(1) Born, M.; Heisenberg, W. *Ann. Phys.* **1924**, *379* (9), 1−31.
(2) Bowers, C. R.; Weitekamp, D. P. *Phys. Rev. Lett.* **1986**, *57* (21), 2645−2648.
(3) Bowers, C. R.; Weitekamp, D. P. *J. Am. Chem. Soc.* **1987**, *109* (18), 5541−5542.
(4) Eisenschmid, T. C.; Kirss, R. U.; Deutsch, P. P.; Hommeltoft, S. I.; Eisenberg, R.; Bargon, J.; Lawler, R. G.; Balch, A. L. *J. Am. Chem. Soc.* **1987**, *109* (26), 8089−8091.
(5) Golman, K.; Axelsson, O.; Johannesson, H.; Mansson, S.; Olofsson, C.; Petersson, J. S. *Magn. Reson. Med.* **2001**, *46* (1), 1−5.
(6) Johansson, E.; Olsson, L. E.; Månsson, S.; Petersson, J. S.; Golman, K.; Ståhlberg, F.; Wirestam, R. *Magn. Reson. Med.* **2004**, *52* (5), 1043−1051.
(7) Bargon, J.; Kandels, J.; Kating, P. *J. Chem. Phys.* **1993**, *98* (8), 6150−6153.
(8) Messerle, B. A.; Sleigh, C. J.; Partridge, M. G.; Duckett, S. B. *J. Chem. Soc., Dalton Trans.* **1999**, 1429−1436.
(9) Eills, J.; Stevanato, G.; Bengs, C.; Glöggler, S.; Elliott, S. J.; Alonso-Valdesueiro, J.; Pileio, G.; Levitt, M. H. *J. Magn. Reson.* **2017**, *274*, 163−172.
(10) Duckett, S. B.; Wood, N. J. *Coord. Chem. Rev.* **2008**, *252* (21), 2278−2291.
(11) Nelson, S. J.; Kurhanewicz, J.; Vigneron, D. B.; Larson, P. E. Z.; Harzstark, A. L.; Ferrone, M.; van Criekinge, M.; Chang, J. W.; Bok, R.; Park, I.; Reed, G.; Carvajal, L.; Small, E. J.; Munster, P.; Weinberg, V. K.; Ardenkjaer-Larsen, J. H.; Chen, A. P.; Hurd, R. E.; Odegardstuen, L.-I.; Robb, F. J.; Tropp, J.; Murray, J. A. *Sci. Transl. Med.* **2013**, *5* (198), 108.
(12) Ardenkjær-Larsen, J. H.; Bowen, S.; Petersen, J. R.; Rybalko, O.; Vinding, M. S.; Ullisch, M.; Nielsen, N. C. *Magn. Reson. Med.* **2019**, *81* (3), 2184−2194.
(13) Adams, R. W.; Aguilar, J. A.; Atkinson, K. D.; Cowley, M. J.; Elliott, P. I. P.; Duckett, S. B.; Green, G. G. R.; Khazal, I. G.; López-Serrano, J.; Williamson, D. C. *Science* **2009**, *323* (5922), 1708−1711.
(14) Barskiy, D. A.; Coffey, A. M.; Nikolaou, P.; Mikhaylov, D. M.; Goodson, B. M.; Branca, R. T.; Lu, G. J.; Shapiro, M. G.; Telkki, V.-V.; Zhivonitko, V. V.; Koptyug, I. V.; Salnikov, O. G.; Kovtunov, K. V.; Bukhtiyarov, V. I.; Rosen, M. S.; Barlow, M. J.; Safavi, S.; Hall, I. P.; Schröder, L.; Chekmenev, E. Y. *Chem. - Eur. J.* **2017**, *23* (4), 725−751.
(15) Kovtunov, K. V.; Koptyug, I. V.; Fekete, M.; Duckett, S. B.; Theis, T.; Joalland, B.; Chekmenev, E. Y. *Angew. Chem., Int. Ed.* **2020**, *59* (41), 17788−17797.
(16) Hövener, J.-B.; Schwaderlapp, N.; Lickert, T.; Duckett, S. B.; Mewis, R. E.; Highton, L. A. R.; Kenny, S. M.; Green, G. G. R.; Leibfritz, D.; Korvink, J. G.; Hennig, J.; von Elverfeldt, D. *Nat. Commun.* **2013**, *4*, 2946.
(17) Hale, W. G.; Zhao, T. Y.; Choi, D.; Ferrer, M.-J.; Song, B.; Zhao, H.; Hagelin-Weaver, H. E.; Bowers, C. R. *ChemPhysChem* **2021**, *22* (9), 822−827.
(18) Eshuis, N.; Aspers, R. L. E. G.; van Weerdenburg, B. J. A.; Feiters, M. C.; Rutjes, F. P. J. T.; Wijmenga, S. S.; Tessari, M. *Angew. Chem., Int. Ed.* **2015**, *54* (48), 14527−14530.
(19) Reineri, F.; Boi, T.; Aime, S. *Nat. Commun.* **2015**, *6*, 5858.
(20) Appelt, S.; Kentner, A.; Lehmkuhl, S.; Blümich, B. *Prog. Nucl. Magn. Reson. Spectrosc.* **2019**, *114*−*115*, 1−32.
(21) Pravdivtsev, A. N.; Sönnichsen, F. D.; Hövener, J.-B. *ChemPhysChem* **2020**, *21* (7), 667−672.
(22) Korchak, S.; Kaltschnee, L.; Dervisoglu, R.; Andreas, L.; Griesinger, C.; Glöggler, S. *Angew. Chem., Int. Ed.* **2021**, *60* (38), 20984−20990.
(23) Joalland, B.; Ariyasingha, N. M.; Lehmkuhl, S.; Theis, T.; Appelt, S.; Chekmenev, E. Y. *Angew. Chem., Int. Ed.* **2020**, *59* (22), 8654−8660.
(24) Knecht, S.; Blanchard, J. W.; Barskiy, D.; Cavallari, E.; Dagys, L.; Van Dyke, E.; Tsukanov, M.; Bliemel, B.; Munnemann, K.; Aime, S.; Reineri, F.; Levitt, M. H.; Buntkowsky, G.; Pines, A.; Blumler, P.; Budker, D.; Eills, J. *Proc. Natl. Acad. Sci. U. S. A.* **2021**, *118* (13), e2025383118.
(25) Roy, S. S.; Appleby, K. M.; Fear, E. J.; Duckett, S. B. *J. Phys. Chem. Lett.* **2018**, *9* (5), 1112−1117.
(26) Them, K.; Ellermann, F.; Pravdivtsev, A. N.; Salnikov, O. G.; Skovpin, I. V.; Koptyug, I. V.; Herges, R.; Hövener, J.-B. *J. Am. Chem. Soc.* **2021**, *143* (34), 13694−13700.
(27) Marshall, H.; Stewart, N. J.; Chan, H.-F.; Rao, M.; Norquay, G.; Wild, J. M. *Prog. Nucl. Magn. Reson. Spectrosc.* **2021**, *122*, 42−62.
(28) Hoevener, J.-B.; Bär, S.; Leupold, J.; Jenne, K.; Leibfritz, D.; Hennig, J.; Duckett, S. B.; von Elverfeldt, D. *NMR Biomed.* **2013**, *26*, 124−131.
(29) Feng, B.; Coffey, A. M.; Colon, R. D.; Chekmenev, E. Y.; Waddell, K. W. *J. Magn. Reson.* **2012**, *214*, 258−262.
(30) Wagner, S. *MAGMA* **2014**, *27* (3), 195−199.
(31) Aroulanda, C.; Starovoytova, L.; Canet, D. *J. Phys. Chem. A* **2007**, *111* (42), 10615−10624.
(32) Buntkowsky, G.; Walaszek, B.; Adamczyk, A.; Xu, Y.; Limbach, H.-H.; Chaudret, B. *Phys. Chem. Chem. Phys.* **2006**, *8* (16), 1929−1935.
(33) Schmidt, A. B.; Worner, J.; Pravdivtsev, A.; Knecht, S.; Scherer, H.; Weber, S.; Hennig, J.; Elverfeldt, D.; Hovener, J.-B. *ChemPhysChem* **2019**, *20* (19), 2408−2412.
(34) Kiryutin, A. S.; Sauer, G.; Yurkovskaya, A. V.; Limbach, H.-H.; Ivanov, K. L.; Buntkowsky, G. *J. Phys. Chem. C* **2017**, *121* (18), 9879−9888.
(35) Freeman, R.; Wittekoek, S.; Ernst, R. R. *J. Chem. Phys.* **1970**, *52* (3), 1529−1544.
(36) Kadlecek, S.; Vahdat, V.; Nakayama, T.; Ng, D.; Emami, K.; Rizi, R. *NMR Biomed.* **2011**, *24* (8), 933−942.

https://doi.org/10.1021/acs.analchem.1c04863
Anal. Chem. 2022, 94, 479−502

(37) Pravdivtsev, A. N.; Ivanov, K. L.; Kaptein, R.; Yurkovskaya, A. V. *Appl. Magn. Reson.* **2013**, *44* (1), 23−39.
(38) Schmidt, A. B.; Berner, S.; Schimpf, W.; Muller, C.; Lickert, T.; Schwaderlapp, N.; Knecht, S.; Skinner, J. G.; Dost, A.; Rovedo, P.; Hennig, J.; von Elverfeldt, D.; Hovener, J. -B. *Nat. Commun.* **2017**, *8*, 14535.
(39) Berner, S.; Schmidt, A. B.; Zimmermann, M.; Pravdivtsev, A. N.; Glöggler, S.; Hennig, J.; von Elverfeldt, D.; Hövener, J.-B. *ChemistryOpen* **2019**, *8* (6), 728−736.
(40) Natterer, J.; Bargon, J. *Prog. Nucl. Magn. Reson. Spectrosc.* **1997**, *31* (4), 293−315.
(41) Nasibulov, E. A.; Pravdivtsev, A. N.; Yurkovskaya, A. V.; Lukzen, N. N.; Vieth, H.-M.; Ivanov, K. L. *Z. Phys. Chem.* **2013**, *227* (6−7), 929−953.
(42) Goldman, M.; Johannesson, H. *C. R. Phys.* **2005**, *6*, 575−581.
(43) Torres, O.; Procacci, B.; Halse, M. E.; Adams, R. W.; Blazina, D.; Duckett, S. B.; Eguillor, B.; Green, R. A.; Perutz, R. N.; Williamson, D. C. *J. Am. Chem. Soc.* **2014**, *136* (28), 10124−10131.
(44) Pravdivtsev, A. N.; Yurkovskaya, A. V.; Petrov, P. A.; Vieth, H.-M. *Phys. Chem. Chem. Phys.* **2017**, *19* (38), 25961−25969.
(45) Bowers, C. R. *EMagRes* **2007**, DOI: 10.1002/9780470034590.emrstm0489.
(46) Bowers, C. R. *Parahydrogen and Synthesis Allow Dramatically Enhanced Nuclear Alignment*. Ph.D. Thesis, California Institute of Technology, Pasadena, CA, 1991; DOI: 10.7907/R5TV-Z220.
(47) Natterer, J.; Schedletzky, O.; Barkemeyer, J.; Bargon, J.; Glaser, S. J. *J. Magn. Reson.* **1998**, *133* (1), 92−97.
(48) Berner, S.; Schmidt, A. B.; Ellermann, F.; Korchak, S.; Chekmenev, E. Y.; Gloggler, S.; von Elverfeldt, D.; Hennig, J.; Hovener, J.-B. *Phys. Chem. Chem. Phys.* **2021**, *23* (3), 2320−2330.
(49) Pravica, M. G.; Weitekamp, D. P. *Chem. Phys. Lett.* **1988**, *145* (4), 255−258.
(50) Plaumann, M.; Bommerich, U.; Trantzschel, T.; Lego, D.; Dillenberger, S.; Sauer, G.; Bargon, J.; Buntkowsky, G.; Bernarding, J. *Chem. - Eur. J.* **2013**, *19* (20), 6334−6339.
(51) Bar, S.; Lange, T.; Leibfritz, D.; Hennig, J.; von Elverfeldt, D.; Hovener, J.-B. *J. Magn. Reson.* **2012**, *225*, 25−35.
(52) Svyatova, A.; Skovpin, I. V.; Chukanov, N. V.; Kovtunov, K. V.; Chekmenev, E. Y.; Pravdivtsev, A. N.; Hövener, J.-B.; Koptyug, I. V. *Chem. - Eur. J.* **2019**, *25* (36), 8465−8470.
(53) Shchepin, R. V.; Coffey, A. M.; Waddell, K. W.; Chekmenev, E. Y. *Anal. Chem.* **2014**, *86* (12), 5601−5605.
(54) Schmidt, A. B.; Brahms, A.; Ellermann, F.; Knecht, S.; Berner, S.; Hennig, J.; von Elverfeldt, D.; Herges, R.; Hovener, J.-B.; Pravdivtsev, A. *Phys. Chem. Chem. Phys.* **2021**, DOI: 10.1039/D1CP04153C.
(55) Jóhannesson, H.; Axelsson, O.; Karlsson, M. *C. R. Phys.* **2004**, *5* (3), 315−324.
(56) Cavallari, E.; Carrera, C.; Boi, T.; Aime, S.; Reineri, F. *J. Phys. Chem. B* **2015**, *119* (31), 10035−10041.
(57) Kadlecek, S.; Emami, K.; Ishii, M.; Rizi, R. *J. Magn. Reson.* **2010**, *205* (1), 9−13.
(58) Cai, C.; Coffey, A. M.; Shchepin, R. V.; Chekmenev, E. Y.; Waddell, K. W. *J. Phys. Chem. B* **2013**, *117* (5), 1219−1224.
(59) Duckett, S. B.; Newell, C. L.; Eisenberg, R. *J. Am. Chem. Soc.* **1993**, *115* (3), 1156−1157.
(60) Haake, M.; Natterer, J.; Bargon, J. *J. Am. Chem. Soc.* **1996**, *118* (36), 8688−8691.
(61) Stevanato, G. *J. Magn. Reson.* **2017**, *274*, 148−162.
(62) Korchak, S.; Yang, S.; Mamone, S.; Glöggler, S. *ChemistryOpen* **2018**, *7* (5), 344−348.
(63) Pravdivtsev, A. N.; Kozinenko, V. P.; Hövener, J.-B. *J. Phys. Chem. A* **2018**, *122* (45), 8948−8956.
(64) Stevanato, G.; Eills, J.; Bengs, C.; Pileio, G. *J. Magn. Reson.* **2017**, *277*, 169−178.
(65) Pravdivtsev, A. N.; Hövener, J.-B. *Phys. Chem. Chem. Phys.* **2020**, *22* (16), 8963−8972.
(66) Hogben, H. J.; Krzystyniak, M.; Charnock, G. T. P.; Hore, P. J.; Kuprov, I. *J. Magn. Reson.* **2011**, *208* (2), 179−194.
(67) Smith, S. A.; Levante, T. O.; Meier, B. H.; Ernst, R. R. *J. Magn. Reson., Ser. A* **1994**, *106* (1), 75−105.
(68) Bengs, C.; Levitt, M. H. *Magn. Reson. Chem.* **2018**, *56* (6), 374−414.
(69) Bhattacharya, P.; Harris, K.; Lin, A. P.; Mansson, M.; Norton, V. A.; Perman, W. H.; Weitekamp, D. P.; Ross, B. D. *MAGMA* **2005**, *18* (5), 245−256.
(70) Skovpin, I. V.; Zhivonitko, V. V.; Koptyug, I. V. *Appl. Magn. Reson.* **2011**, *41* (2), 393−410.
(71) Kovtunov, K. V.; Zhivonitko, V. V.; Corma, A.; Koptyug, I. V. *J. Phys. Chem. Lett.* **2010**, *1* (11), 1705−1708.
(72) Abdulhussain, S.; Breitzke, H.; Ratajczyk, T.; Grünberg, A.; Srour, M.; Arnaut, D.; Weidler, H.; Kunz, U.; Kleebe, H. J.; Bommerich, U.; Bernarding, J.; Gutmann, T.; Buntkowsky, G. *Chem. - Eur. J.* **2014**, *20* (4), 1159−1166.
(73) Koptyug, I. V.; Kovtunov, K. V.; Burt, S. R.; Anwar, M. S.; Hilty, C.; Han, S.-I.; Pines, A.; Sagdeev, R. Z. *J. Am. Chem. Soc.* **2007**, *129* (17), 5580−5586.
(74) Kovtunov, K. V.; Beck, I. E.; Bukhtiyarov, V. I.; Koptyug, I. V. *Angew. Chem., Int. Ed.* **2008**, *47* (8), 1492−1495.
(75) Glöggler, S.; Grunfeld, A. M.; Ertas, Y. N.; McCormick, J.; Wagner, S.; Schleker, P. P. M.; Bouchard, L.-S. *Angew. Chem., Int. Ed.* **2015**, *54* (8), 2452−2456.
(76) Kovtunov, K. V.; Barskiy, D. A.; Salnikov, O. G.; Shchepin, R. V.; Coffey, A. M.; Kovtunova, L. M.; Bukhtiyarov, V. I.; Koptyug, I. V.; Chekmenev, E. Y. *RSC Adv.* **2016**, *6* (74), 69728−69732.
(77) Kaltschnee, L.; Jagtap, A. P.; McCormick, J.; Wagner, S.; Bouchard, L.-S.; Utz, M.; Griesinger, C.; Glöggler, S. *Chem. - Eur. J.* **2019**, *25* (47), 11031−11035.
(78) Jagtap, A. P.; Kaltschnee, L.; Glöggler, S. *Chem. Sci.* **2019**, *10* (37), 8577−8582.
(79) Reineri, F.; Viale, A.; Ellena, S.; Boi, T.; Daniele, V.; Gobetto, R.; Aime, S. *Angew. Chem., Int. Ed.* **2011**, *50* (32), 7350−7353.
(80) Cavallari, E.; Carrera, C.; Sorge, M.; Bonne, G.; Muchir, A.; Aime, S.; Reineri, F. *Sci. Rep.* **2018**, *8* (1), 8366.
(81) Barskiy, D. A.; Ke, L. A.; Li, X.; Stevenson, V.; Widarman, N.; Zhang, H.; Truxal, A.; Pines, A. *J. Phys. Chem. Lett.* **2018**, *9* (11), 2721−2724.
(82) Dagys, L.; Jagtap, A. P.; Korchak, S.; Mamone, S.; Saul, P.; Levitt, M. H.; Glöggler, S. *Analyst* **2021**, *146* (5), 1772−1778.
(83) Goldman, M.; Johannesson, H.; Axelsson, O.; Karlsson, M. *C. R. Chim.* **2006**, *9*, 357−363.
(84) Goldman, M.; Axelsson, O.; Johannesson, H.; Ardenkjaer-Larsen, J. *Method and Apparatus for Producing Contrast Agents for Magnetic Resonance Imaging*. U.S. Patent Application 20060127313 A1, June 15, 2006.
(85) Waddell, K. W.; Coffey, A. M.; Chekmenev, E. Y. *J. Am. Chem. Soc.* **2011**, *133* (1), 97−101.
(86) Coffey, A. M.; Shchepin, R. V.; Truong, M. L.; Wilkens, K.; Pham, W.; Chekmenev, E. Y. *Anal. Chem.* **2016**, *88*, 8279−8288.
(87) Coffey, A. M.; Shchepin, R. V.; Feng, B.; Colon, R. D.; Wilkens, K.; Waddell, K. W.; Chekmenev, E. Y. *J. Magn. Reson.* **2017**, *284*, 115−124.
(88) Joalland, B.; Schmidt, A. B.; Kabir, M. S. H.; Chukanov, N. V.; Kovtunov, K. V.; Koptyug, I. V.; Hennig, J.; Hövener, J.-B.; Chekmenev, E. Y. *Anal. Chem.* **2020**, *92* (1), 1340−1345.
(89) Hövener, J.-B.; Chekmenev, E. Y.; Harris, K. C.; Perman, W. H.; Tran, T. T.; Ross, B. D.; Bhattacharya, P. *MAGMA* **2009**, *22*, 123−134.
(90) Hövener, J.-B.; Chekmenev, E. Y.; Harris, K. C.; Perman, W. H.; Robertson, L. W.; Ross, B. D.; Bhattacharya, P. *MAGMA* **2009**, *22*, 111−121.
(91) Schmidt, A. B.; Berner, S.; Braig, M.; Zimmermann, M.; Hennig, J.; von Elverfeldt, D.; Hovener, J.-B. *PLoS One* **2018**, *13* (7), No. e0200141.
(92) Agraz, J.; Grunfeld, A. M.; Cunningham, K.; Pozos, R.; Li, D.; Wagner, S. *Adv. Biomed. Sci. Eng.* **2014**, *1*, 8−18.

(93) Borowiak, R.; Schwaderlapp, N.; Huethe, F.; Lickert, T.; Fischer, E.; Bar, S.; Hennig, J.; von Elverfeldt, D.; Hovener, J.-B. *MAGMA* **2013**, *26* (5), 491−499.
(94) Coffey, A. M.; Shchepin, R. V.; Wilkens, K.; Waddell, K. W.; Chekmenev, E. Y. *J. Magn. Reson.* **2012**, *220*, 94−101.
(95) Kiryutin, A. S.; Sauer, G.; Hadjiali, S.; Yurkovskaya, A. V.; Breitzke, H.; Buntkowsky, G. *J. Magn. Reson.* **2017**, *285*, 26−36.
(96) Hövener, J.-B.; Schwaderlapp, N.; Borowiak, R.; Lickert, T.; Duckett, S. B.; Mewis, R. E.; Adams, R. W.; Burns, M. J.; Highton, L. A. R.; Green, G. G. R.; Olaru, A.; Hennig, J.; von Elverfeldt, D. *Anal. Chem.* **2014**, *86* (3), 1767−1774.
(97) Agraz, J.; Grunfeld, A. M.; Li, D.; Cunningham, K.; Willey, C.; Pozos, R.; Wagner, S. *Rev. Sci. Instrum.* **2014**, *85*, 044705.
(98) Ellermann, F.; Pravdivtsev, A.; Hövener, J.-B. *Magn. Reson.* **2021**, *2* (1), 49−62.
(99) Juarez, A. M.; Cubric, D.; King, G. C. *Meas. Sci. Technol.* **2002**, *13* (5), N52−N55.
(100) Sullivan, N. S.; Zhou, D.; Edwards, C. M. *Cryogenics* **1990**, *30* (8), 734−735.
(101) Hövener, J.-B.; Bär, S.; Leupold, J.; Jenne, K.; Leibfritz, D.; Hennig, J.; Duckett, S. B.; von Elverfeldt, D. *NMR Biomed.* **2013**, *26* (2), 124−131.
(102) Meier, B.; Dumez, J.-N.; Stevanato, G.; Hill-Cousins, J. T.; Roy, S. S.; Håkansson, P.; Mamone, S.; Brown, R. C. D.; Pileio, G.; Levitt, M. H. *J. Am. Chem. Soc.* **2013**, *135* (50), 18746−18749.
(103) Birchall, J. R.; Coffey, A. M.; Goodson, B. M.; Chekmenev, E. Y. *Anal. Chem.* **2020**, *92* (23), 15280−15284.
(104) Sundararajan, K.; Sankaran, K.; Ramanathan, N.; Gopi, R. *J. Mol. Struct.* **2016**, *1117*, 181−191.
(105) Nantogma, S.; Joalland, B.; Wilkens, K.; Chekmenev, E. Y. *Anal. Chem.* **2021**, *93* (7), 3594−3601.
(106) Du, Y.; Zhou, R.; Ferrer, M.-J.; Chen, M.; Graham, J.; Malphurs, B.; Labbe, G.; Huang, W.; Bowers, C. R. *J. Magn. Reson.* **2020**, *321*, 106869.
(107) Buckenmaier, K.; Scheffler, K.; Plaumann, M.; Fehling, P.; Bernarding, J.; Rudolph, M.; Back, C.; Koelle, D.; Kleiner, R.; Hövener, J.; Pravdivtsev, A. N. *ChemPhysChem* **2019**, *20* (21), 2823−2829.
(108) Kiryutin, A. S.; Pravdivtsev, A. N.; Ivanov, K. L.; Grishin, Y. A.; Vieth, H.-M.; Yurkovskaya, A. V. *J. Magn. Reson.* **2016**, *263*, 79−91.
(109) Jeong, K.; Min, S.; Chae, H.; Namgoong, S. K. *Magn. Reson. Chem.* **2018**, *56* (11), 1089−1093.
(110) Gamliel, A.; Allouche-Arnon, H.; Nalbandian, R.; Barzilay, C. M.; Gomori, J. M.; Katz-Brull, R. *Appl. Magn. Reson.* **2010**, *39* (4), 329−345.
(111) Parrott, A. J.; Dallin, P.; Andrews, J.; Richardson, P. M.; Semenova, O.; Halse, M. E.; Duckett, S. B.; Nordon, A. *Appl. Spectrosc.* **2018**, *73* (1), 88−97.
(112) Chapman, B.; Joalland, B.; Meersman, C.; Ettedgui, J.; Swenson, R. E.; Krishna, M. C.; Nikolaou, P.; Kovtunov, K. V.; Salnikov, O. G.; Koptyug, I. V.; Gemeinhardt, M. E.; Goodson, B. M.; Shchepin, R. V.; Chekmenev, E. Y. *Anal. Chem.* **2021**, *93* (24), 8476−8483.
(113) Mhaske, Y.; Sutter, E.; Mahoney, C.; Daley, J.; Whiting, N. 65% Parahydrogen from a Liquid Nitrogen Cooled Generator. In *Parahydrogen Enhanced Resonance Meeting (PERM) 2021*, online, June 21−232021.
(114) Hövener, J.-B.; Pravdivtsev, A. N.; Kidd, B.; Bowers, C. R.; Glöggler, S.; Kovtunov, K. V.; Plaumann, M.; Katz-Brull, R.; Buckenmaier, K.; Jerschow, A.; Reineri, F.; Theis, T.; Shchepin, R. V.; Wagner, S.; Bhattacharya, P.; Zacharias, N. M.; Chekmenev, E. Y. *Angew. Chem., Int. Ed.* **2018**, *57* (35), 11140−11162.
(115) Stewart, N. J.; Nakano, H.; Sugai, S.; Tomohiro, M.; Kase, Y.; Uchio, Y.; Yamaguchi, T.; Matsuo, Y.; Naganuma, T.; Takeda, N.; Nishimura, I.; Hirata, H.; Hashimoto, T.; Matsumoto, S. *ChemPhysChem* **2021**, *22* (10), 915−923.
(116) Sengstschmid, H.; Freeman, R.; Barkemeyer, J.; Bargon, J. *J. Magn. Reson., Ser. A* **1996**, *120* (2), 249−257.
(117) Kiryutin, A. S.; Ivanov, K. L.; Yurkovskaya, A. V.; Vieth, H.-M.; Lukzen, N. N. *Phys. Chem. Chem. Phys.* **2013**, *15* (34), 14248−14255.
(118) Pravdivtsev, A. N.; Sönnichsen, F.; Hövener, J.-B. *J. Magn. Reson.* **2018**, *297*, 86−95.
(119) Pravdivtsev, A. N.; Ivanov, K. L.; Yurkovskaya, A. V.; Vieth, H.-M.; Sagdeev, R. Z. *Dokl. Phys. Chem.* **2015**, *465* (1), 267−269.
(120) Korchak, S.; Emondts, M.; Mamone, S.; Blümich, B.; Glöggler, S. *Phys. Chem. Chem. Phys.* **2019**, *21* (41), 22849−22856.
(121) Sørensen, O. W.; Ernst, R. R. *J. Magn. Reson.* **1983**, *51* (3), 477−489.
(122) Barkemeyer, J.; Bargon, J.; Sengstschmid, H.; Freeman, R. *J. Magn. Reson., Ser. A* **1996**, *120* (1), 129−132.
(123) Pravdivtsev, A. N.; Ellermann, F.; Hövener, J.-B. *Phys. Chem. Chem. Phys.* **2021**, *23* (26), 14146−14150.
(124) Pravdivtsev, A.; Hövener, J.-B.; Schmidt, A. B. Frequency-Selective Manipulations of Spins for Effective and Robust Transfer of Spin Order from Parahydrogen to Heteronuclei in Weakly-Coupled Spin Systems. *ChemPhysChem* DOI: 10.1002/cphc.202100721.
(125) Stewart, N. J.; Kumeta, H.; Tomohiro, M.; Hashimoto, T.; Hatae, N.; Matsumoto, S. *J. Magn. Reson.* **2018**, *296*, 85−92.
(126) Pravdivtsev, A. N.; Yurkovskaya, A. V.; Lukzen, N. N.; Ivanov, K. L.; Vieth, H.-M. *J. Phys. Chem. Lett.* **2014**, *5* (19), 3421−3426.
(127) Rodin, B. A.; Kozinenko, V. P.; Kiryutin, A. S.; Yurkovskaya, A. V.; Eills, J.; Ivanov, K. L. *J. Magn. Reson.* **2021**, *327*, 106978.
(128) Kozinenko, V. P.; Kiryutin, A. S.; Yurkovskaya, A. V.; Ivanov, K. L. *J. Magn. Reson.* **2019**, *309*, 106594.
(129) Korchak, S.; Mamone, S.; Glöggler, S. *ChemistryOpen* **2018**, *7* (9), 672−676.
(130) Svyatova, A.; Kozinenko, V. P.; Chukanov, N. V.; Burueva, D. B.; Chekmenev, E. Y.; Chen, Y.-W.; Hwang, D. W.; Kovtunov, K. V.; Koptyug, I. V. *Sci. Rep.* **2021**, *11* (1), 5646.
(131) Schmidt, A. B. *Liquid-State Nuclear Hyperpolarization without a Polarizer: Synthesis amid the Magnet Bore Allows a Dramatically Enhanced Nuclear Alignment*. Ph.D. Thesis, Albert-Ludwigs-Universität, Freiburg im Breisgau, Germany, 2020.
(132) Korchak, S.; Jagtap, A. P.; Glöggler, S. *Chem. Sci.* **2021**, *12* (1), 314−319.
(133) Lippens, G.; Dhalluin, C.; Wieruszeski, J. M. *J. Biomol. NMR* **1995**, *5* (3), 327−331.
(134) Sklenar, V. *J. Magn. Reson., Ser. A* **1995**, *114* (1), 132−135.
(135) Price, W. S.; Wälchli, M. *Magn. Reson. Chem.* **2002**, *40* (13), S128−S132.
(136) de Maissin, H.; Berner, S.; Ivantaev, V.; Hoevener, J.-B.; Hennig, J.; von Elverfeldt, D.; Schmidt, A. B. Dramatic Effect of Pulse Length and Bandwidth on the Efficiency of Pulsed Spin-Order-Transfer Sequences at High Field. In *Proceedings of the International Socety for Magnetic Resonance in Medicine 29*, online, 2021; 3805
(137) Ivantaev, V.; Berner, S.; de Maissin, H.; Hoevener, J.-B.; Hennig, J.; von Elverfeldt, D.; Kiselev, V.; Schmidt, A. B. Molecular Translation in Inhomogeneous Field Can Dramatically Reduce the Efficiency of Spin-Order Transfer at High Field. In *Proceedings of the International Socety for Magnetic Resonance in Medicine 29*, online, 2021; 3798.
(138) Golman, K.; Olsson, L. E.; Axelsson, O.; Månsson, S.; Karlsson, M.; Petersson, J. S. *Br. J. Radiol.* **2003**, *76* (suppl_2), S118−S127.
(139) Goldman, M.; Jóhannesson, H.; Axelsson, O.; Karlsson, M. *Magn. Reson. Imaging* **2005**, *23* (2), 153−157.
(140) Shchepin, R. V.; Coffey, A. M.; Waddell, K. W.; Chekmenev, E. Y. *J. Phys. Chem. Lett.* **2012**, *3* (22), 3281−3285.
(141) Goodson, B. M.; Whiting, N.; Coffey, A. M.; Nikolaou, P.; Shi, F.; Gust, B. M.; Gemeinhardt, M. E.; Shchepin, R. V.; Skinner, J. G.; Birchall, J. R.; Barlow, M. J.; Chekmenev, E. Y. *eMagRes.* **2015**, *4* (4), 797.
(142) Schmidt, A. B.; Andrews, D. L.; Rohrbach, A.; Gohn-Kreuz, C.; Shatokhin, V. N.; Kiselev, V. G.; Hennig, J.; von Elverfeldt, D.; Hövener, J.-B. *J. Magn. Reson.* **2016**, *268*, 58−67.

(143) Shchepin, R. V.; Coffey, A. M.; Waddell, K. W.; Chekmenev, E. Y. *J. Am. Chem. Soc.* **2012**, *134* (9), 3957−3960.
(144) Bhattacharya, P.; Chekmenev, E. Y.; Perman, W. H.; Harris, K. C.; Lin, A. P.; Norton, V. A.; Tan, C. T.; Ross, B. D.; Weitekamp, D. P. *J. Magn. Reson.* **2007**, *186* (1), 150−155.
(145) Bhattacharya, P.; Chekmenev, E. Y.; Reynolds, W. F.; Wagner, S.; Zacharias, N.; Chan, H. R.; Bünger, R.; Ross, B. D. *NMR Biomed.* **2011**, *24* (8), 1023−1028.
(146) Perman, W. H.; Bhattacharya, P.; Leupold, J.; Lin, A. P.; Harris, K. C.; Norton, V. A.; Hövener, J.-B.; Ross, B. D. *Magn. Reson. Imaging* **2010**, *28* (4), 459−465.
(147) Zacharias, N. M.; Chan, H. R.; Sailasuta, N.; Ross, B. D.; Bhattacharya, P. *J. Am. Chem. Soc.* **2012**, *134* (2), 934−943.
(148) Zacharias, N. M.; McCullough, C. R.; Wagner, S.; Sailasuta, N.; Chan, H. R.; Lee, Y.; Hu, J.; Perman, W. H.; Henneberg, C.; Ross, B. D.; Bhattacharya, P. *J. Mol. Imag. Dyn.* **2016**, *6*, 1000123.
(149) Coffey, A. M.; Feldman, M. A.; Shchepin, R. V.; Barskiy, D. A.; Truong, M. L.; Pham, W.; Chekmenev, E. Y. *J. Magn. Reson.* **2017**, *281* (Supplement C), 246−252.
(150) Salnikov, O. G.; Shchepin, R. V.; Chukanov, N. V.; Jaigirdar, L.; Pham, W.; Kovtunov, K. V.; Koptyug, I. V.; Chekmenev, E. Y. *J. Phys. Chem. C* **2018**, *122* (43), 24740−24749.
(151) Chekmenev, E. Y.; Hövener, J.; Norton, V. A.; Harris, K.; Batchelder, L. S.; Bhattacharya, P.; Ross, B. D.; Weitekamp, D. P. *J. Am. Chem. Soc.* **2008**, *130* (13), 4212−4213.
(152) Olsson, L. E.; Chai, C.-M.; Axelsson, O.; Karlsson, M.; Golman, K.; Petersson, J. S. *Magn. Reson. Med.* **2006**, *55* (4), 731−737.
(153) Reineri, F.; Cavallari, E.; Carrera, C.; Aime, S. *MAGMA* **2021**, *34* (1), 25−47.
(154) Butler, M. C.; Kervern, G.; Theis, T.; Ledbetter, M. P.; Ganssle, P. J.; Blanchard, J. W.; Budker, D.; Pines, A. *J. Chem. Phys.* **2013**, *138* (23), 234201.
(155) Theis, T.; Ganssle, P.; Kervern, G.; Knappe, S.; Kitching, J.; Ledbetter, M. P.; Budker, D.; Pines, A. *Nat. Phys.* **2011**, *7* (7), 571−575.
(156) Emondts, M.; Colell, J. F. P.; Blumich, B.; Schleker, P. P. M. *Phys. Chem. Chem. Phys.* **2017**, *19* (33), 21933−21937.
(157) Pravdivtsev, A. N.; Ivanov, K. L.; Yurkovskaya, A. V.; Vieth, H.-M.; Sagdeev, R. Z. *Dokl. Phys. Chem.* **2015**, *464* (2), 247−250.
(158) Eills, J.; Blanchard, J. W.; Wu, T.; Bengs, C.; Hollenbach, J.; Budker, D.; Levitt, M. H. *J. Chem. Phys.* **2019**, *150* (17), 174202.
(159) Cavallari, E.; Carrera, C.; Aime, S.; Reineri, F. *J. Magn. Reson.* **2018**, *289*, 12−17.
(160) Kuhn, L. T.; Bommerich, U.; Bargon, J. *J. Phys. Chem. A* **2006**, *110* (10), 3521−3526.
(161) Stephan, M.; Kohlmann, O.; Niessen, H. G.; Eichhorn, A.; Bargon, J. *Magn. Reson. Chem.* **2002**, *40* (2), 157−160.
(162) Jonischkeit, T.; Bommerich, U.; Stadler, J.; Woelk, K.; Niessen, H. G.; Bargon, J. *J. Chem. Phys.* **2006**, *124* (20), 201109.
(163) Theis, T.; Truong, M. L.; Coffey, A. M.; Shchepin, R. V.; Waddell, K. W.; Shi, F.; Goodson, B. M.; Warren, W. S.; Chekmenev, E. Y. *J. Am. Chem. Soc.* **2015**, *137* (4), 1404−1407.
(164) Truong, M. L.; Theis, T.; Coffey, A. M.; Shchepin, R. V.; Waddell, K. W.; Shi, F.; Goodson, B. M.; Warren, W. S.; Chekmenev, E. Y. *J. Phys. Chem. C* **2015**, *119* (16), 8786−8797.
(165) Pravdivtsev, A. N.; Ivanov, K. L.; Yurkovskaya, A. V.; Petrov, P. A.; Limbach, H.-H.; Kaptein, R.; Vieth, H.-M. *J. Magn. Reson.* **2015**, *261*, 73−82.
(166) Zhivonitko, V. V.; Skovpin, I. V.; Koptyug, I. V. *Chem. Commun.* **2015**, *51* (13), 2506−2509.
(167) Lindale, J. R.; Eriksson, S. L.; Tanner, C. P. N.; Zhou, Z.; Colell, J. F. P.; Zhang, G.; Bae, J.; Chekmenev, E. Y.; Theis, T.; Warren, W. S. *Nat. Commun.* **2019**, *10* (1), 395.
(168) Pravdivtsev, A. N.; Kempf, N.; Plaumann, M.; Bernarding, J.; Scheffler, K.; Hövener, J.-B.; Buckenmaier, K. *ChemPhysChem* **2021**, DOI: 10.1002/cphc.202100543.
(169) Dagys, L.; Bengs, C.; Levitt, M. H. *J. Chem. Phys.* **2021**, *155* (15), 154201.
(170) Buckenmaier, K.; Rudolph, M.; Fehling, P.; Steffen, T.; Back, C.; Bernard, R.; Pohmann, R.; Bernarding, J.; Kleiner, R.; Koelle, D.; Plaumann, M.; Scheffler, K. *Rev. Sci. Instrum.* **2018**, *89* (12), 125103.
(171) Blanchard, J. W.; Ripka, B.; Suslick, B. A.; Gelevski, D.; Wu, T.; Münnemann, K.; Barskiy, D. A.; Budker, D. *Magn. Reson. Chem.* **2021**, *59*, 1208.
(172) Arunkumar, N.; Bucher, D. B.; Turner, M. J.; TomHon, P.; Glenn, D.; Lehmkuhl, S.; Lukin, M. D.; Park, H.; Rosen, M. S.; Theis, T.; Walsworth, R. L. *PRX Quantum* **2021**, *2* (1), 010305.
(173) Blanchard, J. W.; Ledbetter, M. P.; Theis, T.; Butler, M. C.; Budker, D.; Pines, A. *J. Am. Chem. Soc.* **2013**, *135* (9), 3607−3612.
(174) Blanchard, J. W.; Wu, T.; Eills, J.; Hu, Y.; Budker, D. *J. Magn. Reson.* **2020**, *314*, 106723.
(175) Burueva, D. B.; Eills, J.; Blanchard, J. W.; Garcon, A.; Picazo-Frutos, R.; Kovtunov, K. V.; Koptyug, I. V.; Budker, D. *Angew. Chem., Int. Ed.* **2020**, *59* (39), 17026−17032.
(176) Tayler, M. C. D.; Theis, T.; Sjolander, T. F.; Blanchard, J. W.; Kentner, A.; Pustelny, S.; Pines, A.; Budker, D. *Rev. Sci. Instrum.* **2017**, *88* (9), 091101.
(177) Myers, W.; Slichter, D.; Hatridge, M.; Busch, S.; Mößle, M.; McDermott, R.; Trabesinger, A.; Clarke, J. *J. Magn. Reson.* **2007**, *186* (2), 182−192.
(178) Theis, T.; Blanchard, J. W.; Butler, M. C.; Ledbetter, M. P.; Budker, D.; Pines, A. *Chem. Phys. Lett.* **2013**, *580*, 160−165.
(179) Theis, T.; Ledbetter, M. P.; Kervern, G.; Blanchard, J. W.; Ganssle, P. J.; Butler, M. C.; Shin, H. D.; Budker, D.; Pines, A. *J. Am. Chem. Soc.* **2012**, *134* (9), 3987−3990.
(180) Lee, S.-J.; Jeong, K.; Shim, J. H.; Lee, H. J.; Min, S.; Chae, H.; Namgoong, S. K.; Kim, K. *Sci. Rep.* **2019**, *9* (1), 12422.
(181) Vesanen, P. T.; Nieminen, J. O.; Zevenhoven, K. C. J.; Dabek, J.; Parkkonen, L. T.; Zhdanov, A. V.; Luomahaara, J.; Hassel, J.; Penttilä, J.; Simola, J.; Ahonen, A. I.; Mäkelä, J. P.; Ilmoniemi, R. J. *Magn. Reson. Med.* **2013**, *69* (6), 1795−1804.
(182) Bucher, D. B.; Glenn, D. R.; Park, H.; Lukin, M. D.; Walsworth, R. L. *Phys. Rev. X* **2020**, *10* (2), 021053.
(183) Zheng, H.; Xu, J.; Iwata, G. Z.; Lenz, T.; Michl, J.; Yavkin, B.; Nakamura, K.; Sumiya, H.; Ohshima, T.; Isoya, J.; Wrachtrup, J.; Wickenbrock, A.; Budker, D. *Phys. Rev. Appl.* **2019**, *11* (6), 064068.
(184) Kimmich, R. *Chapter 1 Principle, Purpose and Pitfalls of Field-Cycling NMR Relaxometry.* **2018**, 1−41.
(185) Ivanov, K. L.; Pravdivtsev, A. N.; Yurkovskaya, A. V.; Vieth, H.-M.; Kaptein, R. *Prog. Nucl. Magn. Reson. Spectrosc.* **2014**, *81*, 1−36.
(186) Shchepin, R. V.; Barskiy, D. A.; Coffey, A. M.; Manzanera Esteve, I. V.; Chekmenev, E. Y. *Angew. Chem., Int. Ed.* **2016**, *55* (20), 6071−6074.
(187) Reineri, F.; Viale, A.; Dastrù, W.; Gobetto, R.; Aime, S. *Contrast Media Mol. Imaging* **2011**, *6* (2), 77−84.
(188) Reineri, F.; Viale, A.; Ellena, S.; Alberti, D.; Boi, T.; Giovenzana, G. B.; Gobetto, R.; Premkumar, S. S. D.; Aime, S. *J. Am. Chem. Soc.* **2012**, *134* (27), 11146−11152.
(189) Ellena, S.; Viale, A.; Gobetto, R.; Aime, S. *Magn. Reson. Chem.* **2012**, *50* (8), 529−533.
(190) Eills, J.; Cavallari, E.; Carrera, C.; Budker, D.; Aime, S.; Reineri, F. *J. Am. Chem. Soc.* **2019**, *141* (51), 20209−20214.
(191) Ripka, B.; Eills, J.; Kourilova, H.; Leutzsch, M.; Levitt, M. H.; Munnemann, K. *Chem. Commun.* **2018**, *54* (86), 12246−12249.
(192) Rodin, B. A.; Eills, J.; Picazo-Frutos, R.; Sheberstov, K. F.; Budker, D.; Ivanov, K. L. *Phys. Chem. Chem. Phys.* **2021**, *23* (12), 7125−7134.
(193) Reineri, F.; Santelia, D.; Gobetto, R.; Aime, S. *J. Magn. Reson.* **2009**, *200* (1), 15−20.
(194) Pokochueva, E. V.; Burueva, D. B.; Salnikov, O. G.; Koptyug, I. V. *ChemPhysChem* **2021**, *22* (14), 1421−1440.
(195) Kovtunov, K. V.; Barskiy, D. A.; Shchepin, R. V.; Coffey, A. M.; Waddell, K. W.; Koptyug, I. V.; Chekmenev, E. Y. *Anal. Chem.* **2014**, *86* (13), 6192−6196.
(196) Kovtunov, K. V.; Zhivonitko, V. V.; Skovpin, I. V.; Barskiy, D. A.; Salnikov, O. G.; Koptyug, I. V. *J. Phys. Chem. C* **2013**, *117* (44), 22887−22893.

(197) Salnikov, O. G.; Kovtunov, K. V.; Koptyug, I. V. *Sci. Rep.* **2015**, *5* (1), 13930.
(198) Salnikov, O. G.; Svyatova, A.; Kovtunova, L. M.; Chukanov, N. V.; Bukhtiyarov, V. I.; Kovtunov, K. V.; Chekmenev, E. Y.; Koptyug, I. V. *Chem. - Eur. J.* **2021**, *27* (4), 1316−1322.
(199) Du, Y.; Behera, R.; Maligal-Ganesh, R. V.; Chen, M.; Chekmenev, E. Y.; Huang, W.; Bowers, C. R. *J. Phys. Chem. C* **2020**, *124* (15), 8304−8309.
(200) Zhou, R.; Cheng, W.; Neal, L. M.; Zhao, E. W.; Ludden, K.; Hagelin-Weaver, H. E.; Bowers, C. R. *Phys. Chem. Chem. Phys.* **2015**, *17* (39), 26121−26129.
(201) Burueva, D. B.; Kozinenko, V. P.; Sviyazov, S. V.; Kovtunova, L. M.; Bukhtiyarov, V. I.; Chekmenev, E. Y.; Salnikov, O. G.; Kovtunov, K. V.; Koptyug, I. V. *Appl. Magn. Reson.* **2021**, DOI: 10.1007/s00723-021-01377-4.
(202) Salnikov, O. G.; Nikolaou, P.; Ariyasingha, N. M.; Kovtunov, K. V.; Koptyug, I. V.; Chekmenev, E. Y. *Anal. Chem.* **2019**, *91* (7), 4741−4746.
(203) Kovtunov, K. V.; Barskiy, D. A.; Coffey, A. M.; Truong, M. L.; Salnikov, O. G.; Khudorozhkov, A. K.; Inozemtseva, E. A.; Prosvirin, I. P.; Bukhtiyarov, V. I.; Waddell, K. W.; Chekmenev, E. Y.; Koptyug, I. V. *Chem. - Eur. J.* **2014**, *20* (37), 11636−11639.
(204) Salnikov, O. G.; Kovtunov, K. V.; Nikolaou, P.; Kovtunova, L. M.; Bukhtiyarov, V. I.; Koptyug, I. V.; Chekmenev, E. Y. *ChemPhysChem* **2018**, *19* (20), 2621−2626.
(205) Burueva, D. B.; Kovtunov, K. V.; Bukhtiyarov, A. V.; Barskiy, D. A.; Prosvirin, I. P.; Mashkovsky, I. S.; Baeva, G. N.; Bukhtiyarov, V. I.; Stakheev, A. Yu; Koptyug, I. V. *Chem. - Eur. J.* **2018**, *24* (11), 2547−2553.
(206) Telkki, V.-V.; Zhivonitko, V. V.; Ahola, S.; Kovtunov, K. V.; Jokisaari, J.; Koptyug, I. V. *Angew. Chem., Int. Ed.* **2010**, *49* (45), 8363−8366.
(207) Telkki, V.-V.; Zhivonitko, V. V. *J. Magn. Reson.* **2011**, *210* (2), 238−245.
(208) Bouchard, L.-S.; Burt, S. R.; Anwar, M. S.; Kovtunov, K. V.; Koptyug, I. V.; Pines, A. *Science* **2008**, *319* (5862), 442−445.
(209) Zhivonitko, V. V.; Telkki, V.-V.; Koptyug, I. V. *Angew. Chem.* **2012**, *124* (32), 8178−8182.
(210) Kovtunov, K. V.; Lebedev, D.; Svyatova, A.; Pokochueva, E. V.; Prosvirin, I. P.; Gerasimov, E. Y.; Bukhtiyarov, V. I.; Müller, C. R.; Fedorov, A.; Koptyug, I. V. *ChemCatChem* **2018**, *11* (3), 969−973.
(211) Svyatova, A.; Kononenko, E. S.; Kovtunov, K. V.; Lebedev, D.; Gerasimov, E. Y.; Bukhtiyarov, A. V.; Prosvirin, I. P.; Bukhtiyarov, V. I.; Muller, C. R.; Fedorov, A.; Koptyug, I. V. *Catal. Sci. Technol.* **2020**, *10* (1), 99−104.
(212) Barskiy, D. A.; Kovtunov, K. V.; Gerasimov, E. Y.; Phipps, M. A.; Salnikov, O. G.; Coffey, A. M.; Kovtunova, L. M.; Prosvirin, I. P.; Bukhtiyarov, V. I.; Koptyug, I. V.; Chekmenev, E. Y. *J. Phys. Chem. C* **2017**, *121* (18), 10038−10046.
(213) Ariyasingha, N. M.; Salnikov, O. G.; Kovtunov, K. V.; Kovtunova, L. M.; Bukhtiyarov, V. I.; Goodson, B. M.; Rosen, M. S.; Koptyug, I. V.; Gelovani, J. G.; Chekmenev, E. Y. *J. Phys. Chem. C* **2019**, *123* (18), 11734−11744.
(214) Barskiy, D. A.; Salnikov, O. G.; Romanov, A. S.; Feldman, M. A.; Coffey, A. M.; Kovtunov, K. V.; Koptyug, I. V.; Chekmenev, E. Y. *J. Magn. Reson.* **2017**, *276*, 78−85.
(215) Ariyasingha, N. M.; Joalland, B.; Younes, H. R.; Salnikov, O. G.; Chukanov, N. V.; Kovtunov, K. V.; Kovtunova, L. M.; Bukhtiyarov, V. I.; Koptyug, I. V.; Gelovani, J. G.; Chekmenev, E. Y. *Chem. - Eur. J.* **2020**, *26* (60), 13621−13626.
(216) Zhao, E. W.; Maligal-Ganesh, R.; Xiao, C.; Goh, T.-W.; Qi, Z.; Pei, Y.; Hagelin-Weaver, H. E.; Huang, W.; Bowers, C. R. *Angew. Chem.* **2017**, *129* (14), 3983−3987.
(217) Zhao, E. W.; Xin, Y.; Hagelin-Weaver, H. E.; Bowers, C. R. *ChemCatChem* **2016**, *8* (13), 2197−2201.
(218) Barskiy, D. A.; Salnikov, O. G.; Kovtunov, K. V.; Koptyug, I. V. *J. Phys. Chem. A* **2015**, *119* (6), 996−1006.
(219) Sharma, R.; Bouchard, L.-S. *Sci. Rep.* **2012**, *2* (1), 277.
(220) Kidd, B. E.; Gesiorski, J. L.; Gemeinhardt, M. E.; Shchepin, R. V.; Kovtunov, K. V.; Koptyug, I. V.; Chekmenev, E. Y.; Goodson, B. M. *J. Phys. Chem. C* **2018**, *122* (29), 16848−16852.
(221) Cavallari, E.; Carrera, C.; Di Matteo, G.; Bondar, O.; Aime, S.; Reineri, F. *Front. Oncol.* **2020**, *10*, 497.
(222) Bondar, O.; Cavallari, E.; Carrera, C.; Aime, S.; Reineri, F. *arXiv* **2021**, 210801497.
(223) Cavallari, E.; Carrera, C.; Aime, S.; Reineri, F. *ChemPhysChem* **2019**, *20* (2), 318−325.
(224) Cavallari, E.; Carrera, C.; Reineri, F. *Isr. J. Chem.* **2017**, *57* (9), 833−842.
(225) Srour, M.; Hadjiali, S.; Brunnengräber, K.; Weidler, H.; Xu, Y.; Breitzke, H.; Gutmann, T.; Buntkowsky, G. *J. Phys. Chem. C* **2021**, *125* (13), 7178−7187.
(226) Pokochueva, E. V.; Kovtunov, K. V.; Salnikov, O. G.; Gemeinhardt, M. E.; Kovtunova, L. M.; Bukhtiyarov, V. I.; Chekmenev, E. Y.; Goodson, B. M.; Koptyug, I. V. *Phys. Chem. Chem. Phys.* **2019**, *21* (48), 26477−26482.
(227) Salnikov, O. G.; Chukanov, N. V.; Shchepin, R. V.; Manzanera Esteve, I. V.; Kovtunov, K. V.; Koptyug, I. V.; Chekmenev, E. Y. *J. Phys. Chem. C* **2019**, *123* (20), 12827−12840.
(228) McCormick, J.; Grunfeld, A. M.; Ertas, Y. N.; Biswas, A. N.; Marsh, K. L.; Wagner, S.; Glöggler, S.; Bouchard, L.-S. *Anal. Chem.* **2017**, *89* (13), 7190−7194.
(229) Pei, Y.; Chen, M.; Zhong, X.; Zhao, T. Y.; Ferrer, M.-J.; Maligal-Ganesh, R. V.; Ma, T.; Zhang, B.; Qi, Z.; Zhou, L.; Bowers, C. R.; Liu, C.; Huang, W. *Nanoscale* **2020**, *12* (15), 8519−8524.
(230) McCormick, J.; Korchak, S.; Mamone, S.; Ertas, Y.; Liu, Z.; Verlinsky, L.; Wagner, S.; Gloeggler, S.; Bouchard, L. *Angew. Chem., Int. Ed.* **2018**, *57* (33), 10692.
(231) Kadlecek, S.; Shaghaghi, H.; Siddiqui, S.; Profka, H.; Pourfathi, M.; Rizi, R. *NMR Biomed.* **2014**, *27* (12), 1557−1570.
(232) Eills, J.; Alonso-Valdesueiro, J.; Salazar Marcano, D. E.; Ferreira da Silva, J.; Alom, S.; Rees, G. J.; Hanna, J. V.; Carravetta, M.; Levitt, M. H. *ChemPhysChem* **2018**, *19* (1), 40−44.
(233) Eills, J.; Hale, W.; Sharma, M.; Rossetto, M.; Levitt, M. H.; Utz, M. *J. Am. Chem. Soc.* **2019**, *141* (25), 9955−9963.
(234) Bordonali, L.; Nordin, N.; Fuhrer, E.; MacKinnon, N.; Korvink, J. G. *Lab Chip* **2019**, *19* (3), 503−512.
(235) Ostrowska, S. J.; Rana, A.; Utz, M. *ChemPhysChem* **2021**, *22* (19), 2004−2013.
(236) Eills, J.; Hale, W.; Utz, M. *Prog. Nucl. Magn. Reson. Spectrosc.* **2021**, DOI: 10.1016/j.pnmrs.2021.09.001.
(237) Suefke, M.; Lehmkuhl, S.; Liebisch, A.; Blümich, B.; Appelt, S. *Nat. Phys.* **2017**, *13* (6), 568−572.
(238) Joalland, B.; Theis, T.; Appelt, S.; Chekmenev, E. Y. *Angew. Chem., Int. Ed.* **2021**, *60* (50), 26298−26302.
(239) Gilles, H.; Monfort, Y.; Hamel, J. *Rev. Sci. Instrum.* **2003**, *74* (10), 4515−4520.
(240) Heil, W.; Gemmel, C.; Karpuk, S.; Sobolev, Y.; Tullney, K.; Allmendinger, F.; Schmidt, U.; Burghoff, M.; Kilian, W.; Knappe-Grüneberg, S.; Schnabel, A.; Seifert, F.; Trahms, L. *Ann. Phys.* **2013**, *525* (8−9), 539−549.
(241) Chen, H.-Y.; Lee, Y.; Bowen, S.; Hilty, C. *J. Magn. Reson.* **2011**, *208* (2), 204−209.
(242) Iali, W.; Rayner, P. J.; Duckett, S. B. *Sci. Adv.* **2018**, *4* (1), No. eaao6250.
(243) Richardson, P. M.; John, R. O.; Parrott, A. J.; Rayner, P. J.; Iali, W.; Nordon, A.; Halse, M. E.; Duckett, S. B. *Phys. Chem. Chem. Phys.* **2018**, *20* (41), 26362−26371.
(244) Knecht, S.; Barskiy, D. A.; Buntkowsky, G.; Ivanov, K. L. *J. Chem. Phys.* **2020**, *153* (16), 164106.

Applied Magnetic Resonance
https://doi.org/10.1007/s00723-021-01377-4

Applied
Magnetic Resonance

ORIGINAL PAPER

Gas-Phase NMR of Hyperpolarized Propane with ^{1}H-to-^{13}C Polarization Transfer by PH-INEPT

Dudari B. Burueva[1,2] · Vitaly P. Kozinenko[1,2] · Sergey V. Sviyazov[1,2] · Larisa M. Kovtunova[1,3] · Valerii I. Bukhtiyarov[2,3] · Eduard Y. Chekmenev[4,5] · Oleg G. Salnikov[1,2,3] · Kirill V. Kovtunov[1,2] · Igor V. Koptyug[1]

Received: 28 April 2021 / Revised: 16 June 2021 / Accepted: 20 June 2021
© The Author(s), under exclusive licence to Springer-Verlag GmbH Austria, part of Springer Nature 2021

Abstract

In this work we demonstrate the possibility to transfer parahydrogen-derived ^{1}H polarization to ^{13}C nuclei in the gas phase using PH-INEPT-based pulse sequences. The propane with hyperpolarized ^{1}H nuclei was produced via hydrogenation of propylene (at natural ^{13}C abundance) with parahydrogen over the heterogeneous 1 wt% Rh/TiO_2 catalyst at 7.05 T magnetic field of a NMR spectrometer. The apparent proton polarization was estimated as $1.8 \pm 0.4\%$, taking into account the polarization losses caused by spin relaxation. The optimal inter-pulse delays for both the PH-INEPT and the PH-INEPT + sequences were determined via the numerical calculations considering the full spin system of propane which includes eight protons and one ^{13}C nucleus. The application of the optimized PH-INEPT polarization transfer sequence resulted in the ^{13}C polarization values of $0.07 \pm 0.01\%$ and $0.030 \pm 0.006\%$ for the methyl group of [1-^{13}C]propane and the methylene group of [2-^{13}C]propane, respectively. The experimental dependence of the ^{13}C polarization values for [1-^{13}C]propane and [2-^{13}C]propane on the inter-pulse delay τ_1 of the PH-INEPT sequence is in a good agreement with the simulation. The resulting ^{13}C polarization using PH-INEPT + sequence is ~ 2.5 times lower than that via PH-INEPT, which is also consistent with the numerical calculations.

Kirill V. Kovtunov: Deceased.

✉ Igor V. Koptyug
koptyug@tomo.nsc.ru

[1] International Tomography Center SB RAS, 3A Institutskaya St., Novosibirsk 630090, Russia

[2] Novosibirsk State University, 2 Pirogova St., Novosibirsk 630090, Russia

[3] Boreskov Institute of Catalysis SB RAS, 5 Acad. Lavrentiev Ave., Novosibirsk 630090, Russia

[4] Wayne State University, 5101 Cass Ave, Detroit, MI 48202, USA

[5] Russian Academy of Sciences, 14 Leninskiy Prospekt, Moscow 119991, Russia

Published online: 14 July 2021

1 Introduction

One of the most promising and robust hyperpolarization (HP) techniques aiming to increase sensitivity in NMR and MRI experiments is parahydrogen-induced nuclear polarization (PHIP) [1]. It relies on the conversion of the singlet order of parahydrogen (p-H_2, the spin isomer of molecular hydrogen with a total nuclear spin $I=0$) into observable NMR signals, which can be enhanced by several orders of magnitude. In canonical PHIP, signal enhancement is achieved via p-H_2 pairwise addition to an unsaturated substrate during catalytic hydrogenation [2, 3]. To preserve the spin correlation of p-H_2-derived protons upon their incorporation into a product molecule, hydrogenation must proceed via pairwise H_2 addition, and p-H_2-derived protons must end up in magnetically inequivalent positions in order for the enhancement of the NMR signals to be observed. In theory, proton polarization achieved by PHIP can approach 100%, meaning that NMR signal enhancement values of up to 10^4–10^5 are possible in high-field NMR [4]. The PHIP effect was first demonstrated by Bowers and Weitekamp in a homogeneous hydrogenation of acrylonitrile over Wilkinson's catalyst, the catalytic cycle of which is known to proceed via pairwise addition of H_2 [2]. In contrast, it was believed that PHIP effects cannot be observed using solid heterogeneous catalysts, which activate H_2 molecule in a dissociative manner and should lead to a rapid loss of spin correlation between p-H_2-derived chemisorbed hydrogen atoms [5]. However, despite this commonly accepted wisdom, PHIP effects were successfully demonstrated in a heterogeneous hydrogenation over Wilkinson's catalyst immobilized on a solid support [6] and shortly after over Pt metal catalyst supported on alumina [7]. The latter research gave rise to a vast majority of works in the field of PHIP in heterogeneous hydrogenations (HET-PHIP). As hyperpolarization in PHIP is created in a chemical reaction, the HET-PHIP technique allows one to study heterogeneous catalytic reactions [8]. Due to a significant NMR signal enhancement, detection of short-lived intermediates of catalytic reactions becomes possible in principle, which has a potential to greatly advance understanding of the mechanisms of these reactions. Applications of HET-PHIP in catalysis are covered in the most recent reviews [8, 9], but the utility of HET-PHIP is not limited to the studies of catalytic processes. An important advantage of HET-PHIP is the possibility to produce catalyst-free hyperpolarized fluids for biomedical MRI, since heterogeneous catalysts can be easily separated from a hyperpolarized product. In this context, HP propane, which can be potentially used as a safe and inexpensive contrast agent [10] for in vivo lung MRI, is of particular interest [11, 12]. The possibility of producing HP propane on a clinical scale in the heterogeneous hydrogenation of propylene with parahydrogen over Rh/TiO_2 catalyst was recently demonstrated [13]. HP propane was also produced in the hydrogenation of cyclopropane [14, 15]. The use of cyclopropane as a substrate instead of propylene for propane production seems promising—the resulting propane has surprisingly high polarization levels, and an incomplete conversion is not an issue, since the remaining cyclopropane is nontoxic. Besides, the possibility to use diethyl ether as a promising HP contrast agent has recently been

demonstrated [16]. Diethyl ether is attractive as a contrast agent because it was used for a long time in anesthesia, which should accelerate clinical translation. Moreover, the ethyl vinyl ether precursor, which was hydrogenated to yield diethyl ether, is also used as an anesthetic.

One of the most promising strategies for PHIP applications is the transfer of proton hyperpolarization to magnetic heteronuclei, namely, ^{13}C, ^{15}N, and others [17]. These nuclei exhibit such unique features as long relaxation times (typically, in liquid phase) and background-free detection, which makes them ideal sensors for biomedical NMR and MRI applications [18, 19]. However, detection of such nuclei is rather difficult, which is the result of small values of their magnetic moments and a low natural abundance. Fortunately, transferring the proton polarization supplied by PHIP to heteronuclei provides an effective remedy for this problem. It can be performed via different approaches—by magnetic field cycling [20–27] and by radiofrequency (rf) pulse sequences [28–36]. However, to the best of our knowledge, neither approach was applied to gases so far. Here in this work, we demonstrate ^{1}H-to-^{13}C polarization transfer for propane isotopomers at natural isotopic abundance in the gas phase using PH-INEPT pulse sequence [33]. Since the gas molecules constitute a well-defined uniform physical system, ^{13}C HP gases can be advantageous for studying fundamental intramolecular and intermolecular interactions and the mechanisms of nuclear spin relaxation using ^{13}C NMR spectroscopy [37, 38].

Hyperpolarized propane was produced via HET-PHIP using a heterogeneous Rh/TiO_2 catalyst under PASADENA conditions and the ^{1}H polarization was subsequently transferred to ^{13}C nuclei. In the case of a gas-phase process implemented under continuous flow conditions, rapid relaxation of spins and escape of HP molecules from the detection zone forced us to seek the fastest way to transfer polarization. Among the variety of polarization transfer techniques, PH-INEPT-based transfer is the best option for the case of weakly coupled p-H_2-derived protons, which is the case for propane molecule in the high magnetic field of an NMR spectrometer. The total time of transfer is determined by the J-coupling between the p-H_2 derived protons and a heteronucleus, and for propane molecule possessing a ^{13}C nucleus it is on the order of tens of milliseconds. The rf-based polarization transfer occurs directly in the NMR signal detection zone, which reduces polarization losses during the time between the formation of HP molecules and their NMR detection. PH-INEPT-based transfer utilizes hard rf pulses, making it non-selective with respect to the chemical shifts of heteronuclei in the molecules under study.

2 Experimental Section

2.1 Catalyst Preparation and Characterization

The Rh/TiO_2 catalyst used in this work was prepared by wet impregnation of titanium dioxide with a rhodium nitrate solution [39]. Titanium dioxide TiO_2 (HombifineN, 100% anatase, BET specific surface area $S_{BET} = 360$ m^2 g^{-1}) was calcined at 550 °C for 2 h, which resulted in a decrease of S_{BET} to 109 m^2 g^{-1}. The required amount of rhodium(III) nitrate hydrate (Sigma Aldrich, 83750; Rh content ~ 36 wt%)

was dissolved in distilled water, and this aqueous solution was used to impregnate titanium dioxide for 1 h at room temperature. Solvent excess was evaporated at a reduced pressure. The sample was dried at 120 °C for 3 h and then calcined at 400 °C for 4 h followed by reduction in H_2 flow (75 cm^3 min^{-1}, 1 atm) at 330 °C for 3 h. The catalyst contained ~ 1% Rh by weight.

2.2 Hydrogenation Experiments

Propylene (purity > 99.6%; Chistye Gazy Plus Ltd, Russia) and ultra-high-purity hydrogen (purity > 99.999%; AlfaGas Ltd, Russia) gases were used without additional purification. Hydrogen gas was enriched with the para isomer using a Bruker BPHG-90 parahydrogen generator operating at 45 K, resulting in 83% p-H_2 enrichment. The volumetric feed flow rates of hydrogen and propylene were regulated using Bronkhorst mass flow controllers; hydrogen gas flow rate was set at 180 ± 2 ml_n min^{-1}; propylene gas flow rate was set at 45 ± 1 ml_n min^{-1} to achieve the propylene:p-H_2 enriched hydrogen gas ratio of 1:4. The gases were mixed in a 500 ml stainless steel double-end cylinder and the resulting mixture was supplied to the catalyst (20 mg) placed at the bottom of a 10 mm o.d. NMR tube through a 1/16 in. o.d. (1/32 in. i.d.) PTFE capillary. In the NMR tube, the gas mixture was flowing from the bottom to the top and then to the vent through a 1/8 in. o.d. PTFE tubing connected with the NMR tube through a wye-type fitting. NMR tube with the catalyst was heated up to 130 °C using Bruker variable temperature unit. All hydrogenation experiments were performed at 2 bar; the reaction pressure was controlled using a Swagelok membrane back pressure regulator.

Hydrogenation was performed in the 7.05 T magnetic field of a 300 MHz Bruker AV 300 NMR spectrometer (PASADENA procedure [2]). A 10 mm BBO 300 MHz Bruker probe head was used. ^{1}H PASADENA NMR spectra were acquired using a $\pi/4$ rf pulse, and the spectra of a reaction mixture in thermal equilibrium were acquired using a $\pi/2$ rf pulse.

2.3 Calculations

2.3.1 Evaluation of Conversion

Propylene conversion was calculated as the molar ratio of the reaction product—propane—to the sum of propane and unreacted propylene. Catalytic reactor effluent gas was collected in an empty 10 mm o.d. NMR tube to evaluate propylene conversion over Rh/TiO_2. Conversion values were evaluated from ^{1}H NMR spectra acquired in thermal equilibrium after a complete relaxation of hyperpolarization.

2.3.2 Evaluation of Proton Polarization Losses Caused by Relaxation

To evaluate proton polarization losses caused by nuclear spin relaxation, the longitudinal relaxation times (T_1) were measured using the standard inversion-recovery pulse sequence; inverse gated ^{1}H decoupling was applied during ^{13}C NMR spectra

acquisition. It was found that proton T_1 relaxation times for the CH_2 and CH_3 groups of propane are 350 ± 20 and 345 ± 20 ms, respectively, under the reaction conditions (130 °C; 2 bar; propane:n-H_2 ratio of 1:3). Then, the time that propane molecules spent on the way from the catalyst, on the surface of which propane is formed, to the end of the detection coil region was estimated. The geometry of the NMR tube and the detection coil were described in detail previously [40, 41]. The volumetric gas flow rate u was recalculated to account for the difference in the actual and normal conditions (actual conditions: 130 °C, 2 bar; 0.25 is the mole fraction of propane at 100% conversion):

$$u = \frac{45}{60} \cdot \frac{1}{2} \cdot \frac{1}{0.25} \cdot \frac{403.15}{273.15} = 2.21 \text{ ml s}^{-1}.$$

Considering the flow rate of 2.21 ml s^{-1}, the residence time (τ_1) of propane molecules at the bottom of NMR tube below the sensitive zone with the volume V_1 estimated as 0.3 ml can be evaluated as

$$\tau_1 = \frac{V_1}{u} = \frac{0.30}{2.21} = 0.14\, s.$$

Polarization losses can be estimated based on the ratio of the averaged polarization of the molecules in the detection coil region (P_2) to the initial polarization (P_0) using the formula [41]:

$$\frac{P_2}{P_0} = \frac{uT_1}{V_2}\left(1 - e^{-\frac{V_2}{uT_1}}\right) \cdot e^{-\frac{\tau_1}{T_1}}$$

where V_2 is the volume of the sensitive region of the detection coil estimated as 1.2 ml. The ratio $\frac{P_2}{P_0}$ is ~ 0.34 for both propane groups under these conditions.

2.3.3 Evaluation of the Uncertainty in the ^{13}C T_1 Measurements

The uncertainty in the ^{13}C T_1 measurements was estimated from the uncertainty in the integration. For different delays after an inversion pulse (τ), the signal-to-noise ratio (SNR) for both methyl and methylene signals in ^{13}C spectra was determined and the relative standard deviation (RSD) value for the signal integrals was calculated as $\text{RSD} = \frac{86}{\text{SNR}}$ [42]. Then, the obtained relative standard deviations of the integrals were used in the experimental data approximation.

2.3.4 Reproducibility Analysis

To evaluate the reproducibility of the results, PHIP experiments were independently repeated three times, each time with a new catalyst loading. The standard deviation values were found to be 9% for conversion and 20% for proton and carbon polarization levels.

3 Results and Discussion

It is known that rhodium metal catalysts supported on titania exhibit high activity in pairwise parahydrogen addition providing higher polarization levels in HET-PHIP among other supported metal catalysts [43]. Here in this work, we used a 1 wt% Rh/TiO_2 catalyst; its preparation procedure is described in the Experimental Section. Propylene hydrogenation was performed in the high magnetic field of the NMR spectrometer under PASADENA experimental conditions [2]; the catalyst was placed at the bottom of the NMR tube so that it was located below the sensitive region of the detection coil. To ensure high catalytic activity, the NMR tube with the catalyst was heated up to 130 °C and hydrogenation reaction was performed at 2 bar. The propylene:parahydrogen-enriched H_2 ratio was set to 1:4 using mass flow controllers and the total flow rate was set at 225 ml_n min^{-1}. The mixture of gases was supplied directly to the catalyst. The PASADENA ^1H NMR spectra of the reaction mixture containing propane produced in the reaction, the unreacted propylene, and H_2 were acquired in a steady-state regime using a $\pi/4$ rf pulse. To evaluate propylene conversion, the catalytic reactor effluent gas was collected in an empty 10 mm o.d. NMR tube and ^1H NMR spectra were acquired with a $\pi/2$ rf pulse under thermal equilibrium achieved after a complete relaxation of hyperpolarization. It was found that the Rh/TiO_2 catalyst exhibits high activity in propylene hydrogenation under these reaction conditions—the conversion reached $91 \pm 8\%$ (Fig. 1). Details of the conversion evaluation are given in the Experimental Section.

In the ^1H NMR spectrum of the flowing gas (Fig. 1, red spectrum), the characteristic antiphase PHIP patterns were observed. The absorptive and the emissive parts of each PASADENA antiphase multiplet were integrated independently, and their co-added absolute values were compared with the integral (normalized by the number of contributing protons) of the corresponding multiplet at thermal equilibrium to evaluate the experimentally observed signal enhancement values (SE). Under these conditions, the Rh/TiO_2 catalyst demonstrated moderate SE levels of 33 and 52 for CH_2 and CH_3 groups of propane, respectively. To estimate the polarization levels, one needs to compare the experimentally observed SE to a maximum possible SE_{theor} in such experiment. Under our experimental conditions, the maximum ^1H signal enhancement in a PASADENA experiment numerically evaluates to

$$SE_{theor} = \frac{1}{2} \cdot \frac{4x_p - 1}{3} \cdot \frac{2\gamma\hbar B_0}{kT} = \frac{4x_p - 1}{3} \cdot 27990 \quad (1)$$

at $T = 403.15$ K, $B_0 = 7.05$ T, $\pi/4$ detection pulse for PASADENA spectrum and $\pi/2$ detection pulse for the ^1H spectrum in thermal equilibrium, where x_p is the fraction of p-H_2 in the hydrogen gas [4]. This is valid for an AX spin system, while for a larger number of magnetic nuclei in a product molecule, the maximum ^1H signal enhancement in a PASADENA experiment is reduced due to the partial cancelation of individual components of the antiphase multiplet upon further splitting by the couplings with extra protons. In the case of an A_2X_6 spin system of propane with six equivalent protons in two methyl groups and two equivalent protons in the methylene group, the maximum ^1H signal enhancement that can be produced in a PASADENA

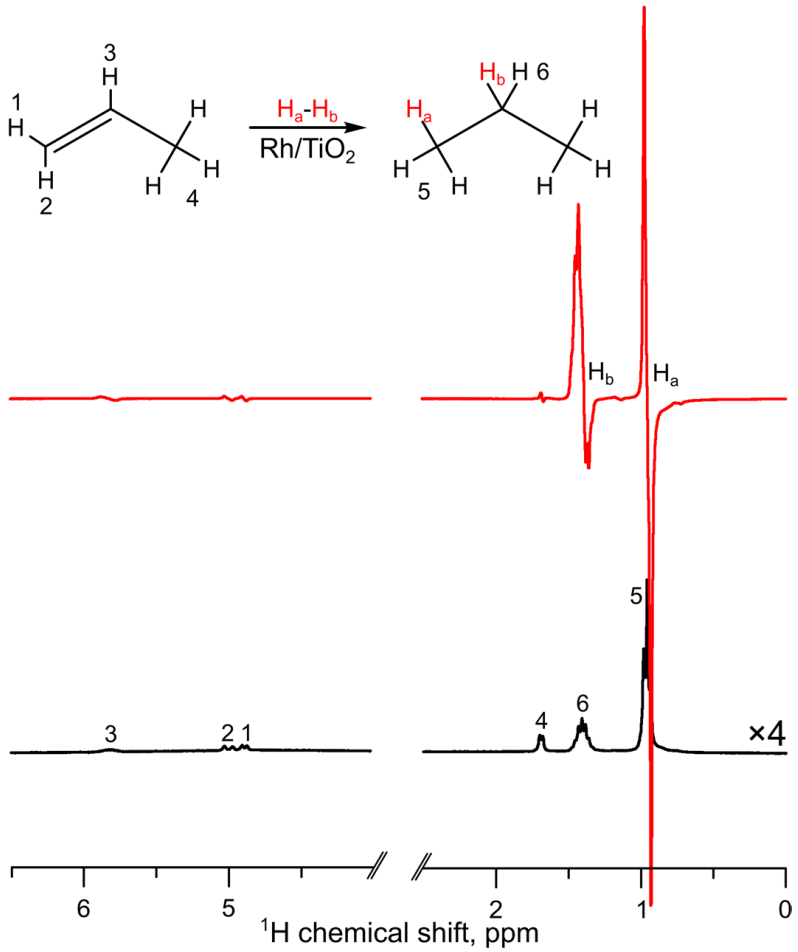

Fig. 1 Top: the reaction scheme of pairwise addition of p-H_2 to propylene over Rh/TiO_2 catalyst. Bottom: ^{1}H NMR spectrum acquired during propylene hydrogenation with p-H_2 over Rh/TiO_2 catalyst, while the gas was flowing with the flow rate of 225 ml_n min^{-1} (red spectrum), and ^{1}H NMR spectrum of the catalytic reactor effluent gas collected in an empty 10 mm o.d. NMR tube (black spectrum, intensity is multiplied by a factor of 4). The ^{1}H PASADENA spectrum was acquired using a $\pi/4$ rf pulse; the corresponding ^{1}H spectrum in thermal equilibrium was acquired using a $\pi/2$ rf pulse (Color figure online)

experiment reduces differently for the CH_2 and CH_3 groups. The pattern of line intensities for the CH_2 group coupled to six equivalent protons in a ^{1}H NMR spectrum is (1,6,15,20,15,6,1) for thermally polarized propane and $(1,4,5,0,-5,-4,-1)$ for the PASADENA experiment [44]. In the case of a CH_3 group coupled to two equivalent protons, the pattern of line intensities is (1,2,1) under thermal equilibrium and $(1,0,-1)$ for the PASADENA experiment. Therefore, the maximum possible ^{1}H signal enhancement is reduced by factors of 3.2 and 2 for the CH_2 and the CH_3 group, respectively (both the emissive and the absorptive parts of the antiphase multiplet are taken into account). Moreover, it should be noted that the maximum possible ^{1}H SE_{theor} in a PASADENA experiment significantly depends on the line broadening because of a partial signal cancellation of the overlapping absorption and emission parts of the antiphase multiplet. The simulation of the experimental ^{1}H

PASADENA spectrum was performed to determine the width of individual lines in the experimental spectra. The maximum possible ^{1}H SE_{theor} value was determined from the simulated spectra of both hyperpolarized and thermally polarized propane with the corresponding line width. At $x_p = 83\%$ parahydrogen enrichment level, the maximum ^{1}H signal enhancement for the CH_2 and the CH_3 groups of propane is 5440 and 8500, respectively. Therefore, the estimated proton polarization was $0.6 \pm 0.1\%$ for both groups under these reaction conditions.

The ^{1}H polarization levels estimated above are the lower estimates, since the relaxation losses were not taken into account. To evaluate polarization losses caused by nuclear spin relaxation, the longitudinal relaxation times for both CH_2 and CH_3 groups of propane were measured under reaction conditions (130 °C, 2 bar). To that end, propane and normal hydrogen (n-H_2) gases were supplied with a 1:3 ratio (as if propylene completely converted to propane; the propane:n-H_2 ratio was set using mass flow controllers) to the bottom of an empty 10 mm o.d. NMR tube. The NMR tube was heated up to 130 °C, and the ^{1}H T_1 measurements were performed at 2 bar for a static gas. It was found that proton T_1 relaxation times for the CH_2 and CH_3 groups of propane are 350 ± 20 and 345 ± 20 ms, respectively. The estimates provided in the Experimental Section demonstrate that only one-third of the initial polarization is observed and that the initial ^{1}H polarization levels are thus ~ $1.8 \pm 0.4\%$.

To examine the possibility of polarization transfer from ^{1}H to ^{13}C nuclei in the gas phase, the application of an rf pulse sequence seems the best choice, since longitudinal T_1 relaxation times for both ^{1}H and ^{13}C nuclei of propane in the gas phase are short. This makes the alternative approach based on magnetic field cycling ineffective in this case, because it requires multi-second-long sample manipulation time period, during which the produced ^{13}C hyperpolarized state would decay. The proton T_1 relaxation time for propane in propane/H_2 mixtures increases nearly linearly with propane mole fraction and pressure [45, 46], indicating that propane T_1 relaxation in the gas phase is mostly governed by the spin-rotation interaction [47]. As stated above, the T_1 times for propane protons under reaction conditions are ~ 350 ms. For ^{13}C nuclei in propane, we found that ^{13}C T_1 relaxation times for the methylene ($^{13}CH_2$) and methyl ($^{13}CH_3$) groups are 140 ± 10 and 149 ± 8 ms for propane mixed with hydrogen gas in the 1:3 molar ratio at room temperature, and even shorter values can be expected at 130 °C [37]. The T_1 relaxation times being shorter for heteronuclei compared to ^{1}H nuclei is a common situation in the NMR of gases [48, 49]; it is attributed to the predominance of the spin-rotation relaxation mechanism for molecular gases and vapors and is associated with the properties of the spin-rotation tensor for a specific nucleus.

It is important to note that propylene gas used in the hydrogenation experiments was not isotopically labeled. Taking into account the natural abundance of ^{13}C nuclei, it is assumed that the mole fraction of [1-^{13}C]propane is 2.2% (positions #1 and #3 are identical in thermal equilibrium, Fig. 2) and the fraction of [2-^{13}C] propane is 1.1%. The molecules containing two ^{13}C nuclei were not considered due to vanishingly low probabilities. Therefore, ^{13}C NMR spectrum of propane in thermal equilibrium is the superposition of the signals from two different isotopomers—[1-^{13}C]propane and [2-^{13}C]propane (see ^{13}C spectra in Fig. 2). It can be seen from

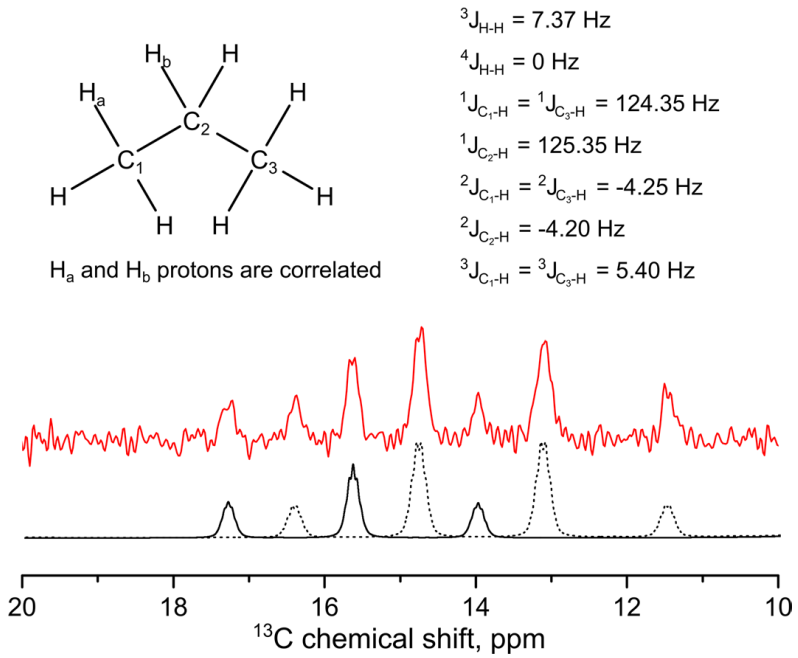

Fig. 2 Top: propane J-couplings. Most of the coupling constants were taken from the literature [50]. The corrected $^{2}J_{C_2-H}$ and $^{3}J_{C_1-H}$ coupling constant values were obtained from the experimental ^{13}C NMR spectrum of thermally polarized propane (saturated solution in acetone-d_6). Bottom: an experimental ^{13}C NMR spectrum of thermally polarized propane in the gas phase (red line). Simulated spectra of [2-^{13}C] propane (solid black line) and [1-^{13}C]propane (dashed black line) are shown below (Color figure online)

Fig. 2 that the experimental and simulated ^{13}C NMR spectra of propane gas in thermal equilibrium are in a good agreement. However, the incorporation of p-H_2-derived protons in a molecule (denoted as H_a and H_b in Fig. 2) makes carbons #1 and #3 non-identical, so in the case of PHIP, three different isotopomers—[1-^{13}C]propane, [2-^{13}C]propane and [3-^{13}C]propane—should be considered.

The PH-INEPT pulse sequence was chosen for the experiments aiming to transfer the parahydrogen-derived polarization from ^{1}H to ^{13}C nuclei in the gas phase as one of the most robust and effective approaches. However, the performance of INEPT-based polarization transfer schemes strongly depends on the precise choice of the inter-pulse delays. The optimal delay values are determined by the network of scalar couplings in the molecule and in some simple cases they can be derived analytically [33], but numerical calculations are more appropriate when analyzing complex molecules with a large number of spins. Here, we simulated the spectra expected after the application of PH-INEPT and PH-INEPT + sequences utilizing the approach described earlier [51]. We have considered the full spin system of propane, including eight protons and one ^{13}C nucleus. In the initial spin density matrix, one proton from the CH_3 group and one proton from the CH_2 group are in the singlet spin state, while other nuclei are not polarized. To take into account the rapid decay of coherences occurring in the course of the reaction, the non-diagonal terms of the initial spin density matrix were omitted, which is a common procedure. Thus, the initial spin order corresponds to $\widehat{I}_{1z}\widehat{I}_{2z}$ operator (neglecting the unity matrix), where $\widehat{I}_{1,2}$ are spin operators of the p-H_2-derived protons in the propane molecule.

This density matrix was then subjected to a set of rotations and periods of free evolution under Zeeman and J-coupling interactions corresponding to PH-INEPT and PH-INEPT + pulse sequences. The schemes of corresponding experiments are depicted in Figs. 3a and 5a. In the case of PH-INEPT, we assessed the efficiency of polarization transfer by calculating the expectation value for transverse magnetization of heteronucleus being antiphase with respect to the p-H_2-derived protons. To do this, the trace of the product of the final density matrix and the sum of antiphase product operators $2\widehat{I}_{1z}\widehat{S}_y$ and $2\widehat{I}_{2z}\widehat{S}_y$ was taken, where $\widehat{S}$ is the spin operator of ^{13}C nucleus. It should be noted that, while in the experimental NMR spectra exhibiting antiphase signals their broadening causes partial overlap of the signals of opposite sign and thus a reduction in signal intensity, these effects are not present in the theoretical treatment of the performance of pulse sequences which evaluates spin density matrix elements. In the PH-INEPT + sequence, additional refocusing allows one to produce net magnetization of a heteronucleus. Thus, to determine the efficiency of transfer by PH-INEPT + we calculated the trace of the product of the final density matrix and the $\widehat{S}_x$ operator. The fact that ^{1}H polarization levels achieved in the HET-PHIP experiment are not 100% is immaterial and was not taken into account in the polarization transfer efficiency calculations.

The PH-INEPT sequence has only one parameter to optimize: the inter-pulse delay τ_1; the results of numerical simulation of the ^{13}C polarization achieved by PH-INEPT as a function of delay τ_1 are presented in Fig. 3b for three different propane isotopomers. It is found that for both [1-^{13}C]propane and [2-^{13}C]propane the optimal τ_1 delay is 14.0 ms; at this delay time the efficiency of p-H_2-derived polarization transfer to ^{13}C nucleus in [1-^{13}C]propane and [2-^{13}C]propane isotopomers using PH-INEPT is estimated as ~ 14%. In the case of [3-^{13}C]propane the efficiency of the polarization transfer using PH-INEPT is lower (green spectrum in Fig. 3c) due to small J-coupling constants between the p-H_2-derived protons and the ^{13}C nucleus (Fig. 2). It should be noted that PH-INEPT pulse sequence does not transfer any proton magnetization of thermally polarized propane isotopomers [33]; thus, only the molecules with p-H_2-derived protons contribute to ^{13}C PH-INEPT spectrum provided that the thermal equilibrium ^{13}C NMR signal can be neglected. The efficiency of the PH-INEPT sequence primarily depends on the value of the mutual spin–spin coupling constant of the two p-H_2-derived protons ($H_a - H_b$) and their couplings to the ^{13}C nucleus ($H_{a(b)}$–^{13}C). In propane these couplings are large; however, coupling to additional nuclei in the 9-spin system of propane isotopomers causes a significant signal reduction.

The PH-INEPT pulse sequence with a 14.0 ms delay τ_1 was applied, while propylene:parahydrogen-enriched H_2 gas mixture was supplied to the catalyst and ^{1}H HP propane was constantly formed at the bottom of the NMR tube and was then flowing upward in the NMR tube through the sensitive region of the detection coil. An experimental ^{13}C NMR spectrum acquired after ^{13}C hyperpolarization of propane isotopomers using PH-INEPT pulse sequence is presented in Fig. 3c (red spectrum). Two multiplets are observed in the spectrum—a quartet with a (−1, −1,1,1) lines pattern at 13.87 ppm attributed to the methyl group of [1-^{13}C] propane, and a triplet with a (−1,0,1) pattern at 15.26 ppm attributed to the methylene group of [2-^{13}C]propane. Moreover, the ^{13}C NMR spectra were simulated for

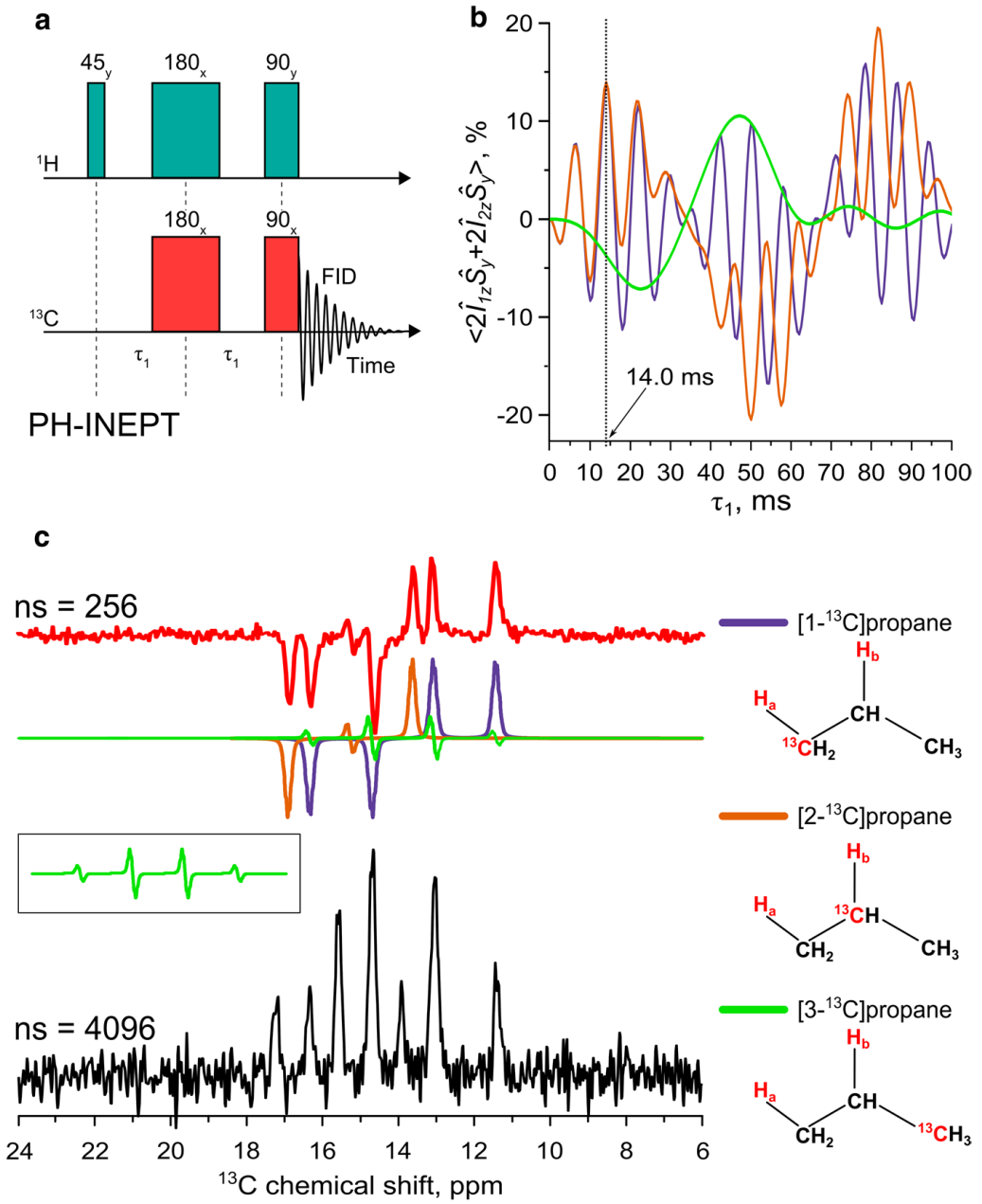

Fig. 3 **a** PH-INEPT pulse sequence used to transfer polarization from ^{1}H-to-^{13}C nuclei in propane. **b** Numerical simulation of the ^{13}C polarization transferred by PH-INEPT for three different propane isotopomers as a function of delay τ_1. **c** Experimental ^{13}C NMR spectrum acquired after ^{13}C hyperpolarization of propane isotopomers using PH-INEPT pulse sequence (red spectrum; the optimal delay τ_1 of 14.0 ms was used; 256 accumulations) during propylene hydrogenation with p-H_2 and simulated spectra presented separately for the three different isotopomers (the scaled spectrum for [3-^{13}C]propane is presented in the inset). The experimental ^{13}C NMR spectrum of pure thermally polarized propane (black spectrum; 4096 accumulations) is presented below

all three propane isotopomers, demonstrating a good agreement with the experiment (Fig. 3c). It is interesting to note that for ^{13}C HP [3-^{13}C]propane all lines of the quartet are antiphase (green spectrum in Fig. 3c), meaning that [3-^{13}C]propane

molecules do not contribute to the line integrals used in the evaluation of ^{13}C NMR signal enhancement.

To evaluate ^{13}C SE values, a ^{13}C NMR spectrum of pure propane in thermal equilibrium and 1 atm was acquired. ^{13}C SE values were calculated as the ratio of the sum of absolute integrals of the polarized multiplets to the integral in ^{13}C spectrum at thermal equilibrium, with the difference in the number of signal accumulations, the total pressure, and the gas mixture composition taken into account. It was found that the experimentally observed signal enhancement values are 29 and 13 for the methyl group of [1-^{13}C]propane and the methylene group of [2-^{13}C]propane, respectively. The effect of the splitting of an antiphase multiplet due to the coupling to several equivalent nuclei should be taken into account for ^{13}C polarization calculations, similar to the ^{1}H case described above. The pattern of line intensities for the ^{13}C nucleus coupled to three equivalent protons in the methyl group is $(-1,-1,1,1)$ in the case of hyperpolarization and (1,3,3,1) in thermal equilibrium. The ^{13}C nucleus coupled to two equivalent protons in the methylene group gives a $(-1,0,1)$ pattern in the case of hyperpolarization and a (1,2,1) pattern in thermal equilibrium. This means that the maximum achievable ^{13}C signal enhancement is reduced by a factor of 2 for both $^{13}CH_2$ and $^{13}CH_3$ groups. The maximum possible ^{13}C signal enhancement under PASADENA condition is ~ 3.977 times higher than in Eq. (1) due to the difference in the gyromagnetic ratios for ^{13}C and ^{1}H nuclei, and taking into account the effect of signal splitting the maximum ^{13}C SE_{theor} is 43030 at $x_p = 83\%$ parahydrogen enrichment level. Therefore, ^{13}C polarization is estimated as $0.07 \pm 0.01\%$ and $0.030 \pm 0.006\%$ for the methyl group of [1-^{13}C]propane and the methylene group of [2-^{13}C]propane, respectively.

The τ_1 delays in the experiments with PH-INEPT pulse sequence were also varied. Experimental ^{13}C NMR spectra acquired after ^{1}H-to-^{13}C hyperpolarization transfer in propane isotopomers using the PH-INEPT pulse sequence with different τ_1 delays are shown in Fig. 4b along with the corresponding simulated spectra presented separately for three different isotopomers. The experimental dependence of ^{13}C polarization for the methyl group of [1-^{13}C]propane (purple circles in Fig. 4a) and for the methylene group of [2-^{13}C]propane (orange diamonds in Fig. 4a) on the inter-pulse delay τ_1 is well fitted by the numerically simulated function; the positions of all extremes are consistent with the calculations. The significantly lower experimentally observed ^{13}C polarization compared to the calculated ones are primarily due to the moderate initial proton polarization. The second reason why the experimental ^{13}C polarization values are reduced is the ^{13}C spin relaxation, and possibly not so much T_1 as T_2 during the duration of the sequence. As can be seen, the oscillations in the τ_1-dependence are strongly damped for the experimentally observed ^{13}C polarization of the methylene group (the ^{13}C polarization for $^{13}CH_2$ group at $\tau_1 = 23.0$ ms is close to zero, Fig. 4a). This is most likely associated with a lower value of T_2 for the methylene ($^{13}CH_2$) group compared to methyl ($^{13}CH_3$), since ^{13}C T_1 relaxation times for methylene and methyl groups are similar (140 ± 10 and 149 ± 8 ms). The experimental dependence of ^{13}C polarization on τ_1 also demonstrates that the precise calculations for PH-INEPT pulse sequence are needed—even a 1 ms variation in the τ_1 delay is relevant.

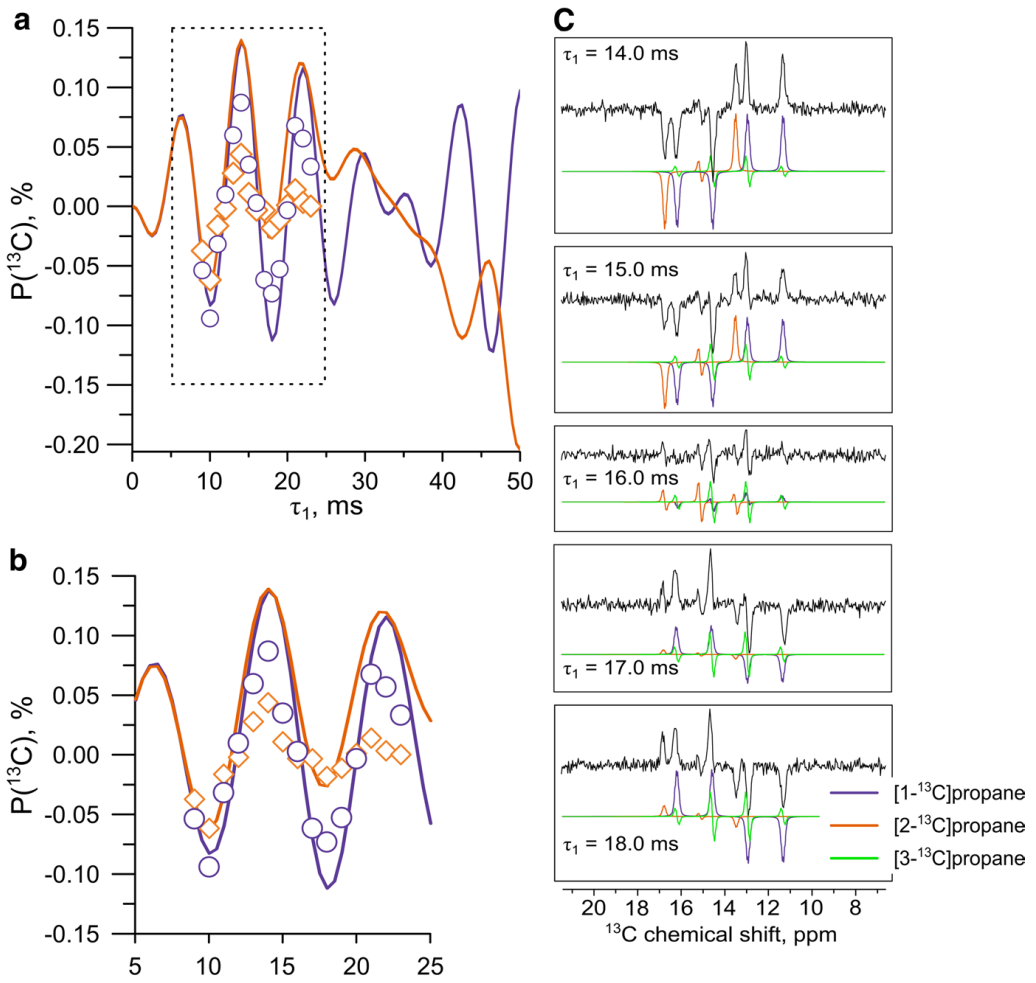

Fig. 4 **a** Experimental dependence of ^{13}C polarization for [1-^{13}C]propane and [2-^{13}C]propane (purple circles and orange diamonds, respectively) on delay τ_1 in the 9.0–23.0 ms range and the results of corresponding theoretical calculations (solid lines). Part of the graph enclosed in dashed rectangle is shown expanded in **b** to better demonstrate that experimental extremes and polarization sign changes are in a good agreement with the simulation (rescaled). **c** Experimental ^{13}C NMR spectra acquired after ^{13}C hyperpolarization of propane isotopomers using the PH-INEPT pulse sequence with different τ_1 delays, and the corresponding simulated spectra presented separately for the three different isotopomers

In addition, the PH-INEPT + pulse sequence was applied under the same experimental conditions. The antiphase signals of the PH-INEPT sequence can be refocused by employing the additional 180° pulses with a τ_2 delay on both sides (Fig. 5a). Then, the in-phase ^{13}C NMR signals obtained with PH-INEPT + can be proton-decoupled. Numerical simulations of the efficiency of the PH-INEPT + pulse sequence were performed for all propane isotopomers. The τ_1 delay was set to 14.0 ms; the ^{13}C polarization provided by PH-INEPT + for three different propane isotopomers as a function of delay τ_2 is presented in Fig. 5b. It was found that for $\tau_2 = 3.0$ ms, [1-^{13}C]propane and [2-^{13}C]propane demonstrate the polarization of opposite signs. An experimental ^{13}C{^{1}H} NMR spectrum acquired after the ^{1}H-to-^{13}C hyperpolarization transfer in the propane

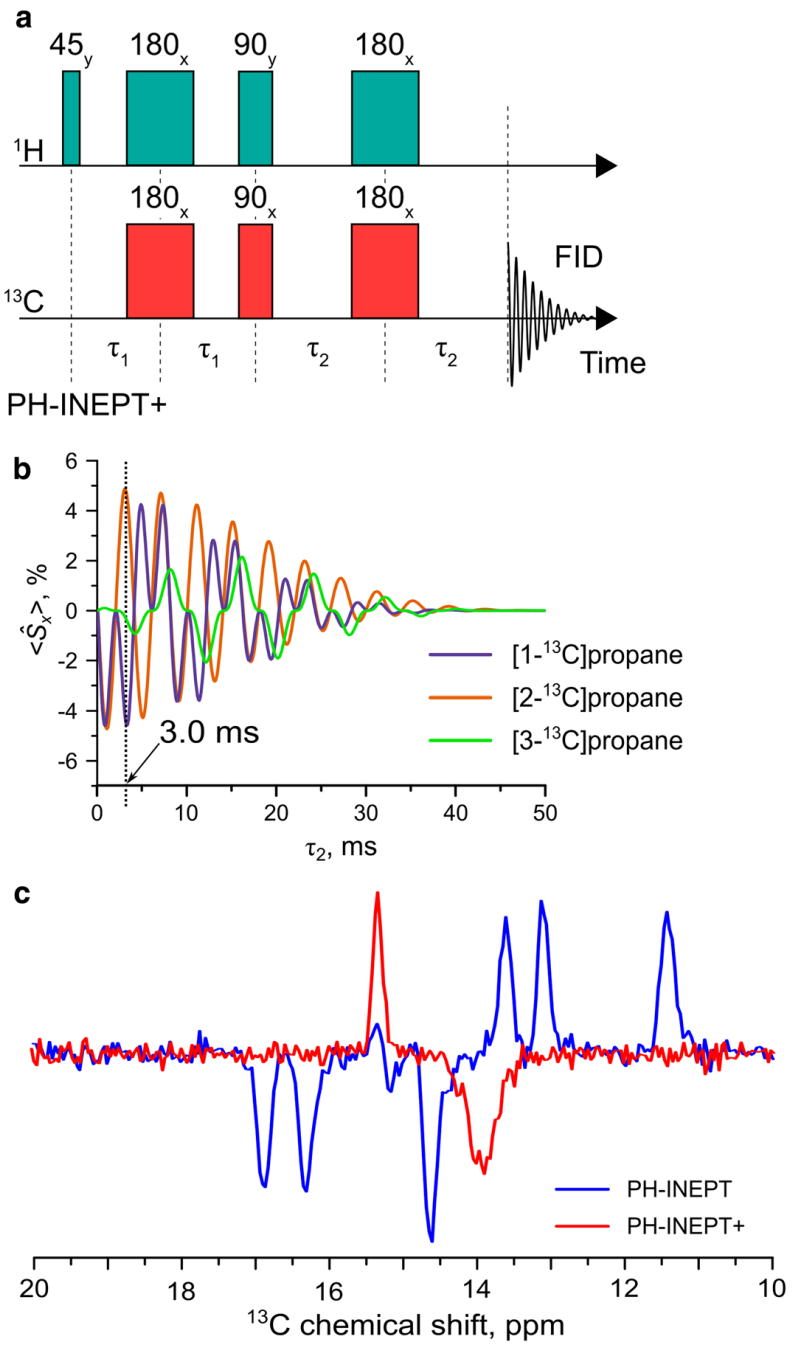

Fig. 5 **a** PH-INEPT + pulse sequence used to transfer polarization from ^{1}H to ^{13}C in propane. **b** Numerical simulation of the ^{13}C polarization as a function of delay τ_2 presented for all three propane isotopomers. For numerical calculation delay τ_1 was set at 14.0 ms as the optimal delay for PH-INEPT. **c** Experimental ^{13}C NMR spectrum acquired after the ^{1}H-to-^{13}C hyperpolarization transfer in the propane isotopomers using the PH-INEPT + pulse sequence (red spectrum; the optimal delay τ_1 of 14.0 ms and τ_2 of 3.0 ms was used; proton decoupling was used during ^{13}C signal acquisition) during propylene hydrogenation with p-H_2 and the spectrum of ^{13}C hyperpolarized propane via PH-INEPT (blue spectrum; τ_1 of 14.0 ms was used). Both spectra are presented on the same vertical scale

isotopomers using PH-INEPT + pulse sequence ($\tau_1 = 14.0$ ms, $\tau_2 = 3.0$ ms) is presented in Fig. 5c (red spectrum). This spectrum exhibits only two signals of opposite signs at the chemical shifts of the corresponding multiplets, as expected. The ^{13}C NMR signal enhancement is 13 and 7 for the methyl group of [1-^{13}C]propane and the methylene group of [2-^{13}C]propane, respectively. These SE values correspond to the ^{13}C polarization of 0.029 and 0.015%, which are about 2.5 times lower compared to those obtained with PH-INEPT; this observation is also consistent with the numerical calculations (polarization efficiency of 14% and 5% in the case of the PH-INEPT and the PH-INEPT + sequence, respectively). The fact that theoretically calculated efficiency of PH-INEPT + sequence is measurably lower than that of PH-INEPT indicates that additional protons in the spin system interfere strongly with the complete refocusing of ^{13}C antiphase magnetization by the PH-INEPT + sequence. Moreover, the refocusing step requires an additional delay of $2\tau_2 = 6.0$ ms, which in the experimental spectra leads to further polarization losses due to rapid T_2 relaxation. All these effects surpass the positive effect of alleviated partial cancellation for antiphase signals, thus demonstrating the suboptimal performance of PH-INEPT + in the case of propane.

4 Conclusions

Here, in this work, we examined the possibility of the polarization transfer from ^{1}H to ^{13}C nuclei in the gas phase using PH-INEPT-based sequences. Proton hyperpolarization was produced via parahydrogen-induced polarization method using a heterogeneous hydrogenation catalyst. Natural abundance propylene was hydrogenated with p-H_2 over 1 wt% Rh/TiO_2 catalyst under PASADENA experimental conditions. The apparent proton polarization was estimated as 1.8 ± 0.4%, taking into account the polarization losses caused by spin relaxation. PH-INEPT and PH-INEPT + pulse sequences were examined in this work. The optimal interpulse delays for both PH-INEPT and PH-INEPT + sequences were determined via numerical calculations for the full spin system of propane that includes eight protons and one ^{13}C nucleus. All three propane ^{13}C isotopomers were considered. The application of an optimized PH-INEPT polarization transfer sequence resulted in the ^{13}C polarization values of 0.07 ± 0.01% and 0.030 ± 0.006% for the methyl group of [1-^{13}C]propane and the methylene group of [2-^{13}C]propane, respectively. The experimental dependence of ^{13}C polarization values for [1-^{13}C]propane and [2-^{13}C]propane on the PH-INEPT delay τ_1 is in a good agreement with the simulation. The resulting ^{13}C polarization using PH-INEPT + sequence is ~ 2.5 times lower, which is also consistent with the numerical calculations.

Acknowledgements VPK thanks Prof. Konstantin L. Ivanov, deceased on March 5, 2021 at the age of 44, for the expert guidance in his mastering the spin dynamics calculations. All authors acknowledge Prof. Konstantin L. Ivanov and Dr. Kirill V. Kovtunov who initiated this work and made a major contribution to the field of hyperpolarized NMR.

Author Contributions Conceptualization: KVK; supervision: OGS, KVK, IVK, EYC; resources—catalyst: LMK, VIB; investigation—DBB, VPK, OGS, SVS; writing–original draft preparation: DBB, VPK, SVS; writing–review and editing: OGS, IVK, EYC. The manuscript was reviewed by all authors.

Funding The HET-PHIP experiments performed by DBB, SVS, OGS, and IVK were funded by Russian Foundation for Basic Research (RFBR; Grants no. 19-29-10003 and 19-33-60045). The spin dynamics calculation performed by VPK was supported by RFBR grant no. 19-29-10028. The catalyst preparation performed by LMK was supported by the Ministry of Science and Higher Education of the Russian Federation (project # AAAA-A21-121011390011-4). EYC thanks the following for funding support: DOD CDMRP W81XWH15-1-0271 and W81XWH-20-10576, National Heart, Lung, and Blood Institute 1 R21 HL154032-01 and NSF CHE-1904780.

Declarations

Conflict of Interest EYC declares a stake of ownership in XeUS Technologies LTD.

References

1. R.A. Green, R.W. Adams, S.B. Duckett, R.E. Mewis, D.C. Williamson, G.G.R. Green, Prog. Nucl. Magn. Reson. Spectrosc. **67**, 1 (2012)
2. C.R. Bowers, D.P. Weitekamp, J. Am. Chem. Soc. **109**, 5541 (1987)
3. M.G. Pravica, D.P. Weitekamp, Chem. Phys. Lett. **145**, 255 (1988)
4. C.R. Bowers, in *Encycl. Magn. Reson.*, ed. by R.K. Harris, R. Wasylishen (John Wiley, Chichester, 2007), p. 750. https://doi.org/10.1002/9780470034590.emrstm0489
5. A. Eichhorn, A. Koch, J. Bargon, J. Mol. Catal. A Chem. **174**, 293 (2001)
6. L.-S. Bouchard, S.R. Burt, M.S. Anwar, K.V. Kovtunov, I.V. Koptyug, A. Pines, Science **319**, 442 (2008)
7. K.V. Kovtunov, I.E. Beck, V.I. Bukhtiyarov, I.V. Koptyug, Angew. Chem. Int. Ed. **47**, 1492 (2008)
8. K.V. Kovtunov, O.G. Salnikov, I.V. Skovpin, N.V. Chukanov, D.B. Burueva, I.V. Koptyug, Pure Appl. Chem. **92**, 1029 (2020)
9. E.V. Pokochueva, D.B. Burueva, O.G. Salnikov, I.V. Koptyug, ChemPhysChem (2021). https://doi.org/10.1002/cphc.202100153
10. A. Kopanski, F. Hane, T. Li, M. Albert, in *25th ISMRM Conf.* (Honolulu, HI, USA, 2017), p. 2162
11. K.V. Kovtunov, I.V. Koptyug, M. Fekete, S.B. Duckett, T. Theis, B. Joalland, E.Y. Chekmenev, Angew. Chem. Int. Ed. **59**, 17788 (2020)
12. K.V. Kovtunov, M.L. Truong, D.A. Barskiy, I.V. Koptyug, A.M. Coffey, K.W. Waddell, E.Y. Chekmenev, Chem. A Eur. J. **20**, 14629 (2014)
13. O.G. Salnikov, P. Nikolaou, N.M. Ariyasingha, K.V. Kovtunov, I.V. Koptyug, E.Y. Chekmenev, Anal. Chem. **91**, 4741 (2019)
14. O.G. Salnikov, K.V. Kovtunov, P. Nikolaou, L.M. Kovtunova, V.I. Bukhtiyarov, I.V. Koptyug, E.Y. Chekmenev, ChemPhysChem **19**, 2621 (2018)
15. Y. Du, R. Behera, R.V. Maligal-Ganesh, M. Chen, E.Y. Chekmenev, W. Huang, C.R. Bowers, J. Phys. Chem. C **124**, 8304 (2020)
16. O.G. Salnikov, A. Svyatova, L.M. Kovtunova, N.V. Chukanov, V.I. Bukhtiyarov, K.V. Kovtunov, E.Y. Chekmenev, I.V. Koptyug, Chem. A Eur. J. **27**, 1316 (2021)
17. L.T. Kuhn, J. Bargon, in *Situ NMR Methods Catal.*, ed. by J. Bargon, L.T. Kuhn (Springer, Berlin, Heidelberg, 2006), p. 25. https://doi.org/10.1007/128_064
18. F. Reineri, E. Cavallari, C. Carrera, S. Aime, Magn. Reson. Mater. Phys. Biol. Med. **34**, 25 (2021)
19. S. Siddiqui, S. Kadlecek, M. Pourfathi, Y. Xin, W. Mannherz, H. Hamedani, N. Drachman, K. Ruppert, J. Clapp, R. Rizi, Adv. Drug Deliv. Rev. **113**, 3 (2017)
20. B. Joalland, A.B. Schmidt, M.S.H. Kabir, N.V. Chukanov, K.V. Kovtunov, I.V. Koptyug, J. Hennig, J.-B. Hövener, E.Y. Chekmenev, Anal. Chem. **92**, 1340 (2020)
21. H. Jóhannesson, O. Axelsson, M. Karlsson, Comptes Rendus Phys. **5**, 315 (2004)
22. E. Cavallari, C. Carrera, M. Sorge, G. Bonne, A. Muchir, S. Aime, F. Reineri, Sci. Rep. **8**, 8366 (2018)

23. S. Knecht, J.W. Blanchard, D. Barskiy, E. Cavallari, L. Dagys, E. van Dyke, M. Tsukanov, B. Bliemel, K. Münnemann, S. Aime, F. Reineri, M.H. Levitt, G. Buntkowsky, A. Pines, P. Blümler, D. Budker, J. Eills, Proc. Natl. Acad. Sci. **118**, e2025383118 (2021)
24. A.N. Pravdivtsev, A.V. Yurkovskaya, H.-M. Vieth, K.L. Ivanov, J. Chem. Phys. **139**, 244201 (2013)
25. A.S. Kiryutin, A.N. Pravdivtsev, K.L. Ivanov, Y.A. Grishin, H.-M. Vieth, A.V. Yurkovskaya, J. Magn. Reson. **263**, 79 (2016)
26. K. Golman, O. Axelsson, H. Jóhannesson, S. Månsson, C. Olofsson, J.S.S. Petersson, Magn. Reson. Med. **46**, 1 (2001)
27. M. Goldman, H. Jóhannesson, O. Axelsson, M. Karlsson, Magn. Reson. Imaging **23**, 153 (2005)
28. M. Roth, A. Koch, P. Kindervater, J. Bargon, H.W. Spiess, K. Münnemann, J. Magn. Reson. **204**, 50 (2010)
29. G. Stevanato, J. Eills, C. Bengs, G. Pileio, J. Magn. Reson. **277**, 169 (2017)
30. G. Stevanato, J. Magn. Reson. **274**, 148 (2017)
31. S. Bär, T. Lange, D. Leibfritz, J. Hennig, D. von Elverfeldt, J.-B. Hövener, J. Magn. Reson. **225**, 25 (2012)
32. A.N. Pravdivtsev, A.V. Yurkovskaya, N.N. Lukzen, K.L. Ivanov, H.-M. Vieth, J. Phys. Chem. Lett. **5**, 3421 (2014)
33. M. Haake, J. Natterer, J. Bargon, J. Am. Chem. Soc. **118**, 8688 (1996)
34. M. Goldman, H. Jóhannesson, Comptes Rendus Phys. **6**, 575 (2005)
35. S. Kadlecek, K. Emami, M. Ishii, R. Rizi, J. Magn. Reson. **205**, 9 (2010)
36. C. Cai, A.M. Coffey, R.V. Shchepin, E.Y. Chekmenev, K.W. Waddell, J. Phys. Chem. B **117**, 1219 (2013)
37. C.J. Jameson, in *Gas phase NMR*. ed. by K. Jackowski, M. Jaszuński (The Royal Society of Chemistry, Cambridge, 2016), p. 1
38. K. Jackowski, M. Jaszuński, Concepts Magn. Reson. Part A **30A**, 246 (2007)
39. E.V. Pokochueva, D.B. Burueva, L. Kovtunova, A.V. Bukhtiyarov, A.Y. Gladky, K.V. Kovtunov, I.V. Koptyug, V.I. Bukhtiyarov, Faraday Discuss. **229**, 161 (2021)
40. D.A. Barskiy, O.G. Salnikov, K.V. Kovtunov, I.V. Koptyug, J. Phys. Chem. A **119**, 996 (2015)
41. O.G. Salnikov, L.M. Kovtunova, I.V. Skovpin, V.I. Bukhtiyarov, K.V. Kovtunov, I.V. Koptyug, ChemCatChem **10**, 1178 (2018)
42. P.A. Hays, T. Schoenberger, Anal. Bioanal. Chem. **406**, 7397 (2014)
43. K.V. Kovtunov, D.A. Barskiy, A.M. Coffey, M.L. Truong, O.G. Salnikov, A.K. Khudorozhkov, E.A. Inozemtseva, I.P. Prosvirin, V.I. Bukhtiyarov, K.W. Waddell, E.Y. Chekmenev, I.V. Koptyug, Chem. A Eur. J. **20**, 11636 (2014)
44. K.V. Kovtunov, I.V. Koptyug, in *Magn. Reson. Microsc. Spat. Resolv. NMR Tech. Appl.*, ed. by S.L. Codd, J.D. Seymour (Wiley-VCH, Weinheim, 2008), p. 99. https://doi.org/10.1002/9783527626052.ch7
45. D.A. Barskiy, K.V. Kovtunov, E.Y. Gerasimov, M.A. Phipps, O.G. Salnikov, A.M. Coffey, L.M. Kovtunova, I.P. Prosvirin, V.I. Bukhtiyarov, I.V. Koptyug, E.Y. Chekmenev, J. Phys. Chem. C **121**, 10038 (2017)
46. N.M. Ariyasingha, O.G. Salnikov, K.V. Kovtunov, L.M. Kovtunova, V.I. Bukhtiyarov, B.M. Goodson, M.S. Rosen, I.V. Koptyug, J.G. Gelovani, E.Y. Chekmenev, J. Phys. Chem. C **123**, 11734 (2019)
47. R.E.D. McClung, in *Encycl. Magn. Reson.*, ed. by R.K. Harris, R.L. Wasylishen (John Wiley, Chichester, 2007), p. 1. https://doi.org/10.1002/9780470034590.emrstm0524
48. C.J. Jameson, A.K. Jameson, N.C. Smith, J.K. Hwang, T. Zia, J. Phys. Chem. **95**, 1092 (1991)
49. M.M. Folkendt, B.E. Weiss-Lopez, N.S. True, J. Phys. Chem. **92**, 4859 (1988)
50. R.E. Wasylishen, T. Schaefer, Can. J. Chem. **52**, 3247 (1974)
51. A. Svyatova, V.P. Kozinenko, N.V. Chukanov, D.B. Burueva, E.Y. Chekmenev, Y.W. Chen, D.W. Hwang, K.V. Kovtunov, I.V. Koptyug, Sci. Rep. **11**, 5646 (2021)

Publisher's Note Springer Nature remains neutral with regard to jurisdictional claims in published maps and institutional affiliations.

ChemPhysChem

Essays
doi.org/10.1002/cphc.202001031

Chemistry Europe
European Chemical Societies Publishing

Special Collection

Bridging the Gap: From Homogeneous to Heterogeneous Parahydrogen-induced Hyperpolarization and Beyond

Eduard Y. Chekmenev,[a, b] Boyd M. Goodson,[c] Valerii I. Bukhtiyarov,[d] and Igor V. Koptyug*[e]

In memoriam Kirill V. Kovtunov

Demonstration of parahydrogen-induced polarization effects in hydrogenations catalyzed by heterogeneous catalysts instead of metal complexes in a homogeneous solution has opened an entirely new dimension for parahydrogen-based research, demonstrating its applicability not only for the production of catalyst-free hyperpolarized liquids and gases and long-lived non-equilibrium spin states for potential biomedical applications, but also for addressing challenges of modern fundamental and industrial catalysis including advanced mechanistic studies of catalytic reactions and operando NMR and MRI of reactors. This essay summarizes the progress achieved in this field by highlighting the research contributed to it by our colleague and friend Kirill V. Kovtunov whose scientific career ended unexpectedly and tragically at the age of 37. His role in this research was certainly crucial, further enhanced by a vast network of his contacts and collaborations at the national and international level.

It is a curious coincidence that parahydrogen-induced polarization (PHIP) effects were reported[1] – albeit not yet recognized as such and interpreted as chemically induced dynamic nuclear polarization (CIDNP) – in 1983, the same year that Kirill Kovtunov (Figure 1) was born. The true meaning of the 1983 observations of Bryndza et al. became clear after the publication of the work of Bowers and Weitekamp[2,3] in 1986–1987. They demonstrated, first theoretically and then experimentally, that if parahydrogen is used in the hydrogenation of acrylonitrile to propionitrile in a solution of Wilkinson's organometallic catalyst, this results in the enhancement of NMR signals. Since then, the field of PHIP has grown tremendously,[4,5] and a number of remarkable developments of this hyperpolarization technique have emerged over the last 10 years or so, including PHIP by side-arm hydrogenation (PHIP-SAH),[6] signal amplification by reversible exchange (SABRE),[7] SABRE-RELAY,[8] etc.

Nowadays, parahydrogen-based research is mostly driven by the incentive to develop novel contrast agents for biomedical MRI and MRS.[9,10] There is, however, another point of entry to the field of PHIP – through chemical engineering

Figure 1. Kirill V. Kovtunov (14.01.1983–19.05.2020) was born in Barnaul, the Altai region of Russia. In 2000–2005 he was a student at the Novosibirsk State University. After graduation in 2005, he joined the MR microimaging laboratory at ITC SB RAS as a PhD student. He defended his PhD thesis entitled "Parahydrogen-induced polarization of nuclear spins in heterogeneous catalytic hydrogenation reactions" on June 18, 2008. After that, he continued to explore this research field further, and defended his Habilitation thesis entitled "Parahydrogen-induced NMR signal enhancement in heterogeneous catalysis" on December 25, 2019.

[a] *Prof. E. Y. Chekmenev*
Department of Chemistry, Integrative Biosciences (Ibio)
Wayne State University
Karmanos Cancer Institute (KCI)
Detroit, MI 48202, USA
[b] *Prof. E. Y. Chekmenev*
Russian Academy of Sciences
14 Leninskiy prospect, Moscow 119991, Russia
[c] *Prof. B. M. Goodson*
Southern Illinois University
Department of Chemistry and Biochemistry
Materials Technology Center
Carbondale, IL 62901, USA
[d] *Prof. V. I. Bukhtiyarov*
Boreskov Institute of Catalysis, SB RAS
5 Acad. Lavrentiev pr., Novosibirsk 630090, Russia
[e] *Prof. I. V. Koptyug*
International Tomography Center, SB RAS
3A Institutskaya st., Novosibirsk 630090, Russia
E-mail: koptyug@tomo.nsc.ru

Special Collection An invited contribution to a Special Collection on Parahydrogen Enhanced Resonance

© 2021 Wiley-VCH GmbH

and catalysis. Already in the first publications on the subject[3,11] it was recognized that PHIP can be observed not only for the reaction products but also for the short-lived intermediates such as metal dihydride complexes, thereby holding the potential to unveil the underlying sophistication of reaction mechanisms. This has been explored later in the context of H_2 activation by transition metal complexes in solution.[12]

During his undergraduate studies at Novosibirsk State University (NSU), Kirill was involved in the pulsed-field-gradient NMR and MRI studies of gas and liquid transport in various geometries including porous media and microreactors at the NMR microimaging group at ITC. Other research that was done by group members included operando studies of catalytic processes, with a setup designed to place a single catalyst pellet or a catalyst bed in the probe of a microimaging instrument to study dynamic redistribution of the liquid phase in the catalyst and performing MR imaging and spatially resolved NMR spectroscopy of the reaction progress.[13] Heterogeneous hydrogenations, which are widely used in industrial catalysis, were of primary interest in those studies, and not surprisingly, the idea to use parahydrogen in these processes was being entertained for some time. After graduating from NSU in 2005, Kirill joined the group at ITC as a PhD student. From then on, his research was about combining magnetic resonance, catalysis, and parahydrogen.

The main objective for his PhD thesis was to demonstrate PHIP in heterogeneous hydrogenations, even though it has been pronounced impossible earlier in the literature.[14] The solution to this "impossible" problem was sought via the known bridge between homogeneous and heterogeneous catalysis, namely by immobilizing PHIP-active organometallic complexes on a suitable solid support. Despite its deceptive conceptual simplicity, this approach has proven difficult to implement. Many unsuccessful attempts to immobilize various Rh and Ir metal complexes and use them in PHIP experiments resulted in no catalytic activity, or no PHIP effects, or metal complex leaching into solution, or all of the above. The breakthrough came in the end of 2006 when Kirill was visiting the Department of Chemistry at UC Berkeley within the framework of a joint project of the CRDF cooperative grants program implemented by the ITC microimaging team and the group of Alex Pines.

The first successful experiments (Figure 2a) were performed initially with the hydrogenation of styrene in solution using Wilkinson's catalyst immobilized on silica or a polymer.[15] In these experiments, clear PASADENA (PArahydrogen and Synthesis Allow Dramatically Enhanced Nuclear Alignment)[3] effects were observed for the reaction product ethylbenzene. Importantly, essentially no PHIP effects were detected once the catalyst was removed from the slurry, which is very easy to achieve with these solid materials. While these first successful observations were encouraging, they were not completely unambiguous. A more clear-cut proof was thus sought that PHIP effects were observed in a heterogeneous reaction and not as a result of metal complex leaching. This was achieved as well, based on the hydrogenation of propylene into propane over silica-immobilized cationic Rh complex or Wilkinson's catalyst (Figure 2b). Leaching of the metal complex is not possible in such gas-solid hydrogenation processes performed in the absence of any liquid phase. Successful demonstration of both PASADENA and ALTADENA (Adiabatic Longitudinal Transport After Dissociation Engenders Nuclear Alignment)[16] effects in those experiments provided an ultimate proof that those experiments indeed resulted in the first demonstration of PHIP in heterogeneous catalysis (HET-PHIP).

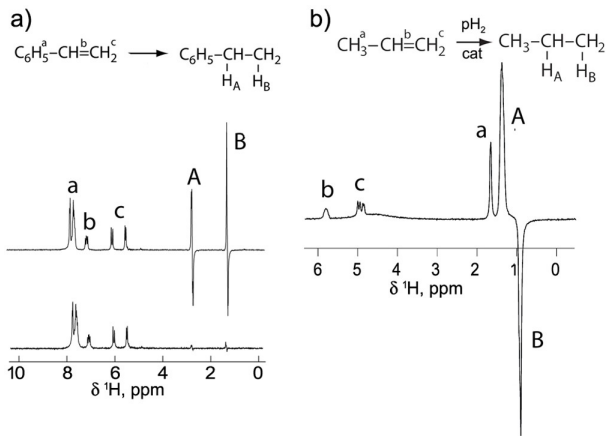

Figure 2. a) ^{1}H NMR spectra acquired after bubbling parahydrogen through the C_6D_6 solution of styrene at 7 T in the presence of polymer-supported Wilkinson's catalyst (top) or after catalyst removal (bottom). b) ^{1}H NMR spectrum acquired during gas-solid hydrogenation of propylene with parahydrogen over silica-supported Wilkinson's catalyst in the Earth's magnetic field. Adapted with permission from Ref. [15] Copyright (2007) American Chemical Society.

Coincidentally, this happened at the same location (Department of Chemistry, UC Berkeley) where 23 years earlier homogeneous PHIP effects were observed for the first time.

The PHIP studies with immobilized metal complexes continue, and by now many other examples have been demonstrated, for instance the cationic Au complex immobilized on a metal-organic framework (MOF).[17] Immobilized metal complexes certainly represent a useful model system which can provide a useful bridge between homogeneous and heterogeneous hydrogenations with parahydrogen and can help in advancing our understanding of HET-PHIP in general.

At the same time, such immobilized metal complexes are not very stable, particularly at high temperatures and in the presence of reducing agents such as H_2, and thus are not used in industrial applications. Instead, much more robust catalysts such as supported metal NPs are preferred for such reactions. However, supported and bulk metals were not expected to be able to achieve pairwise H_2 addition to an unsaturated substrate, which is a major prerequisite for efficient PHIP production. Indeed, H_2 chemisorption on metals is very efficient but dissociative, and hydrogen atoms are known to be extremely mobile on the metal surface. Therefore, hydrogenation would be expected to inevitably involve random H atoms, making pairwise addition of H_2 impossible. But Kirill was not quite convinced by this common knowledge, and in less than a year demonstrated both PASADENA- and ALTADENA-

© 2021 Wiley-VCH GmbH

type effects in hydrogenation of propylene to propane over supported Pt and Pd NPs.[18] Remarkably, for the very first such experiments he accidentally used a Pd/Al_2O_3 catalyst which was heavily doped with Mn^{2+} for performing rapid MRI experiments of hydrogenations and was certainly not intended for para-hydrogen studies. Luckily, this experiment worked despite the paramagnetic doping of the catalyst. Later studies also confirmed that magnetic nature of a catalyst is not necessarily an obstacle for observing PHIP effects, as demonstrated, for instance for the catalyst comprising superparamagnetic Co nanoparticles on TiO_2 support.[19]

Observation of PHIP effects with supported metal NPs contradicted the commonly accepted Horiuti-Polanyi mechanism of hydrogenation by metals and required some explanation. The one advanced originally was based on the fact that under realistic conditions the surface of a catalytically active metal is never clean during the reaction; it is covered with various species and is thus possibly partitioned into smaller clean patches of metal so that the reactants are forced to stay together. This may prevent H atoms from separating freely on the catalyst surface. However, this explanation has never been experimentally tested, and recent results show that it may be incorrect.[19,20]

Based on these innovative and exciting results, Kirill defended his PhD thesis in 2008 with flying colors. But the work certainly didn't stop there. The scope of HET-PHIP has been growing ever since, covering all sorts of different catalysts, which now include various bulk and supported metals (Pt, Pd, Rh, Ir, Au, Ag, Co, Cu), metal oxides (Cr_2O_3, CeO_2, CaO, TiO_2),[21] carbides (Mo_2C)[22] and sulfides (MoS_2),[23] different particle sizes, various solid supports, substrates, conditions, etc.[19,20] One example is shown in Figure 3 for hydrogenation of propyne over supported Cu NPs, demonstrating pronounced PHIP

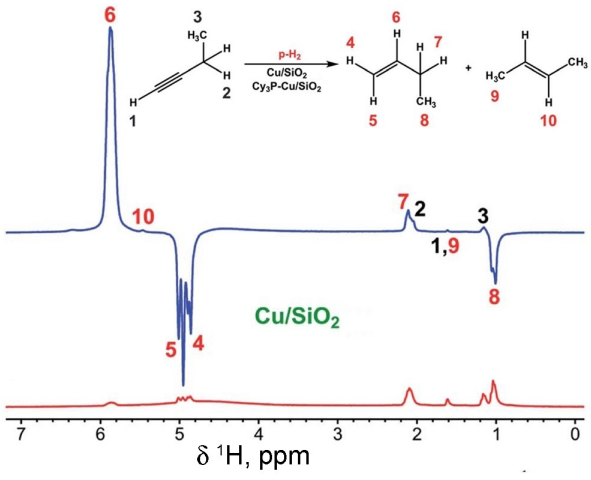

Figure 3. The reaction scheme of 1-butyne hydrogenation over Cu/SiO_2 catalysts, and the ^1H NMR spectra acquired during the reaction while the gas was flowing (top) and after rapid interruption of the gas flow and subsequent relaxation of nuclear spins to thermal equilibrium (bottom). Adapted from Ref. [24] published by The Royal Society of Chemistry in accordance with the term of the CC-BY 3.0 licence. Copyright (2017) The Authors.

effects.[24] It is also observed that introduction of a phosphine ligand to the Cu NPs decreases the catalytic activity markedly but at the same time NMR signal enhancements become larger. Observation of HET-PHIP effects with Mo sulfide catalysts[23] made it possible to study thiophene hydrodesulfurization reaction, which is a model for industrial purification of fuels. Other industrially important processes can certainly be addressed and their mechanisms and kinetics studied.

From the very beginning, a lot of PHIP work was performed with gases with their rather short polarization lifetimes, usually below 1 s for hydrocarbon gases at normal pressures. Many efforts were thus directed at extending these lifetimes, particularly by exploring the properties of long-lived spin states (LLSS) at low magnetic fields[25,26] and also by condensing hyperpolarized (HP) gases into a liquid state or dissolving them in liquids,[27] with up to tens of seconds of HP lifetime achieved this way. Also, alternative ways were explored to produce HP propane, for instance by hydrogenating cyclopropane with parahydrogen.[28] One very recent example of HET-PHIP with gases is the production of HP diethylether,[29,30] an inhalable anesthetic, by hydrogenation of an unsaturated precursor in the liquid or in the gas phase, as well as exploring its LLSS in a low magnetic field. HET-PHIP was also successfully used to enhance MR imaging experiments, for instance to address gas flow in various geometries (Figure 4), and to obtain 2D and 3D maps of product distribution in a model catalytic reactor.[31]

While supported metals do work in PHIP experiments, at present the achieved polarizations normally do not exceed a few percent in experiments where significant product yields have been achieved. Therefore, an active search for better heterogeneous catalysts continues. One of the current trends is to explore the so-called single-atom and single site heterogeneous catalysts.[32,33] This can be exemplified by intermetallic Pd–In NPs supported on Al_2O_3.[34] In this system, individual Pd atoms are essentially surrounded by inactive In atoms, providing a single metal atom configuration of the active catalytic center. And indeed, this catalyst provides substantial polarization levels and reaction yields and is able to enhance the NMR signals significantly, thus facilitating the MR imaging of gases (Figure 5).

The scope of the research Kirill was involved in is very broad. Exploring the concept of PHIP-SAH introduced by Silvio Aime,[6,35,36] which involves hydrogenation of unsaturated precursors followed by hyperpolarization transfer to ^{13}C nuclei, is exemplified by the efforts to produce catalyst-free HP liquids or solutions by hydrogenation of a substrate vapor and its subsequent dissolution and hydrolysis, for instance, to yield HP ethanol in solution which never contained any catalyst.[37] In the context of potential biomedical applications, aqueous hydrogenations are very important and are being addressed.[38] Other remarkable achievements include the demonstration of the unexpected spontaneous SABRE in high magnetic fields[39] and observation of HET-SABRE with an Ir complex immobilized on a solid material.[40] Another approach is to perform SABRE in a traditional way in solution with subsequent removal of the dissolved metal complex with a thiol-functionalized porous solid material to produce a clear catalyst-free HP solution.[41]

© 2021 Wiley-VCH GmbH

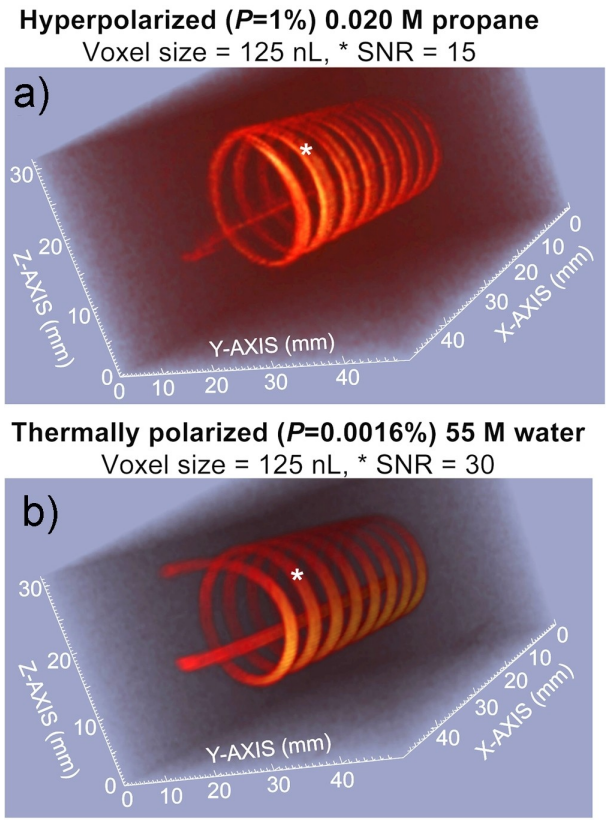

Figure 4. 3D gradient echo MRI of a spiral tube with continuously flowing HP propane (a) and static water (b) acquired with 0.5 mm isotropic spatial voxel resolution in 21.4 s at 4.7 T. A comparable SNR is obtained despite the dramatic difference in gas and liquid spin densities. Adapted with permission from Ref. [25]. Copyright (2014) Wiley-VCH Verlag GmbH & Co. KGaA, Weinheim.

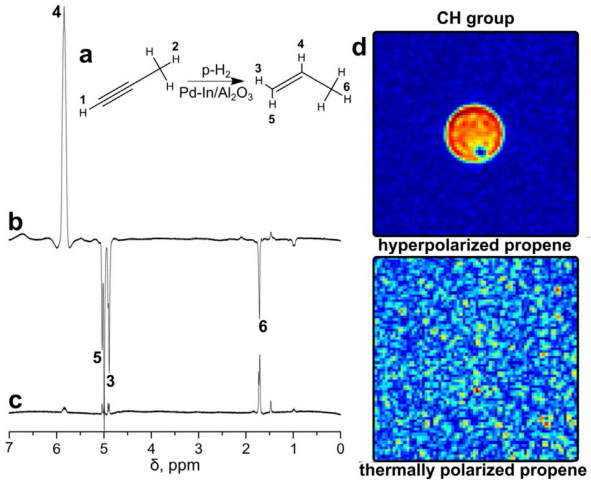

Figure 5. a) The reaction scheme for propyne hydrogenation over Pd–In/Al_2O_3 catalyst. b) and c) ^{1}H NMR spectra acquired during the reaction (b) while the gas was flowing and (c) after an abrupt interruption of the gas flow and the subsequent relaxation of nuclear spins to thermal equilibrium. (d) MR images of a 10 mm NMR tube filled with propylene in thermal equilibrium (bottom) or hyperpolarized propylene (top). Adapted with permission from Ref. [34]. Copyright (2018) Wiley-VCH Verlag GmbH & Co. KGaA, Weinheim.

Some notable work has been done on polarization transfer to ^{15}N nuclei to extend hyperpolarization lifetimes to many minutes.[42–44] For instance, SABRE of nitrogen-containing drugs is exemplified by HP fampridine which made it possible to perform ^{15}N MRI at natural abundance of the ^{15}N isotope.[45]

The joint CRDF project mentioned earlier, in addition to its successfully achieved primary objective of demonstrating HET-PHIP effects, encompassed numerous other objectives which were rather challenging and ambitious. One of those was about the use of ultralow field NMR to monitor catalytic processes in metal containers. It has been finally achieved this year, in collaboration between the Novosibirsk team and the group of Prof. D. Budker at Helmholtz Institute in Mainz. In that study,[46] unsaturated acetylenic compound was hydrogenated with parahydrogen in a metal tube and the NMR spectra were detected with an atomic magnetometer at zero magnetic field, demonstrating that such approach is indeed promising for studying heterogeneous systems and for applications in heterogeneous catalysis. This was one of the last studies in which Kirill was involved.

For many years now, one of the incentives was to think outside the box and go beyond parahydrogen, and in particular to introduce the use of nuclear spin isomers of molecules (NSIM) other than H_2 and D_2 for nuclear spin hyperpolarization. One remarkable example is the successful chemical enrichment of NSIM of ethylene by hydrogenation of acetylene with parahydrogen.[47] Ethylene is a symmetric molecule, so to demonstrate the NSIM enrichment of ethylene, a further reaction is required to break its symmetry by producing a non-symmetric product. And indeed, in such an experiment the PHIP effects were clearly observable for the non-symmetric product, proving that enrichment of NSIM of ethylene does take place in acetylene hydrogenation with parahydrogen. While a more direct experiment to confirm chemical synthesis of NSIM would be a plus,[48] these preliminary results provide a clear glimpse into the bright and promising future of NSIM-based hyperpolarization. Notably, NSIM of ethylene is also a remarkable example of the molecular long-lived spin states (LLSS), which are becoming increasingly popular for achieving spin hyperpolarization storage times (T_{LLSS}) that significantly exceed the conventional spin relaxation times (e.g., T_1).[49] In particular, transferring the singlet spin state of a p-H_2 molecule to a reaction product is a natural way of producing such states, and the chemical NSIM enrichment of ethylene convincingly demonstrates such a possibility – the ratio $T_{LLSS}/T_1 \sim 3500$ measured for ethylene is likely the largest value reported so far for any molecule except p-H_2 itself.

While a lot has been already achieved in bridging the gap between utilizing parahydrogen in homogeneous and heterogeneous processes, this is clearly just the tip of an iceberg. Further progress in this field requires a much deeper understanding of the processes involved, particularly for nanoparticle-based catalysts, and further optimization of catalysts and reaction conditions to implement these processes with maximum possible efficiency. The extent of knowledge accumulated to date is already adequate for developing mechanistic models that are sufficiently realistic to guide further research

© 2021 Wiley-VCH GmbH

and applications in this field. In particular, as revealed by previous studies, one clear possibility to improve the PHIP efficiency of heterogeneous catalysts is a broader exploration of single-site and single-atom catalyst structures. This parallels the recent trend in fundamental catalysis, and can thus potentially spearhead future research and applications toward multiple goals, from producing highly polarized catalyst-free fluids for advanced spectroscopic and imaging studies to exploring the mechanistic details of important catalytic transformations. Future advances in these directions will be the best possible tribute to the efforts of Kirill Kovtunov to launch and promote this field of research.

Acknowledgements

I.V.K. thanks RFBR for supporting this research with a number of grants over the years, including the ongoing grant # 19-29-10003. B.M.G. and E.Y.C. thank NCI R21CA220137 and NIBIB 1R01EB029829. E.Y.C. thanks NHLBI R21 HL154032, NSF CHE-1904780, DOD PRMRP W81XWH-15-1-0271 and W81XWH-20-1-0576. B.M.G. thanks NSF CHE-1905341, DOD PRMRP W81XWH-15-1-0272 and W81XWH-20-1-0578. We particularly thank those who made a donation on the PERM 2020 meeting webpage to support Kirill's family.

Conflict of Interest

The authors declare no conflict of interest.

Keywords: parahydrogen-induced hyperpolarization · NMR signal enhancement · heterogeneous hydrogenation · immobilized metal complexes · supported metal catalysts

[1] P. F. Seidler, H. E. Bryndza, J. E. Frommer, L. S. Stuhl, R. G. Bergman, *Organometallics* **1983**, *2*, 1701–1705.
[2] C. R. Bowers, D. P. Weitekamp, *Phys. Rev. Lett.* **1986**, *57*, 2645–2648.
[3] C. R. Bowers, D. P. Weitekamp, *J. Am. Chem. Soc.* **1987**, *109*, 5541–5542.
[4] S. B. Duckett, R. E. Mewis, *Acc. Chem. Res.* **2012**, *45*, 1247–1257.
[5] R. A. Green, R. W. Adams, S. B. Duckett, R. E. Mewis, D. C. Williamson, G. G. R. Green, *Progr. NMR Spectr.* **2012**, *67*, 1–48.
[6] F. Reineri, T. Boi, S. Aime, *Nat. Commun.* **2015**, *6*, 5858.
[7] R. W. Adams, J. A. Aguilar, K. D. Atkinson, M. J. Cowley, P. I. P. Elliott, S. B. Duckett, G. G. R. Green, I. G. Khazal, J. Lopez-Serrano, D. C. Williamson, *Science* **2009**, *323*, 1708–1711.
[8] W. Iali, P. J. Rayner, S. B. Duckett, *Sci. Adv.* **2018**, *4*, eaao6250.
[9] J. Hovener, A. N. Pravdivtsev, B. Kidd, C. R. Bowers, S. Gloggler, K. V. Kovtunov, M. Plaumann, R. Katz-Brull, K. Buckenmaier, A. Jerschow, F. Reineri, T. Theis, R. V. Shchepin, S. Wagner, N. M. M. Zacharias, P. Bhattacharya, E. Y. Chekmenev, *Angew. Chem. Int. Ed.* **2018**, *57*, 11140–11162; *Angew. Chem.* **2018**, *130*, 11310–11333.
[10] E. Cavallari, C. Carrera, F. Reineri, *Isr. J. Chem.* **2017**, *57*, 833–842.
[11] S. B. Duckett, C. J. Sleigh, *Progr. NMR Spectr.* **1999**, *34*, 71–92.
[12] S. B. Duckett, N. J. Wood, *Coord. Chem. Rev.* **2008**, *252*, 2278–2291.
[13] I. V. Koptyug, in *Spectroscopic Properties of Inorganic and Organometallic Compounds* Vol. 45 (Eds: R. Douthwaite, S. Duckett, J. Yarwood), Royal Society of Chemistry, Cambridge, **2014**, pp. 1–42.
[14] A. Eichhorn, A. Koch, J. Bargon, *J. Molec. Catal. A Chem.* **2001**, *174*, 293–295.
[15] I. V. Koptyug, K. V. Kovtunov, S. R. Burt, M. S. Anwar, C. Hilty, S. Han, A. Pines, R. Z. Sagdeev, *J. Am. Chem. Soc.* **2007**, *129*, 5580–5586.
[16] M. G. Pravica, D. P. Weitekamp, *Chem. Phys. Lett.* **1988**, *145*, 255–258.
[17] K. V. Kovtunov, V. V. Zhivonitko, A. Corma, I. V. Koptyug, *J. Phys. Chem. Lett.* **2010**, *1*, 1705–1708.
[18] K. V. Kovtunov, I. E. Beck, V. I. Bukhtiyarov, I. V. Koptyug, *Angew. Chem. Int. Ed.* **2008**, *47*, 1492–1495; *Angew. Chem.* **2008**, *120*, 1514–1517.
[19] K. V. Kovtunov, V. V. Zhivonitko, I. V. Skovpin, O. G. Salnikov, I. V. Koptyug, in *Magnetic nanomaterials: applications in catalysis and life sciences* (Eds: S. H. Bossmann, H. Wang), The Royal Society of Chemistry, **2017**, pp. 142–171.
[20] V. V. Zhivonitko, K. V. Kovtunov, I. V. Skovpin, D. A. Barskiy, O. G. Salnikov, I. V. Koptyug, in *Understanding organometallic reaction mechanisms and catalysis* (Eds: V. P. Ananikov), Wiley-VCH Verlag GmbH & Co. KGaA, **2014**, pp. 145–186.
[21] K. V. Kovtunov, D. A. Barskiy, O. G. Salnikov, A. K. Khudorozhkov, V. I. Bukhtiyarov, I. P. Prosvirin, I. V. Koptyug, *Chem. Commun.* **2014**, *50*, 875–878.
[22] D. B. Burueva, A. A. Smirnov, O. A. Bulavchenko, I. P. Prosvirin, E. Y. Gerasimov, V. A. Yakovlev, K. V. Kovtunov, I. V. Koptyug, *Top. Catal.* **2020**, *63*, 2–11.
[23] O. G. Salnikov, D. B. Burueva, D. A. Barskiy, G. A. Bukhtiyarova, K. V. Kovtunov, I. V. Koptyug, *ChemCatChem* **2015**, *7*, 3508–3512.
[24] O. G. Salnikov, H.-J. Liu, A. Fedorov, D. Burueva, K. V. Kovtunov, C. Coperet, I. V. Koptyug, *Chem. Sci.* **2017**, *8*, 2426–2430.
[25] K. V. Kovtunov, M. L. Truong, D. A. Barskiy, I. V. Koptyug, A. M. Coffey, K. W. Waddell, E. Y. Chekmenev, *Chem. Eur. J.* **2014**, *20*, 14629–14632.
[26] K. V. Kovtunov, M. L. Truong, D. A. Barskiy, O. G. Salnikov, V. I. Bukhtiyarov, A. M. Coffey, K. W. Waddell, I. V. Koptyug, E. Y. Chekmenev, *J. Phys. Chem. C* **2014**, *118*, 28234–28243.
[27] D. B. Burueva, A. S. Romanov, O. G. Salnikov, V. V. Zhivonitko, Y.-W. Chen, D. A. Barskiy, E. Y. Chekmenev, D. W.-H. Hwang, K. V. Kovtunov, I. V. Koptyug, *J. Phys. Chem. C* **2017**, *121*, 4481–4487.
[28] O. Salnikov, K. Kovtunov, P. Nikolaou, L. Kovtunova, V. I. Bukhtiyarov, I. V. Koptyug, E. Y. Chekmenev, *ChemPhysChem* **2018**, *19*, 2621–2626.
[29] N. M. Ariyasingha, B. Joalland, H. R. Younes, O. G. Salnikov, N. V. Chukanov, K. V. Kovtunov, L. M. Kovtunova, V. I. Bukhtiyarov, I. V. Koptyug, J. G. Gelovani, E. Y. Chekmenev, *Chem. Eur. J.* **2020**, *26*, 13621–13626.
[30] O. G. Salnikov, A. Svyatova, L. M. Kovtunova, N. V. Chukanov, V. I. Bukhtiyarov, K. V. Kovtunov, E. Y. Chekmenev, I. V. Koptyug, *Chem. Eur. J.* **2020**, *V3638*, P3638.
[31] K. V. Kovtunov, D. Lebedev, A. Svyatova, E. V. Pokochueva, I. P. Prosvirin, E. Y. Gerasimov, V. I. Bukhtiyarov, C. R. Muller, A. Fedorov, I. V. Koptyug, *ChemCatChem* **2019**, *11*, 969–973.
[32] J. Liu, B. R. Bunes, L. Zang, C. Wang, *Environ. Chem. Lett.* **2018**, *16*, 477–505.
[33] M. K. Samantaray, V. D'Elia, E. Pump, L. Falivene, M. Harb, S. Ould Chikh, L. Cavallo, J.-M. Basset, *Chem. Rev.* **2020**, *120*, 734–813.
[34] D. B. Burueva, K. V. Kovtunov, A. V. Bukhtiyarov, D. A. Barskiy, I. P. Prosvirin, I. S. Mashkovsky, G. N. Baeva, V. I. Bukhtiyarov, A. Y. Stakheev, I. V. Koptyug, *Chem. Eur. J.* **2018**, *24*, 2547–2553.
[35] O. G. Salnikov, N. V. Chukanov, R. V. Shchepin, I. V. Manzanera Esteve, K. V. Kovtunov, I. V. Koptyug, E. Y. Chekmenev, *J. Phys. Chem. C* **2019**, *123*, 12827–12840.
[36] N. V. Chukanov, O. G. Salnikov, R. V. Shchepin, K. V. Kovtunov, I. V. Koptyug, E. Y. Chekmenev, *ACS Omega* **2018**, *3*, 6673–6682.
[37] O. G. Salnikov, K. V. Kovtunov, I. V. Koptyug, *Sci. Rep.* **2015**, *5*, 13930.
[38] L. B. Bales, K. V. Kovtunov, D. A. Barskiy, R. V. Shchepin, A. M. Coffey, L. M. Kovtunova, A. V. Bukhtiyarov, M. A. Feldman, V. I. Bukhtiyarov, E. Y. Chekmenev, I. V. Koptyug, B. M. Goodson, *J. Phys. Chem. C* **2017**, *121*, 15304–15309.
[39] D. A. Barskiy, K. V. Kovtunov, I. V. Koptyug, P. He, K. A. Groome, Q. A. Best, F. Shi, B. M. Goodson, R. V. Shchepin, A. M. Coffey, K. W. Waddell, E. Y. Chekmenev, *J. Am. Chem. Soc.* **2014**, *136*, 3322–3325.
[40] K. V. Kovtunov, L. M. Kovtunova, M. E. Gemeinhardt, A. V. Bukhtiyarov, J. Gesiorski, V. I. Bukhtiyarov, E. Y. Chekmenev, I. V. Koptyug, B. Goodson, *Angew. Chem. Int. Ed.* **2017**, *56*, 10433–10437; *Angew. Chem.* **2017**, *129*, 10569–10573.
[41] B. E. Kidd, J. L. Gesiorski, M. E. Gemeinhardt, R. V. Shchepin, K. V. Kovtunov, I. V. Koptyug, E. Y. Chekmenev, B. M. Goodson, *J. Phys. Chem. C* **2018**, *122*, 16848–16852.
[42] J. R. Birchall, M. S. H. Kabir, O. G. Salnikov, N. V. Chukanov, A. Svyatova, K. V. Kovtunov, I. V. Koptyug, J. G. Gelovani, B. M. Goodson, W. Pham, E. Y. Chekmenev, *Chem. Commun.* **2020**, *56*, 9098–9101.
[43] R. V. Shchepin, J. R. Birchall, N. V. Chukanov, K. V. Kovtunov, I. V. Koptyug, T. Theis, W. S. Warren, J. G. Gelovani, B. M. Goodson, S.

© 2021 Wiley-VCH GmbH

Shokouhi, M. S. Rosen, Y.-F. Yen, W. Pham, E. Y. Chekmenev, *Chem. Eur. J.* **2019**, *25*, 8829–8836.
[44] O. G. Salnikov, N. V. Chukanov, A. Svyatova, I. A. Trofimov, M. S. H. Kabir, J. G. Gelovani, K. V. Kovtunov, I. V. Koptyug, E. Y. Chekmenev, *Angew. Chem. Int. Ed.* **2021**, *60*, 2406–2413.
[45] I. V. Skovpin, A. Svyatova, N. V. Chukanov, E. Y. Chekmenev, K. V. Kovtunov, I. V. Koptyug, *Chem. Eur. J.* **2019**, *25*, 12694–12697.
[46] D. B. Burueva, J. Eills, J. W. Blanchard, A. Garcon, R. Picazo-Frutos, K. V. Kovtunov, I. V. Koptyug, D. Budker, *Angew. Chem. Int. Ed.* **2020**, *59*, 17026–17032.
[47] V. V. Zhivonitko, K. V. Kovtunov, P. L. Chapovsky, I. V. Koptyug, *Angew. Chem. Int. Ed.* **2013**, *52*, 13251–13255; *Angew. Chem.* **2013**, *125*, 13493–13497.
[48] P. L. Chapovsky, *Quantum Electron.* **2019**, *49*, 623–627.
[49] M. H. Levitt, *J. Magn. Reson.* **2019**, *306*, 69–74.

Manuscript received: December 20, 2020
Revised manuscript received: February 19, 2021
Version of record online: April 6, 2021

© 2021 Wiley-VCH GmbH

molecules

MDPI

Article

Pilot Quality-Assurance Study of a Third-Generation Batch-Mode Clinical-Scale Automated Xenon-129 Hyperpolarizer

Jonathan R. Birchall [1,*,†], Md Raduanul H. Chowdhury [1,†], Panayiotis Nikolaou [2], Yuri A. Chekmenev [2], Anton Shcherbakov [3,4], Michael J. Barlow [5], Boyd M. Goodson [6] and Eduard Y. Chekmenev [1,7,*]

1 Department of Chemistry, Integrative Biosciences (Ibio), Karmanos Cancer Institute (KCI), Wayne State University, Detroit, MI 48202, USA; raduanul@wayne.edu
2 XeUS Technologies Ltd., Nicosia 2312, Cyprus; peternikolaou78@gmail.com (P.N.); yura_chekmenev@mail.ru (Y.A.C.)
3 Smart-A, 614000 Perm, Russia; xbister@gmail.com
4 Custom Medical Systems (CMS) Ltd., Nicosia 2312, Cyprus
5 Sir Peter Mansfield Imaging Centre, University of Nottingham, Nottingham NG7 2RD, UK; michaelj.barlow@me.com
6 Department of Chemistry and Biochemistry, Materials Technology Center, Southern Illinois University, Carbondale, IL 62901, USA; bgoodson@chem.siu.edu
7 Russian Academy of Sciences, Leninskiy Prospekt 14, 119991 Moscow, Russia
* Correspondence: jonathan.birchall@outlook.com (J.R.B.); chekmenevlab@gmail.com (E.Y.C.)
† These authors contributed equally to this work.

check for updates

Citation: Birchall, J.R.; Chowdhury, M.R.H.; Nikolaou, P.; Chekmenev, Y.A.; Shcherbakov, A.; Barlow, M.J.; Goodson, B.M.; Chekmenev, E.Y. Pilot Quality-Assurance Study of a Third-Generation Batch-Mode Clinical-Scale Automated Xenon-129 Hyperpolarizer. *Molecules* **2022**, *27*, 1327. https://doi.org/10.3390/molecules27041327

Academic Editor: Elena G. Bagryanskaya

Received: 27 December 2021
Accepted: 10 February 2022
Published: 16 February 2022

Publisher's Note: MDPI stays neutral with regard to jurisdictional claims in published maps and institutional affiliations.

Copyright: © 2022 by the authors. Licensee MDPI, Basel, Switzerland. This article is an open access article distributed under the terms and conditions of the Creative Commons Attribution (CC BY) license (https://creativecommons.org/licenses/by/4.0/).

Abstract: We present a pilot quality assurance (QA) study of a clinical-scale, automated, third-generation (GEN-3) ^{129}Xe hyperpolarizer employing batch-mode spin-exchange optical pumping (SEOP) with high-Xe densities (50% natural abundance Xe and 50% N_2 in ~2.6 atm total pressure sourced from Nova Gas Technologies) and rapid temperature ramping enabled by an aluminum heating jacket surrounding the 0.5 L SEOP cell. ^{129}Xe hyperpolarization was performed over the course of 700 gas loading cycles of the SEOP cell, simulating long-term hyperpolarized contrast agent production in a clinical lung imaging setting. High levels of ^{129}Xe polarization (avg. $\%P_{Xe}$ = 51.0% with standard deviation σ_{PXe} = 3.0%) were recorded with fast ^{129}Xe polarization build-up time constants (avg. T_b = 25.1 min with standard deviation σ_{Tb} = 3.1 min) across the first 500 SEOP cell refills, using moderate temperatures of 75 °C. These results demonstrate a more than 2-fold increase in build-up rate relative to previously demonstrated results in a comparable QA study on a second-generation (GEN-2) ^{129}Xe hyperpolarizer device, with only a minor reduction in maximum achievable $\%P_{Xe}$ and with greater consistency over a larger number of SEOP cell refill processes at a similar polarization lifetime duration (avg. T_1 = 82.4 min, standard deviation σ_{T1} = 10.8 min). Additionally, the effects of varying SEOP jacket temperatures, distribution of Rb metal, and preparation and operation of the fluid path are quantified in the context of device installation, performance optimization and maintenance to consistently produce high ^{129}Xe polarization values, build-up rates (T_b as low as 6 min) and lifetimes over the course of a typical high-throughput ^{129}Xe polarization SEOP cell life cycle. The results presented further demonstrate the significant potential for hyperpolarized ^{129}Xe contrast agent in imaging and bio-sensing applications on a clinical scale.

Keywords: NMR; hyperpolarization; MRI; Xenon-129; Xenon; spin exchange optical pumping; hyperpolarizer; automation; quality assurance; polarimetry

1. Introduction

Nuclear magnetic resonance (NMR) has seen widespread application in the fields of anatomical and physiological clinical imaging. Magnetic resonance imaging (MRI) techniques are advantageous by virtue of their non-invasive, non-ionizing nature, as well

as their good spatial and temporal resolution and superb contrast in soft tissues. One area where traditional MRI techniques are less effective, however, is in the study of lung structure and function. This is primarily due to the inherently low density of requisite proton nuclear spins and B_0 inhomogeneities in lung air sacks, coupled with the low degree of nuclear spin alignment with the applied static magnetic field, i.e., nuclear spin polarization (P). For example, in vivo proton P (P_H) at thermal equilibrium is only ~1×10^{-5} in modern 3 T MRI scanners.

Hyperpolarization of NMR-active nuclear species such as ^{3}He, ^{129}Xe, and other gases can overcome both of these issues. Hyperpolarization techniques are capable of boosting P to the order of unity, resulting in five or more orders of magnitude increase in the detection sensitivity of MR spectroscopic and imaging techniques [1–4]. Such gains in sensitivity facilitate detection of these hyperpolarized (HP) nuclear species in the form of inhalable MR contrast agents [5–16], as well as other applications related to molecular sensing [8,9,17–20]. Their relative safety and suitability for this task are underpinned by both the inert nature and the low natural abundance of ^{3}He and ^{129}Xe, minimizing background signal from non-HP nuclei.

Since straightforward brute force hyperpolarization techniques, reliant on strong magnetic fields (>10 T) and low temperatures (T $\rightarrow$ 0 K), are relatively impractical in an in vivo clinical imaging setting, alternative approaches have been developed to achieve sufficient MR signal enhancement. In the case of HP ^{129}Xe contrast agent production, the spin-exchange optical pumping (SEOP) process is typically employed. In this two-stage process, circular polarization is transferred from laser photons to ^{129}Xe nuclei via Fermi contact interactions with an intermediary electronic alkali metal (e.g., rubidium) vapor [21,22]. There are two available modalities for HP ^{129}Xe contrast agent production, each with their own advantages and drawbacks [23,24]. The first of these is the "continuous-flow" modality [25–29], whereby a continuous flow of a ^{129}Xe-containing gas mixture at low Xe densities is hyperpolarized to high ^{129}Xe P (P_{Xe}), with the HP ^{129}Xe exiting the sealed vessel (termed "SEOP cell") and being collected on a cryogenically-cooled cold finger. The frozen HP ^{129}Xe is then thawed and dispensed in a Tedlar bag, where it can be transiently stored in the gas phase for up to a few hours prior to administration to a human subject. The second modality is a "batch-mode" (stopped-flow) SEOP approach [30–37], whereby a fixed volume of ^{129}Xe-containing gas mixture at high Xe densities is hyperpolarized to high P_{Xe} inside the SEOP cell, which is typically pressurized over 1 atm. After P_{Xe} is built up over time, the HP ^{129}Xe gas mixture can then be ejected into a Tedlar bag without the need for cryo-collection [34,35,38,39].

In addition to high levels of P_{Xe}, either approach can be utilized to produce HP ^{129}Xe gas mixtures in clinically relevant volumes (~1 L or more) and on timescales (<60 min) for imaging studies [23,25,28,35,39–43]. Inhalation of HP ^{129}Xe in this way enables the determination of lung morphology and function via MRI in both human and animal subjects for a wide variety of purposes [7,43–47]. In addition to lung imaging, the solubility of ^{129}Xe in blood allows for this source of hyperpolarization to traverse the alveolar wall and even the blood–brain barrier, additionally facilitating imaging of the brain [48–51], brown fat [52,53], and other bio-sensing [17,19,54,55]. The electronic structure of ^{129}Xe bolsters this advantage by demonstrating measurable changes in chemical shift in response to even small changes in the local environment, providing a novel sensing mechanism.

Despite the inert nature of the typical Xe/N_2 gas mixture utilized in the production of HP ^{129}Xe contrast agents, the procedure is not without some risk. In addition to possessing anesthetic properties, Xe is as a dense gas, and inhalation of sufficiently large quantities has the potential for asphyxiation as oxygen necessary for respiration is displaced. Therefore, in all of the above-mentioned applications in the field of biomedical imaging, HP ^{129}Xe is considered a drug, and as such, production and use are highly regulated and controlled. Producing large quantities of highly-polarized contrast agent in a short time-span is obviously important, but it is also important to ensure a high degree of consistency between

subsequent production cycles to demonstrate excellent reproducibility, and along with it, build trust in the technology.

Although modern ^{129}Xe hyperpolarizer devices utilize ultra-high-purity (UHP) gas mixture sources and inert gas purifiers, these cannot eliminate the presence of impurities completely. Oxygen, water vapor, and other gases may remain in trace quantities, or may ingress from minute leaks from the atmosphere. Over the course of many production cycles, these contaminants will bind with the highly-reactive spin-exchanging alkali metal intermediary, causing the system to degrade in performance. This degradation happens firstly because the presence of small quantities of alkali metal oxide and hydroxide can increase the Rb boiling point compared to that of the pure metal; this change in the colligative properties reduces the alkali metal vapor pressure, and by extension, the efficiency of pump laser absorption. Additionally, the presence of paramagnetic centers results in more rapid relaxation of passing ^{129}Xe nuclei, decreasing the effective longitudinal spin relaxation time constant (T_1) within the SEOP cell. Both of these possibilities result in a detrimental effect on the maximum achievable net spin polarization (%P_{Xe}) [56–58].

Regeneration of SEOP cells containing slightly Rb is possible to a certain extent with high-heat temperature-cycling methods [40], but complete recovery is difficult to achieve. Eventually, SEOP cells will need to be replaced by new ones containing fresh Rb (note the process of Rb refilling of the SEOP cell is a time- and labor-intensive operation spanning several days to ensure sufficient SEOP cell purity). This potential for disruption to operation is particularly problematic when applied to clinical-scale imaging operations, where subjects may need to undergo imaging at scheduled intervals to monitor disease progression or treatment efficacy.

Following on from our previous second-generation (GEN-2) stopped-flow ^{129}Xe hyperpolarizer [59–61] quality-assurance (QA) study [40], we present an expanded pilot QA assessment of a third-generation (GEN-3) automated batch-mode ^{129}Xe hyperpolarizer [39,62] under clinically-relevant conditions of operation. The central motivation for this work is two-fold. First, we determine the effective range of the device parameters in the context of robust operation. Second, we demonstrate the feasibility of refilling the SEOP cell gas mixture many hundreds of times in order to simulate clinical-scale production of HP ^{129}Xe. More specifically, we investigated a course of 700 SEOP cell refills—Xe/N_2 interleaved with UHP N_2 to reduce waste and make experimentation time more feasible—with all experiments described being conducted within a timespan of two months: Over the course of the first 500 refills, we observed negligible decrease in maximum achievable ^{129}Xe polarization (%P_{Xe}), as well as negligible changes in either polarization build-up rates or relaxation time constants (T_1). All SEOP cell refills were complete, i.e., the cell content was evacuated to 5×10^{-2} Torr prior to receiving a fresh load of gas. Hyperpolarization efficiency and effective HP ^{129}Xe T_1 in the SEOP cell were observed to reduce over the course of the final 200 SEOP cell refills, but not to terminal levels where insufficient levels of useful ^{129}Xe polarization were recorded. This study is supplemented by a variety of miscellaneous QA-related measurements, including time- and temperature-dependent mapping of NMR radio frequency (RF) excitation pulse duration (employed for in situ P_{Xe} monitoring), off-resonance RF excitation, and magnetic field calibration. In addition to comparing ^{129}Xe hyperpolarization build-up efficiency as a function of SEOP cell temperature, we also describe how variation in other polarizer-specific parameters, such as the time interval between NMR acquisitions (i.e., repetition time of NMR data sampling) and the amount of cooling power supplied to external fans on the device impact operation of the hyperpolarizer performance.

This work demonstrates that the high reproducibility demanded for clinical-scale HP ^{129}Xe contrast agent production is achievable on our automated GEN-3 hyperpolarizer device, as well as provides a guide concerning good practice for mapping the operational conditions of a ^{129}Xe hyperpolarizer to enable a device's robust and efficient installation and operation in both clinical and research environments. These procedures are intended to be applicable to many designs of batch-mode hyperpolarizers [34,35,37–39] regardless

of site or scale, and should be of interest to those seeking to determine the feasibility of efficiently scaling up ^{129}Xe hyperpolarization from a laboratory setting to a clinical one. Future potential improvements of the GEN-3 hyperpolarizer are also discussed.

2. Materials and Methods

2.1. GEN-3 ^{129}Xe Hyperpolarizer Overall Design

The GEN-3 ^{129}Xe hyperpolarizer is an automated, batch-mode configuration device that can perform rapid and robust HP ^{129}Xe gas production via the SEOP process. Figure 1a schematically displays the GEN-3 hyperpolarizer upper chassis, which illustrates the essential components required for performing the SEOP process and also to perform acquisition of in situ NMR and IR data, respectively required for the calculation of nuclear ^{129}Xe spin polarization ($\%P_{Xe}$) and electronic Rb polarization ($\%P_{Rb}$). Figure 1b,c depict the SEOP processes that takes place inside the sealed SEOP cell. The automated nature of the GEN-3 hyperpolarizer enables the control of all essential components, e.g., optical pumping laser, SEOP cell jacket temperature, B_0 solenoid coil current, and gas-handling manifold solenoid valves. All of these parameters can be configured from an easily-accessible graphical user interface (GUI), operating on a custom-built micro-controller driver module. A GUI screenshot is provided in Figure S8 in the Supporting Information (SI).

An annotated photo of the device is shown in Figure 2. The Rb-loaded SEOP cell (discussed in more detail in Section 2.2) is placed inside the aluminum jacket/cell holder of the GEN-3 hyperpolarizer [39] with an external coating of Arctic Alumina thermal paste (thermal conductivity ~4 $W{\cdot}K^{-1}{\cdot}m^{-1}$ at 25 °C and suitable for operation from −40 to 160 °C), ensuring good thermal contact between the SEOP cell and the aluminum jacket (see Figure 2a). The combination of the aluminum jacket and thermal paste distributes heat application from the heating element to the jacket extremities. Four 6 mm diameter heating cartridges (50 W each) are attached to the jacket via aluminum couplers. The cartridges are used for heating the SEOP cell—temperature ramping from ~25 to ~75 °C can be accomplished within 4 min [39]. The high thermal conductivity of aluminum allows dissipating the heat uniformly along the 7 mm thick jacket body. Heating cartridge operation is controlled by a PID controller (P/N 16B-23, Dwyer Instruments).

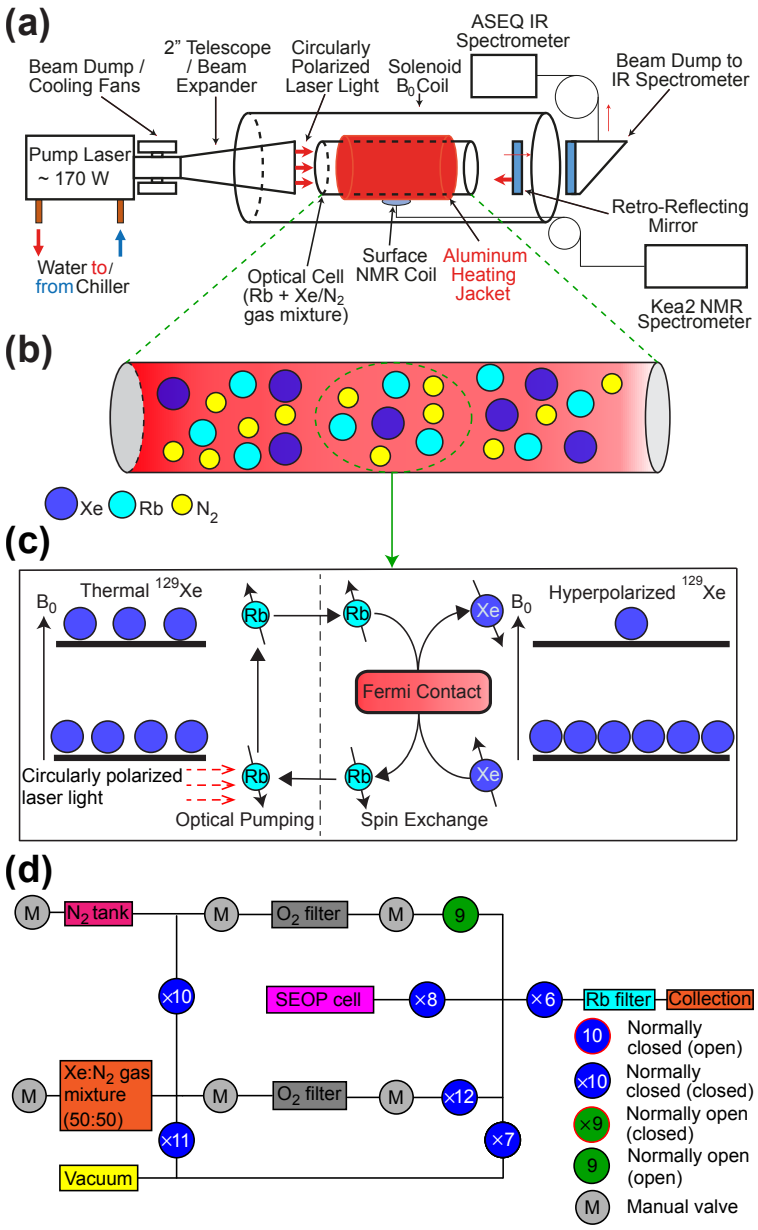

Figure 1. (**a**) Schematic of the GEN-3 ^{129}Xe hyperpolarizer; (**b**) gaseous species involved in the SEOP process; (**c**) ^{129}Xe SEOP process diagram; (**d**) GEN-3 ^{129}Xe hyperpolarizer gas-handling manifold providing the connection of the valves and their numbers. "Normally open (open)" refers to the valve being open in the de-energized state; "normally closed (closed)" refers to the valve being closed in the de-energized state; "normally closed (open)" refers to the valve being open in the energized state; "normally open (closed)" refers to the valve being closed in the energized state. The numbers inside the circles indicate the numbering of the valves, which is employed for automated QA sequence actuation (see the text and figures below for details).

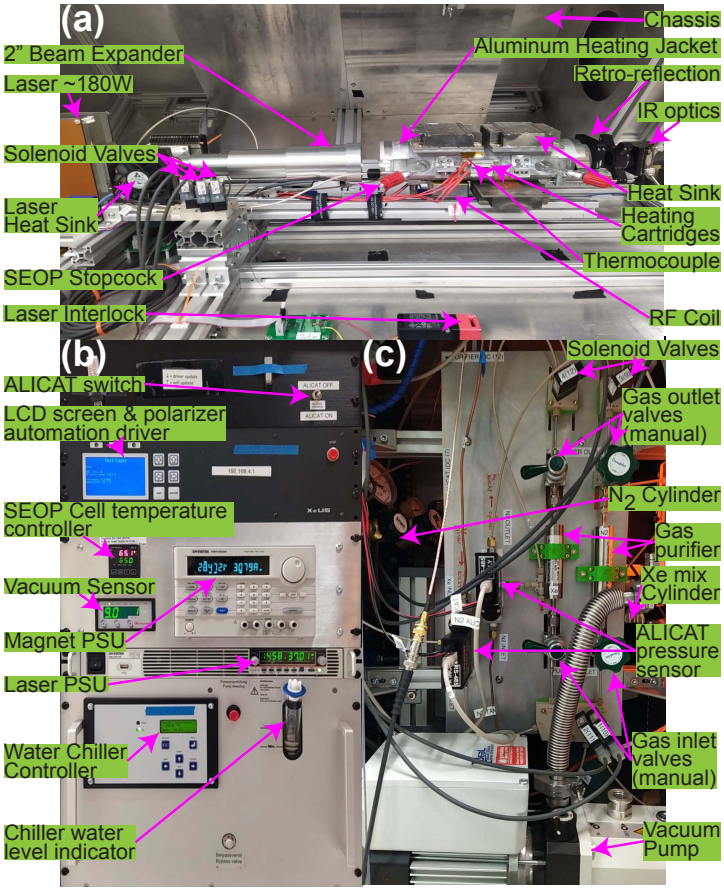

Figure 2. Annotated photographs of the GEN-3 ^{129}Xe hyperpolarizer: (**a**) upper chassis with magnetic solenoid coil removed to show the SEOP cell, NMR coil, and heating jacket, (**b**) front panel housing the driver module, pump laser and magnetic solenoid coil power supply units, temperature and vacuum sensors, and water chiller, and (**c**) side panel housing the gas-handling manifold, gas cylinders and vacuum pump.

Cooling of the SEOP cell is achieved by using three heat sinks adjacent to the aluminum jacket. The circulating air removes excess of heat. The cooling process is facilitated by the dissipation of excess heat outside of the polarizer with the help of ten independent fans attached to the upper chassis of the polarizer. The degree of fan operation can be varied during the SEOP hyperpolarization process and during SEOP cell cooldown (see Figure S6); keeping all fans on facilitates a faster cooling process, whereas keeping fewer fans on during SEOP allows for less cartridge heating power to be utilized. The air ventilation design employed here helps to mitigate Rb runaway [63–66], an undesirable phenomenon whereby the cell temperature and Rb density rapidly increase in a self-reinforcing fashion, destabilizing SEOP and depolarizing the Xe (because the Rb-dense cell becomes opaque to the laser, impeding Rb polarization). Temperature measurement of the SEOP cell surface is performed by using a non-magnetic TKX-type thermocouple (FTC Foil Thermocouple, FluxTeq, Blacksburg, VA, USA).

Circularly-polarized photons (>98% polarization) are supplied by a continuous-wave (CW) pump laser (nominal ~170 W (actual ~140–150 W), Bright-Lock Ultra-500, QPC Laser Technologies, Sylmar, CA, USA), for which maximum driving current for long-term use is 37.5 A. A beam expanding telescope and collimating lens of 2" is used to match the laser output to the diameter of the SEOP cell to help ensure uniform SEOP cell illumination (telescope also provides circular polarization via a $\frac{1}{4}$ wave plate). The pump laser full width

at half maximum (FWHM) was 0.154 nm. The laser resonance was tuned to the Rb D_1 absorption wavelength of 794.77 nm with the help of a thermistor and P312 water chiller (Termotek, Baden-Baden, Germany). The water chiller used for this device runs with a flow rate of >4 L/min and provides 930 W of cooling power. Along with the laser heat sink, the water chiller plays an integral role in maintaining a stable and safe laser temperature, as overheating can cause irreparable damage to the laser diode array (LDA).

A B_0 magnetic solenoid coil (~300 ppm field variance over a 5 cm sphere with up to 3.6 mT magnetic field) surrounds the aluminum jacket and the SEOP cell to produce a field that enables efficient SEOP, while providing sufficient homogeneity for sensitive NMR. The NMR data were collected using a RF surface coil positioned underneath the SEOP cell using a low-frequency Kea2 NMR spectrometer (Magritek, Wellington, New Zealand). An RF pulse amplifier (250 W, BT00250-AlphaA, Tomco Technologies, Stepney, Australia) was used to deliver the desired B_1 RF pulse strength. The RF coil employs a parallel LC circuit optimized for detection at 40.8 kHz, with a resistance R = 20 Ohm (X_R = 20 Ohm), a tuning capacitor of C_T = 33,000 pF with impedance XC of ~130 Ohm at 40 kHz, and a multi-turn inductor of L = 0.5 mH with impedance X_L of ~130 Ohm at 40 kHz (total impedance of 280 Ohm). The RF coil is encased in an aluminum enclosure that is directly mated to the aluminum jacket; the RF coil faces the SEOP cell through a rectangular opening in the jacket. This shielded design eliminates much of the noise from the surroundings, which alternatively can be suppressed using a noise-canceling RF coil operating at the same frequency [38].

Near-infrared (NIR) spectroscopy was performed to estimate the rubidium polarization, $\%P_{Rb}$, as well as monitor the pump laser absorption status in real-time with a high-resolution optical spectrometer (HR1-B, ASEQ Instruments, Vancouver, Canada). At the rear of the SEOP cell, a mirror is used to retro-reflect the laser beam to provide a second pass through the SEOP cell. NMR and NIR data were processed automatically using a MATLAB software package described previously [67]. This automated open-source software package is freely available in the electronic supplemental information of Ref. # [67].

Vacuum and gas handling is performed using a custom manifold equipped with solenoid valves (type 6126, Burkert, Germany), Figures 1d and 2c. These valves are mounted on four polyether ether ketone (PEEK) bases. Manual valves are additionally employed to gate the gas purifiers, reducing the minute amount of contamination from gas mixtures during filling. We anticipate eliminating the manual gating valves for the future operation. All gas/vacuum handling, as well laser power, water chiller, magnet PSU, fans, and SEOP cell temperature are controlled via a Wi-Fi enabled graphical user interface (GUI).

2.2. SEOP Cell Design

The core of the GEN-3 hyperpolarizer device is the SEOP cell that is used to produce HP ^{129}Xe gas. The SEOP cell (made from Pyrex glass) has an internal volume of 500 mL and the diameter of 2″ (Mid Rivers Glassblowing, Saint Peters, MO, USA), which matches the expanded pump laser beam. Preparation and Rb filling protocols of the SEOP cell can be found elsewhere [39]. Briefly, the cell glass surface is extensively cleaned with a base solution (potassium hydroxide in methanol) and treated with a solution of Surfasil™ siliconizing agent in hexane to create a protective surface layer on the inner cell wall. This serves to reduce the effects of depolarizing collisions between HP ^{129}Xe nuclei and paramagnetic centers within the walls of the SEOP cell, enhancing ^{129}Xe in-cell T_1—often to >2 h [39]. After the preparation and filling of the SEOP cell with ~0.5 g of Rb, the Rb metal was distributed across the inner surface by applying heat (using a heat gun) on one side while applying cooling on the exterior SEOP cell surface (e.g., by using dry ice) to condense the Rb vapor. Distributing the Rb metal as a high-surface-area film along the cell surface facilitates the process of creating a high-density vapor when the cell is heated for SEOP, as discussed below (see also Figures S4 and S5 in the SI; Figures S4 and S11 provide an annotated photo and the gas manifold schematic of the Rb “spreading”/distribution

setup, respectively). The SEOP cell is closed from the external environment with the help of two independent stopcocks. We only use one of the stopcocks for gas and vacuum manipulations when the SEOP cell is installed within the hyperpolarizer. The second stopcock is helpful during SEOP cell cleaning and preparation. After placing the SEOP cell inside the aluminum heating jacket, PEEK tubing (1/8 in. OD) is employed to connect one side of the SEOP cell to the inlet valve of the gas manifold—see valve 8 in Figure 1d.

The SEOP process was performed with the stopcock in either an open or closed configuration. For the closed configuration, the stopcock is closed after filling the SEOP cell with a Xe/N_2 gas mixture, and then the SEOP process is performed. The 'stopcock-open' configuration is useful for production and ejection of HP ^{129}Xe and SEOP cell reloading with fresh, unpolarized gas, because the cell must be mated to the rest of the gas-handling manifold for these operations. The 'stopcock-closed' configuration seals the SEOP cell entirely from the outside environment for the long-term (weeks) storage to minimize the ingress of minute amount of impurities into the SEOP cell.

2.3. GEN-3 ^{129}Xe Hyperpolarizer Calibration

For computation of $\%P_{Xe}$, we compare the signal from HP ^{129}Xe to that of a signal reference phantom with the same geometry and known concentration and nuclear spin polarization (see Section 2.4). In our device, we perform NMR detection of HP ^{129}Xe and the thermally polarized proton signal reference phantom (500 mL water doped (placed in the same shaped glassware) with 10 mM $CuSO_4$; ^{1}H T_1 ~ 0.05 s) at the same resonance frequency, 40.8 kHz (Figure 3a,b)—achieved by adjusting the electromagnetic field current to compensate for the ~3.6-fold difference between the ^{1}H and ^{129}Xe gyromagnetic ratios (γ_{1H} and γ_{129Xe}). While in principle, the magnetic field can be adjusted with the aid of a gaussmeter, in practice, the precision of typical gaussmeters is generally insufficient for this task. This practical challenge was also confronted in the context of low-field parahydrogen induced hyperpolarizers [68], because the B_1 strength of RF pulses and the quality factor of the RF coil itself allows robust operation only in a limited resonance frequency range. Therefore, two experimental challenges must be addressed in the context of quantitative comparison of the HP signal and thermally polarized reference signal with the goal to robustly determine $\%P_{Xe}$. The first one of these challenges is precise calibration of the electromagnet current to ensure on-resonance condition, and the second one is identification of a frequency and electromagnet current range with robust device operation. The latter is important in the context of operation at off-resonance conditions due to ambient field variance.

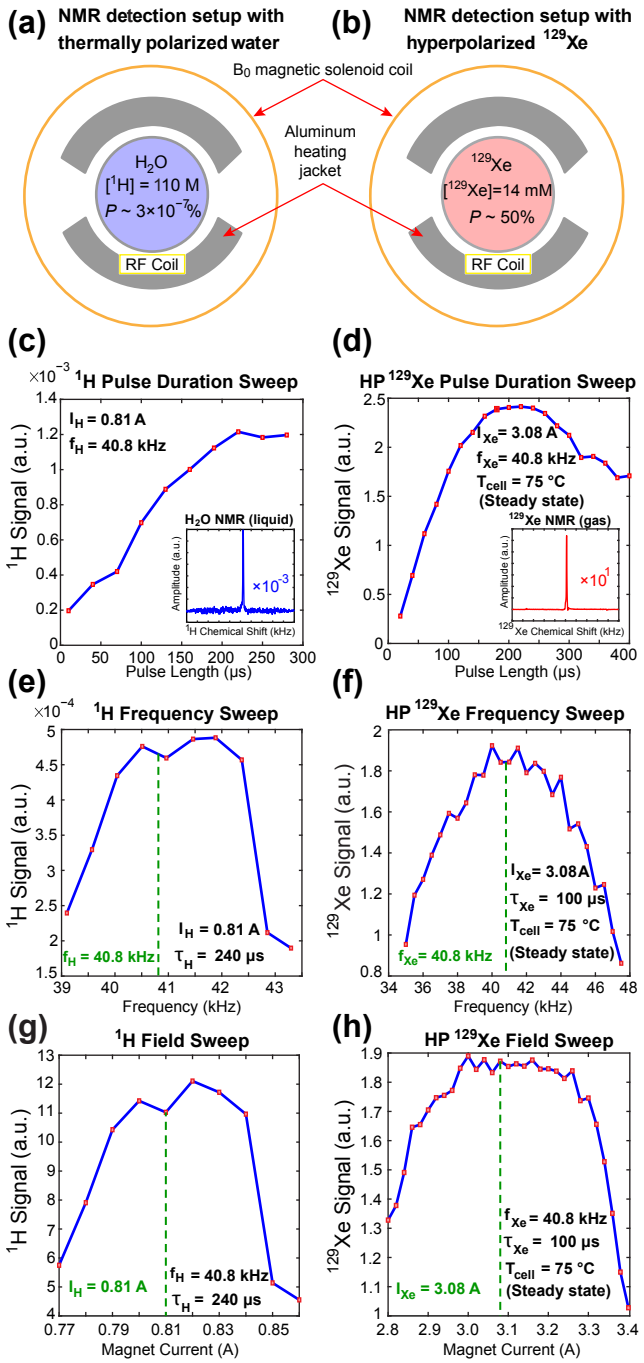

Figure 3. Schematic representation of the ^{1}H (**a**) and ^{129}Xe (**b**) sample arrangements. Displays (**c**,**d**) show RF pulse duration sweep for thermal ^{1}H and HP ^{129}Xe, respectively, with NMR spectra shown as inserts. Displays (**e**,**f**) show NMR signal intensity as a function of resonant frequency for thermal ^{1}H and HP ^{129}Xe, respectively, at fixed magnetic field current. Displays (**g**,**h**) show NMR signal intensity as a function of magnetic field driver current for thermal ^{1}H and HP ^{129}Xe samples, respectively. For protons, the ~1 mT field is swept over the 10% range reflecting the maximum possible fluctuation due to polarizer magnet alignment with the Earth's magnetic field of ±0.05 mT. Note, RF amplifier outputs a 3.6-fold higher voltage for ^{129}Xe RF excitation pulses compared to that for proton RF pulses to compensate for the difference in gyromagnetic ratios of the nuclei.

The HP ^{129}Xe signal can be readily detected with a single shot, due to the significant signal enhancement (7–8 orders of magnitude) arising from hyperpolarization. Calibration of the RF pulse duration (τ_{Xe}), B_0 electromagnet current (I_{Xe}), and resonant frequency (f_{Xe}) was performed using single-shot NMR spectroscopy of steady-state HP ^{129}Xe after $\%P_{Xe}$ build-up in a 1000 Torr Xe/1000 Torr N_2 SEOP cell (Figure 3). Note, when the thermally polarized water phantom was employed, NMR signal was decreased by ~4 orders of magnitude, thus requiring signal averaging. In total, ~20,000 scans were employed to obtain a good signal-to-noise ratio (SNR)—see Figure 3c (inset). This approach facilitated calibration of RF pulse duration (τ_H), B_0 electromagnet current (I_H), and resonant frequency (f_H). $CuSO_4$ doping enabled the repetition time to be reduced to 0.3 s. The ratio of I_{Xe} and I_H corresponding to the precise resonance conditions of the two spins may deviate from $\gamma_{1H}/\gamma_{129Xe}$ due to the presence of the Earth's magnetic field; therefore, a magnetic field sweep should be performed for both nuclei during the device installation process. On-resonance condition for ^{129}Xe (f_{Xe} = 40.8 kHz at ~3.6 mT) was found with I_{Xe} = 3.08 A.

Application of RF pulses with larger effective pulse tipping angle leads to increased depolarization of HP ^{129}Xe nuclei within the SEOP cell, and frequent application may alter apparent parameters measured during SEOP process (e.g., reduced apparent T_1 relaxation time constants—see below). Therefore, it is important to determine an appropriate balance between the amount of NMR signal generated by each pulse and polarization consumption. Because $\gamma_{1H} \approx 3.6 \cdot \gamma_{129Xe}$, the RF power of the ^{129}Xe excitation RF pulse was increased by $(3.6)^2$ in order to achieve the same B_1 strength (and by extension spatial RF excitation profile) for both spins. Note, when the RF power (measured as $(V_{RMS})^2/50$, where $V_{RMS} = Vpp/2/\sqrt{2}$; Vpp is the voltage of the oscilloscope set to 50 Ohm load) is mis-calibrated, the non-identical B_1 fields applied to ^{1}H and ^{129}Xe spins lead to an over- or under-estimate of measured P_{Xe}; for example, Figure S9 shows an example of using "stronger than required" ^{129}Xe B_1, leading to overestimation of P_{Xe} by a factor of 1.22. Based on the RF pulse calibrations shown in Figure 3c,d, we selected $\tau_H = \tau_{Xe}$ = 150 µs as the pulse length for the subsequent QA studies. In some cases, where signal quantification for polarimetry purposes is not required (e.g., Figure 3), other pulse durations were employed that we tailored to the need of the experiment. For example, the water experiments used a pulse length of τ_H = 240 µs to maximize the otherwise-limited SNR.

Furthermore, we also performed resonance frequency sweeps (Figure 3e,f) and electromagnet current sweeps (Figure 3g,h). Besides measuring the respective Larmor frequencies and resonance electromagnet current values for ^{1}H and ^{129}Xe, these plots also provide insights about the robust ranges of operation for the electromagnetic solenoid coil. In the context of resonance frequency, the linear range of operation is ~2 kHz in both cases, likely reflecting limitations imposed by the RF coil quality factor, Q (estimated at ~30). With respect to the electromagnet current, the linear range of operation is ~0.05 A for ^{1}H and 0.25 A for ^{129}Xe. These operational ranges ensure the ability to perform robust and reproducible measurements of corresponding NMR signals. For this study, we used 0.810 A and 3.080 A current values for ^{1}H and ^{129}Xe spins, respectively, to reach the nominal 40.8 kHz resonance frequency for both spins.

2.4. SEOP Process

The photons supplied by the pump laser are absorbed by the outer-shell electron of Rb vapor atoms inside the SEOP cell. This absorption happens at the Rb D_1 wavelength (794.77 nm, air referenced). Rb evaporation is much more efficient once the temperature is above the melting point (~39.3 °C [69]), allowing one to establish a sufficiently high concentration in the gas phase to induce laser light absorption. Nevertheless, the absorption of laser photons may still be limited at lower SEOP cell temperatures, as the Rb inside the SEOP cell may have limited surface distribution. As a result, the process to establish equilibrium gas-phase concentration (at a given temperature) may be kinetically limited due to small surface area of the Rb metal layer on SEOP cell surfaces. To mitigate this

practical experimental limitation, it is often helpful to distribute the Rb metal as a thin film to increase the effective surface area inside the SEOP cell (see SI for more details).

Once the SEOP cell preparation has been completed and the cell loaded with a gas mixture (nominally 1000 Torr Xe/1000 Torr N_2; the custom mixture employing natural-abundance Xe (ca. 26.4%) was sourced from Nova Gas Technologies, North Charleston, SC, USA), the cell is "broken in" with a thermal cycling procedure: first, polarization build-up is typically performed at the highest stable temperature (i.e., below the temperature at which Rb runaway is observed to occur). Polarization build-up continues until steady state is reached, Figure 4c. After reaching these conditions, the SEOP cell is then cooled to room temperature (~25 °C) and maintained there for 30 min to allow for sufficient amount of time to the gas-phase Rb metal to evenly condense on SEOP walls. During the cooling process, the laser power is reduced gradually (down to ~15 W minimum power) until the recorded SEOP cell jacket temperature reaches ~38 °C (i.e., below the Rb melting point); this practice helps to ensure that no significant accumulation of condensed Rb occurs on the front or rear windows of SEOP cell (which can otherwise lead to hot spots).

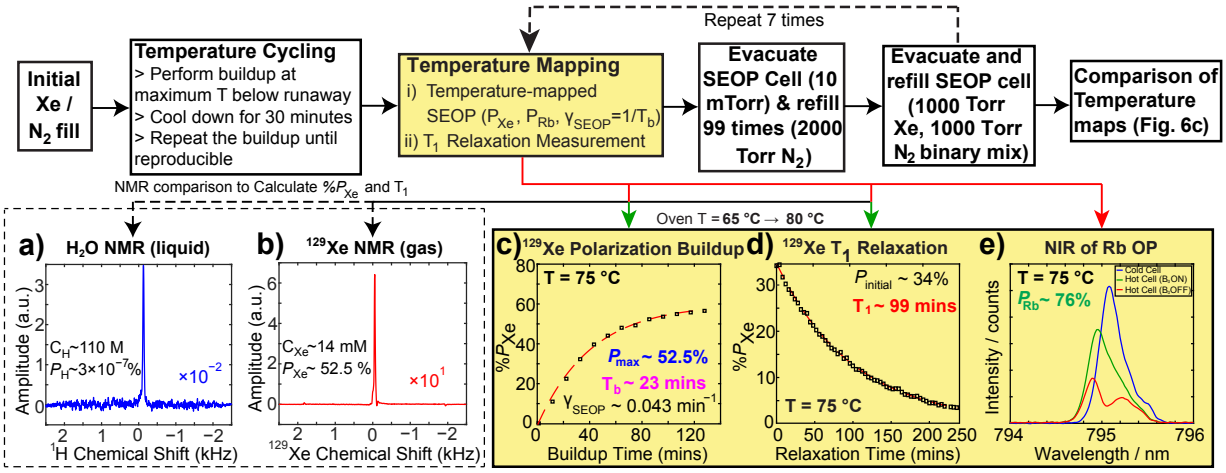

Figure 4. Synopsis of SEOP cell reloading quality assurance (QA) study consisting of 700 total SEOP cell gas mixture refills. ^{129}Xe polarization ($\%P_{Xe}$) is calculated by comparing the peak area integral of HP ^{129}Xe NMR spectra (**b**) with thermally-polarized ^{1}H reference spectra (**a**). This process is repeated at fixed intervals to observe ^{129}Xe polarization build-up (**c**) and decay (**d**) over time, respectively, providing a build-up rate (γ_{SEOP}) and a relaxation time constant (T_1) for each corresponding curve. Comparison of NIR pump laser spectra (**e**) facilitates calculation of an estimate of the average Rb polarization ($\%P_{Rb}$) throughout the cell. Key performance indicator (KPI) variables include steady-state $\%P_{Xe}$, γ_{SEOP}, T_1, and $\%P_{Rb}$, which can also be plotted as a function of SEOP cell temperature, as described in the text.

This process is repeated until we obtain two nearly-identical polarization build-up curves (Figure 4c) under identical conditions; in case additional rounds of temperature cycling are determined to be necessary, we have found this to be an indication of insufficient distribution of Rb metal in the SEOP cell.

Before measuring the HP ^{129}Xe build-up rate, the SEOP cell was heated to the desired set point while the laser current was maintained below the nominal operating current of 37.5 A, corresponding to an off-resonance condition, i.e., virtually no photon absorption occurs by Rb. This practice ensures effectively negligible polarization at the start of each build-up experiment (performed at full laser power and on D_1 resonance corresponding to 37.5 A current), which simplifies the fitting mono-exponential build-up function to $y = \%P_{Xe}*(1-\exp(-x/T_b))$, where T_b is the build-up time constant (mins), x is time (mins), and $\%P_{Xe}$ is the maximum P_{Xe} at $t \rightarrow \infty$ (note the fitting function has two variables as $y(0) = 0$), described in detail in previous work [67].

During hyperpolarization build-up experiments, NMR signals from the SEOP cell were acquired at six-minute intervals (or more frequently if needed) to calculate P_{Xe} using Equation (1),

$$P_{Xe} = P_H\left(\frac{C_H}{C_{Xe}} \cdot \frac{\gamma_H}{\gamma_{Xe}} \cdot \frac{S_{Xe}}{S_H}\right) * Corr(T_2^*) \quad (1)$$

where P_H is the thermal polarization of protons and ^{129}Xe at 40.8 kHz—equilibrium thermal polarization values are the same for both ^{1}H and ^{129}Xe when utilizing this detection frequency. C_H and C_{Xe} are proton and ^{129}Xe concentrations, γ_H and γ_{Xe} are ^{1}H and ^{129}Xe gyromagnetic ratios, and S_H and S_{Xe} are signal peak integral values of ^{1}H and ^{129}Xe nuclei, respectively, obtained at an RF pulse length of 150 µs and at a pulse amplitude of -36 dB for ^{1}H and -25.3 dB for ^{129}Xe, corresponding to ~30 mW and 360 mW, respectively). Because of the difference in the rate of transverse signal decay T_2^* for ^{129}Xe and ^{1}H, a correction factor, $Corr(T_2^*)$, was utilized [60]:

$$Corr(T_2^*) = \frac{T_{aq}}{T_2^*Xe} - \frac{T_{aq}}{T_2^*H} \quad (2)$$

Here, T_{aq} is the pre-acquisition delay time to mitigate the ring-down effect of the RF coil (3 ms in our experiments), and T_2^*Xe and T_2^*H are the observed T_2* spin relaxation time constants in ms for ^{129}Xe and ^{1}H, respectively. At the end of each build-up experiment, an exponential curve fit of ^{129}Xe polarization build-up over time was performed using Equation (3) via automated MATLAB processing software described previously [67]:

$$P_{Xe}(t) = P_{max}[1 - \exp(-\gamma_{SEOP}(t))] + P_{Xe}(0) \quad (3)$$

At any time, t (in seconds) after commencement of polarization, the ^{129}Xe polarization is determined as a function of the maximum achievable polarization (P_{max}) at steady state and the polarization build-up rate (γ_{SEOP}). P_{Xe} at the start of the build-up experiment (i.e., t = 0) is negligible because of high-flip angle "crushing" RF pulses (at least 1000 pulses of ~900 µs duration each, applied over the course of 300 s with repetition time of ~0.3 s) are applied before the start of a new polarization build-up experiment.

The polarization build-up rate (γ_{SEOP}) determines how quickly steady-state conditions are reached,

$$\gamma_{SEOP} = \frac{1}{T_b} = \gamma_{SE} + \Gamma_{Xe} = \gamma_{SE} + \frac{1}{T_1} \quad (4)$$

where T_b is the polarization build-up time constant, γ_{SE} is the spin-exchange rate (min^{-1}) between Rb electrons and ^{129}Xe nuclei, Γ_{Xe} is the rate of spin destruction (min^{-1}) for ^{129}Xe nuclear spins, and T_1 is the longitudinal spin relaxation time constant (min). γ_{SEOP} is obtained from the mono-exponential data fitting of the build-up experiment (e.g., Figure 4c), and T_1 is obtained from the mono-exponential data fitting of HP ^{129}Xe relaxation, monitored by small-angle RF excitation pulses, i.e., T_1 decay curve, Figure 4d.

Five NIR spectroscopic measurements (each) were collected under steady-state conditions at the end of each build-up experiment without changing cell temperature or laser power. These spectra were acquired under two different configurations, with the B_0 magnetic field either powered on (I_{Xe} = 3.08 A) or off (I_{Xe} = 0 A). From these signal-averaged NIR spectra and using Equation (5), we can estimate the Rb polarization, P_{Rb} [32],

$$|P_{Rb}| = \left|\frac{ln(I_{hot}) - ln(I_{cold})}{ln(I_0) - ln(I_{cold})}\right| \quad (5)$$

where I_{hot} and I_0 represent the peak area integrals of the pump laser transmission spectra acquired at the temperature where SEOP is performed, with homogeneous B_0 magnetic field powered on and off, respectively. I_{cold} represents the peak area integral of the pump laser transmission spectra acquired under conditions of no optical pumping at room temperature with the magnetic field powered on, as described above. These calculations were performed for each SEOP cell temperature investigated.

At the conclusion of each day of experimentation, an overnight T_1 relaxation measurement was performed to determine the ^{129}Xe polarization decay rate (e.g., Figure 4d). From steady-state polarization conditions, the SEOP cell was cooled down to room temperature (~25 °C) by turning on all ten chassis exhaust fans (six already having been on during the SEOP process). While cooling down the SEOP cell, the laser current was maintained as follows. The laser amperage was set to 37.5 A (max power) at the Rb D_1 resonance frequency at the temperature above 50 °C to minimize $\%P_{Xe}$ losses during the cool-down process [59]. Laser power was reduced to ~20 W (corresponding to laser PSU current of 15 A and being off-resonance) between 38–50 °C to minimize Rb deposition on the optical flats. The laser power was reduced to 0 W at the temperature below 38 °C, i.e., below Rb melting point. Only once the SEOP cell was cooled down to below 38 °C and the pump laser was completely powered down to ensure no additional laser heating (or optical pumping) occurs did further NMR spectroscopic acquisitions begin. T_1 relaxation measurements were then performed by acquiring ^{129}Xe spectra at 4- or 6- minute intervals using 150 µs RF pulses (unless otherwise noted) with I_{Xe} = 3.08 A. The ^{129}Xe in-cell T_1 measurements were not corrected for RF-pulse-associated magnetization losses.

2.5. SEOP Temperature Mapping

We utilized a SEOP experiment temperature range of 65 to 95 °C (typically with 5 °C intervals) for performing polarization build-up and acquisition of the ^{129}Xe NMR and pump laser NIR spectra. The recorded data were then analyzed and presented in the form of a pseudo-2D plot, which we refer to as temperature map. At SEOP cell temperatures below 65 °C, the Rb vapor density and consequent polarization build-up rate was considered too slow to be useful in a clinical-scale production setting. With the increase in temperature inside the SEOP cell, the Rb vapor density increases exponentially, resulting in an accelerated rate of spin exchange, but also reduced overall $\%P_{Rb}$ (due to increased cell opacity to the incident laser light).

We performed 'temperature mapping' of the SEOP cell across the given temperature range, acquiring ^{129}Xe polarization build-up, NIR absorption, and ^{129}Xe T_1 relaxation spectroscopic data. In the context of the cell-refill QA study, these temperature-mapping experiments helped to monitor the SEOP process performance under various experimental conditions (and also the change in the key parameters). Furthermore, the finding of an optimal temperature that balances between polarization build-up rate and Rb runaway temperature is essential for consistency in clinical HP ^{129}Xe production.

2.6. NMR Sampling Frequency

NMR measurements for the calculation of P_{Xe} and T_1 were acquired at 6 min intervals for this study unless noted otherwise. This value was chosen to provide enough data points for reliable calculation of both P_{Xe} and T_1, while minimizing depolarization of HP ^{129}Xe gas. A comparison of NMR build-up and relaxation experiments performed at different NMR pulse acquisition frequencies can be found in Figure S6 (SI).

2.7. SEOP Cell Reloading QA Study Design

The QA study to test SEOP cell longevity with respect to gas reloading was performed to demonstrate the performance and reproducibility of the GEN-3 ^{129}Xe hyperpolarizer to produce highly-polarized, high-density HP ^{129}Xe gas mixtures in the batch-mode configuration. Before filling the SEOP cell with a Xe/N_2 gas mixture (2000 Torr total pressure with 50% Xe and 50% N_2), the gas-handling manifold inlet line was evacuated to a pressure of 10 mTorr followed by ultra-high-purity (UHP, >99.999%) N_2 purging (3 cycles). UHP N_2 gas was obtained from Airgas in Detroit, MI, USA. This procedure reduced the probability of any significant presence of unwanted impurities (e.g., O_2 and H_2O) within the PEEK tubing or inside the SEOP cell that could otherwise result in Rb oxidation. After the completion of temperature mapping with a given Xe/N_2 gas mixture (see Section 2.5), we performed 99 SEOP cell refills with UHP N_2. The refills with UHP N_2 were followed by refill with a

Xe/N_2 gas mixture with SEOP temperature mapping. Note, only 98 UHP N_2 refills were performed between the first two points in the study. This practice simulated the process of normal SEOP cell evacuation and refilling on a clinical production scale, without the need to use large quantities of comparatively expensive Xe gas [40]. Moreover, this practice reduces the enormous amount of time that would be otherwise required for refilling the cell with a Xe/N_2 gas mixture every time and performing temperature mapping (1–2 days per temperature map). The overall flowchart describing the SEOP cell reloading QA study process is outlined in Figure 4.

The sequence for performing automatic vacuum and gas manipulations on the GEN-3 hyperpolarizer is coded into the controller driver module, and is represented schematically in Figure 5. This sequence facilitates the safe and reproducible automated evacuation and refilling of the SEOP cell with either UHP N_2 or Xe/N_2 gas mixtures. This process retains some manual checks that will ensure the user is performing the correct adjustments (e.g., manual opening and closing of gas cylinders) and will ensure that all the configurations are correct (e.g., valves are correctly open/closed at the correct times). The sequence allows the user to choose between Xe/N_2 gas mixture or N_2 SEOP cell refills, and in the case of N_2 refills, how many cycles to perform. Therefore, a high degree of consistency in the study can be achieved.

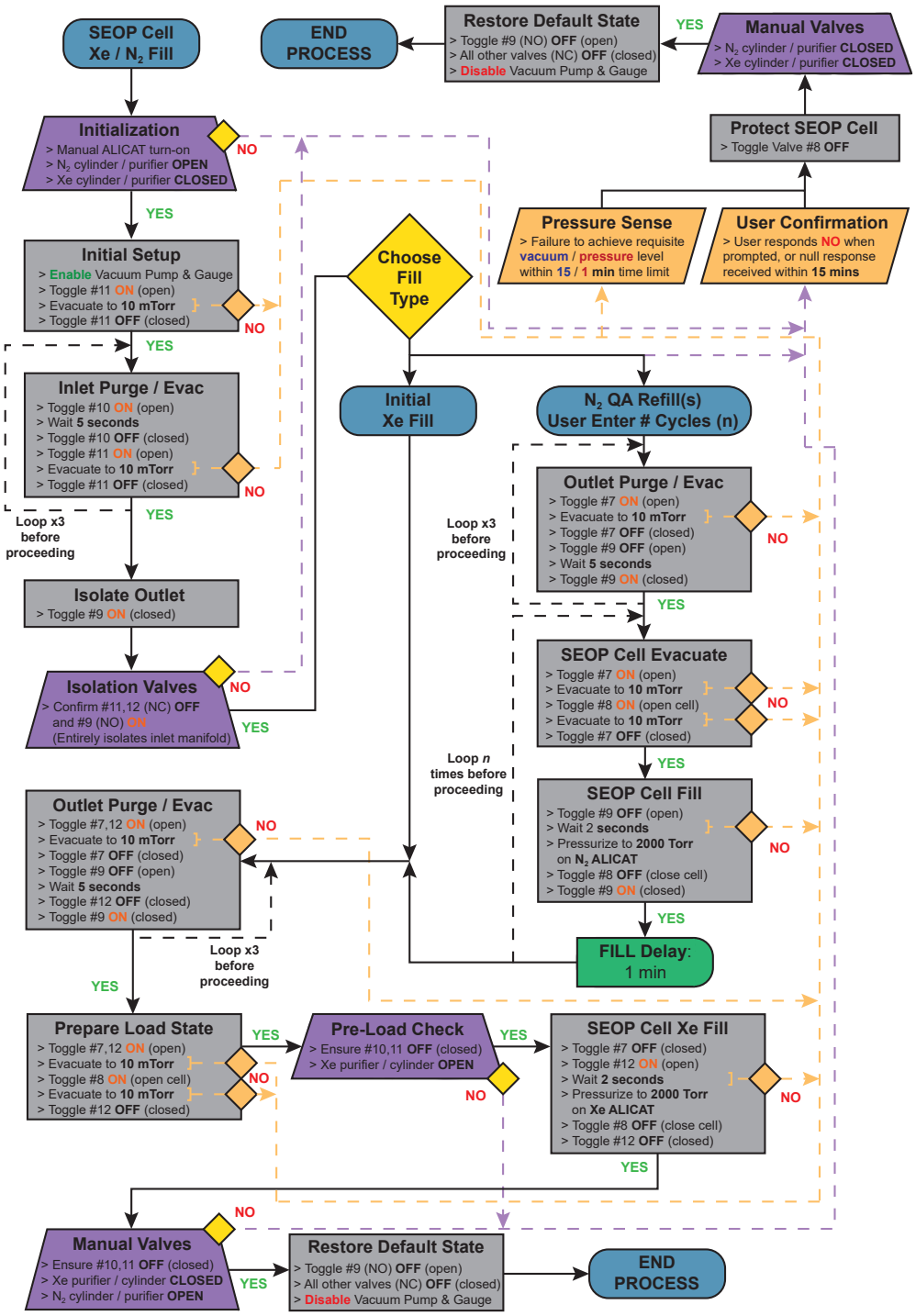

Figure 5. Process flowchart depicting the automated SEOP cell reloading quality assurance (QA) refill sequence coded into the GEN-3 ^{129}Xe hyperpolarizer driver module for the purpose of evacuating and refilling SEOP cells. Note, the yellow diamonds indicate condition states. For example, when the user does not provide input within 15 min, the sequence follows the "NO" path. Another example is vacuum level reaching 10 mTorr, which has to be achieved within 15 min, otherwise the sequences defaults to the "NO" path. The timeout duration is 15 min for all yellow diamonds. The valve numbering is provided in Figure 1d.

3. Results and Discussion

3.1. SEOP Cell Reloading QA Study

The GEN-3 hyperpolarizer exhibits robust performance reproducibility. In our previous QA study on the second-generation (GEN-2) ^{129}Xe hyperpolarizer [40], we performed an initial temperature-mapping experiment on the first Xe/N_2 gas mixture fill, and selected a single temperature point (80 °C) from that experiment at which to compare $\%P_{Xe}$, γ_{SEOP}, and $\%P_{Rb}$ from subsequent SEOP cell refills. In this GEN-3 device study, a temperature map was acquired at SEOP jacket temperatures between 65 and 80 °C (intervals of 5 °C) for all 1000 Torr Xe/1000 Torr N_2 gas mixture refills, starting with the first fill (Figure 6a), then every 100th subsequent fill to a maximum of 700 (Figure 6b). Temperature-dependent build-up maps for the intermediary fills are shown in Figure S1 (SI). The selected temperature range was chosen to provide polarization build-up rates fast enough to ensure a reasonable time-frame for experimentation, while also avoiding unstable Rb runaway regimes at high temperatures.

The studied SEOP cell exhibited a maximum ^{129}Xe polarization exceeding 50%, in overall agreement with previous studies employing a GEN-3 ^{129}Xe hyperpolarizer device [39,62]. This level of polarization was reasonably consistent across the range of temperatures investigated, with only a slight reduction at the highest temperature of 80 °C, where the increased vapor density of Rb inside the cell likely led to a reduction in optical pumping rates at the rear of the cell—see the significant reduction in $\%P_{Rb}$ from ~100% to 65% across the investigated temperature range. This was mitigated by high spin-exchange rates, and hence, high hyperpolarization build-up rates ($\gamma_{SEOP} = 0.082 \pm 0.011$ min^{-1} at 80 °C), equating to a build-up time constant of only ~12 min, Figure 6a.

This temperature-mapping process was repeated seven more times at intervals of 100 total SEOP cell refills, with all refills comprising the same 1000 Torr Xe/1000 Torr N_2 fraction. Figure 6b displays the results of the last set of experiments for comparison. Of particular note is the drastic reduction in steady-state $\%P_{Xe}$ compared to Figure 6a, especially at low temperatures (47.5 ± 1.7% dropping to 10.0 ± 1.3% at 65 °C). This effect also manifests as a reduced ^{129}Xe T_1 (70.1 ± 0.8 dropping to 32.0 ± 2.3 min). The reduction in maximum achievable ^{129}Xe polarization was less pronounced at higher SEOP cell temperatures, however. This result would be consistent with the change of Rb colligative properties affecting the Rb gas-phase density and hence optical pumping rate. This explanation would be consistent with the decreased optical pumping rate γ_{SEOP}.

A comparison of ^{129}Xe polarization build-up efficiency at a selected SEOP cell temperature (75 °C in this example, all other variables remained constant) as a function of the number of SEOP cell refills is presented in Figure 6c. The key observation from these results is that no noticeable decrease in $\%P_{Xe}$ was observed for the first 500 cell refills (avg. $\%P_{Xe} = 51.0$ with standard deviation $\sigma_{PXe} = 3.02\%$). A noticeable decrease in $\%P_{Xe}$ was seen in subsequent experiments, but a final polarization value (after completing 700 refills) $\%P_{Xe} = 24.4 \pm 2.4\%$ with $\gamma_{SEOP} = 0.019 \pm 0.003$ min. Although the ^{129}Xe hyperpolarization build-up rate was significantly reduced by the final SEOP cell gas mixture refill, across the first 600 refills a high degree of consistency was observed (avg. $T_b = 25.1$ min with standard deviation $\sigma_{Tb} = 3.05$ min). The HP ^{129}Xe T_1 exhibited more variation than other key performance indicators, but was still reasonably consistent across the first 400 SEOP cell gas mixture refills (avg. $T_1 = 82.4$ min with standard deviation $\sigma_{T1} = 10.8$ min). The ^{129}Xe hyperpolarization build-up rate γ_{SEOP} (=$1/T_b$) remained consistent throughout the study with the exception of the last refill at 700 cycles, where T_b has increased—likely reflecting a decrease in the Rb vapor pressure because of partial Rb oxidation as discussed above. Finally, the rubidium polarization $\%P_{Rb}$ showed similarly negligible change across the first 500 SEOP cell gas mixture refills (avg. $\%P_{Rb} = 77.8\%$ with standard deviation $\sigma_{PRb} = 7.4\%$), only increasing to ~100% for the final 200 refills where Rb oxidization likely became more substantial; a lower Rb density would translate to higher photon to Rb ratio at a given temperature. Thus, while $\%P_{Rb}$ is higher, lower $\%P_{Xe}$ is attained at the near-end of the SEOP cell lifetime because of the significantly lower γ_{SEOP} and T_1.

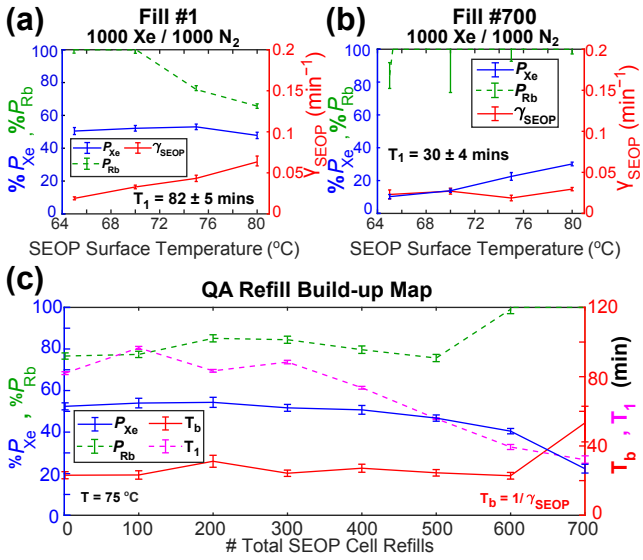

Figure 6. (**a**) Steady-state $\%P_{Xe}$, γ_{SEOP}, and $\%P_{Rb}$ measurements as a function of cell jacket temperature following fill #1 (the initial 1000 Torr Xe/1000 Torr N_2 gas mixture fill at the commencement of the QA study). (**b**) Steady-state $\%P_{Xe}$, γ_{SEOP}, and $\%P_{Rb}$ measurements as a function of SEOP cell surface temperature following fill #700 (the final gas fill of the QA study); note the reduction in $\%P_{Xe}$ and T_1 values. (**c**) Steady-state $\%P_{Xe}$, $\%P_{Rb}$, and T_b measurements after polarization build-up at a SEOP cell surface temperature of 75 °C, as well as post-build-up T_1 relaxation measurements, plotted versus the number of total gas mixture refills. The solid lines are added to guide the eye.

3.2. SEOP Cell Operation with Open Stopcock

One important limitation of the QA study described above was the fact that the (manually controlled) SEOP cell stopcock was closed during hyperpolarization throughout; however, the stopcock was opened for the duration of each 100 refill cycles, which lasted ~18 h. This requirement for manual operation of the stopcock is undesirable for routine clinical use, and it was employed for this QA study only. Opening and closing the SEOP cell requires the pump laser to be powered down so that the upper chassis of the GEN-3 hyperpolarizer device can safely be opened for access, thus increasing the turnaround time between polarization build-up experiments. To more closely simulate routine clinical-scale production conditions, a series of additional SEOP experiments were performed with the SEOP cell stopcock open to the gas-handling manifold inlet, which is automatically and fully controlled by the solenoid valves and mass flow controllers (Figure S8). Figure 7 shows a pair of SEOP temperature maps obtained with the cell stopcock closed (Figure 7a) or open (Figure 7b), respectively—but under otherwise-identical experimental conditions. A difference in optimal temperature (T_{OPT}) for performing SEOP likely arises as a consequence of the increased volume and reduced effective Rb vapor density in the stopcock-open configuration compared to the stopcock-closed configuration. From a comparison of Figure 7a,b, it can be inferred that this optimal temperature delta is on the order of ~5–10 °C, with maximum achievable ^{129}Xe polarization $\%P_{Xe}$ values of 47.6 ± 1.6% and 42.4 ± 1.5% observed at SEOP jacket temperatures of 70 and 80 °C in the stopcock-closed and stopcock-open configurations, respectively. In both configurations, a reduction in $\%P_{Xe}$ is observed at high temperatures and Rb vapor densities; the reduction is more pronounced in the stopcock open configuration, where $\%P_{Xe}$ drops to 28.5 ± 1.0% at the maximum SEOP jacket temperature of 95 °C—a reduction by 1.33-fold from T_{OPT}. However, this loss in maximum achievable $\%P_{Xe}$ is offset by a significant gain in polarization build-up rate γ_{SEOP} in the stopcock open configuration—peaking at 0.149 ± 0.027 min^{-1} at a SEOP cell temperature of 95 °C, compared to a maximum recorded value of 0.070 ± 0.005 min^{-1} at 85 °C in the stopcock closed configuration. This build-up rate increase is welcomed, because it allows

for significant scaling up of production efficiency. ^{129}Xe T_1 under both configurations was comparable and appreciably long, i.e., in excess of two hours, Figure 7a,b, respectively.

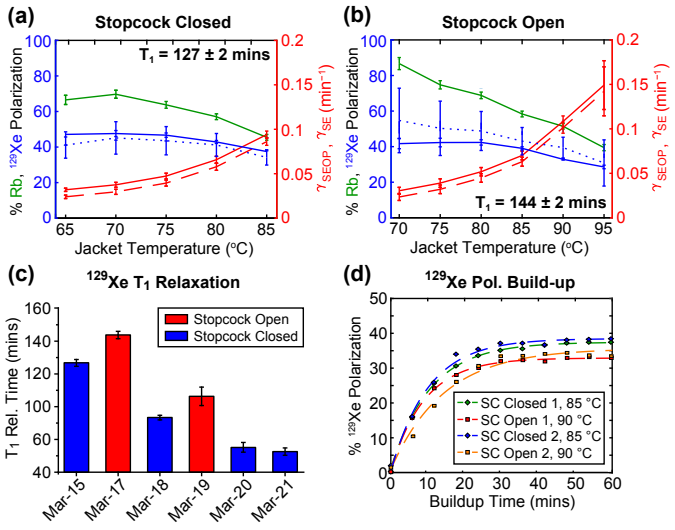

Figure 7. Upper displays (**a**,**b**) describe steady-state $\%P_{Xe}$, γ_{SEOP}, and $\%P_{Rb}$ measurements as a function of SEOP cell surface temperature in a 1000 Torr Xe/1000 Torr N_2 gas mixture fill obtained with the SEOP cell stopcock (**a**) closed and (**b**) open. Note, the solid blue line denotes experimental $\%P_{Xe}$ and dashed blue line denotes theoretically predicated $\%P_{Xe(theor)}$ based on the experimental values of $\%P_{Rb}$, γ_{SEOP} and ^{129}Xe T_1 as described previously [67] (see SI). Lower displays show comparisons of (**c**) ^{129}Xe T_1 values (note the *y*-axis starts at 40 min to better delineates the differences) and (**d**) ^{129}Xe polarization build-up curves recorded for the first four experimental points shown in display c—note the consistency in the polarization dynamics for a given cell configuration.

3.3. Preparation and Operation of Fluid Path

The results presented in Section 3.1 clearly indicate that the SEOP cell can be reloaded hundreds of times, when good manufacturing practices (GMPs) are properly followed. As a negative control of our experiments, we also provide examples of device points of failure when GMPs were not followed. Results presented in Figure 7c describe the study of ^{129}Xe T_1 relaxation time constant over the course of repeated opening and closing of the SEOP cell stopcock. In each instance before opening the SEOP cell stopcock, the inlet line of the gas-handling manifold underwent three cycles of filling and evacuation with UHP N_2 with the goal to remove any trace quantities of atmospheric air remaining in the inlet line to prevent Rb oxidation in the SEOP cell. This purge-cycling procedure followed an identical GMP protocol as that used in the SEOP cell refilling procedure used within the QA study in Section 3.1, but with two differences: First, when opening the SEOP cell loaded with a 50/50 Xe/N_2 gas mixture, the cell was not evacuated; instead, the sequence was aborted so that the SEOP cell would remain open. The second and the most critical difference was failure to follow GMPs with respect to a lack of suppression of air contamination of N_2 loading line. Specifically, before acquiring data from this experiment, the UHP N_2 cylinder installed on the GEN-3 hyperpolarizer was replaced: normally, we purge the entire N_2 fluid path (including N_2 gas purifier as shown in Figure S8) with ten cycles of vacuum ($<5 \times 10^{-2}$ Torr) and UHP N_2 over the course of at least 1 h. However, no purging of the full gas-handling manifold inlet line and inert gas purifiers with this new UHP N_2 was performed before performing the described build-up experiments. A steady reduction in recorded T_1 from 126.9 ± 1.5 to 52.9 ± 1.1 min was observed due to the ingress of atmospheric air left over from disconnecting the inlet line to the N_2 cylinder. Surprisingly, somewhat higher values of T_1 were recorded with the SEOP cell stopcocks being open, with reductions in the T_1 value after closing the SEOP cell stopcock, Figure 7c: the origin of

this effect is under study. The step-wise T_1 reduction was reproducible for each stopcock actuation cycle (Figure 7c). In any case, it is imperative that adequate purge-cycling of all parts of the gas-handling manifold is performed when replacing gas cylinders.

It should also be noted that reproducibility of ^{129}Xe polarization build-up was good across the experiments these non-GMP compliant experiments as shown by Figure 7d. The four color-coded build-up curves presented are ascribed to the first four entries in Figure 7c, i.e., in alternating configurations of the SEOP cell stopcock being closed and open. $\%P_{Xe}$ build-up in the closed configuration was performed at a SEOP jacket temperature of 85 °C, whereas open configuration build-up experiments were conducted at 90 °C. We rationalize these findings as follows: when ^{129}Xe T_1 is relatively good (i.e., well over 1h), the $1/T_1$ term in Eq. 4 is effectively negligible, and therefore, has no substantial impact of the build-up curve parameters. As a result, T_1 measurements can provide an early indication of SEOP cell deterioration before the deleterious effects can be seen on the build-up curves. A representative comparison example of T_1 relaxation processes in an open- and closed-stopcock configuration SEOP cell following ten full-manifold UHP N_2 purge-cycles is presented in Figure S5, showing no substantial T_1 decrease.

In a separate experiment with a different SEOP cell, we have studied the SEOP open-stopcock configuration to investigate the ^{129}Xe T_1 as an indicator on overall SEOP cell "health", Figure S3. The ^{129}Xe T_1 was measured daily (with the exception of one weekend), and the results clearly indicate slow but steady decrease in T_1 from ~139 $\pm$ 2 min to ~87 $\pm$ 2 min at the end of an 8-day-long study. We rationalize these findings as the result of a slow leak of atmospheric impurities into the part of the PEEK manifold that remained open to the SEOP cell (see also photo of this section in Figure S10); these minor leaks can lead to Rb oxidation over time. Although the SEOP cell after 8 days can still be employed for obtaining highly polarized ^{129}Xe (because $\%P_{Xe}$ is sufficiently high), such SEOP cell deterioration is concerning in the context of long-term use. Therefore, we conclude that once the SEOP experiments are finished for the day, the SEOP cell must be closed for overnight- or longer-term storage to extend the useable lifetime of the SEOP cell for HP ^{129}Xe production.

3.4. Effect of Rb Distribution in SEOP Cells

As described in the Materials and Methods section above, each SEOP cell studied underwent a robust Rb distribution procedure during preparation for this series of experiments. An additional set of experiments was performed with inadequate distribution (judged by the lack of Rb metal layer "banding" in the SEOP cell—see comparative photos in Figure S4a,b, respectively) of the loaded fresh Rb metal droplet in order to observe the effects on HP ^{129}Xe contrast agent production efficiency. The results presented in Figures S5 and S3 show two clear trends: (1) substantial temperature cycling of the inadequately distributed SEOP cell is required; and (2) $\%P_{Xe}$ levels can be overall similar to those of a cell with well-distributed Rb, albeit with a longer polarization build-up time: see comparison of maps in Figure 6a, Figures S3 and S5a, respectively.

3.5. Limitations of Current Design and Future Work

In our original design of the aluminum SEOP cell jacket [39], the ends of the SEOP cell (ca. ~1 inch of the front and rear portions of the cylinder) were not enclosed by the aluminum jacket due to the slightly larger SEOP cell diameter at the ends (where the optical flats are fused with the glass tube, as a consequence of the glass welding process). Here, we have employed three jacket extenders (two 42 mm long pieces in the front and one 38 mm long piece on the back, see Figure S10 for details) to improve the SEOP cell coverage by the variable-temperature aluminum jacket. Our rationale was to improve overall thermal management of the SEOP cell. To our surprise, the results of SEOP cell temperature mapping with and without these jacket extensions (Figure S12) demonstrate no substantial difference between the two jacket configurations. We rationalize our findings in terms of the following hypothesis: the circulating air inside the polarizer chassis removes a substantial

amount of heat from the SEOP cell, causing larger-than-anticipated temperature gradients across the SEOP cell jacket (and by extension, the SEOP cell), with the SEOP cell ends being much cooler than anticipated—as a result, the addition of extenders does not substantially improve the SEOP cell coverage by the hot SEOP jacket during the hyperpolarization process (we note that in the current design, the temperature is sensed only in the center of the SEOP cell jacket). We aim to perform further studies to investigate this finding, with the overall goal of improving thermal management of the SEOP cell and improving efficiency of the ^{129}Xe SEOP process.

4. Conclusions

We performed a pilot QA study of a GEN-3 batch-mode clinical-scale automated ^{129}Xe hyperpolarizer. Production of good $\%P_{Xe}$ levels of ~50% has been demonstrated with high reproducibility of hyperpolarizer performance in a clinical-scale ^{129}Xe contrast agent production setting, using high-Xe densities (50% Xe fraction in ~2.6 atm total pressure) and rapid temperature ramping enabled by an aluminum heating jacket surrounding the SEOP cell. ^{129}Xe hyperpolarization was performed over the course of 700 gas-loading cycles, simulating long-term HP contrast agent production. Good reproducibility was observed over the first 500 SEOP cell refills. Our results demonstrate a more than 2-fold increase in build-up rate (T_b of ~26 min vs. ~53 min—note that even faster build-up rates are demonstrated at the expense of slightly lower $\%P_{Xe}$, Figure 5) relative to previously demonstrated results in a comparable QA study on a second-generation (GEN-2) ^{129}Xe hyperpolarizer device [40], with only a minor reduction in maximum achievable $\%P_{Xe}$. Additionally, we investigated the effects of varying SEOP jacket temperatures, distribution of the Rb metal (as a film across the cell surface), preparation and operation of the fluid path with ultra-high-purity N_2, when running in open- and closed-cell configurations in the context of the GEN-3 hyperpolarizer installation, performance optimization, and maintenance to consistently produce high ^{129}Xe polarization values. We attribute lower than expected $\%P_{Xe}$ in the GEN-3 design versus the GEN-2 design (~51% vs. ~71%, respectively) [40] in part due to some potential limitations of the current jacket design—work is in progress to address these limitations. The results presented further demonstrate the significant potential for the HP ^{129}Xe contrast agent in imaging and bio-sensing applications on a clinical-scale.

Supplementary Materials: The following are available online, Figure S1: Summary figure displaying all temperature-dependent ^{129}Xe polarization build-up maps for each of the six intermediate (100–600) Xe/N_2 gas mixture SEOP cell refills performed in the QA study. T_1 values describing the ^{129}Xe relaxation process immediately after concluding each temperature-mapping experiment are included for reference. Note the solid blue line denotes experimental $\%P_{Xe}$ and dashed blue line denotes theoretically predicated $\%P_{Xe(theor)}$ based on the experimental values of $\%P_{Rb}$, γ_{SEOP} and ^{129}Xe T_1. Figure S2: Comparison of ^{129}Xe polarization build-up curves under minor modifications to device configuration and operation. Displays (a,b) compare ^{129}Xe polarization build-up at 70 °C with the use of a magnetic and non-magnetic thermocouple on the aluminium heating jacket surface for SEOP cell temperature control. Displays (c,d) compare build-up at 75 °C using both the standard heating jacket described in Ref. [39], and an extended variant covering the entire length of the SEOP cell. Displays (e,f,g) compare build-up at 75 °C with 3, 6 and all 10 external chassis fans enabled, respectively, for the purpose of maintaining thermal stability. Figure S3: Steady-state $\%P_{Xe}$, γ_{SEOP}, and $\%P_{Rb}$ measurements as a function of SEOP cell surface temperature following polarization build-up in a 1000 Torr Xe/1000 Torr N_2 gas mixture fill under (a) SEOP cell stopcocks in the closed configuration and (b) SEOP cell stopcocks in the open configuration. (c) Polarization build-up under identical conditions in a 1000 Torr Xe/1000 Torr N_2 gas mixture test-retest scenario. (d) Reduction of T_1 relaxation time constant over time in the SEOP cell with open-stopcock configuration (note the y-axis starts at 60 mins to better delineates the differences), when gas handling manifold inlet line purge-cycling with UHP N_2 was not performed. Displays (e) and (f) show the difference between polarization build-up dynamics under otherwise-identical conditions when performing insufficient and sufficient temperature cycling (respectively) of moderately-oxidized SEOP cells. Figure S4: (left)

Photos of a GEN-3 SEOP cell (a) before, and (b) after undergoing a Rb distribution procedure over half of the SEOP cell. Note the banded silver-colored film along the inner surface of the SEOP cell where Rb vapor has condensed in significant quantities. Virtually complete vaporization of the Rb droplet is possible over longer timescales, with large cold areas and high temperature gradients (e.g., use of liquid N_2). (right) Annotated photographs of a Rb distribution setup—see Figure S11 for details of the manifold. Figure S5: Steady-state $\%P_{Xe}$, γ_{SEOP}, and $\%P_{Rb}$ measurements as a function of SEOP cell surface temperature following polarization build-up in a cell with poorly-distributed Rb and a 1000 Torr Xe/1000 Torr N_2 gas mixture fill under (a) SEOP cell stopcock in the closed configuration and (b) SEOP cell stopcock in the open configuration. Display (c) shows the difference between polarization build-up dynamics under otherwise-identical conditions of the first (non-temperature-cycled) and subsequent (temperature-cycled) experiments. Display (d) compares the reproducibility of polarization build-up dynamics at the maximum stable SEOP cell temperatures for stopcock closed and open configurations (85 and 95 °C, respectively) on subsequent days of polarizer operation. Display (e) shows the variation in T_1 (performed at the end of each day of experimentation) over the course of this portion of the study. Figure S6: Comparison of ^{129}Xe polarization build-up and relaxation rates as a function of delay period between NMR acquisitions. The number situated above each pair of curves indicates the time interval between acquisition pulses for that set of data. The first curve of each interval (a,c,e,g,i,k) displays the ^{129}Xe polarization build-up curve. The second curve of each pair (b,d,f,h,j,l) depicts the HP ^{129}Xe T_1 relaxation decay curve. Displays (m,n) show further HP ^{129}Xe T_1 relaxation curves acquired when properly purge-cycling the SEOP cell inlet between experiments. Figure S7: Automated process flowchart depicting the Xe/N_2 gas mixture ejection sequence to a Tedlar bag and subsequent SEOP cell refilling. Purple trapezoids represent manual/user-led confirmations or actions. Grey rectangles are automated processes. Yellow diamonds are decisions the user can choose between or confirm through the GUI. Orange parallelograms represent active sensing and response to parameters observed outside of acceptable range. Figure S8: A representative state of the XeUS GEN-3 hyperpolarizer Graphical User Interface (GUI) while performing SEOP. Note valve #9 is normally open in the de-energized state. Figure S9: ^{129}Xe polarization buildup monitored by RF pulse duration of 150 µs with amplified gain of −23.3 dB during the build-up process. Once the steady-state is achieved the amplitude of RF excitation pulse was corrected to −25.3 dB (correct) value. Note the overestimation of P_{Xe} by a factor of 1.22-fold due to stronger B_1 strength. Figure S10: Photographs of the aluminum jacket extenders employed for the SEOP cell. Figure S11: Schematic Diagram of SEOP Cell "Cleaner" and Rb distribution setup (a.k.a. the Rb "spreader"). Figure S12: Comparison of ^{129}Xe polarization build-up at different temperatures and temperature map with extended jacket (a,c,e,g,i,k) and without the extended jacket (b,d,f,h,j,l).

Author Contributions: Conceptualization, J.R.B., P.N. and E.Y.C.; methodology, J.R.B., E.Y.C., B.M.G. and M.J.B.; software, J.R.B. and A.S.; validation, J.R.B., Y.A.C. and M.R.H.C.; formal analysis, J.R.B. and M.R.H.C.; investigation, J.R.B. and M.R.H.C.; resources, B.M.G., M.J.B. and E.Y.C.; data curation, J.R.B., B.M.G., M.J.B. and E.Y.C.; writing—original draft preparation, J.R.B. and M.R.H.C.; writing—review and editing, J.R.B., M.J.B., B.M.G. and E.Y.C.; visualization, J.R.B., A.S. and M.R.H.C.; supervision, E.Y.C.; project administration, E.Y.C. and B.M.G.; funding acquisition, B.M.G., M.J.B., P.N. and E.Y.C. All authors have read and agreed to the published version of the manuscript.

Funding: This work was supported by DOD CDMRP under W81XWH-15-1-0271, W81XWH-15-1-0272, W81XWH-20-10576 and W81XWH-20-10578. BMG acknowledges a Cottrell SEED grant from Research Corporation for Science Advancement. University of Nottingham: MJB acknowledges financial support from The James Tudor Foundation.

Institutional Review Board Statement: Not applicable.

Informed Consent Statement: Not applicable.

Data Availability Statement: MATLAB-based software for automated NIR and NMR data processing is available for download in Reference #67.

Acknowledgments: We thank Aaron M. Coffey for discussions, and Brent Dummit (Mid Rivers Glass-blowing, Inc., St Charles, MO, USA) for assistance with custom glassware production. The authors also thank anonymous reviewer for providing constructive feedback to improve the manuscript.

Conflicts of Interest: P.N., B.M.G. and E.Y.C. declare a stake of ownership in XeUS Technologies, Ltd.

Sample Availability: Samples of the compounds are not available from the authors.

References

1. Goodson, B.M.; Whiting, N.; Coffey, A.M.; Nikolaou, P.; Shi, F.; Gust, B.M.; Gemeinhardt, M.E.; Shchepin, R.V.; Skinner, J.G.; Birchall, J.R.; et al. Hyperpolarization methods for MRS. *Emagres* **2015**, *4*, 797–810. [CrossRef]
2. Kovtunov, K.V.; Pokochueva, E.V.; Salnikov, O.G.; Cousin, S.; Kurzbach, D.; Vuichoud, B.; Jannin, S.; Chekmenev, E.Y.; Goodson, B.M.; Barskiy, D.A.; et al. Hyperpolarized NMR Spectroscopy: *d*-DNP, PHIP, and SABRE Techniques. *Chem. Asian J.* **2018**, *13*, 1857–1871. [CrossRef]
3. Nikolaou, P.; Goodson, B.; Chekmenev, E.Y. NMR hyperpolarization techniques for biomedicine. *Chemistry* **2015**, *21*, 3156–3166. [CrossRef] [PubMed]
4. Ardenkjaer-Larsen, J.H.; Fridlund, B.; Gram, A.; Hansson, G.; Hansson, L.; Lerche, M.H.; Servin, R.; Thaning, M.; Golman, K. Increase in signal-to-noise ratio of >10,000 times in liquid-state NMR. *Proc. Natl. Acad. Sci. USA* **2003**, *100*, 10158–10163. [CrossRef] [PubMed]
5. Walkup, L.L.; Woods, J.C. Translational applications of hyperpolarized ^{3}He and ^{129}Xe. *NMR Biomed.* **2014**, *27*, 1429–1438. [CrossRef]
6. Goodson, B. Nuclear magnetic resonance of laser-polarized noble gases in molecules, materials, and organisms. *J. Magn. Reson.* **2002**, *155*, 157–216. [CrossRef] [PubMed]
7. Mugler, J.P.; Altes, T.A. Hyperpolarized ^{129}Xe MRI of the human lung. *J. Magn. Reson. Imaging* **2013**, *37*, 313–331. [CrossRef]
8. Schröder, L. Xenon for NMR biosensing—Inert but alert. *Phys. Med.* **2013**, *29*, 3–16. [CrossRef]
9. Witte, C.; Schröder, L. NMR of hyperpolarised probes. *NMR Biomed.* **2013**, *26*, 788–802. [CrossRef]
10. Barskiy, D.A.; Coffey, A.M.; Nikolaou, P.; Mikhaylov, D.M.; Goodson, B.M.; Branca, R.T.; Lu, G.J.; Shapiro, M.G.; Telkki, V.-V.; Zhivonitko, V.V.; et al. NMR hyperpolarization techniques of gases. *Chem. Eur. J.* **2017**, *23*, 725–751. [CrossRef]
11. Kovtunov, K.V.; Koptyug, I.V.; Fekete, M.; Duckett, S.B.; Theis, T.; Joalland, B.; Chekmenev, E.Y. Parahydrogen-induced hyperpolarization of gases. *Angew. Chem. Int. Ed.* **2020**, *59*, 17788–17797. [CrossRef] [PubMed]
12. Babcock, E.; Nelson, I.; Kadlecek, S.; Driehuys, B.; Anderson, L.W.; Hersman, F.W.; Walker, T.G. Hybrid spin-exchange optical pumping of ^{3}He. *Phys. Rev. Lett.* **2003**, *91*, 123003. [CrossRef] [PubMed]
13. Ruset, I.; Tsai, L.; Mair, R.; Patz, S.; Hrovat, M.; Rosen, M.; Muradian, I.; Ng, J.; Topulos, G.; Butler, J.; et al. A system for open-access ^{3}He human lung imaging at very low field. *Concepts Magn. Reson. Part B* **2006**, *29B*, 210–221. [CrossRef]
14. Albert, M.S.; Cates, G.D.; Driehuys, B.; Happer, W.; Saam, B.; Springer, C.S., Jr.; Wishnia, A. Biological magnetic resonance imaging using laser-polarized ^{129}Xe. *Nat. Cell Biol.* **1994**, *370*, 199–201. [CrossRef] [PubMed]
15. Kaushik, S.S.; Cleveland, Z.I.; Cofer, G.P.; Metz, G.; Beaver, D.; Nouls, J.; Kraft, M.; Auffermann, W.; Wolber, J.; McAdams, H.P.; et al. Diffusion-weighted hyperpolarized ^{129}Xe MRI in healthy volunteers and subjects with chronic obstructive pulmonary disease. *Magn. Reson. Med.* **2011**, *65*, 1154–1165. [CrossRef] [PubMed]
16. Lilburn, D.M.; Pavlovskaya, G.E.; Meersmann, T. Perspectives of hyperpolarized noble gas MRI beyond ^{3}He. *J. Magn. Reson.* **2013**, *229*, 173–186. [CrossRef]
17. Wang, Y.; Roose, B.W.; Palovcak, E.J.; Carnevale, V.; Dmochowski, I.J. A genetically encoded β-lactamase reporter for ultrasensitive ^{129}Xe NMR in mammalian cells. *Angew. Chem.* **2016**, *55*, 8984–8987. [CrossRef]
18. Wang, Y.; Dmochowski, I.J. An expanded palette of Xenon-129 NMR biosensors. *Accounts Chem. Res.* **2016**, *49*, 2179–2187. [CrossRef]
19. Hane, F.T.; Li, T.; Smylie, P.; Pellizzari, R.M.; Plata, J.A.; DeBoef, B.; Albert, M.S. In vivo detection of cucurbit[6]uril, a hyperpolarized xenon contrast agent for a xenon magnetic resonance imaging biosensor. *Sci. Rep.* **2017**, *7*, 41027. [CrossRef]
20. Schröder, L.; Lowery, T.J.; Hilty, C.; Wemmer, D.E.; Pines, A. Molecular imaging using a targeted magnetic resonance hyperpolarized biosensor. *Science* **2006**, *314*, 446–449. [CrossRef]
21. Walker, T.G.; Happer, W. Spin-exchange optical pumping of noble-gas nuclei. *Rev. Mod. Phys.* **1997**, *69*, 629–642. [CrossRef]
22. Walker, T.G. Fundamentals of spin-exchange optical pumping. *J. Phys. Conf. Ser.* **2011**, *294*, 012001. [CrossRef]
23. He, M.; Robertson, S.H.; Kaushik, S.S.; Freeman, M.S.; Virgincar, R.S.; Davies, J.; Stiles, J.; Foster, W.M.; McAdams, H.P.; Driehuys, B. Dose and pulse sequence considerations for hyperpolarized ^{129}Xe ventilation MRI. *Magn. Reson. Imaging* **2015**, *33*, 877–885. [CrossRef] [PubMed]
24. Khan, A.S.; Harvey, R.L.; Birchall, J.R.; Irwin, R.K.; Nikolaou, P.; Schrank, G.; Emami, K.; Dummer, A.; Barlow, M.J.; Goodson, B.M.; et al. Enabling clinical technologies for hyperpolarized Xenon-129 MRI and spectroscopy. *Angew. Chem. Int. Ed.* **2021**, *60*, 22126–22147.
25. Ruset, I.C.; Ketel, S.; Hersman, F.W. Optical pumping system design for large production of hyperpolarized ^{129}Xe. *Phys. Rev. Lett.* **2006**, *96*, 053002. [CrossRef]
26. Driehuys, B.; Cates, G.D.; Miron, E.; Sauer, K.; Walter, D.K.; Happer, W. High-volume production of laser-polarized ^{129}Xe. *Appl. Phys. Lett.* **1996**, *69*, 1668–1670. [CrossRef]
27. Zook, A.L.; Adhyaru, B.B.; Bowers, C.R. High capacity production of >65% spin polarized Xenon-129 for NMR spectroscopy and imaging. *J. Magn. Reson.* **2002**, *159*, 175–182. [CrossRef]
28. Freeman, M.S.; Emami, K.; Driehuys, B. Characterizing and modeling the efficiency limits in large-scale production of hyperpolarized ^{129}Xe. *Phys. Rev. A* **2014**, *90*, 023406. [CrossRef]

29. Kennedy, D.J.; Seltzer, S.J.; Jiménez-Martínez, R.; Ring, H.L.; Malecek, N.S.; Knappe, S.; Donley, E.A.; Kitching, J.; Bajaj, V.S.; Pines, A. An optimized microfabricated platform for the optical generation and detection of hyperpolarized ^{129}Xe. *Sci. Rep.* **2017**, *7*, 43994. [CrossRef]
30. Rosen, M.; Chupp, T.E.; Coulter, K.P.; Welsh, R.C.; Swanson, S.D. Polarized ^{129}Xe optical pumping/spin exchange and delivery system for magnetic resonance spectroscopy and imaging studies. *Rev. Sci. Instrum.* **1999**, *70*, 1546–1552. [CrossRef]
31. Norquay, G.; Collier, G.J.; Rao, M.; Stewart, N.J.; Wild, J.M. ^{129}Xe-Rb spin-exchange optical pumping with high photon efficiency. *Phys. Rev. Lett.* **2018**, *121*, 153201. [CrossRef] [PubMed]
32. Nikolaou, P.; Whiting, N.; Eschmann, N.A.; Chaffee, K.E.; Goodson, B.M.; Barlow, M. Generation of laser-polarized xenon using fiber-coupled laser-diode arrays narrowed with integrated volume holographic gratings. *J. Magn. Reson.* **2009**, *197*, 249–254. [CrossRef] [PubMed]
33. Whiting, N.; Nikolaou, P.; Eschmann, N.A.; Barlow, M.J.; Lammert, R.; Ungar, J.; Hu, W.; Vaissie, L.; Goodson, B.M. Using frequency-narrowed, tunable laser diode arrays with integrated volume holographic gratings for spin-exchange optical pumping at high resonant fluxes and xenon densities. *Appl. Phys. A* **2012**, *106*, 775–788. [CrossRef]
34. Nikolaou, P.; Coffey, A.M.; Walkup, L.L.; Gust, B.M.; Whiting, N.; Newton, H.; Barcus, S.; Muradyan, I.; Dabaghyan, M.; Moroz, G.D.; et al. Near-unity nuclear polarization with an open-source ^{129}Xe hyperpolarizer for NMR and MRI. *Proc. Natl. Acad. Sci. USA* **2013**, *110*, 14150–14155. [CrossRef] [PubMed]
35. Nikolaou, P.; Coffey, A.M.; Walkup, L.L.; Gust, B.M.; Whiting, N.R.; Newton, H.; Muradyan, I.; Dabaghyan, M.; Ranta, K.; Moroz, G.D.; et al. XeNA: An automated 'open-source' ^{129}Xe hyperpolarizer for clinical use. *Magn. Reson. Imaging* **2014**, *32*, 541–550. [CrossRef] [PubMed]
36. Skinner, J.G.; Ranta, K.; Whiting, N.; Coffey, A.M.; Nikolaou, P.; Rosen, M.S.; Chekmenev, E.Y.; Morris, P.G.; Barlow, M.J.; Goodson, B.M. High Xe density, high photon flux, stopped-flow spin-exchange optical pumping: Simulations versus experiments. *J. Magn. Reson.* **2020**, *312*, 106686. [CrossRef]
37. Hughes-Riley, T.; Six, J.S.; Lilburn, D.M.; Stupic, K.F.; Dorkes, A.C.; Shaw, D.; Pavlovskaya, G.E.; Meersmann, T. Cryogenics free production of hyperpolarized ^{129}Xe and ^{83}Kr for biomedical MRI applications. *J. Magn. Reson.* **2013**, *237*, 23–33. [CrossRef] [PubMed]
38. Birchall, J.R.; Irwin, R.K.; Nikolaou, P.; Coffey, A.M.; Kidd, B.E.; Murphy, M.; Molway, M.; Bales, L.B.; Ranta, K.; Barlow, M.J.; et al. XeUS: A second-generation automated 'open-source' batch-mode clinical-scale hyperpolarizer. *J. Magn. Reson.* **2020**, *319*, 106813. [CrossRef]
39. Birchall, J.R.; Nikolaou, P.; Coffey, A.M.; Kidd, B.E.; Murphy, M.; Molway, M.; Bales, L.B.; Goodson, B.M.; Irwin, R.K.; Barlow, M.J.; et al. Batch-mode clinical-scale optical hyperpolarization of Xenon-129 using an aluminum jacket with rapid temperature ramping. *Anal. Chem.* **2019**, *92*, 4309–4316. [CrossRef]
40. Birchall, J.R.; Irwin, R.K.; Nikolaou, P.; Pokochueva, E.; Kovtunov, K.V.; Koptyug, I.V.; Barlow, M.J.; Goodson, B.M.; Chekmenev, E.Y. Pilot multi-site quality assurance study of batch-mode clinical-scale automated Xenon-129 hyperpolarizers. *J. Magn. Reson.* **2020**, *316*, 106755. [CrossRef]
41. Schrank, G.; Ma, Z.; Schoeck, A.; Saam, B. Characterization of a low-pressure high-capacity Xe-129 flow-through polarizer. *Phys. Rev. A* **2009**, *80*, 063424. [CrossRef]
42. Hersman, F.W.; Ruset, I.C.; Ketel, S.; Muradian, I.; Covrig, S.D.; Distelbrink, J.; Porter, W.; Watt, D.; Ketel, J.; Brackett, J.; et al. Large production system for hyperpolarized ^{129}Xe for human lung imaging studies. *Acad. Radiol.* **2008**, *15*, 683–692. [CrossRef] [PubMed]
43. Patz, S.; Hersman, F.W.; Muradian, I.; Hrovat, M.I.; Ruset, I.C.; Ketel, S.; Jacobson, F.; Topulos, G.P.; Hatabu, H.; Butler, J.P. Hyperpolarized ^{129}Xe MRI: A viable functional lung imaging modality? *Eur. J. Radiol.* **2007**, *64*, 335–344. [CrossRef] [PubMed]
44. Mugler, J.P.; Driehuys, B.; Brookeman, J.R.; Cates, G.D.; Berr, S.S.; Bryant, R.G.; Daniel, T.M.; De Lange, E.E.; Downs, J.H.; Erickson, C.J.; et al. MR imaging and spectroscopy using hyperpolarized ^{129}Xe gas: Preliminary human results. *Magn. Reson. Med.* **1997**, *37*, 809–815. [CrossRef]
45. Mugler, J.P.; Altes, T.A.; Ruset, I.C.; Dregely, I.; Mata, J.F.; Miller, G.W.; Ketel, S.; Ketel, J.; Hersman, F.W.; Ruppert, K. Simultaneous magnetic resonance imaging of ventilation distribution and gas uptake in the human lung using hyperpolarized xenon-129. *Proc. Natl. Acad. Sci. USA* **2010**, *107*, 21707–21712. [CrossRef]
46. Dregely, I.; Ruset, I.C.; Mata, J.F.; Ketel, J.; Ketel, S.; Distelbrink, J.; Altes, T.A.; Mugler, J.P.; Miller, G.W.; Hersman, F.W.; et al. Multiple-exchange-time xenon polarization transfer contrast (MXTC) MRI: Initial results in animals and healthy volunteers. *Magn. Reson. Med.* **2011**, *67*, 943–953. [CrossRef]
47. Muradyan, I.; Butler, J.P.; Dabaghyan, M.; Hrovat, M.; Dregely, I.; Ruset, I.; Topulos, G.P.; Ms, E.F.; Hatabu, H.; Hersman, W.F.; et al. Single-breath xenon polarization transfer contrast (SB-XTC): Implementation and initial results in healthy humans. *J. Magn. Reson. Imaging* **2013**, *37*, 457–470. [CrossRef]
48. Rao, M.R.; Stewart, N.J.; Griffiths, P.D.; Norquay, G.; Wild, J.M. Imaging human brain perfusion with inhaled hyperpolarized ^{129}Xe MR Imaging. *Radiology* **2018**, *286*, 659–665. [CrossRef]
49. Swanson, S.D.; Rosen, M.S.; Agranoff, B.W.; Coulter, K.P.; Welsh, R.C.; Chupp, T.E. Brain MRI with laser-polarized ^{129}Xe. *Magn. Reson. Med.* **1997**, *38*, 695–698. [CrossRef]

50. Driehuys, B.; Martinez-Jimenez, S.; Cleveland, Z.I.; Metz, G.M.; Beaver, D.M.; Nouls, J.C.; Kaushik, S.S.; Firszt, R.; Willis, C.; Kelly, K.T.; et al. Chronic obstructive pulmonary disease: Safety and tolerability of hyperpolarized ^{129}Xe MR imaging in healthy volunteers and patients. *Radiology* **2012**, *262*, 279–289. [CrossRef]
51. Driehuys, B. Crossing the chasm(s): Demonstrating the clinical value of hyperpolarized gas MRI. *Acad. Radiol.* **2017**, *24*, 1–3. [CrossRef]
52. Branca, R.T.; He, T.; Zhang, L.; Floyd, C.S.; Freeman, M.; White, C.; Burant, A. Detection of brown adipose tissue and thermogenic activity in mice by hyperpolarized xenon MRI. *Proc. Natl. Acad. Sci. USA* **2014**, *111*, 18001–18006. [CrossRef] [PubMed]
53. Antonacci, M.A.; McHugh, C.; Kelley, M.; McCallister, A.; Degan, S.; Branca, R.T. Direct detection of brown adipose tissue thermogenesis in UCP1−/− mice by hyperpolarized ^{129}Xe MR thermometry. *Sci. Rep.* **2019**, *9*, 14865. [CrossRef] [PubMed]
54. Witte, C.; Martos, V.; Rose, H.M.; Reinke, S.; Klippel, S.; Schröder, L.; Hackenberger, C.P.R. Live-cell MRI with Xenon hyper-CEST biosensors targeted to metabolically labeled cell-surface glycans. *Angew. Chem. Int. Ed.* **2015**, *54*, 2806–2810. [CrossRef] [PubMed]
55. Jayapaul, J.; Schröder, L. Molecular sensing with host systems for hyperpolarized ^{129}Xe. *Molecules* **2020**, *25*, 4627. [CrossRef] [PubMed]
56. Saam, B. T_1 Relaxation of ^{129}Xe and how to keep it long. In *Hyperpolarized Xenon-129 Magnetic Resonance: Concepts, Production, Techniques and Applications*; Meersmann, T., Brunner, E., Eds.; The Royal Society of Chemistry: London, UK, 2015; pp. 122–141.
57. Anger, B.C.; Schrank, G.; Schoeck, A.; Butler, K.A.; Solum, M.S.; Pugmire, R.J.; Saam, B. Gas-phase spin relaxation of ^{129}Xe. *Phys. Rev. A* **2008**, *78*, 043406. [CrossRef]
58. Chann, B.; Nelson, I.A.; Anderson, L.W.; Driehuys, B.; Walker, T.G. ^{129}Xe—Xe molecular spin relaxation. *Phys. Rev. Lett.* **2002**, *88*, 4. [CrossRef]
59. Nikolaou, P.; Coffey, A.M.; Barlow, M.J.; Rosen, M.S.; Goodson, B.M.; Chekmenev, E.Y. Temperature-ramped ^{129}Xe spin-exchange optical pumping. *Anal. Chem.* **2014**, *86*, 8206–8212. [CrossRef]
60. Nikolaou, P.; Coffey, A.M.; Ranta, K.; Walkup, L.L.; Gust, B.; Barlow, M.J.; Rosen, M.S.; Goodson, B.M.; Chekmenev, E.Y. Multi-dimensional mapping of spin-exchange optical pumping in clinical-scale batch-mode ^{129}Xe hyperpolarizers. *J. Phys. Chem. B* **2014**, *118*, 4809–4816. [CrossRef]
61. Nikolaou, P.; Coffey, A.M.; Walkup, L.L.; Gust, B.M.; LaPierre, C.D.; Koehnemann, E.; Barlow, M.J.; Rosen, M.S.; Goodson, B.M.; Chekmenev, E.Y. A 3D-printed high power nuclear spin polarizer. *J. Am. Chem. Soc.* **2014**, *136*, 1636–1642. [CrossRef]
62. Birchall, J.R.; Nikolaou, P.; Irwin, R.K.; Barlow, M.J.; Ranta, K.; Coffey, A.M.; Goodson, B.M.; Pokochueva, E.V.; Kovtunov, K.V.; Koptyug, I.V.; et al. Helium-rich mixtures for improved batch-mode clinical-scale spin-exchange optical pumping of Xenon-129. *J. Magn. Reson.* **2020**, *315*, 106739. [CrossRef] [PubMed]
63. Witte, C.; Kunth, M.; Rossella, F.; Schröder, L. Observing and preventing rubidium runaway in a direct-infusion xenon-spin hyperpolarizer optimized for high-resolution hyper-CEST (chemical exchange saturation transfer using hyperpolarized nuclei) NMR. *J. Chem. Phys.* **2014**, *140*, 084203. [CrossRef] [PubMed]
64. Antonacci, M.; Burant, A.; Wagner, W.; Branca, R.T. Depolarization of nuclear spin polarized ^{129}Xe gas by dark rubidium during spin-exchange optical pumping. *J. Magn. Reson.* **2017**, *279*, 60–67. [CrossRef] [PubMed]
65. Atutov, S.N.; Plekhanov, A.I.; Shalagin, A.M.; Calabrese, R.; Tomassetti, L.; Guidi, V. Explosive evaporation of Rb or K fractal clusters by low power CW radiation in the presence of excited atoms. *Eur. Phys. J. D* **2012**, *66*, 140–145. [CrossRef]
66. Saha, I.; Nikolaou, P.; Whiting, N.; Goodson, B.M. Characterization of violet emission from Rb optical pumping cells used in laser-polarized xenon NMR experiments. *Chem. Phys. Lett.* **2006**, *428*, 268–276. [CrossRef]
67. Birchall, J.R.; Irwin, R.K.; Chowdhury, M.R.H.; Nikolaou, P.; Goodson, B.M.; Barlow, M.J.; Shcherbakov, A.; Chekmenev, E.Y. Automated low-cost in situ IR and NMR spectroscopy characterization of clinical-scale ^{129}Xe spin-exchange optical pumping. *Anal. Chem.* **2021**, *93*, 3883–3888. [CrossRef]
68. Hövener, J.-B.; Chekmenev, E.Y.; Harris, K.C.; Perman, W.H.; Tran, T.T.; Ross, B.D.; Bhattacharya, P. Quality assurance of PASADENA hyperpolarization for ^{13}C biomolecules. *Magn. Reson. Mater. Phys. Biol. Med.* **2008**, *22*, 123–134. [CrossRef]
69. Lide, D. *Handbook of Chemistry and Physics*, 85th ed.; CRC Press: Boca Raton, FL, USA, 2004.

PHYSICS

RASER MRI: Magnetic resonance images formed spontaneously exploiting cooperative nonlinear interaction

Sören Lehmkuhl[1,2]*, Simon Fleischer[3], Lars Lohmann[3], Matthew S. Rosen[4,5], Eduard Y. Chekmenev[6,7], Alina Adams[3], Thomas Theis[2,8,9]*, Stephan Appelt[3,10]*

Copyright © 2022 The Authors, some rights reserved; exclusive licensee American Association for the Advancement of Science. No claim to original U.S. Government Works. Distributed under a Creative Commons Attribution License 4.0 (CC BY).

The spatial resolution of magnetic resonance imaging (MRI) is limited by the width of Lorentzian point spread functions associated with the transverse relaxation rate $1/T_2^*$. Here, we show a different contrast mechanism in MRI by establishing RASER (radio-frequency amplification by stimulated emission of radiation) in imaged media. RASER imaging bursts emerge out of noise and without applying radio-frequency pulses when placing spins with sufficient population inversion in a weak magnetic field gradient. Small local differences in initial population inversion density can create stronger image contrast than conventional MRI. This different contrast mechanism is based on the cooperative nonlinear interaction between all slices. On the other hand, the cooperative nonlinear interaction gives rise to imaging artifacts, such as amplitude distortions and side lobes outside of the imaging domain. Contrast mechanism and artifacts are explored experimentally and predicted by simulations on the basis of a proposed RASER MRI theory.

INTRODUCTION

RASER [radio-frequency (RF) amplification by stimulated emission of radiation], also referred to as Zeeman maser, is a nuclear magnetic resonance (NMR) phenomenon as a result of stimulated nuclear spin transitions. RASERs have been investigated using hyperpolarized rare gases (*1*–*4*) as well as ^{1}H, ^{17}O, and even ^{27}Al spins in liquids and solids (*5*–*9*). Multimode RASERs enable comagnetometry, which, in turn, allows for precision measurements (*10*–*13*). In addition, multimode RASER activity gives insight into fundamental phenomena in nonlinear mathematics (*14*) and synergetics (*15*) such as line collapse, multiple-period doubling, intermittence, and chaos (*4*, *12*, *16*). Most recently, the parahydrogen (p-H_2) pumped (*17*, *18*) RASER has been established (*12*, *16*, *19*–*21*), by creating strong population inversions directly in room-temperature solutions. RASER magnetic resonance imaging (MRI) is associated with an alternative contrast mechanism than standard MRI, and it appears natural to wonder whether it could serve as a means to overcome fundamental limits of Lorentzian-based point spread functions (PSFs) in MRI (*22*, *23*).

The spatial resolution of MRI is limited by the width $w = 1/(\pi T_2^*)$ of the Lorentzian PSF. Here, we show that nonlinearly coupled slices can spontaneously form an image out of nuclear spin noise, as an alternative to the superposition of uncoupled Lorentzian PSFs. We describe previously unknown nonlinear MRI physics in a p-H_2 RASER while noting that nonlinear spin evolution in the presence of a gradient including radiation damping effects and dipolar fields has been reported before (*24*–*26*). We note that other hyperpolarization techniques may be used for RASER MRI as described here (*7*).

Conventional MRI uses spin or gradient echoes of nuclear magnetization that need to be excited with RF pulses. An interesting alternative is spin noise imaging, which measures projections without external RF excitation and fast gradient switching (*27*). Spin noise imaging does not require any initial hyperpolarization procedure but requires cryogenically cooled NMR probes and averaging to compensate for the low signal-to-noise ratio (SNR ~ 1).

The system under study here uses hyperpolarized samples in combination with an external high Q resonator at room temperature (*28*), thereby achieving an SNR of >200 in a single scan. The spontaneous RASER burst, which forms in the absence of external RF excitation, reflects the superposition of nonlinearly coupled slices. The corresponding spectrum (RASER MRI) of the burst reports on the spatial distribution of the samples spin number density and can have complicated and distorted shapes. On the other side, the image is very sensitive to local variations in the input profile. Therefore, RASER MRI entails new MRI physics challenges and opportunities caused by the nonlinear coupling.

In the presented work, RASERs emerge when placing a proton spin 1/2 ensemble with a large initial population inversion $d_0 = N_2 - N_1$, above the RASER threshold $d_{th} = 4\,V_s/(\mu_0 \hbar \gamma_H^2\, T_2^* Q)$ in a resonant LC circuit with quality factor Q. In this system, N_2 and N_1 are the populations of the corresponding Zeeman levels 2 and 1; V_s is the sample volume; and μ_0, $\hbar$, and γ_H denote the vacuum permeability, Planck's constant, and the proton gyromagnetic ratio, respectively. For RASER MRI, the proton spins are first pumped into a state of highly negative spin polarization P_H. This corresponds to a positive d_0 value, which is assumed to be several orders of magnitude above the RASER threshold d_{th}. An equivalent and convenient way to characterize the threshold condition for one singular mode is given by $\varepsilon = d_0/d_{th} = T_2^*/\tau_{rd} \gg 1$ (*29*, *30*), where ε is a dimensionless

[1]Institute of Microstructure Technology, Karlsruhe Institute of Technology, 76344 Eggenstein-Leopoldshafen, Germany. [2]Department of Chemistry, North Carolina State University, Raleigh, NC 27606, USA. [3]Institute of Technical and Macromolecular Chemistry, RWTH Aachen University, 52056 Aachen, Germany. [4]Massachusetts General Hospital, A. A. Martinos Center for Biomedical Imaging, Boston, MA 02129, USA. [5]Department of Physics, Harvard University, Cambridge, MA 02138, USA. [6]Department of Chemistry, Integrative Biosciences (IBio), Karmanos Cancer Institute (KCI), Wayne State University, Detroit, MI 48202, USA. [7]Russian Academy of Sciences, Leninskiy Prospekt 14, Moscow 119991, Russia. [8]Department of Physics, North Carolina State University, Raleigh, NC 27695, USA. [9]Joint Department of Biomedical Engineering, University of North Carolina at Chapel Hill and North Carolina State University, Raleigh, NC 27695, USA. [10]Central Institute for Engineering, Electronics and Analytics – Electronic Systems (ZEA-2), Forschungszentrum Jülich GmbH, D-52425 Jülich, Germany.
*Corresponding author. Email: lehmkuhl@kit.edu (S.L.); ttheis@ncsu.edu (T.T.); st.appelt@fz-juelich.de (S.A.)

Downloaded from https://www.science.org at Wayne State University on July 14, 2022

quantity. Note that ε is the enhancement above the RASER threshold, not above thermal nuclear spin polarization. The radiation damping rate is given by $\tau_{rd}^{-1} = \mu_0 \hbar \gamma_H^2 Q\, d_0/(4\, V_s)$, which includes inverted states (positive d_0), and has been studied extensively in NMR spectroscopy (*24*, *29*, *31*–*33*).

To understand how the RASER can be used for MRI, we introduce an analysis of the RASER action in the presence of a magnetic field gradient G_z. The gradient creates a frequency range $\Delta = \gamma_H \cdot G_z \cdot L$ that spans the image domain of the object of length L (section S1). The initial nuclear spin population inversion is spread over the imaging domain Δ and is given by $d_0 = \int_{\nu_0-\Delta/2}^{\nu_0+\Delta/2} \rho_d(\nu)\, d\nu$, where $\rho_d(\nu)$ is the population inversion density and ν_0 is the off-resonance frequency in the center of the imaging domain. The integrand $\rho_d(\nu)d\nu$ can be described as the number of negatively polarized spins in the frequency interval $[\nu, \nu + d\nu]$. Given a profile $\rho_d(\nu)$, a total RASER MRI signal emerges spontaneously out of nuclear spin noise.

To generate a system where a numerical evaluation is feasible, we divide the image domain Δ into $N = \Delta/\delta\nu$ individual slices. To avoid numerical artifacts, the distance δν between consecutive slices has to be chosen small enough. Specifically, $\delta\nu < w$ has to be fulfilled, where $w = 1/(\pi T_2^*)$ is the natural linewidth. Furthermore, to estimate whether a given d_0 is RASER active in a given gradient G_z, we also introduce the threshold population density $\rho_d^{th} = d_{th}/w$ as used below.

To calculate the dynamics of the nonlinearly coupled slices, each slice $\mu = 1, \ldots, N$ is characterized by an initial population inversion $d_\mu(0) = \int_{\nu_0-\Delta/2+(\mu-1)\delta\nu}^{\nu_0-\Delta/2+(\mu)\delta\nu} \rho_d(\nu)\, d\nu$. With a given initial $d_\mu(0)$, the time evolution of the RASER modes or slices can be modeled by a set of $\mu = 1, \ldots, N$ nonlinearly coupled differential equations for the population inversion d_μ and the transverse spin component $\alpha_\mu = A_\mu \exp(i\phi_\mu)$

$$\dot{d}_\mu = -\frac{d_\mu}{T_1} - 4\beta \sum_{\sigma,\tau=1}^{N} A_\sigma A_\tau \cos(\phi_\sigma - \phi_\tau) \quad (1)$$

$$\dot{A}_\mu = -\frac{A_\mu}{T_2^*} + \beta\, d_\mu \sum_{\tau=1}^{N} A_\tau \cos(\phi_\tau - \phi_\mu) \quad (2)$$

$$\dot{\phi}_\mu = 2\pi\{\nu_0 - 0.5\,[\Delta - \delta\nu(2\mu - 1)]\} + \beta \frac{d_\mu}{A_\mu} \sum_{\tau=1}^{N} A_\tau \sin(\phi_\tau - \phi_\mu) \quad (3)$$

$$d_\mu(0) = \int_{\nu_0-\Delta/2+(\mu-1)\delta\nu}^{\nu_0-\Delta/2+\mu\delta\nu} \rho_d(\nu)\, d\nu \quad (4)$$

The coupling constant β is given as $\beta = \mu_0 \hbar \gamma_H^2 Q/(4\, V_s)$. The model for RASER MRI represented by Eqs. 1 to 4 is formulated in the rotating frame (for a complete derivation, see section S1) and is a modification of the existing multimode RASER theory (*12*, *16*). The modifications comprise the initial boundary conditions for $d_\mu(0)$ in Eq. 4, the absence of pumping in Eq. 1, and the definition of the slice frequencies in Eq. 3. Numerical simulations of Eqs. 1 to 4 reveal three important invariance principles for RASER MRI: Provided that $\delta\nu << w$ and $T_1 >> T_2^*$, the shape of the RASER images is independent of (i) the value of the slicing δν, (ii) the longitudinal relaxation time T_1, and (iii) the values of the initial conditions $A_\mu(0)$ and $\phi_\mu(0)$ (see section S6). According to the invariance principle (iii), the shape of the RASER image is the same, irrespective that the initial conditions for $A_\mu(0)$ and $\phi_\mu(0)$ are random values (i.e., nuclear spin noise) or a weak RF pulse with fixed values for $A_\mu(0)$ and $\phi_\mu(0)$. The three invariance principles are crucial for RASER MRI, because they guaranty reproducibility of RASER MRI.

Certain processes can be identified by examining the dynamics described by Eqs. 1 to 3: The population inversion of a given mode μ in Eq. 1 decays with the rate $1/T_1$ and is decreased by the rate given by the sum over all quadratic terms $-4\beta A_\sigma A_\tau \cos(\phi_\sigma - \phi_\tau)$. In turn, the amplitude of A_μ in Eq. 2 decays with the rate $1/T_2^*$ and increases for $\tau = \mu$ with the rate βd_μ. The last term on the right side of Eq. 2, $\beta\, d_\mu \sum_{\tau=1}^{N} A_\tau \cos(\phi_\tau - \phi_\mu)$ for $\tau \neq \mu$, involves a sum over all other amplitudes $A_\tau \cos(\phi_\tau - \phi_\mu)$. This sum can be a growth or decay rate for A_μ, depending on the specific values of all other phase differences $\phi_\tau - \phi_\mu$. The collective action of all modes strongly influences the amplitude and sign of the rate dA_μ/dt, which defines the amplitudes A_μ of the final image.

The spatial encoding of each slice $\mu = 1, \ldots, N$ is reflected by the first term in Eq. 3, where each slice is oscillating at the angular frequency $\omega_\mu = 2\pi(\nu_0 - 0.5\,(\Delta - \delta\nu(2\mu - 1)))$. Apart from this linear evolution of ϕ_μ with time t, there is a nonlinear collective term $(\beta\, d_\mu/A_\mu) \sum_{\tau=1}^{N} A_\tau \sin(\phi_\tau - \phi_\mu)$, which is responsible for synchronism. Equation 3 is analogous to Kuramoto's model of synchronized oscillators (*34*–*36*). The dynamics of RASER MRI given by Eqs. 1 to 4 can be described by a collection of synchronized oscillators or slices with distinct angular frequencies ω_μ, where the amplitude A_μ of each oscillator depends on the self-organization controlled by the collective interaction with all other slices. Therefore, the derivative of the amplitude of each slice depends on the mean-field amplitude produced by all other slices.

Last, the total RASER signal is obtained by the sum of all transverse spin components $\mathrm{Sig}(t) = N^{-1/2} \sum_{\mu=1}^{N} \mathrm{Re}(\alpha_\mu) = N^{-1/2} \sum_{\mu=1}^{N} A_\mu \mathrm{Re}(\exp[i\phi_\mu])$, where $N^{-1/2}$ is a normalization constant. Here, we focus on the difference between the concept of single PSFs to analyze conventional magnetic resonance image formation and the collective mean-field approach, which is the basis of RASER MRI. Numerical solutions of Eqs. 1 to 4 are evaluated (see Fig. 1) to highlight the difference of the spin dynamics for a single RASER slice and the collective behavior of coupled slices.

The simplest case is shown in Fig. 1A for $N = 1$ and $T_1 = \infty$, where the numerically evaluated form matches the exact solution introduced by Mao *et al.* (*31*, *37*, *38*) and discussed by others (*39*, *40*). The corresponding phased and absolute spectra of $\alpha = \alpha_1$ are displayed Fig. 1A (bottom right). For this case, $T_1 = \infty$, the PSF is a hyperbolic secant with width w_{sech} (section S2 and eq. S19). Close to the threshold, such a PSF is narrower than the Lorentzian NMR linewidth $w = 1/(\pi T_2^*)$, because the RASER signal involves dedamping.

No exact solution exists for a finite T_1, but the MR signal represents an asymmetrically shaped PSF (Fig. 1B and section S3). The linewidth w_{as} in the spectrum is slightly broader compared to the symmetric case (Fig. 1A) but still smaller than w.

Here, we include both the effects of finite T_1 and the nonlinear interactions between N slices formed in the presence of a gradient. In contrast to standard MRI, the image contrast and the spatial resolution cannot be explained by independent individual PSFs. Each slice is sensitive to the collective action of all slices, which makes RASER imaging highly sensitive to local variations in d_μ (section S4A), providing interesting avenues for future investigations for RASER MRI.

Downloaded from https://www.science.org at Wayne State University on July 14, 2022

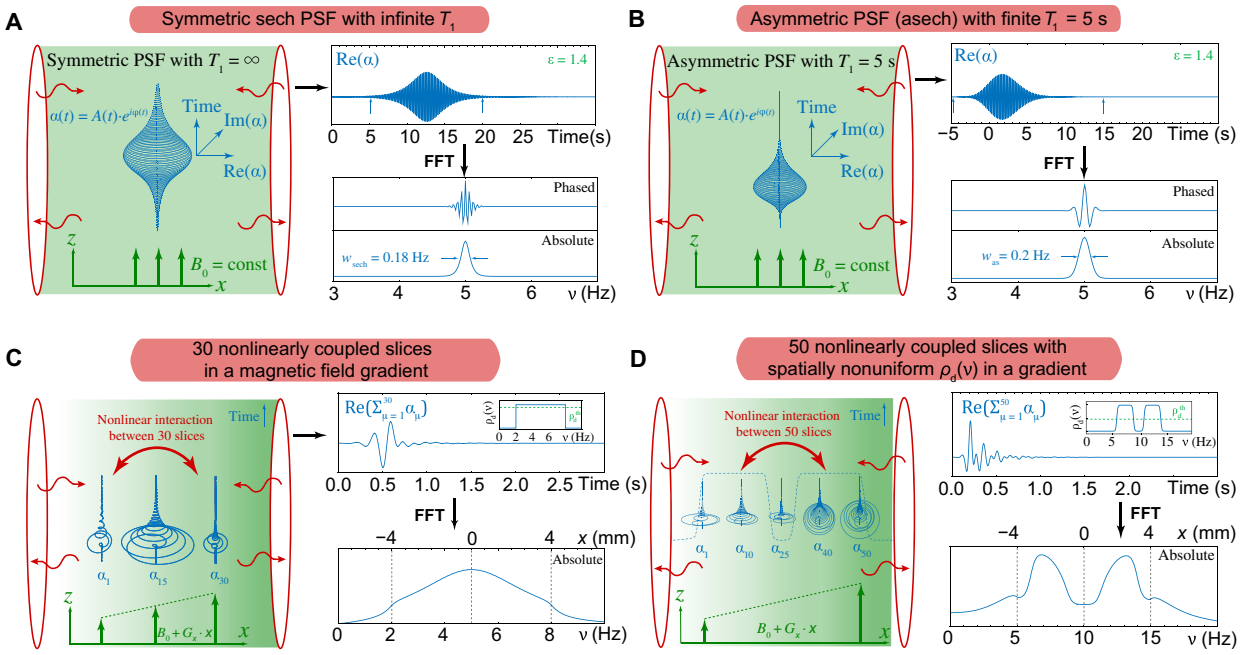

Fig. 1. Simulated RASER signals and the corresponding Fourier-transformed spectra for different numbers of interacting slices. The nonlinear interaction between all slices is mediated by the virtual photons (wavy arrows, wavelength ≫ sample dimension) in the resonator (red) (*51*). After the RASER burst, the Zeeman energy of the spins is fully transferred to the current of the coil (*52*). (**A**) For $N = 1$ and $T_1 = \infty$, the signal $\alpha_1(t) = \alpha(t)$ is plotted in the [t, Re(α), Im(α)] space (left). The projection Re(α) for $d_0 = 4.2 \cdot 10^{15}$ and the corresponding Fourier-transformed spectra are shown on the right. (**B**) For $N = 1$, $T_1 = 5$ s and $d_0 = 4.2 \cdot 10^{15}$, the signal burst $\alpha(t)$ is asymmetric with respect to time. (**C**) Sketch of three representative signals α_μ, where μ = 1, 15, and 30 of $N = 30$ interacting slices [$T_1 = 5$ s, $\Delta = 6$ Hz, rectangular profile with $\rho_d(\nu) = 7.5 \cdot 10^{15}$/Hz]. (**D**) Five representative signals α_μ of $N = 50$ coupled slices [$T_1 = 5$ s, $\Delta = 10$ Hz, nonuniform density $\rho_d(\nu)$]. Threshold population density $\rho_d^{th} = d_{th}/w = 6.6 \cdot 10^{15}$/Hz is indicated as dotted line in the insets in (C) and (D). FFT, fast Fourier transform.

RESULTS

RASER MRI explored by numerical simulation

In the simulation in Fig. 1C, a rectangular polarization profile (inset, top right) is assumed to generate a RASER signal in the presence of a field gradient. The time evolution of three of the $N = 30$ slices is depicted on the left. The shape of signal of these slices differs significantly from the uncoupled PSFs in Fig. 1 (A and B). A corresponding one-dimensional (1D) RASER image (projection) is obtained as the Fourier transform from $\mathrm{Sig}(t) = \mathrm{Re}\left(\sum \alpha_\mu\right)$. The amplitude in the center of the RASER image is larger, and decaying side lobes arise outside of the image boundaries at $x = \pm 4$ mm (bottom right). These artifacts are expected from the theory described in Eqs. 1 to 4 and evaluated in detail by numerical simulations in section S4.

In Fig. 1D, we simulate a RASER image using a spin density profile $\rho_d(\nu)$ to match the experimental setup described in Fig. 2 (A and B). This nonuniform spin density profile $\rho_d(\nu)$ entails two equal compartments separated by a gap. The evolution of five representative RASER slices of $N = 50$ coupled slices is shown (Fig. 1D, left). The image after Fourier transformation (bottom right) reflects roughly the shape $\rho_d(\nu)$ except for the deformed amplitudes of the flat tops and the side lobes, which occur outside the imaging boundaries.

Experimental realization of RASER MRI: 1D demonstrations

To experimentally examine the RASER MRI theory, a simple phantom was prepared consisting of a cylindrical sample chamber divided into two measurement chambers by a glass slide (Fig. 2, A and B). The two chambers are individually supplied with p-H_2 to generate highly negative polarized proton spins (i.e., $d_0 \gg d_{th}$). The chemical system chosen is pyrazine in a liquid methanol-d_4 solution with a dissolved iridium-based Signal Amplification By Reversible Exchange (SABRE) catalyst for nuclear spin polarization (*18*, *41*). RASER magnetic resonance image were acquired in the presence of weak G_x and G_z magnetic field gradients on the order of a few milligauss per centimeter.

Conventional magnetic resonance images were obtained with a spin echo sequence of 90° followed by a 180° rf pulse (Fig. 2C) as a reference. Before the acquisition of the reference spin echo image (SEI), a crusher field gradient was applied to the hyperpolarized sample, to suppress spontaneous RASER buildup. 1D images were acquired using the G_z gradient to visualize the two chambers separated by the dividing glass slide. 2D images were recorded through stepwise switching of the G_x and G_z gradients to rotate through a circle with constant absolute gradient [$|G| = (G_z^2 + G_x^2)^{1/2}$]. The 2D image was then obtained via projection reconstruction, which is also common in computed tomography.

The RASER images were acquired in a similar way (Fig. 2D), but in contrast to the spin echo sequence, no RF pulses were applied. The signal is acquired in the presence of G_x and G_z field gradients during spontaneous RASER emission, which begins shortly after the crusher field gradient is turned off.

The RASER action can be measured over an indefinite period (Fig. 3A), when p-H_2 is continuously bubbled through the solution. However, the bubbling-induced sample motion in the presence of field gradients is a challenge for imaging. The motion collapses the RASER spectrum in each chamber into one average frequency (Fig. 3B). To avoid line collapse induced by sample motion and to

Downloaded from https://www.science.org at Wayne State University on July 14, 2022

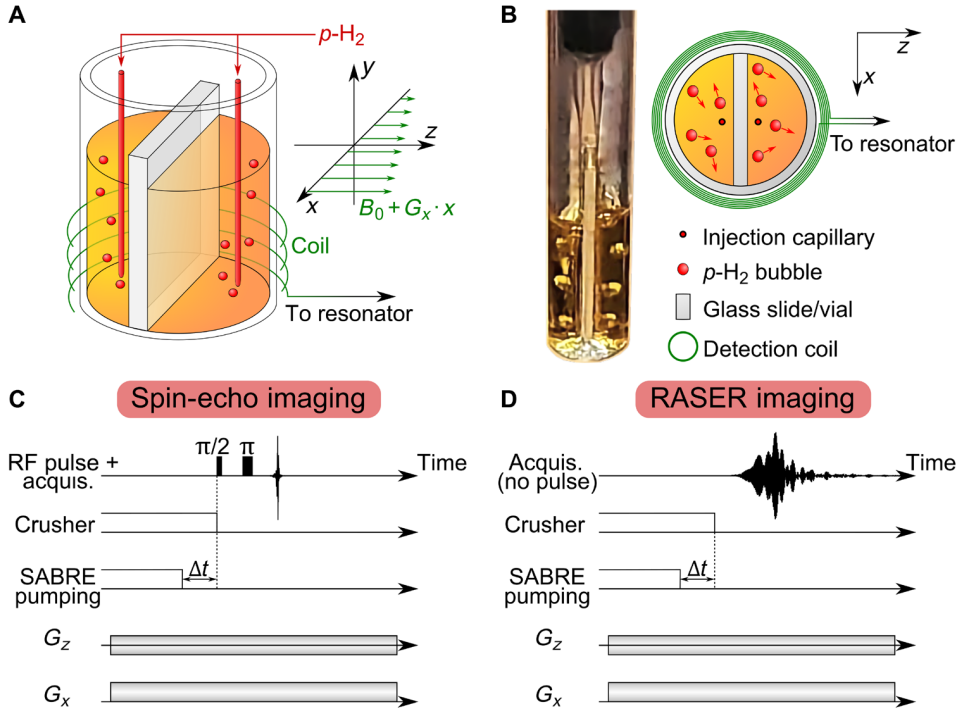

Fig. 2. Experimental setup for MRI of a two-chamber phantom and corresponding pulse sequences for SEI and RASER MRI. (**A**) Schematics of the two imaged chambers and of the gradient directions. (**B**) Photo and top-down schematic of the two chambers (L = 8 mm in diameter and 10 mm in height separated by a 1-mm-thick glass slide) including bubbling of p-H_2 through two capillaries [100 μm in outer diameter (OD) and 30 μm in inner diameter (ID)]. (**C**) Spin echo sequence of 90° followed by a 180° rf pulse for SEI. (**D**) RASER imaging sequence. For both imaging sequences, a crusher gradient is applied to destroy all coherence, while negative proton polarization is built up by SABRE pumping at magnetic fields B_0 of 3.9 and 7.8 mT. p-H_2 bubbling is interrupted to allow the solution to settle for a time Δt. For SEI, the image is encoded in the echo signal. In the case of RASER MRI, the signal builds up spontaneously in the absence of any RF excitation. Frequency encoding is performed in the x and z directions.

enable imaging, the p-H_2 flow had to be stopped and an additional waiting time Δt was introduced, which allows for the solution to settle and the motions to halt. Now, both spin echo and 1D RASER signals could be acquired (Fig. 3, D and G) shortly after the crusher gradient was switched off. The acquired RASER burst in Fig. 3G is significantly longer than the corresponding spin echo in Fig. 3D acquired at the same gradient strength of G_z = 3.84 mG/cm.

The spatial resolution limit is given by $\delta z = w/(\gamma_H \cdot G_z)$ in conventional MRI (*22*). This limit yields δz_{SEI} = 280 μm for the SEI in Fig. 3E, and as a result, the gap and the edges of the sample are not well resolved. However, for RASER 1D projection in Fig. 3H, the slope at the image boundaries at the gap is more than three times steeper. This corresponds to an estimated spatial resolution of $\delta z_{RI} \approx$ 90 μm. However, care has to be taken with this comparison because the contrast mechanism for RASER MRI is based on collective and nonlinear interaction. Spatial resolution might not be a suitable measure for the observed hole in Fig. 3H. Instead, we examine the sensitivity of RASER MRI to local variation in the object $\rho_d(v)$ compared to the sensitivity of conventional MRI to local variations in the object. Simulations support that RASER MRI is more sensitive to small local variations in the imaged object (section S4A and fig. S7).

The measured 1D RASER image in Fig. 3H shows signal lobes outside the boundaries of z = −4 mm, in accordance with the simulation shown in Fig. 1D. These artifacts from 1D RASER MRI are analyzed in section S4B, and a potential correction method is proposed.

Experimental realization of RASER MRI: 2D demonstration and comparison to traditional SEI of hyperpolarized solutions

Both a 2D SEI (Fig. 4A) and a 2D RASER MRI (Fig. 4B) of the same sample are obtained, extending 1D imaging to 2D imaging by reconstructing from 30 angular directions. The field gradient used for the SEI was 3.5 times larger than that for RASER MRI to obtain comparable resolution. Each individual projection in the SEI has a resolution of 50 μm, only about an order of magnitude higher than modern microimaging (*42*–*44*). The two semicircle-shaped halves and the 1-mm gap are visible in Fig. 4 (A and B). These images also display typical projection reconstruction star artifacts outside of the imaging domain. The 2D RASER image in Fig. 4B not only shows sharper features but also exhibits a deformed shape of the sample and its gap, paired with several interfering lines. These lines could be caused by the nonlinear interaction between the slices, analogous to features observed during strong radiation damping at high magnetic field (*45*). An alternative reason could be the residual motion in the liquid after turning off the p-H_2 pumping. These artifacts can be identified in the individual 1D projections, which are used to reconstruct the 2D RASER image (see fig. S11).

RASER MRI dependence on polarization

A stark contrast of RASER MRI to traditional MRI is the dependence of RASER MRI images on the magnitude of the nuclear spin polarization. Figure 5 shows a series of 1D RASER images and SEIs

Downloaded from https://www.science.org at Wayne State University on July 14, 2022

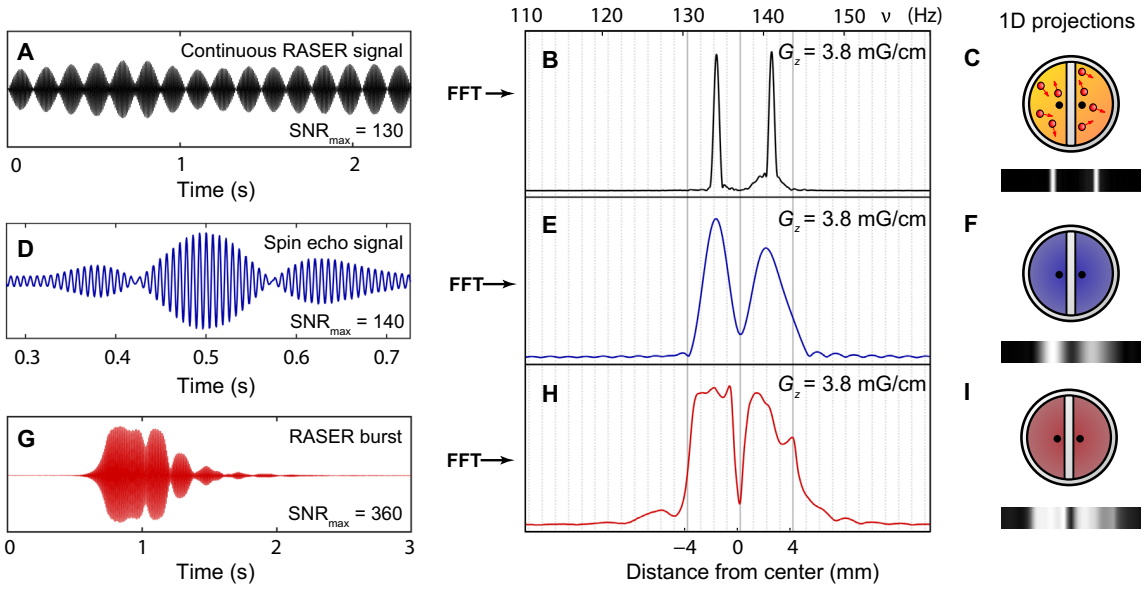

Fig. 3. 1D projections of a continuously pumped proton RASER, a SEI, and a RASER image. (**A**) Continuously SABRE pumped proton RASER signal and corresponding fast Fourier transform spectrum (**B**) in the presence of a gradient G_z. A Hamming window is applied to the signal before fast Fourier transform to suppress sinc wiggles. (**D**) Spin echo acquired with the sequence in Fig. 2C and (**E**) corresponding Fourier-transformed SEI. (**G**) RASER burst acquired with the sequence in Fig. 2D. (**H**) Corresponding RASER 1D projection, which is three times better resolved ($\delta z_{RI} \approx 90$ μm) than the SEI in (E). $B_0 = 7.8$ mT (proton resonance frequency of 333 kHz), and no slice selection is applied. The RASER image (H) has $SNR_{max} = 360$ at $\Delta t = 2$ s, while the SEI in (B) yields $SNR_{max} = 140$ at $\Delta t = 5$ s. All images are phased in the absolute mode and were measured in a single scan. (**C**, **F**, and **I**) Corresponding image phantom and 1D projections.

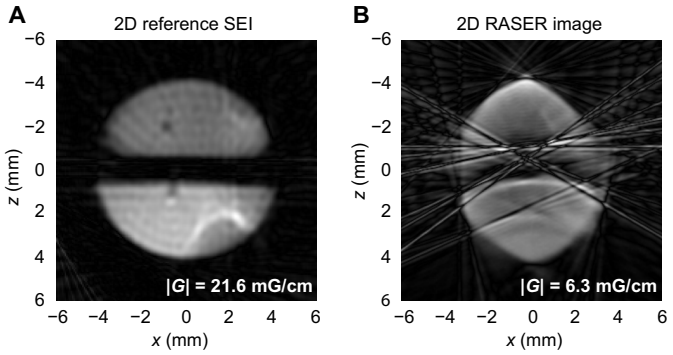

Fig. 4. 2D SEI and 2D RASER image. (**A**) 2D SEI and (**B**) 2D RASER MRI measured at 3.9 mT. The 2D images (A and B) are obtained by projection reconstruction of 30 projections each. These 1D projections are measured with the sequence in Fig. 2 (C and D) from different angles by varying G_x and G_z such that $G_x^2 + G_z^2 =$ constant. In (A), the two capillaries used for *p*-H_2 supply are visible around $x = -1$ mm, $z = 0.5$ mm and $x = -1.5$ mm, $z = -2$ mm for each chamber. The RASER image (B) is recorded at a 3.5 times smaller gradient than (A), but both spatial resolutions are similar. The RASER image is affected by interference lines. The origin of these artifacts is discussed in the text and in section S5.

of the phantom, acquired with decreasing levels of polarization, i.e., decreasing population inversion d_0. The polarization was adjusted by implementing an increasing waiting time Δt between the polarization step and acquisition.

For SEI, decreasing polarization entails decreasing SNR for each image in Fig. 5A, but the shape of the image in the interval of 2 s < Δt < 20 s (about a few T_1 relaxation periods) remains invariant. The spatial resolution for the SEI is determined by the slope on the sample boundaries with $\delta z_{SEI} \approx 50$ μm. This observation is in overall good agreement with the theoretical expectation of $\delta z_{SEI} = w/(\gamma_H \cdot G_z) = 55$ μm. Although the initial negative polarization (d_0) changes by more than a factor 10 within the first 20 s, the shape of the SEIs is invariant. This behavior exists because the widths of the underlying PSFs barely deviate from a Lorentzian linewidth and radiation damping effects are insignificant. At longer waiting times (Δt > 20 s), noise becomes more dominant, and the shape deteriorates as more efficient relaxation at the walls decreases the image amplitude at the boundaries of the sample.

In contrast, the RASER image shape in Fig. 5B strongly depends on polarization. We attribute the differences between the two image halves to disparities in the bubbling rates and phantom shapes (see section S4C). In the case of low polarization (Δt > 15 s), the maximum amplitude of the right half of the sample is substantially smaller, because the population inversion density $\rho_d(\nu)$ is closer to the RASER threshold density ρ_d^{th}. Because of the collective and nonlinear nature of the contrast mechanism, the slightly larger $\rho_d(\nu)$ of the left half substantially suppresses the amplitude on the right half. This asymmetry in amplitude is much less pronounced if $\rho_d(\nu)$ is further above ρ_d^{th}, for example, at a weaker gradient G_z as in Fig. 3H. Figure 5C shows simulated RASER images for five different initial population inversions d_0 and corresponding profiles $\rho_d(\nu)$ (see fig. S10) to examine the origin of the RASER image distortions. The experiment at Δt = 8 s matches the simulation with only one peak (width = 0.6 Hz; fig. S9), and for the experiments Δt < 8 s, the simulation qualitatively reflects the amplitude deformations and side lobes seen in the measured images. The ripples in some images in Fig. 5B cannot be simulated assuming a uniform division of the RASER image into $N = \Delta/\delta\nu$ slices. Motional artifacts and variations

Downloaded from https://www.science.org at Wayne State University on July 14, 2022

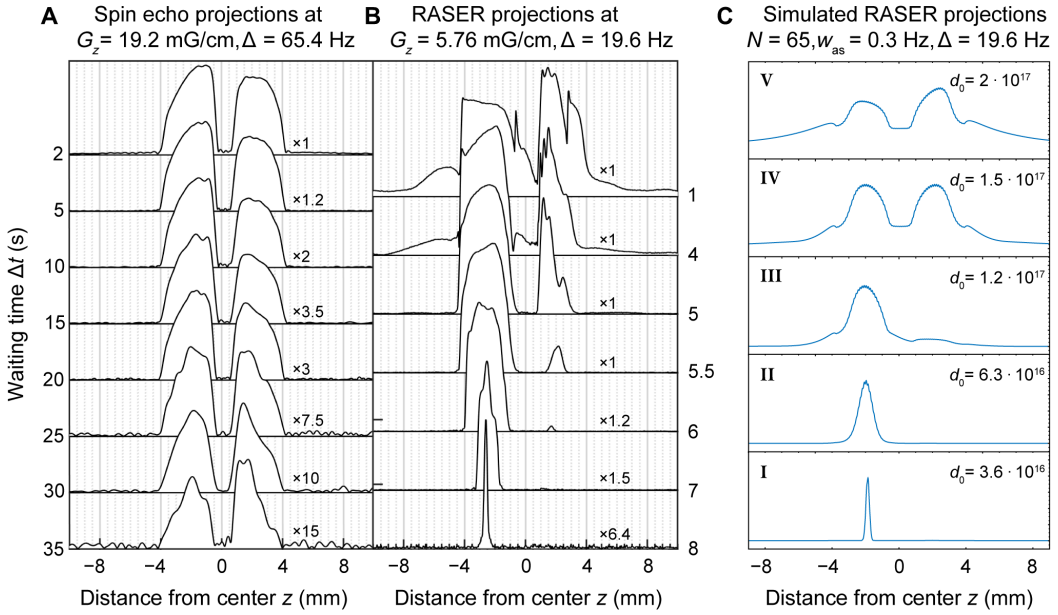

Fig. 5. Projections of measured SEI, RASER MRI at B_0 = 7.8 mT, and simulated RASER MRI at different waiting times Δ*t*. (**A**) The SEI was acquired at G_z = 19.2 mG/cm (δz_{SEI} = 0.055 mm) without slice selection. The shape remains form invariant up until Δ*t* = 20 s. (**B**) The 1D RASER image was acquired at G_z = 5.76 mG/cm. At higher polarizations, i.e., for Δ*t* < 5 s, both sides of the image are governed by strong nonlinear effects. At lower polarization, Δ*t* > 5 s, the amplitude of the right half in the phantom is strongly attenuated. At Δ*t* = 8 s, the RASER image is reduced to one peak of 0.6 Hz width. (**C**) Simulated RASER images, based on Eqs. 1 to 4 and on a profile $\rho_d(v)$ similar to the SEI in (A). These reflect the basic features at different values d_0 (I to V), i.e., side lobes outside of the imaging domain and nonlinear deformations. All spectra are phased in absolute mode and normalized to the maxima of each image.

of T_1, T_2*, and B_1 field over the image domain may be responsible for the observed ripples.

DISCUSSION

The proof-of-principle experiments provided here and the corresponding nascent theoretical framework motivate several new challenges and may provide an opportunity to explore the power of alternative contrast mechanisms provided by RASER MRI. A high sensitivity with respect to local variations in the input profile was found, which is based on collective nonlinear interactions between all regions of the sample. There is negligible background signal from other protons (e.g., water or solvent) in RASER experiments. At low magnetic fields (4 and 8 mT are demonstrated here), the RASER signal is many orders of magnitude larger compared to the signal of the more abundant background protons with low Boltzmann polarization. At higher magnetic fields (1.4 T) in RASER NMR spectroscopy, no proton background signals of water were observed because the RF from the RASER active protons does not excite the chemically shifted water protons (*46*). Further potential advantages are the absence of external RF excitation (*27*) (e.g., caused by the transmission coil), which imply minimal specific absorption rate, avoiding unintended heat deposition. In addition, RASER MRI can produce sufficient contrast with weaker magnetic field gradients, reducing potential concerns over peripheral nerve stimulation (*47*). This is a relevant concern if in vivo translation is possible. Last, the RASER MRI theory is connected to many seemingly disjunct systems in science and technology. The developed system of differential equation (Eqs. 1 to 4) and its solutions for the RASER MRI model are equivalent to the fundamental equations in many other fields with prominent examples in synergetics (*15*) and nonlinear dynamics (*14*, *36*, *48*, *49*). We point the interested reader to section S6, where several of those analogies are detailed.

MATERIALS AND METHODS

Sample preparation and setup

SABRE samples were prepared under Schlenk conditions. The samples contained 5 mM SABRE catalyst precursor [Ir(cyclooctadiene)(1,3-bis(2,4,6-trimethylphenyl)imidazole-2-ylidene)Cl] (*41*), and c_{pyr} = 100 mM pyrazine in methanol-d_4. Pyrazine was chosen because it is associated with a single resonance in the NMR spectrum with $n_{s(pyr)}$ = 4 chemically and magnetically equivalent protons, ideal for RASER and SEI experiments. Three hundred microliters were filled into each chamber, giving a total sample volume V_s = 600 μl. A glass capillary [~100 μm in outer diameter (OD) and 30 μm in inner diameter (ID)] was introduced into each chamber for parallel p-H_2 supply. During polarization buildup, p-H_2 was bubbled through the solution at a flow rate of ~30 sccm and at pressure of 2 bar. p-H_2 was generated using a Bruker p-H_2 generator at 35 K, yielding ~94% enriched p-H_2 gas. The sample is located in a cylindrical glass tube (ID = 8 mm), divided by a glass slide (1 mm in thickness) for two-chamber experiments. The designed phantom is handmade. The 1-mm-thick glass sheet is held in place by chemically resistant glue. The liquid sample inside the two chambers is located in the sensitive volume of a cylindrical NMR detection coil (10 mm in ID and 10 mm in height), which is connected to an external resonator with high quality factor (Q_{ext} = 360 at 166 kHz) for sensitive detection of the NMR or RASER signals (*28*). Typically, a negative pyrazine proton polarization of $P_H \approx -10^{-3}$ to -10^{-2} is achieved in a

Downloaded from https://www.science.org at Wayne State University on July 14, 2022

magnetic field ranging from 3.9 to 7.8 mT. These chosen magnetic fields are close to the field B_0 = 6.5 mT, where the SABRE ^{1}H polarization for pyridine and similar chemical motives such as pyrazine is maximized (*18*). With respect to RASER MRI, low magnetic fields do offer the additional advantage of lower susceptibility artifacts.

Setup-specific parameters

A SABRE-induced ^{1}H polarization of $P_H = -10^{-3}$ corresponds to a population inversion $d_0 = c_{pyr} \cdot V_s \cdot (-P_H) \cdot n_{s(pyr)}\, N_A = 0.1$ mol/l $\cdot\, 6 \cdot 10^{-4}$ l $\cdot\, -(-10^{-3}) \cdot 4,\ 6.022 \cdot 10^{23}$/mol $= 1.4 \cdot 10^{17}$. The total number of ^{1}H spins in the sample is $N_s = 1.4 \cdot 10^{20}$. Analogous calculations yield the initial conditions for simulations in RASER MRI explored by numerical simulation and RASER MRI dependence on polarization and the Supplementary Materials. For example, in Fig. 5, the initial population inversion is assumed to lie between $d_0 = 3.6 \cdot 10^{16}$ and $2 \cdot 10^{17}$. The ^{1}H NMR parameters of pyrazine were measured to be $T_2^* = 0.7$ s (Lorentzian width $w = 1/(\pi T_2^*) = 0.455$ Hz). T_1 values at different positions were measured using the results of the SEIs versus Δt (see Fig. 5A). We found $T_1 = 5.0$ s in the bulk. The measurement close to the walls varied around $T_1 = 2.5 \pm 0.5$ s. For the simulations, we chose a difference in T_1 between the bulk and the walls of 3 s.

The total quality factor of the combined resonator (external resonator and NMR coil) is $Q = 100$. The B_1 field profile from the NMR detection coil in the center of the sample is calculated to be about 10% lower compared to the field at the edges of the sample. As the RASER active slices interact through the B_1 field of the coil, the coupling now depends on space, which is not accounted for in the parameter β in Eqs. 1 to 3. In summary, the dependence of B_1, T_2^*, and T_1 on the location of the sample is the major sources for RASER imaging artifacts. Correction algorithms for artifacts are state of the art for high-field MRI scanners (*50*) and could mostly be adapted to the artifacts presented here. The magnetic fields of the low-cost MRI system are generated by a set of four handmade shim gradients (G_x, G_y, G_z, and G_{crush}) and an electromagnet producing a constant field in the range of 0.5 mT < B_0 < 20 mT. For our experiments, we chose B_0 = 3.9 and 7.8 mT corresponding to 166.6- and 333.3-kHz ^{1}H resonance frequency, respectively. The reference frequency of the spectrometer is chosen such that the off-resonance frequency ν_0 is between 20 and 150 Hz away from the ^{1}H resonance frequency. The homogeneity of the B_0 field is 1 part per million (ppm)/cm^3. The *p*-H_2 supply in a low-field electromagnet in conjunction with sensitive external high-quality-factor enhanced (EHQE) detection avoids the necessity of a shuttling system for rapid transport of the sample into a high-field magnet. The G_x and G_z gradients were used to obtain projections from 30 different angles (in 6° steps). All data were acquired in a single scan. SEIs were acquired at an echo time of 1 s. 2D images were obtained after projection reconstruction of the 1D slices using a MATLAB code, written for this project. The spatial resolution is divided into a resolution along a slice in radial and angular direction. The radial resolution is 50 μm for SEI at 21.6 mG/cm, which corresponds to 160 points along the 8-mm sample diameter. The angular resolution with 30 slices spanning 180° is 6°.

There are frequency shifts due to slow magnetic B_0 field drifts in the order of a few ppm per minute. At 333 kHz (7.8 mT), these drifts on a time scale of 10 min were more pronounced compared to 166 kHz (3.9 mT). The reason is thermal instability of the current supply in conjunction with heating of the resistive B_0 field coil. For one 1D RASER image measured at 7.8 mT with a corresponding RASER burst lasting a few seconds, a drift of a ppm per minute means less than 0.1 ppm or 0.03-Hz frequency drift. The image domain Δ is typically chosen between 10 and 100 Hz (corresponding to about 20 to 200 slices for SEI), so the drift for a single 1D RASER image is negligible. For a 2D RASER image with a total measuring time of about 30 min for all 30 1D slices, the central frequency between the individual 1D slices could differ by a few Hz. Thus, each 1D image was shifted to yield the same center frequency for all 1D images before projection reconstruction.

Simulation details

The simulations based on the model Eqs. 1 to 4 were performed using Mathematica 8. The NDSolve[] routine was used for the numerical evaluation of the variables $d_\mu(t)$, $A_\mu(t)$, and $\phi_\mu(t)$. The computation time of the system eqs. S5 to S8 can be quite long depending on the number of modes *N*. All parameters d_μ, A_μ, and ϕ_μ are coupled in between each other in a nonlinear way by the cos and sin terms on the right sides of eqs. S5 to S7. This is the reason for many nonlinear phenomena, which can arise in this RASER MRI model, ranging from phase locking, collapse phenomena, nonlinear image distortions, and edge effects to multiple-period doubling and chaos. While there are exactly *N* coupling terms for A_μ and ϕ_μ in eqs. S6 and S7, the number of coupling terms for d_μ in Eq. S5 is $N(N-1)/2$. For larger numbers of slices, $N > 100$, the system of equations becomes elaborate and a large amount of computation is required. The computation time is roughly proportional to N^3, so the system eqs. S5 to S7 is classified as a polynomial problem. A typical numerical evaluation using a personal computer takes about 60 s for $N = 50$ and can be many hours to days for $N > 100$.

For these simulations, initial conditions for $d_\mu(0)$, $A_\mu(0)$, and $\phi_\mu(0)$ are required. The initial conditions for $d_\mu(0)$ at $t = 0$ were calculated for a given profile $\rho_d(\nu)$ (Eq. 4). For $N_s = 1.4 \cdot 10^{20}$ ^{1}H spins, the average value for the initial spin noise amplitude is $\langle A \rangle \sim (N_s)^{1/2} = 1.18 \cdot 10^{10}$ with a random phase $\phi_\mu(0)$. For the simulations, constant values were assumed for simplicity [i.e., $A_\mu(0) = 10^{12}$ and $\phi_\mu(0) = 0$] because the RASER image is independent from the initial transverse spin components [see invariance principle (III) in Introduction and section S1).

SUPPLEMENTARY MATERIALS

Supplementary material for this article is available at https://science.org/doi/10.1126/sciadv.abp8483

REFERENCES AND NOTES

1. M. G. Richards, B. P. Cowan, M. F. Secca, K. Machin, The ^{3}He nuclear Zeeman maser. *J. Phys. B. At. Mol. Opt.* **21**, 665–681 (1988).
2. T. E. Chupp, R. J. Hoare, R. L. Walsworth, B. Wu, Spin-exchange-pumped ^{3}He and ^{129}Xe Zeeman masers. *Phys. Rev. Lett.* **72**, 2363–2366 (1994).
3. H. Gilles, Y. Monfort, J. Hamel, ^{3}He maser for earth magnetic field measurement. *Rev. Sci. Instrum.* **74**, 4515–4520 (2003).
4. D. J. Marion, G. Huber, P. Berthault, H. Desvaux, Observation of noise-triggered chaotic emissions in an NMR-maser. *Chem Phys. Chem.* **9**, 1395–1401 (2008).
5. P. Bösiger, E. Brun, D. Meier, Solid-state nuclear spin-flip maser pumped by dynamic nuclear polarization. *Phys. Rev. Lett.* **38**, 602–605 (1977).
6. A. G. Zhuravrev, V. L. Berdinskiĭ, A. L. Buchachenko, Generation of high-frequency current by the products of a photochemical reaction. *JETP Lett.* **28**, 140 (1978).
7. H. Y. Chen, Y. Lee, S. Bowen, C. Hilty, Spontaneous emission of NMR signals in hyperpolarized proton spin systems. *J. Magn. Reson.* **208**, 204–209 (2011).
8. E. M. M. Weber, D. Kurzbach, D. Abergel, A DNP-hyperpolarized solid-state water NMR MASER: Observation and qualitative analysis. *Phys. Chem. Chem. Phys.* **21**, 21278–21286 (2019).
9. M. A. Hope, S. Björgvinsdóttir, C. P. Grey, L. Emsley, A magic angle spinning activated ^{17}O DNP raser. *J. Phys. Chem. Lett.* **12**, 345–349 (2021).
10. S. Appelt, G. Wäckerle, M. Mehring, Deviation from Berry's adiabatic geometric phase in a ^{131}Xe nuclear gyroscope. *Phys. Rev. Lett.* **72**, 3921–3924 (1994).

Downloaded from https://www.science.org at Wayne State University on July 14, 2022

11. T. W. Kornack, R. K. Ghosh, M. V. Romalis, Nuclear spin gyroscope based on an atomic comagnetometer. *Phys. Rev. Lett.* **95**, 230801 (2005).
12. S. Appelt, A. Kentner, S. Lehmkuhl, B. Blümich, From LASER physics to the para-hydrogen pumped RASER. *Prog. Nucl. Magn. Reson. Spectrosc.* **114–115**, 1–32 (2019).
13. V. V. Soshenko, S. V. Bolshedvorskii, O. Rubinas, V. N. Sorokin, A. N. Smolyaninov, V. V. Vorobyov, A. V. Akimov, Nuclear spin gyroscope based on the nitrogen vacancy center in diamond. *Phys. Rev. Lett.* **126**, 197702 (2021).
14. S. H. Strogatz, *Nonlinear Dynamics and Chaos: With Applications to Physics, Biology, Chemistry, and Engineering* (Avalon Publishing, 2014).
15. H. Haken, *Synergertics: An Introduction* (Springer-Verlag, 1983).
16. S. Appelt, S. Lehmkuhl, S. Fleischer, B. Joalland, N. M. Ariyasingha, E. Y. Chekmenev, T. Theis, SABRE and PHIP pumped RASER and the route to chaos. *J. Magn. Reson.* **322**, 106815 (2021).
17. C. R. Bowers, D. P. Weitekamp, Transformation of symmetrization order to nuclear-spin magnetization by chemical reaction and nuclear magnetic resonance. *Phys. Rev. Lett.* **57**, 2645–2648 (1986).
18. R. W. Adams, J. A. Aguilar, K. D. Atkinson, M. J. Cowley, P. I. P. Elliott, S. B. Duckett, G. G. R. Green, I. G. Khazal, J. López-Serrano, D. C. Williamson, Reversible interactions with para-hydrogen enhance NMR sensitivity by polarization transfer. *Science* **323**, 1708–1711 (2009).
19. M. Suefke, S. Lehmkuhl, A. Liebisch, B. Blumich, S. Appelt, Para-hydrogen raser delivers sub-millihertz resolution in nuclear magnetic resonance. *Nat. Phys.* **13**, 568–572 (2017).
20. A. N. Pravdivtsev, F. D. Sönnichsen, J. B. Hövener, Continuous radio amplification by stimulated emission of radiation using parahydrogen induced polarization (PHIP-RASER) at 14 Tesla. *Chem. Phys. Chem.* **21**, 667–672 (2020).
21. B. Joalland, N. M. Ariyasingha, S. Lehmkuhl, T. Theis, S. Appelt, E. Y. Chekmenev, Parahydrogen-induced radio amplification by stimulated emission of radiation. *Angew. Chem. Int. Ed.* **59**, 8654–8660 (2020).
22. P. T. Callaghan, *Principles of Nuclear Magnetic Resonance Microscopy* (Clarendon Press, 1993).
23. P. C. Lauterbur, P. Mansfield, *The Nobel Prize in Physiology or Medicine* (2003); www.nobelprize.org/prizes/medicine/2003/summary/.
24. A. Vlassenbroek, J. Jeener, P. Broekaert, Radiation damping in high resolution liquid NMR: A simulation study. *J. Chem. Phys.* **103**, 5886–5897 (1995).
25. Y. Y. Lin, N. Lisitza, S. Ahn, W. S. Warren, Resurrection of crushed magnetization and chaotic dynamics in solution NMR spectroscopy. *Science* **290**, 118–121 (2000).
26. M. T. Pöschko, V. V. Rodin, J. Schlagnitweit, N. Müller, H. Desvaux, Nonlinear detection of secondary isotopic chemical shifts in NMR through spin noise. *Nat. Commun.* **8**, 13914 (2017).
27. N. Müller, A. Jerschow, Nuclear spin noise imaging. *Proc. Natl. Acad. Sci. U.S.A.* **103**, 6790–6792 (2006).
28. M. Suefke, A. Liebisch, B. Blümich, S. Appelt, External high-quality-factor resonator tunes up nuclear magnetic resonance. *Nat. Phys.* **11**, 767–771 (2015).
29. M. P. Augustine, S. D. Bush, E. L. Hahn, Noise triggering of radiation damping from the inverted state. *Chem. Phys. Lett.* **322**, 111–118 (2000).
30. A. Jurkiewicz, Properties and edition of NMR spontaneous maser emission spectra. *Appl. Magn. Reson.* **50**, 709–724 (2019).
31. X. A. Mao, C. H. Ye, Understanding radiation damping in a simple way. *Concept. Magn. Reson.* **9**, 173–187 (1997).
32. M. P. Augustine, Transient properties of radiation damping. *Prog. Nucl. Magn. Reson. Spectrosc.* **40**, 111–150 (2002).
33. V. V. Krishnan, N. Murali, Radiation damping in modern NMR experiments: Progress and challenges. *Prog. Nucl. Magn. Reson. Spectrosc.* **68**, 41–57 (2013).
34. S. H. Strogatz, From Kuramoto to Crawford: Exploring the onset of synchronization in populations of coupled oscillators. *Physica D* **143**, 1–20 (2000).
35. Y. Kuramoto, D. Battogtokh, Coexistence of coherence and incoherence in nonlocally coupled phase oscillators. *Nonlinear Phenom. Complex Syst.* **5**, 380 (2002).
36. Y. Kuramoto, H. Nakao, On the concept of dynamical reduction: The case of coupled oscillators. *Philos. Trans. Royal Soc. A* **377**, 20190041 (2019).
37. X. A. Mao, C. H. Ye, Line shapes of strongly radiation-damped nuclear magnetic resonance signals. *J. Chem. Phys.* **99**, 7455–7462 (1993).
38. X. A. Mao, J. X. Guo, C. H. Ye, Nuclear-magnetic-resonance line-shape theory in the presence of radiation damping. *Phys. Rev. B* **49**, 15702–15711 (1994).
39. D. J. Y. Marion, P. Berthault, H. Desvaux, Spectral and temporal features of multiple spontaneous NMR-maser emissions. *Eur. Phys. J. D* **51**, 357–367 (2009).
40. V. Henner, H. Desvaux, T. Belozerova, D. J. Y. Marion, P. Kharebov, A. Klots, Collective effects due to dipolar fields as the origin of the extremely random behavior in hyperpolarized NMR maser: A theoretical and numerical study. *J. Chem. Phys.* **139**, 144111 (2013).
41. M. J. Cowley, R. W. Adams, K. D. Atkinson, M. C. R. Cockett, S. B. Duckett, G. G. R. Green, J. A. B. Lohman, R. Kerssebaum, D. Kilgour, R. E. Mewis, Iridium N-heterocyclic carbene complexes as efficient catalysts for magnetization transfer from para-hydrogen. *J. Am. Chem. Soc.* **133**, 6134–6137 (2011).
42. S.-C. Lee, K. Kim, J. Kim, S. Lee, J. H. Yi, S. W. Kim, K.-S. Ha, C. Cheong, One micrometer resolution NMR microscopy. *J. Magn. Reson.* **150**, 207–213 (2001).
43. L. Ciobanu, D. A. Seeber, C. H. Pennington, 3D MR microscopy with resolution 3.7 microm by 3.3 microm by 3.3 microm. *J. Magn. Reson.* **158**, 178–182 (2002).
44. A. J. Ilott, A. Jerschow, Super-resolution surface microscopy of conductors using magnetic resonance. *Sci. Rep.* **7**, 5425 (2017).
45. J. Schlagnitweit, S. W. Morgan, M. Nausner, N. Müller, H. Desvaux, Non-linear signal detection improvement by radiation damping in single-pulse NMR spectra. *Chem. Phys. Chem.* **13**, 482–487 (2012).
46. B. Joalland, T. Theis, S. Appelt, E. Y. Chekmenev, Background-free proton NMR spectroscopy with radiofrequency amplification by stimulated emission radiation. *Angew. Chem. Int. Ed.* **60**, 26298–26302 (2021).
47. J. De Wilde, D. Grainger, D. Price, C. Renaud, Magnetic resonance imaging safety issues including an analysis of recorded incidents within the UK. *Prog. Nucl. Magn. Reson. Spectrosc.* **51**, 37–48 (2007).
48. S. Kaka, M. R. Pufall, W. H. Rippard, T. J. Silva, S. E. Russek, J. A. Katine, Mutual phase-locking of microwave spin torque nano-oscillators. *Nature* **437**, 389–392 (2005).
49. C. Bick, M. Goodfellow, C. R. Laing, E. A. Martens, Understanding the dynamics of biological and neural oscillator networks through exact mean-field reductions: A review. *J. Math. Neurosci.* **10**, 9 (2020).
50. J. T. Vaughan, M. Garwood, C. M. Collins, W. Liu, L. D. Barre, G. Adriany, P. Andersen, H. Merkle, R. Goebel, M. B. Smith, K. Ugurbil, 7T vs. 4T: RF power, homogeneity, and signal-to-noise comparison in head images. *Magn. Reson. Med.* **46**, 24–30 (2001).
51. F. Engelke, Virtual photons in magnetic resonance. *Concepts Magn. Reson. Part A* **36A**, 266–339 (2010).
52. X. A. Mao, Calculation of the energy transferred by radiation damping from nuclear spin system to receiver coil in NMR. *Chem. Phys. Lett.* **756**, 137853 (2020).
53. S. Nadis, All together now. *Nature* **421**, 780–782 (2003).
54. P. Ebrahimzadeh, M. Schiek, P. Jaros, T. Kapitaniak, S. van Waasen, Y. Maistrenko, Minimal chimera states in phase-lag coupled mechanical oscillators. *Eur. Phys. J. Spec. Top.* **229**, 2205–2214 (2020).
55. A. Ruotolo, V. Cros, B. Georges, A. Dussaux, J. Grollier, C. Deranlot, R. Guillemet, K. Bouzehouane, S. Fusil, A. Fert, Phase-locking of magnetic vortices mediated by antivortices. *Nat. Nanotechnol.* **4**, 528–532 (2009).
56. E. N. Lorenz, Deterministic nonperiodic flow. *J. Atmos. Sci.* **20**, 130–141 (1963).

Acknowledgments: S.L. was accepted as a guest scientist in the RWTH Aachen University and acknowledges the university for providing the research environment and equipment to run all experiments of this study at the ITMC (Institute of Technical and Macromolecular Chemistry). S.A. thanks J. Oquendo Mora (S.A.'s wife) for keeping up the moral during difficult situations in the coronavirus disease 2019 pandemic. Excellent cooperative and IT support from S. van Waasen, M. Schiek, and U. Probst from Forschungszentrum Jülich are acknowledged. M. Adams is greatly acknowledged for valuable help in designing the phantom. **Funding:** This work is supported by the Department of Defense CDMRP, W81XWH-20-10576 (to E.Y.C.); National Heart, Lung, and Blood Institute, 1 R21 HL154032-01 (to E.Y.C.); National Science Foundation, CHE-1904780 (to E.Y.C.); National Institute of Biomedical Imaging and Bioengineering, 1R01EB029829 (to E.Y.C. and T.T.); Office of Biological and Environmental Research of the U.S. Department of Energy Atmospheric System Research Program Interagency, agreement grant DE-SC0000001; and National Institute of Health, R21-EB025313 and R01EB029829 (to T.T.). The content is solely the responsibility of the authors and does not necessarily represent the official views of the National Institutes of Health. T.T. acknowledges funding from the Edward Mallinckrodt, Jr. Foundation. SL greatly acknowledges support by the KIT-Publication Fund of the Karlsruhe Institute of Technology.
Author contributions: Conceptualization: S.L. and S.A. Methodology: S.L. and S.A. Software: S.L., L.L., S.F., and S.A. Resources: A.A., T.T., and S.A. Formal analysis: S.L., S.F., L.L., and S.A. Investigation: S.L., S.F., L.L., and S.A. Visualization: S.L., S.F., L.L., T.T., and S.A. Funding acquisition: A.A. and T.T. Project administration: S.A. Writing—original draft: S.L., T.T., and S.A. Writing—review and editing: S.F., L.L., M.S.R., E.Y.C., and A.A. **Competing interests:** T.T. is a founder, equity holder, and president of Vizma Life Sciences LLC (VLS). VLS is developing products related to the research being reported. The terms of this arrangement have been reviewed and approved by NC State University in accordance with its policy on objectivity in research. M.S.R. is a founder and equity holder of VLS. E.Y.C. declares a stake of ownership in XeUS Technologies Ltd. All other authors declare that they have no competing interest.
Data and materials availability: All data needed to evaluate the conclusions in the paper are present in the paper and/or the Supplementary Materials. The raw data are available at https://zenodo.org/record/6606108#.YrtlMS1h2Rs.

Submitted 1 March 2022
Accepted 27 May 2022
Published 13 July 2022
10.1126/sciadv.abp8483

Downloaded from https://www.science.org at Wayne State University on July 14, 2022

Disposable and Handheld Clinical-scale HP Propane Hyperpolarizer

Nuwandi M. Ariyasingha[1] Anna Samoilenko[1], Jonathan R. Birchall[1], Kirill V. Kovtunov[2,3], Larisa M. Kovtunova[3,4], Valerii I. Bukhtiyarov[3,4], Igor V. Koptyug[2,3], Chunqi Qian[5], Eduard Y. Chekmenev[1,6]

[1]Department of Chemistry, Ibio, Karmanos Cancer Institute, Wayne State University, Detroit, MI 48202, USA.

[2]International Tomography Center SB RAS, Novosibirsk, [3]Department of Natural Sciences, Novosibirsk State University, Novosibirsk,[4] Boreskov Institute of Catalysis SB RAS, Novosibirsk, Russia.

[5] College of Engineering, Michigan State University, East lansing, MI, 48824.

[6] Russian Academy of Sciences, Leninskiy Prospekt 14, Moscow 119991, Russia.

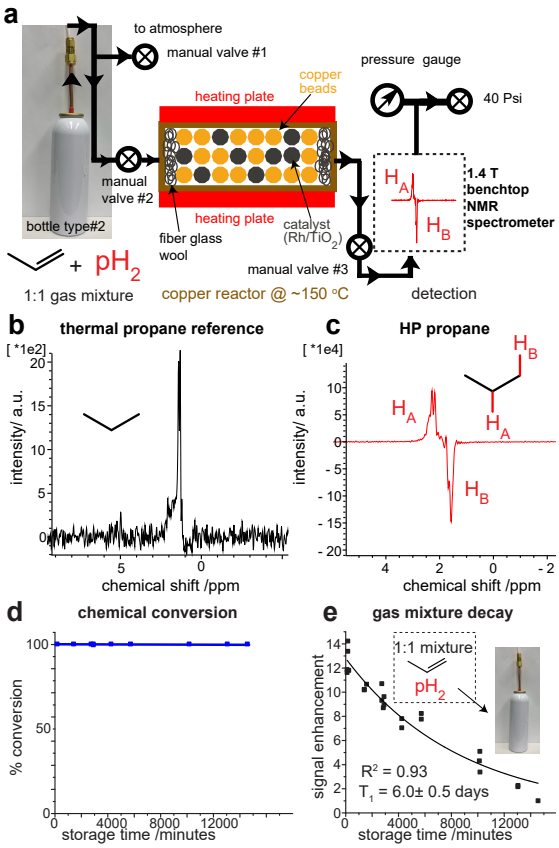

Figure 1. a) Schematic of the experimental setup, valves are optional; b) thermal spectrum of produced propane gas; c) NMR spectrum of HP propane gas acquired using 1.4 T bench-top NMR spectrometer; d) Reactor potency with time. e) exponential decay of the gas mixture potency due to pH_2 back-conversion to normal H_2 in the handheld aluminum storage container (commercial aluminum spray can).

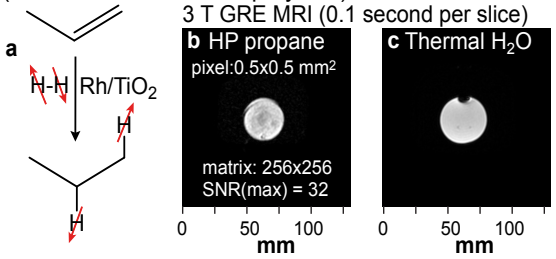

Figure 2. a) Schematic of the heterogeneous pairwise parahydrogen addition to propylene to produce HP propane gas; b) slice-selective (5 mm thickness) 2D GRE imaging of HP propane gas in a hollow-sphere phantom using wrist RF coil of 3T clinical MRI scanner: 256x256 matrix, FOV=130x130 mm², SNR(max) = 32; c) corresponding image of thermally polarized water.

We present a robust disposable low-cost hand-held clinical scale hyperpolarizer for production of hyperpolarized (HP) propane and other *proton*-hyperpolarized gases for potential application in pulmonary MRI and other imaging.

While Parahydrogen Induced Polarization (PHIP) technique is a low-cost method compared to other hyperpolarization techniques and *parahydrogen*-hyperpolarized contrast agents show promising results towards MRI imaging, clinical translation remains a challenge [1-3]. Parahydrogen (pH_2) production and dispensing into high pressure gas cylinders are currently required for temporary storage before hyperpolarization procedure, which usually involves complex infrastructure. As a new solution, we present that pH_2 gas can be stored for several days in commercially available disposable aluminum containers (<$1/each). Parahydrogen gas undergoes slow decay with T_1 = 6.4±1.3 days, which enables pH_2 gas delivery from the production site to utilization site. This finding increases the reach of all PHIP techniques for on-site production of hyperpolarized contrast agents using a simple, safe and economical disposable container.

We also demonstrate that a reactant gas mixture of unsaturated precursor (propylene) and pH_2 can be successfully stored in the disposable storage container. The compressed gas mixture (1:1) stored in the disposable bottle can be released using high-flow valve (>0.5 liter/sec) into a low-cost disposable cartridge reactor (loaded with 200 mg of 1% Rh/TiO_2 catalyst) to produce a clinical dose of the HP propane gas via heterogeneous pairwise pH_2 addition reaction, ***Figure 1***. The performance of the hyperpolarizer was monitored using 1.4 T bench-top NMR spectrometer running dynamic pseudo-2D NMR acquisition. Moreover, polarizer feasibility tests indicate a robust performance of the polarizer over a wide range of reactor operational pressures (including clinically relevant 1 atm).

A 1:1 mixture of propylene gas and pH_2 can be successfully stored for several days without a substantial pH_2 fraction depletion (T_1 = 6.0±0.5 days) to give apparent propane gas polarization of 1-1.5 % with complete chemical conversion. We conclude that the lifetime of pH_2 in pure state and mixtures is limited by the mean-free path, which depends on the container size and pressure.

Finally, we also show that the premixed gas storage (of ~ 6 hours) and delivery (>100 miles) to the clinical imaging site for pilot MRI image acquisition of HP propane (***Figure 2***). HP propane gas was hyperpolarized on remote site using our handheld disposable clinical polarizer. All-in-all, the new instrumentation presented here enables low-cost on-demand production of HP propane (and other HP contrast agents) using a handheld device, and imaging using conventional clinical 3T MRI scanner.

REFEERNCES: (1) Salnikov, O. G.; et al. *Chem. Eur. J.* **2021**, DOI 10.1002/chem.202003638. (2) Ariyasingha, N.M., Salnikov, O.G. *et al, JPCC* **2019**, *123*, 11734. (3) Schmidt, A. B.; et al. *Anal. Chem.* **2022**, https://doi.org/10.1021/acs.analchem.1c04863.

ACKNOWLEDGEMENTS: DOD CDMRP W81XWH-15-1-0271, W81XWH-20-10576, NSF CHE-1904780, NHLBI R21HL154032 and F32HL160108.

Temperature-Ramped Batch-Mode Spin Exchange Optical Pumping of Xenon-129 using 3rd-generation Automated XeUS Hyperpolarizer

Md Raduanul H. Chowdhury,[1] Jonathan R. Birchall,[1] Peter Nikolaou,[2] Michael J. Barlow,[3] Anton Shcherbakov,[4,5] Boyd M. Goodson,[6] Eduard Y. Chekmenev[1,7]

[1]Department of Chemistry, Ibio, Karmanos Cancer Institute, Wayne State University, Detroit, MI 48202, USA
[2]XeUS Technologies LTD, Nicosia, Cyprus
[3]Sir Peter Mansfield Imaging Centre, University of Nottingham, Nottingham, NG7 2RD, United Kingdom
[4]Smart-A, Perm, Perm Region, 614000, Russia,
[5]Custom Medical Systems (CMS) LTD, Nicosia, Cyprus
[6]Department of Chemistry and Biochemistry, Southern Illinois University, Carbondale, Illinois 62901, USA
[7]Russian Academy of Sciences, Moscow, 119991, Russia

We present a clinical-scale production optimization of hyperpolarized ^{129}Xe gas with the help of an automated, third-generation (GEN-3) ^{129}Xe hyperpolarizer device operating via batch-mode spin exchange optical pumping (SEOP) (1-2). Our overall study goal is to increase the production rate of our next-generation device (*i.e.*, to decrease production cycle duration), while maximizing ^{129}Xe hyperpolarization (P_{Xe}). Batch-mode SEOP is typically performed at a fixed pumping cell temperature of 60-95 °C (3). The SEOP build-up rate increases with temperature due to increase of gas-phase Rb density, acting as intermediary for photon absorption and ^{129}Xe nuclear spin hyperpolarization. However, increase in temperature decreases $\%P_{Xe}$, due to increase in of gas-phase Rb concentration resulting in lower $\%P_{Rb}$, which acts as intermediary for ^{129}Xe (4-6).

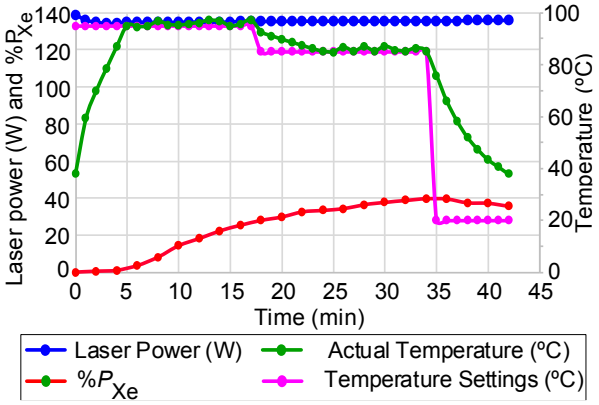

Figure 1. Schematic of polarization buildup process. SEOP cycle for HP ^{129}Xe production starts at 38 °C SEOP jacket temperature (Rb melting point) with on-resonance laser illumination of ~140 W. One T_b time (12 mins) is spent at the highest set point temperature (95°C), where the build-up rate is maximal. Next one more T_b (17 mins) is spent at the temperature setting corresponding to the maximum P_{Xe} (85°C); yet, at slower nominal T_b (the T_b values were obtained via previous systematic SEOP cell temperature mapping). After 2*T_b time, the set temperature was set to room temperature (20 °C) and SEOP jacket temperature decreases to 38 °C while the laser continues to illuminate SEOP cell to minimize P_{Xe} losses during cell cool-down.

Here, we explore a temperature-ramped SEOP approach, where the initial SEOP buildup is performed at an elevated temperature for a certain time period (corresponding to faster buildup regime) and then at a lower temperature, which yields maximum P_{Xe}, Figure 1. In one representative example of fixed-temperature SEOP at 95 °C being the polarization temperature, it takes 42 minutes to finish the total SEOP process and generate P_{Xe} of 35.9%. However, with the temperature-ramped SEOP approach performed initially at 95°C and then at 85 °C, the total SEOP polarization process also takes 42 minutes, and P_{Xe} reaches 39.8%. This example (among many others systematically studied here) shows the utility of ramped-temperature SEOP to overall improve the efficiency of batch-mode SEOP. Although the gain is modest, it is certainly welcome to overall improve the SEOP practice of ^{129}Xe production.

Moreover, the *ex-situ* detection of HP ^{129}Xe gas was also performed in 47.5 mT magnet to investigate the efficacy of HP gas ejection via solenoid valve employed in our new GEN-3 device. Specifically, we measure P_{Xe} *in-situ* of hyperpolarizer at the end of the temperature-ramped process and correlate that in-situ P_{Xe} with *ex-situ* P_{Xe} measurement performed using 47.5 mT NMR. We find that the bulk of PXe is indeed successfully retained during the newly developed HP ^{129}Xe ejection procedure.

Additionally, we report on systematic quality assurance (QA) studies of limits of the device operation parameters and their effect of the robustness of SEOP hyperpolarizer operation. Specifically, we studied back-to-back reproducibility, the effects of SEOP temperature, calibrations of *in-situ* excitation RF pulse length, *in-situ* polarimetry resonance offset from 40.8 kHz resonance condition. The overall results of this study lead to better quality and more robust production of HP ^{129}Xe gas on a clinical scale for imaging and bio-sensing applications.

ACKNOWLEDGMENTS: DOD CDMRP W81XWH-12-1-0159/BC112431, W81XWH-15-1-0271, W81XWH-15-1-0272, W81XWH-20-10576, and W81XWH-20-10576.

REFERENCES: **(1)** Birchall, J.R., et al., *J. Mag. Reson.* **2020,** *316*, 106755. **(2)** Birchall, J.R., et al., *Anal. Chem.* 2020, 92, 6, 4309–4316. **(3)** Birchall, J.R., et al., *Molecules.* **2022**, 1550315. R1 under review. **(4)** Driehuys, B., et al., *Appl. Phys. Lett.* **1996,** *69* (12), 1668-1670. **(5)** Saha, I., et al., *Chem. Phys. Lett.* **2006,** *428* (4-6), 268–276. **(6)** Birchall, J.R., et al., *Anal. Chem.* 2021, 93, 8, 3883–3888.

Two-Orders-of-Magnitude Improvement in SEOP Production (*P*N*) of Hyperpolarized ^{131}Xe and Measurement of ^{131}Xe and ^{129}Xe Spin-Dependent Neutron Scattering Lengths via Pseudomagnetic Precession

A.T. Gafar[1], H. Lu[2], D. Basler[1], D. Cocking[3], M. Prince[3], M.J. Molway[1], L. Bales-Shaffer[1], Md S. Alam[1], Z. Siraj[1], A. Petrilla[1]*, M.S. Rosen[4], E.Y. Chekmenev[5], M.J. Barlow[3], E. Babcock[6], W.M. Snow[2], B.M. Goodson[1]

*[1]School of Chemical & Biomolecular Sciences, Southern Illinois University, Carbondale, IL, USA; [2]Indiana University/CEEM, 2401 Milo B. Sampson Lane, Bloomington, IN 47408, USA; [3]School of Medicine, University of Nottingham, Queens Medical Centre, Nottingham, UK; [4]A.A. Martinos Center for Biomedical Imaging, Massachusetts General Hospital and Harvard Medical School, Boston, MA 02129; Department of Physics, Harvard University, Cambridge, MA 02138, USA; [5]Wayne State University & Karmanos Cancer Institute (KCI), Detroit, MI, USA; [6]Jülich Centre for Neutron Science at FRM2, 85747 Garching Germany; *Undergraduate Researcher*

Although spin exchange optical pumping (SEOP)[1] is routinely capable of hyperpolarizing large amounts of I=1/2 noble gas isotopes like ^{129}Xe and ^{3}He to very high levels for various applications (e.g. Refs. [2-5]), SEOP hyperpolarization of isotopes with I>1/2[6] is generally much more difficult because of their non-zero quadrupolar moments—which contribute to much faster spin relaxation. Of interest here is ^{131}Xe (I=3/2): The ability to produce HP ^{131}Xe in bulk may enable envisioned applications, varying from novel tests of fundamental symmetries to biomedical imaging, respectively exploiting specific neutron resonances and contrast mechanisms that ^{129}Xe does share. In most previous efforts, only minute amounts of HP ^{131}Xe have been created with high polarization values (e.g. Refs.[7-13]). Gatzke et al. transiently polarized larger amounts of ^{131}Xe via cross-polarization with HP ^{129}Xe in cryogenic lattices.[14] Arguably the greatest success with bulk production of HP ^{131}Xe to date was part of pioneering work by Meersmann and co-workers,[15] who reported ^{131}Xe polarizations of 2.2%, 0.44%, and 0.026% at 9.4 T for 0.075, 0.3, and 1.4 bar Xe, respectively, following gas separation from a ~72 mL SEOP cell.

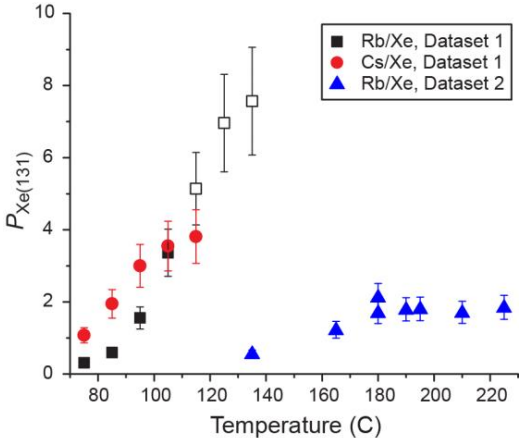

Fig. 1. P(^{131}Xe) values versus cell temperature for two different SEOP datasets with a 2"x2" ~100 cc cell and either ~100-145 W (Rb, FWHM=0.18,0.29 nm) or ~50 W (Cs, FWHM~50 pm) lasers; open icons are single-point acquisitions taken under conditions of "Rb runaway." Polarization was determined via in situ low-field ^{131}Xe NMR, referenced to a signal from thermally polarized water.[19]

Here, we report on our ongoing efforts to prepare bulk quantities of hyperpolarized (HP) ^{131}Xe via SEOP and its potential for use in HP targets in neutron beam experiments. Isotopic enrichment, next-generation spectrally-narrowed laser diode arrays, and in situ low-field NMR permit real-time observation of polarization dynamics and SEOP optimization. Combined with a model of ^{131}Xe relaxation (putting together aspects of previous works[9,15-18]), estimates of alkali-metal/^{131}Xe spin exchange shows that it can compete favorably with ^{131}Xe T_1. ^{131}Xe polarization up to 7.6±1.5% was achieved[19] in ~8.5×10^{20} spins, which would correspond to >100-fold improvement in the total spin angular momentum (*P*N*) compared to previous efforts, **Fig. 1**. To create HP ^{131}Xe targets for neutron science experiments, we prepared larger cells (~300 cc) made of aluminosilicate glass (GE180, created by Jülich glassblowers), avoiding neutron-slowing boron. We report on ongoing efforts to quantify ^{131}Xe polarization in these cells with the same apparatus used for Fig. 1. One such cell (**Fig. 2**) was also successfully installed into the neutron beam line at the J-NSE neutron spin echo instrument at the Heinz Maier-Leibnitz Zentrum (MLZ) in Jülich. P(^{131}Xe) was calibrated using low-field NMR (via comparison to a ^{129}Xe cell) to a ^{3}He cell for which P(^{3}He)=68.0±1.6% was separately determined by neutron transmission, yielding P(^{129}Xe)=17.6±0.8% and P(^{131}Xe)=1.9±0.15%.[20] These values were used to perform the first determinations of the ^{131}Xe and ^{129}Xe spin-dependent neutron scattering lengths via measurements of pseudomagnetic precession of slow neutrons in forward transmission through the gases (values and errors bars are currently being finalized[20]). The incoherent neutron scattering lengths will help determine the sensitivity of envisioned Time Reversal Invariance Violation experiments on the 3.2 eV p-wave resonance of ^{131}Xe[21,22] in the search for new physics beyond the Standard Model.[23-25]

Fig. 2. SEOP GE180 cell made containing 150 Torr ^{131}Xe, 150 Torr N_2 and a few hundred mg of Rb.

Acknowledgements: This work was funded in part by DoD (W81XWH-15-1-0271, W81XWH-15-1-0272, W81XWH-20-10576 and W81XWH-20-10578) as well as a SEED Award from the Research Corp. ***References:*** [1]Walker & Happer *Rev. Mod. Phys.* 69, 629 (1997); [2]Goodson *JMR* 155, 157 (2002); [3]Nikolaou et al. *PNAS* 110, 14150 (2013); [4]Mugler & Altes *JMRI* 37, 313 (2013); [5]Cane, et al. *PRL* 93, 230801 (2004); [6]Lilburn, *et al. JMR* 229, 173 (2013); [7]Volk, et al. *PRL* 44, 136 (1980); [8]Wu, et al. *PRL* 59, 1480 (1987); [9]Butscher et al. *JCP* 100, 6923 (1994); [10]Appelt et al. *PRL* 72, 3921 (1994); [11]Raftery et al. *PRA* 50, 567 (1994); [12]Bulatowicz et al. *PRL* 111, 102001 (2013); [13]Zheng et al. *Nature* 537, 652 (2016); [14]Gatzke et al. *PRL* 70, 690 (1993); [15]Stupic, et al. *JMR*, 208, 58 (2011); [16]Brinkmann & Keller, Helv. Phys. Acta 35, 431 (1962); [17]Chann, *PRL* 88, 113201 (2002); [18]Anger, *PRA* 78, 043406 (2008); [19]Molway et al., submitted; [20]Lu et al., in process; [21]Szymanski et al., PRC 53, R2576 (1996); [22]Skoy et al., PRC 53, R2573 (1996); [23]Mitchell, *RMP* 71, 445 (1999); [24]Bowman & Gudkov, *PRC* 90, 065503 (2014); [25]Flambaum & Mansour, arXiv:2111.02037v1 (2021).

Exploring SABRE-Enhanced Imaging with a Portable Clinical Low-field MRI Scanner

Md Shahabuddin Alam[1], Drew Brittin[1], Nadiya Iqbal[1], A. Tobi Gafar[1], Zahid Siraj[1], Anthony Petrilla[1]*, Ishani Senanayake[1], Margaret Pugh[1]*, Megan Poorman[2], Laura Sacolick[2], Matthew S. Rosen[3], Eduard Y. Chekmenev[4], Boyd M. Goodson[1]

*[1]School of Chemical & Biomolecular Sciences, Southern Illinois University, Carbondale, IL, USA; [2]Hyperfine.io; [3]A.A. Martinos Center for Biomedical Imaging, Massachusetts General Hospital and Harvard Medical School,Boston, MA 02129; [4]Wayne State University & Karmanos Cancer Institute (KCI), Detroit, MI, USA; *Undergraduate Researcher.*

MRI can provide exquisite high-respolution images of anatomical features, function, and pathology of soft tissues in the body, without ionizing radiation. However, the increasingly stronger magnets used in most clinical scanners (~1–7 T) are expensive, bulky, and immobile, and the scans can be time-consuming and confining for many patients. Moreover, these stronger magnetic fields (along with concomitantly higher RF resonance frequencies) can present safety concerns in some circumstances, as well as contraindications for a number of patients and health conditions. Low-field (LF) MRI[1-6] has gained renewed interest because it can potentially obviate all of these limitations. However, signal strength, detection sensitivity, and contast limitations present ongoing challenges to many LF MRI technologies and their applications.

One approach to mitigate the sensitivity and contrast limitations of conventional NMR/MRI is hyperpolarization, which involves the preparation of nuclear spin polarization levels that are far above their equilibrium values.[7,8] Hyperpolarization can thus increase NMR/MRI detection sensitivity by orders of magnitude. Moreover, because the magnetization is endowed by a given hyperpolarization method (and not the magnet), hyperpolarized (HP) LF MRI can even be more sensitive than high-field MRI.[3] Thus, hyperpolarization can be highly synergistic with LF MRI, particularly if the hyperpolarization technique is itself low-cost, rapid, and portable.[4-6] One such approach is signal amplification by reversible exchange (SABRE).[9] In SABRE, para-hydrogen (p-H_2) and molecular substrates are transiently bound to organometallic complexes ("catalysts"), allowing spin order to transfer spontaneously from p-H_2 to substrates when placed within an appropriate magnetic field.

We have sited a portable, point-of-care 64 mT clinical MRI scanner (Hyperfine) in the Goodson Lab at SIUC (**Fig. 1a**). This type of scanner has already been demonstrated in clinical settings for bed-side imaging, including of brain injury and cerebral hemorrhage.[10,11]

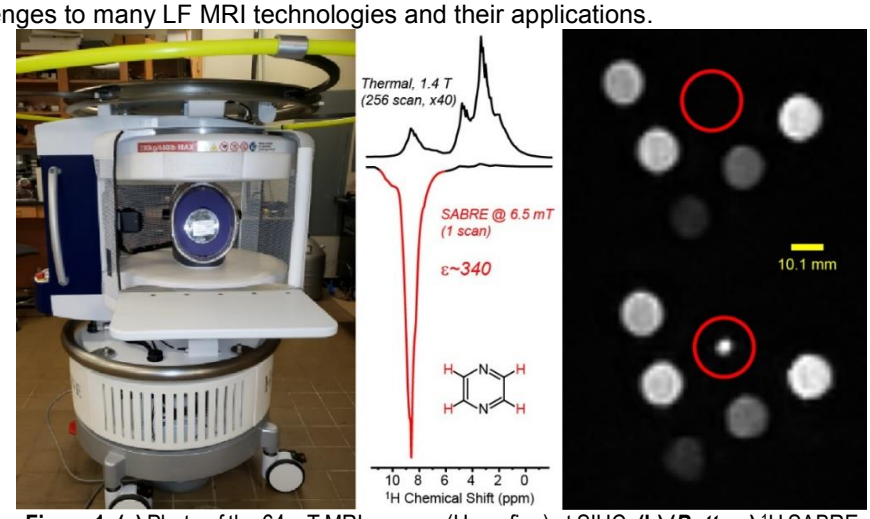

Figure 1: (a) Photo of the 64 mT MRI scanner (Hyperfine) at SIUC. **(b) (*Bottom*)** ^{1}H SABRE-enhanced spectrum taken following 30 s pH_2 bubbling (80 sccm, 65 psi) at 6.5 mT, prior to transfer to a 1.4 T benchtop NMR spectrometer (Nanalysis). Sample contains 100 mM pyrazine and 5 mM IrIMes SABRE catalyst in d_4-methanol; estimated signal enhancement of ~340-fold (*cf.* spectrum from a thermally polarized sample, ***Top***). **(c) (*Bottom*)** close-up of 64 mT ^{1}H MRI scan from a 5 mm NMR tube (inside red circle) containing the solution in (b) after transfer to a short NMR tube and reconnection with the pH_2 bubbler, with 20 sccm pH_2 bubbling during the scan; the 5 other circular signal regions are from 15 mL Falcon tubes with varying H_2O:D_2O ratios (from 100:0, far right, to 10:90, bottom middle). (***Top***): same as (*Bottom*), but no pH_2 bubbling. Images are slices from a 3D coronal (with respect to coil symmetry) T_2-weighted sequence (1.5x1.5x5 mm^3), providing axial tube slices.

Here we are investigating the potential for adapting this type of MRI scanner for use with HP substances. In our first attempt, we have integrated the scanner with a continuous pH_2-blubbling SABRE setup[12] and a pyrazine sample placed inside a shortened 5 mm NMR tube (pH_2 produced by an ~86% pH_2 generator[13]), so that the tube can be placed vertically within the scanner's head coil. Following ^{1}H SABRE detection using a benchtop spectrometer (**Fig. 1b**), the sample was transferred to the MRI scanner where it was imaged *in situ*[4,5,14] at 64 mT under conditions of continuous low-flow (20 sccm) pH_2 (**Fig. 1c**); low-field scanners suffer much less from susceptibility distortions, enabling imaging with gentle bubbling. A few-hundred fold enhancement is evident from the fact that the signal-per-pixel in the tube (near-zero without pH_2) is similar to that obtained with pure water. While 64 mT is much higher than the optimal field for ^{1}H SABRE (~6 mT[9]), the signal in Fig. 1c is believed to be from pyrazine given the low signal from HP oH_2[15] and hydides in high-field SABRE spectra. We are currently working to (1) confirm the origin of the HP signals, as well as (2) quantify the enhancement, (3) optimize sequences for rapid SABRE imaging, and (4) enable continuous delivery of HP solutions created using *ex situ* SABRE at optimal fields.

ACKNOWLEDGEMENTS: This work was funded by by DOD CDMRP under W81XWH-20-10578 and W81XWH-20-10576 and NSF (CHE-1905341 and 1904780). **REFERENCES:** [1]Sarracanie et al., *Sci.Rep.* 5, 1 (2015); [2]Blanchard et al. *JMR* 323, 106886 (2021); [3]Coffey et al. *JMR*, *237*, 169 (2013); [4]Coffey, et al., *Anal. Chem*. 86, 9042 (2014); [5]Barskiy, et al., *CPC*, 15, 4100 (2014); [6]Lehmkuhl et al. *JCP* 152, 184202 (2020); [7]Nikolaou, et al. *CEJ* 21, 3156 (2015); [8]Kovtunov et al. *CAJ* 13, 1857 (2018); [9]Adams et al. *Science* 323, 1708 (2009); [10]Sheth et al. *JAMA Neuro*. 9, 8 (2020); [11]Mazurek et al., *Nature Comm*. 12, 1 (2021); [12]Truong et al., *JPCB*, 118, 13882 (2014); [13]Birchall, et al. *Anal. Chem*. 92, 15280 (2020); [14]Kovtunov, et al. JPCC 121, 25994 (2017); [15]Barskiy, et al. *JACS* 136, 3322 (2014).

Next-generation Equipment for Clinical-scale Parahydrogen Induced Polarization

Ed Chekmenev

Department of Chemistry, Karmanos Cancer Institute (KCI), Integrative Biosciences (Ibio), Wayne State University, Detroit, Michigan, 48202, United States

NMR hyperpolarization enhances the detection sensitivity of magnetic resonance by 4-6 orders of magnitude. As a result, it becomes possible to perform *in vivo* detection of dilute hyperpolarized biocompatible molecules and hyperpolarized products of their metabolic transformation. Hyperpolarized [1-^{13}C]pyruvate is the key injectable hyperpolarized contrast agent currently, and it is under evaluation in over 30 clinical trials registered with clinicaltrials.gov. Hyperpolarized [1-^{13}C]pyruvate and other ^{13}C- and ^{15}N- hyperpolarized biocompatible molecules are currently produced via dissolution Dynamic Nuclear Polarization (d-DNP) technique. However, d-DNP instrumentation has high cost and requires a long time (1h) to hyperpolarize [1-^{13}C]pyruvate and other ^{13}C- and ^{15}N- biocompatible contrast agents. Faster and more cost effective technologies are needed for hyperpolarization of [1-^{13}C]pyruvate and other ^{13}C- and ^{15}N-biocompatible contrast agents to enable their routine clinical use in a manner similar to that of PET tracers.

Here, the next-generation clinical-scale parahydrogen-based hyperpolarizer and other auxiliary instrumentation is presented to enable efficient hyperpolarization of [1-^{13}C]pyruvate and other ^{13}C- and ^{15}N- biocompatible contrast agents. Order-unity ^{13}C polarization of [1-^{13}C]pyruvate (and structurally similar biomolecules such as α-ketogluratate and a-keto-[1-^{13}C]isocaproate) in seconds becomes possible via SABRE-SHEATH (SABRE in SHield Enables Alignment Transfer to Heteronuclei) using this equipment. SABRE-SHEATH relies on non-hydrogenative use of parahydrogen gas that performs simultaneous exchange with to-be-hyperpolarized substrate in microtesla magnetic fields. Moreover, ^{15}N hyperpolarization of [$^{15}N_3$]metronidazole (FDA-approved antibiotic and potential hypoxia sensor) in excess of 20% is demonstrated using this hyperpolarizer. The device has a footprint of 18.5”×24”×18.5” with the cost of the off-shelf components of less than $15,000 (*ca*. 2020).

Although the field of parahydrogen based hyperpolarization techniques enjoys a recent revival, the entry barrier to the field remains high due to high cost ($0.1M) and complex siting of clinical-scale parahydrogen generator capable of producing near 100% parahydrogen. Here, we present on the development and validation of handheld disposable container for temporary parahydrogen storage and utilization. This solution has the potential of enabling convenient access to parahydrogen for research sites that do not have established infrastructure such as clinical environment. We envision this disposable container to provide a dose of parahydrogen gas to enable a clinical-scale production of parahydrogen-based hyperpolarized contrast agents such as [1-^{13}C]pyruvate and others. As a result, one parahydrogen generator can potentially support tens of clinical sites for on-site production of hyperpolarized contrast agents using parahydrogen based hyperpolarization.

As a proof of principle, we demonstrate the utility of this disposable storage container to store a mixture of parahydrogen and propylene gases: the exponential parahydrogen decay T_S contrast was 6.0±0.5 days. This approach allowed us to transport the parahydrogen/propylene gas mixture over 100-mile distance to a clinical site operating 3T MRI scanner. Hyperpolarized propane was produced by ejecting the parahydrogen/propylene gas mixture through disposable handheld non-magnetic propane hyperpolarizer next to the MRI scanner. The mixture reacts on heterogeneous Rh/TiO_2 catalyst to produce pure (from catalyst) batch of hyperpolarized propane gas. The clinical-scale production of *propane*-hyperpolarized propane gas was visualized in phantoms using GRE, FIESTA and EPI pulse sequences without any modification of clinical scanner sequences or hardware. The presented approach potentially enables on-demand clinical-scale production of hyperpolarized propane (FDA-approved gas for unlimited use in foods) for potential applications as inhalable contrast agent for pulmonary imaging.

The presented instrumentation developed through multi-team collaboration bodes well for future clinical translation of hyperpolarized contrast agents.

REFERENCES: **(1)** Nantogma, S.; Joalland, B.; Wilkens, K.; Chekmenev, E. Y. Clinical-Scale Production of Nearly Pure (>98.5%) Parahydrogen and Quantification by Benchtop NMR Spectroscopy. *Anal. Chem.* **2021,** *93* (7), 3594–3601.
(2) Joalland, B.; Nantogma, S.; Chowdhury, M. R. H.; Nikolaou, P.; Chekmenev, E. Y. Magnetic Shielding of Parahydrogen Hyperpolarization Experiments for the Masses. *Magn. Reson. Chem.* **2021,** *59* (12), 1180-1186.
(3) Adelabu, I.; TomHon, P.; Kabir, M. S. H.; Nantogma, S.; Abdulmojeed, M.; Mandzhieva, I.; Ettedgui, J.; Swenson, R. E.; Krishna, M. C.; Theis, T., et al. Order-Unity ^{13}C Nuclear Polarization of [1-^{13}C]Pyruvate in Seconds and the Interplay of Water and SABRE Enhancement. *ChemPhysChem* **2022,** *23* (2), 131–136.
(4) TomHon, P.; Abdulmojeed, M.; Adelabu, I.; Nantogma, S.; Kabir, M. S. H.; Lehmkuhl, S.; Chekmenev, E. Y.; Theis, T. Temperature Cycling Enables Efficient ^{13}C SABRE-SHEATH Hyperpolarization and Imaging of [1-^{13}C]-Pyruvate. *J. Am. Chem. Soc.* **2022,** *144* (1), 282–287.
(5) Theis, T.; Truong, M. L.; Coffey, A. M.; Shchepin, R. V.; Waddell, K. W.; Shi, F.; Goodson, B. M.; Warren, W. S.; Chekmenev, E. Y. Microtesla SABRE Enables 10% Nitrogen-15 Nuclear Spin Polarization. *J. Am. Chem. Soc.* **2015,** *137* (4), 1404-1407.
ACKNOWLEDGEMENTS: NSF CHE-1904780, NCI 1R21CA220137, NIBIB 1R01EB029829, CDMRP W81XWH-20-10576.

Next-generation Clinical-scale Instrumentation for Parahydrogen-Induced Polarization

Shiraz Nantogma,[1] Isaiah Adelabu,[1] Nuwandi M. Ariasingha,[1] Anna Samoilenko,[1] Md Raduanul H. Chowdhury,[1] Mohammad S. H. Kabir,[1] Boyd M. Goodson,[2] Eduard Y. Chekmenev[1,3]

[1] *Department of Chemistry,* [3] *Karmanos Cancer Institute (KCI), Integrative Biosciences (Ibio), Wayne State University, Detroit, Michigan, USA*

[2] *School of Chemical & Biomolecular Sciences, Materials Technology Center, Southern Illinois University, Carbondale, Illinois, USA*

Introduction: NMR hyperpolarization enhances the detection sensitivity of magnetic resonance by 4-6 orders of magnitude. As a result, it becomes possible to perform *in vivo* detection of dilute hyperpolarized biocompatible molecules and hyperpolarized products of their metabolic transformation. Hyperpolarized [1-^{13}C]pyruvate is the key injectable hyperpolarized contrast agent currently, and it is under evaluation in over 30 clinical trials registered with clinicaltrials.gov. Hyperpolarized [1-^{13}C]pyruvate and other ^{13}C- and ^{15}N- hyperpolarized biocompatible molecules are currently produced via dissolution Dynamic Nuclear Polarization (d-DNP). However, d-DNP instrumentation has high cost and requires a long time (1h) to hyperpolarize [1-^{13}C]pyruvate and other ^{13}C- and ^{15}N- biocompatible contrast agents. Faster and more cost-effective technologies are needed for hyperpolarization of [1-^{13}C]pyruvate and other ^{13}C- and ^{15}N- biocompatible contrast agents to enable their routine clinical use in a manner similar to that of PET tracers.

Results and Conclusion: Here, a next-generation clinical-scale parahydrogen-based hyperpolarizer and other auxiliary instrumentation is presented to enable efficient hyperpolarization of [1-^{13}C]pyruvate and other ^{13}C- and ^{15}N- biocompatible contrast agents. Order-unity ^{13}C polarization of [1-^{13}C]pyruvate (and structurally similar biomolecules such as α-ketogluratate and a-keto-[1-^{13}C]isocaproate) in seconds becomes possible via SABRE-SHEATH (SABRE in SHield Enables Alignment Transfer to Heteronuclei) using this equipment. SABRE-SHEATH relies on non-hydrogenative use of parahydrogen gas that performs simultaneous exchange with to-be-hyperpolarized substrates in microtesla magnetic fields. Moreover, ^{15}N hyperpolarization of [$^{15}N_3$]metronidazole (FDA-approved antibiotic and potential hypoxia sensor) in excess of 20% is demonstrated using this hyperpolarizer. The device has a footprint of 18.5"×24"×18.5" with the cost of the off-shelf components of less than $15,000 (*ca*. 2020).

Although the field of parahydrogen-based hyperpolarization techniques has enjoyed a recent revival, the entry barrier to the field remains relatively high due to high cost ($0.1M) and complex siting of clinical-scale parahydrogen generators capable of producing near 100% parahydrogen. Here, we present on the development and validation of a handheld disposable container for temporary parahydrogen storage and utilization. This solution has the potential of enabling convenient access to parahydrogen for research sites that do not have established infrastructure in pre-clinical and clinical setting. We envision this disposable container to provide a dose of parahydrogen gas to enable a clinical-scale production of parahydrogen-based hyperpolarized contrast agents such as [1-^{13}C]pyruvate and others. As a result, one parahydrogen generator can potentially support tens of clinical sites for on-site production of hyperpolarized contrast agents using parahydrogen-based hyperpolarization.

As a proof of principle, we demonstrate the utility of this disposable storage container to store a mixture of parahydrogen and propylene gases: the exponential parahydrogen decay T_S contrast was 6.0±0.5 days. This approach allowed us to transport the parahydrogen/propylene gas mixture over a distance that is >100-mile to a clinical site operating a 3T MRI scanner. Hyperpolarized propane was produced by ejecting the parahydrogen/propylene gas mixture through a disposable handheld non-magnetic propane hyperpolarizer next to the MRI scanner. The mixture reacts with a heterogeneous Rh/TiO_2 catalyst to produce a pure (from catalyst) batch of hyperpolarized propane gas. The clinical-scale production of *parahydrogen*-hyperpolarized propane gas was visualized in phantoms using GRE, FIESTA, and EPI pulse sequences without any modification of the clinical scanner sequences or hardware. The presented approach potentially enables on-demand clinical-scale production of hyperpolarized propane (FDA-approved gas for unlimited use in foods) for potential applications as an inhalable contrast agent for pulmonary imaging.

Conclusion: The presented instrumentation developed through multi-team collaboration bodes well for future clinical translation of hyperpolarized contrast agents.

References: **(1)** Nantogma, S.; Joalland, B.; Wilkens, K.; Chekmenev, E. Y. Clinical-Scale Production of Nearly Pure (>98.5%) Parahydrogen and Quantification by Benchtop NMR Spectroscopy. *Anal. Chem.* **2021,** *93*, 3594. **(2)** Joalland, B.; Nantogma, S.; Chowdhury, M. R. H.; Nikolaou, P.; Chekmenev, E. Y. Magnetic Shielding of Parahydrogen Hyperpolarization Experiments for the Masses. *Magn. Reson. Chem.* **2021,** *59*, 1180. **(3)** Adelabu, I.; TomHon, P.; Kabir, M. S. H.; Nantogma, S.; Abdulmojeed, M.; Mandzhieva, I.; Ettedgui, J.; Swenson, R. E.; Krishna, M. C.; Theis, T., et al. Order-Unity ^{13}C Nuclear Polarization of [1-^{13}C]Pyruvate in Seconds and the Interplay of Water and SABRE Enhancement. *ChemPhysChem* **2022,** *23*, 131. **(4)** TomHon, P.; Abdulmojeed, M.; Adelabu, I.; Nantogma, S.; Kabir, M. S. H.; Lehmkuhl, S.; Chekmenev, E. Y.; Theis, T. Temperature Cycling Enables Efficient ^{13}C SABRE-SHEATH Hyperpolarization and Imaging of [1-^{13}C]-Pyruvate. *J. Am. Chem. Soc.* **2022,** *144* (1), 282–287. **(5)** Theis, T.; Truong, M. L.; Coffey, A. M.; Shchepin, R. V.; Waddell, K. W.; Shi, F.; Goodson, B. M.; Warren, W. S.; Chekmenev, E. Y. Microtesla SABRE Enables 10% Nitrogen-15 Nuclear Spin Polarization. *J. Am. Chem. Soc.* **2015,** *137* (4), 1404-1407.

Acknowledgements: NSF CHE-1905341 and CHE-1904780, NHLBI R21HL154032 and F32HL160108, NIBIB 1R01EB029829, CDMRP W81XWH-20-10576 and W81XWH-20-10578.

Disposable, Handheld Clinical-Scale HP Propane Hyperpolarizer for Pulmonary MRI

Eduard Y Chekmenev[1], Anna Samoilenko[2], Jonathan R. Birchall[2], Kirill V. Kovtunov[3], Larisa M Kovtunova[3], Valeriy I. Bukhtiyarov[4], Igor V. Koptyug[3], Chunqi Qian[5], Boyd M Goodson[6], and Nuwandi M. Ariyasingha[2]
[1]*Chemistry and Oncology, Wayne State University, Detroit, MI, United States,* [2]*Chemistry, Wayne State University, Detroit, MI, United States,* [3]*International Tomography Center RAS, Novosibirsk, Russian Federation,* [4]*Boreskov Institute of Catalysis RAS, Novosibirsk, Russian Federation,* [5]*Radiology, Michigan State University, Lansing, MI, United States,* [6]*Southern Illinois University Carbondale, Carbondale, IL, United States*

Synopsis

We demonstrate a disposable and handheld hyperpolarizer for clinical-scale production of hyperpolarized propane gas for application as an inhalable contrast agent for pulmonary MRI. The device consists of an aluminum commercial spray can, which contains a mixture of pressurized propylene and parahydrogen gases. This filled container can be easily transported and stored for weeks. The hyperpolarized propane production is initialized by valve actuation, which releases the propylene-parahydrogen mixture into a mini-catalytic reactor producing a stream of pure (without catalyst) hyperpolarized propane gas on demand. The feasibility of 3 T EPI, FIESTA, and GRE MRI in hyperpolarized phantoms is demonstrated.

INTRODUCTION: Functional lung imaging is a substantial unaddressed medical need. Hyperpolarized (HP) ^{129}Xe gas has been shown to be promising for clinical-research pulmonary imaging. Since the first ***in-vivo*** MRI demonstration in the 1990s, much of the effort in the field of HP ^{129}Xe gas has been focused on the technologies of ^{129}Xe gas hyperpolarization and on demonstrating the effectiveness of this imaging modality for detection and characterization of a wide range of pulmonary diseases. Despite its demonstrated efficacy in clinical studies, HP ^{129}Xe MRI has not yet enjoyed clinical translation anywhere in the world due to a major critical translational roadblock: high cost and complexity of clinical hyperpolarization equipment and imaging. Clinical MRI scanners are equipped with proton transmission-detection capability only and cannot perform the detection of HP ^{129}Xe. We propose addressing this unmet medical need through the use of ***proton***-hyperpolarized propane gas. HP propane gas is cheap, and it can be readily produced and imaged using clinical MRI scanners. We have demonstrated the feasibility of clinical-scale production of HP propane previously[2]. Here, we report on recent advances in development of a handheld low-cost hyperpolarizer that can be readily disposed after an imaging examination.

METHODS: We employ a 250 mL commercially available aluminum spray can for temporary storage of pressurized mixture of propylene:parahydrogen (1:1 and 1:4) gases at ~9 atm total pressure. We have employed 98.5% parahydrogen prepared using ultra-high purity hydrogen gas[4]. The disposable storage container is equipped with high-flow valve (>0.5 standard liters per second flow). The storage container shown in Figure 2 is mated to the disposable reactor made of food-grade copper tubing filled with 100 mg of 1% Rh/TiO_2 catalyst and copper beads. The beads are added to improve thermal management[2]. Once the valve is actuated, the compressed gas mixture is released through the mini-reactor resulting in production of hyperpolarized propane gas stream. The performance of the hyperpolarizer was monitored using 1.4 T bench-top NMR spectrometer running dynamic pseudo-2D NMR, Figures 2 and 3. Custom MATLAB code[3] was employed for all spectroscopic data processing and determination of relaxation rates and signal enhancement values. All reported imaging studies were performed using a 3.0 T MRI scanner and 2D EPI, GRE and FIESTA pulse sequences. The acquisition parameters are provided in corresponding Figure captions. The photograph of the experimental setup employed for imaging studies is shown in Figure 4.

RESULTS AND DISCUSSION: Parahydrogen gas[1] serves as a source of hyperpolarization (Figure 1) in parahydrogen induced polarization of propane gas via pairwise addition of parahydrogen. The utility of a a commercial aluminum spray can as a temporary storage vessel was evaluated by monitoring the decay of the gas mixture potency over time: parahydrogen decays with the exponential rate constant of 6.0+/-0.5 days, Figure 2e. We conclude that this decay rate is sufficient for temporary storage of the gas mixture and overnight shipping.
Systematic studies of flow rate, flow duration, and reaction pressure revealed that the production of HP propane gas is very robust (Figures 2 and 3) leading to apparent polarization values of 1-1.5% as detected at 1.4 T—in line with our previous studies[2,5] using a benchtop polarizer. Although the polarization levels are substantially lower than those typically obtained for HP ^{129}Xe, we note that each HP molecule carries double the polarization load (two HP protons versus one HP ^{129}Xe atom), and each proton is typically 3.6 times more sensitive than ^{129}Xe at the same nominal polarization. Moreover, protons have nearly 100% natural abundance versus 26% natural abundance of ^{129}Xe. These compounding factors make 1.5%-hyperpolarized propane equivalent to 43%-hyperpolarized ^{129}Xe – this math does not even factor in higher detection frequency of protons and highly-optimized RF coils already available in the clinical practice, which additionally favor HP propane imaging.
For 3T imaging studies, we employed a simplified setup without reactor heating as shown in Figure 4. We note that the valves are introduced only for the purpose of the phantom studies and will be obviated for future in vivo studies. Feasibility, of 2D GRE imaging is shown in Figure 1. Feasibility of multi-slice sub-second 2D EPI is demonstrated in Figure 5 --- three selected slices are shown from the stack of 8 images. Multiple 2D images were obtained from the same batch of HP propane gas, allowing one to monitor gas injection in the phantom and the hyperpolarization decay. We note that this technology will additionally benefit from low-field MRI[5,6], which allows protecting the long-lived spin states of HP propane gas--therefore allowing for a substantially longer time window of gas preparation, administration, and imaging.

CONCLUSION: We conclude that a parahydrogen:propylene mixture can be successfully stored for days in a disposable handheld container that can be potentially shipped. Robust performance of the disposable handheld hyperpolarizer was demonstrated in vitro. The feasibility of ultra-fast 2D EPI, GRE, and FIESTA imaging of HP propane has been demonstrated. This pilot study bodes well for near-future *in vivo* validation of this prospective inhalable contrast agent for functional lung imaging applications. All-in-all, the new instrumentation presented here enabled low-cost on-demand production of HP propane using a handheld device, and imaging using conventional clinical MRI scanners.

Acknowledgements

This work was supported by DOD CDMRP W81XWH-15-1-0271 and W81XWH-15-1-0272, W81XWH-20-10576 and W81XWH-20-10578, NSF CHE-1904780 and CHE-1905341, NHLBI R21HL154032 and F32HL160108. The content is solely the responsibility of the authors and does not necessarily represent the official views of the National Institutes of Health.

References

1. Bowers CR, Weitekamp DP. Transformation of Symmetrization Order to Nuclear-Spin Magnetization by Chemical-Reaction and Nuclear-Magnetic-Resonance. Phys Rev Lett. 1986;57(21):2645-2648.

2. Salnikov OG, Nikolaou P, Ariyasingha NM, Kovtunov KV, Koptyug IV, Chekmenev EY. Clinical-Scale Batch-Mode Production of Hyperpolarized Propane Gas for MRI. Anal Chem. 2019;91(7):4741–4746.

3. Birchall JR, Irwin RK, Chowdhury MRH, Nikolaou P, Goodson BM, Barlow MJ, Shcherbakov A, Chekmenev EY. Automated Low-Cost In Situ IR and NMR Spectroscopy Characterization of Clinical-Scale ^{129}Xe Spin-Exchange Optical Pumping. Anal Chem. 2021;93(8):3883-3888.

4. Nantogma S, Joalland B, Wilkens K, Chekmenev EY. Clinical-Scale Production of Nearly Pure (>98.5%) Parahydrogen and Quantification by Benchtop NMR Spectroscopy. Anal Chem. 2021;93(7):3594–3601.

5. Ariyasingha NM, Salnikov OG, Kovtunov KV, Kovtunova LM, Bukhtiyarov VI, Goodson BM, Rosen MS, Koptyug IV, Gelovani JG, Chekmenev EY. Relaxation Dynamics of Nuclear Long-Lived Spin States in Propane and Propane-d6 Hyperpolarized by Parahydrogen. J Phys Chem C. 2019;18(123):11734–11744.

6. Kovtunov KV, Truong ML, Barskiy DA, Koptyug IV, Coffey AM, Waddell KW, Chekmenev EY. Long-lived Spin States for Low-field Hyperpolarized Gas MRI. Chem Eur J. 2014;20(45):14629–14632.

Figures

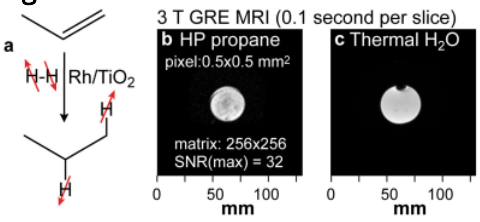

Figure 1. a) Schematic of the heterogeneous reaction of pairwise parahydrogen addition to propylene to produce hyperpolarized propane gas; b) slice-selective (5 mm thickness) 2D GRE imaging of HP propane gas in a hollow-sphere phantom using wrist RF coil of 3T clinical MRI scanner: 256x256 matrix, FOV=130x130 mm^2, SNR(max) = 32; c) corresponding image of thermally polarized water phantom.

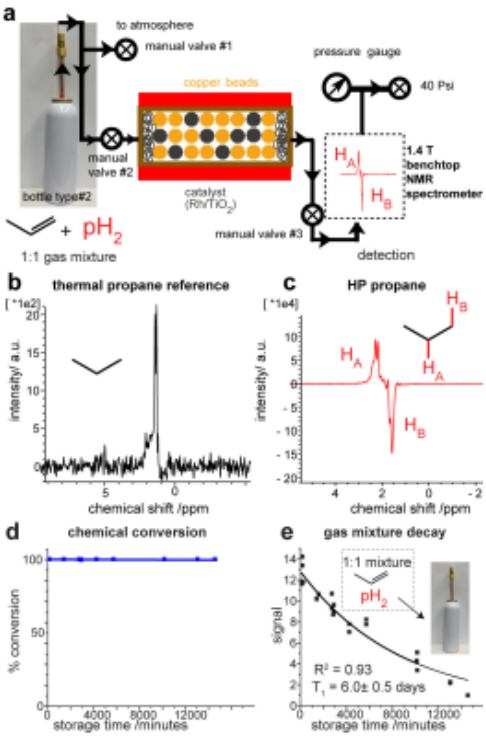

Figure 2. a) Schematic of the experimental setup --- valves are optional and were employed for the phantom studies only; b) thermal spectrum of produced propane gas – the spectrum is employed as a thermal reference for measuring polarization level of produced HP propane gas; c) NMR spectrum of HP propane gas acquired using 1.4 T bench-top NMR spectrometer; d) chemical conversion of the reactor monitored over approximately two week's time; e) exponential decay of the gas mixture potency due to parahydrogen decay in the handheld aluminum storage container (commercial spray can).

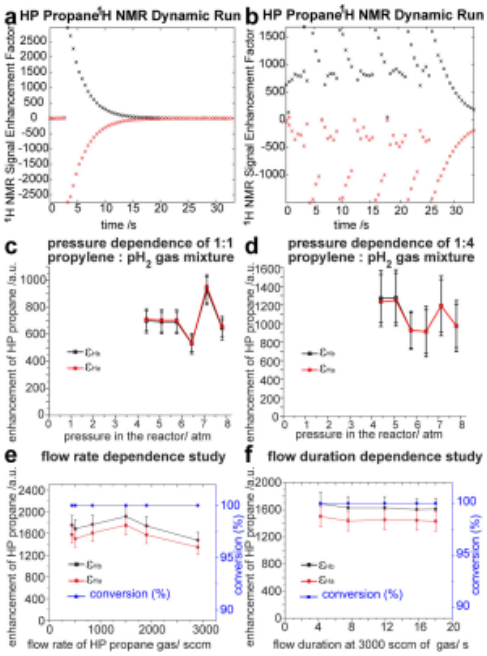

Figure 3. a) production of HP propane gas monitored by pseudo 2D acquisition method at 7.5 standard liters per minute (SML) gas flow rate of the reagent gas mixture. The gas flow is terminated approximately 3 s after acquisition start followed by the T_1 decay. b) Similar dynamic run with multiple gas flow terminations and restarts; c) and d) are the respective signal dependencies of HP propane on the pressure. e) and f) are signal dependencies of HP propane on the flow rate and gas flow duration.

Figure 4. Photograph of the experimental setup employed for 3 T imaging studies in phantoms. The valves are optional and will be obviated for future in vivo studies.

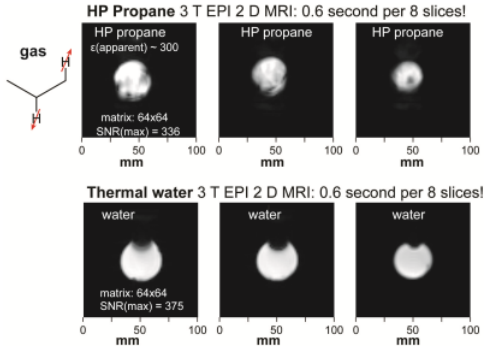

Figure 5. Sub-second multi-slice (8 slices) 2D EPI MRI of hyperpolarized propane gas (top) and thermally polarized (bottom) water phantoms of the same geometry: 17.5 mL hollow phantom sphere. All images were acquired using 3 T clinical MRI scanner using 64x64x8 matrix size, 100x100x40 mm FOV with 5 mm slice thickness. Total scan time is 0.6 seconds. Apparent maximum signal enhancement of HP propane gas was ~300 and the maximum SNR of HP propane gas image was 336.